Tuneable graphite intercalates for hydrogen storage

Arthur Lovell

A Thesis presented for the degree of
Doctor of Philosophy

Condensed Matter and Materials Physics
Department of Physics and Astronomy
University College London
England

September 2007

Declaration

I, Arthur Lovell, confirm that the work presented in this thesis is my own. Where information has been derived from other sources, I confirm that this has been indicated in the thesis. The work in this thesis is based on research carried out at the Condensed Matter and Materials Physics Group, the Department of Physics and Astronomy, University College London, England. No part of this thesis has been submitted elsewhere for any other degree or qualification.

Tuneable graphite intercalates for hydrogen storage

Arthur Lovell

Submitted for the degree of Doctor of Philosophy
September 2007

Abstract

The development of hydrogen as an energy transfer mechanism is of great importance to alleviate environmental damage and economic destabilisation caused by over-reliance on oil, as long as the hydrogen can be generated renewably. To be suitable for road transport applications, safe and compact hydrogen storage systems need to be developed, the primary technological motivation for this PhD project which investigates hydrogen absorbed into graphite intercalation compounds (GICs), to gain a fundamental physical understanding of the sorption processes to improve such materials' capacity for hydrogen storage. Literature searching has led to a principal investigation, primarily using neutron scattering and thermogravimetry, of potassium and calcium-GICs with hydrogen. Inelastic neutron scattering on hydrogenated KC_{24} has shown hydrogen sorption in this system to be quantitatively different from its analogues RbC_{24} and CsC_{24}. A consistent model of the H_2 sites and dynamics has been proposed. Time-resolved structural data on the hydriding phase transition in KC_8H_x have been obtained. A calcium-ammonia intercalate has shown most promise for hydrogen storage, with uptake of 3.2 wt.% H_2 at 77 K and 2 bar, a significant amount of the 6 wt.% target set by the US DoE. It is concluded that available internal volume and donor charge in GICs are critical parameters for optimising hydrogen uptake.

Dedicated to

Jungmin

Acknowledgments

There are many people due thanks for their contributions to this work, and they broadly fall into two categories: academic colleagues, and friends. It is a great privilege for me that so many are members of both camps.

Primarily, I thank Neal Skipper for his equally fine attributes of prolific inspiration, relaxed supervision and unfailing good (not to mention dry) humour. Despite an ever-expanding panoply of research interests, he has always been available for discussion, advice, encouragement, expenses claims, and sitting in instrument cabins until the small hours.

I thank Steve Bennington for his second supervision and CASE sponsorship, collaboration on diffraction refinement and on writing the two papers (so far). Many thanks also to Felix Fernandez-Alonso for, as they say, useful discussions, and for entitling me to include the CASTEP work and the siting model, not to mention being local contact on IRIS. And thanks to Mark Ellerby for advice, help and the occasional pat on the back!

At ISIS I should acknowledge Ron Smith, Mark Adams, Stewart Parker and Timmy Ramirez-Cuesta, instrument scientists; Alex Hannon for assistance with pycnometry; Andy Church and the sample environment staff; Keith Refson, Dickon Champion and the User Office. The list in London is long, but here goes: John Dumper and MAPS workshop; John the glassblower; Catherine Jones, Muna Dar and Denise Ottley; Tony Harker, Peter Storey and the Graduate School for conference funding; Tony again for discussions and support; Sian Fogden for more pycnometry; Bernard Bristoll, Rafid Jawad, Mar-

tin Palmer and Mark Sterling for various lendings and borrowings, and Mike Cresswell for radiation badges.

Steve Leake and Chris Howard made the earlier ammoniated-Ca-GIC samples, and allowed me to use an SEM image. Both helped with running the IGA, and Chris assisted with sample synthesis on various occasions.

Helen Walker I thank for providing me with the thesis template and, with Ross Springell, convincing me to write up in LaTeX. She paid the penalty by having to read my TeXnical queries night and day. I have proven that a minimal command of the coding can produce reasonable results; for deficiencies blame neither them, nor LaTeX, but me. I also have to thank Ross for many fruitful discussions, usually about 21 Down.

Among other friends, colleagues and fellow-travellers, I'm grateful to Tom Weller, Emily Milner, Helen Thompson, Cecilia Gejke, Peter Lock, Jonathan Wasse, Zeynep Kurban, Tom Headen, Emma Wilson, Steve Hussey, Clare Leavey, Helen Hanlon, Jenny Riesz and Kat Stockton (not least for getting a Science paper from her Masters project eventually!), and all office, lab and tea mates past and present. I apologise to anybody omitted from this list, and thank them too.

I wish finally to say a big thank-you to my family, particularly my parents, Martin and Kate, for the unstinting support I've always received and hopefully never under-appreciated, and Jungmin Kim, whose love, faith and encouragement have more than outweighed her ability to distract me, and to whom I dedicate this thesis.

This work was funded by EPSRC and CCLRC.

Thesis information

This thesis was typeset using a LaTeX template originating with M. Imran and modified by H. Walker (2006). The image files were made in a variety of environments down to and including MS Paint. The 3D structure renderings were made using Accelrys Materials Studio. The neutron instrument figures were hand-drawn by the author, scanned and digitally manipulated before being included. I hope I can be forgiven for resisting the urge to start each chapter with an apposite quotation.

The total number of words in the document is 56,324 in chapter body text, or 61,775 including titles, image captions and prefaces.

Contents

List of Figures

List of Tables

Chapter 1

Introduction

1.1 Thesis motivation

Hydrogen storage is an area of research driven by technological and environmental considerations. The unrestricted use of fossil fuels by human society threatens global climate change because of the emission of carbon dioxide and other 'greenhouse gases'. The prospect of energy supplies failing to meet demand in the near future threatens the economic development of society, so there is an acute need for alternative energy sources. While fixed-base energy requirements may be served with renewably-sourced electricity, hydrogen has been visualised as an energy vector underpinning a non-CO_2-emitting transport economy, because in an H_2 fuel cell no emissions other than water are produced. Hydrogen is portable but its low density and flammability make it difficult to store safely in large quantities in road transport applications. The storage problem is exciting much interest in academic and industrial research.

The principal hydrogen storage methods used hitherto have been storage as a compressed gas and as a cryogenic liquid. Solid-state storage of hydrogen

chemically or as a gas inside a host matrix has several potential advantages, including a theoretically higher density of storage and greatly reduced gas leakage in the event of containment failure of the storage medium. Technological rewards notwithstanding, there is a good scientific rationale for the study of candidate hydrogen storage materials to explore the open questions of gaseous behaviour in confined systems, many of which have not been fully addressed to date. This dual approach involving technological potential and physical interest has inspired and informed this project. Whilst researching for this thesis I have analysed previous studies and kept abreast of current research, including the wider ramifications of the debate about climate change and energy supply. I present in this thesis investigations into hydrogen adsorption in graphite intercalation compounds (GICs), a promising class of potential hydrogen storage materials that have not been comprehensively studied in previous work. Aside from maximising the density of hydrogen taken up by the samples, my aim has been to discover more about the characteristics and processes governing adsorption and desorption in GICs. This is hoped to lead to a model outlining how their physical properties can be designed, or 'tuned', to optimise their storage properties, and the investigation has collected evidence to achieve this and thus provide a firm basis for future investigation.

My studies included several complementary techniques, sample synthesis and characterisation studies. The thesis is separated into a progression of literature studies, research plans, theoretical basis for experimental work and the work itself, and results and analysis for each technique. In Chapter 2, I present the background to hydrogen storage and outline the current areas of research. Chapter 3 consists of a motivation for the materials of study, including literature evidence that was used to formulate a research plan. Chapter 4 contains theoretical details of the scientific techniques used in experimentation. Chapter 5 is a detailed description of the experiments I performed including

the synthesis of samples. Chapters 6-8 report the experimental results and analysis including details of a model formed to explain the siting of hydrogen in the GIC KC_{24} by a colleague following our experiments. Chapter 9 details the general conclusions and areas for further study.

Chapter 2

Background

2.1 The motivation for hydrogen storage

2.1.1 The end of the oil era

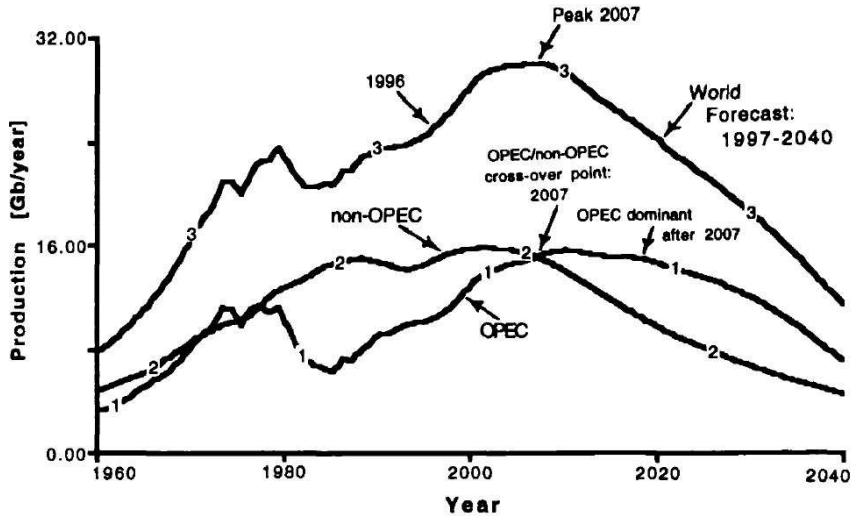

Figure 2.1: OPEC (1), non-OPEC (2) and World (3) oil production cycles for years 1960 - 2040. Shows actual production to 1996, then forecast to 2040 [1]. In this perhaps pessimistic analysis, the peak year of oil production is predicted to be 2007.

Projections for the large scale extraction of crude oil see production reaching a peak within the next few decades, with some authorities predicting that peak much sooner [1, 2]. This is the point at which the greatest rate will be extracted from known oil reserves and marks the beginning of a decline in production as existing oil fields either run dry or become uneconomical to drill (Fig. 2.1). It is unrealistic to do other than extrapolate from current trends and assert that, in the meantime, demand for oil will have grown steadily and will probably outstrip supplies at about the peak moment. In an unchecked oil-based global economy this could prove an unassailable problem. Even allowing for the exploitation of currently uncharted reserves, many of which are suspected to lie under environmentally sensitive areas such as the Alaskan Wildlife Refuge, the combined peak of production in the best case cannot be hoped to lie many years thereafter. Realistically, new discoveries, unless made very soon, can only elongate the depletion curve beyond the peak and not change the date of the peak itself. Given the myriad essential uses to which oil is put, the lack of a single substitute for most of these applications, and the rapid industrialisation of more of the world's population than before, the impending gap between supply and demand should be a cause for far more concern than is currently evident.

2.1.2 Anthropogenic climate change

During the period before and immediately after the peak, the adverse effects of a business-as-usual world economy will be aggravated, and are likely to become a more pressing threat to our activities than the oil supply itself. Potentially the most serious of these effects is human-induced climate change resulting from emissions of atmospheric-heating gases, of which the largest by volume is carbon dioxide. Carbon dioxide is produced as an exhaust product in virtually

all combustion processes using hydrocarbon fuels distilled from crude oil, coal or natural gas. It is also released during deforestation processes, which have the added disadvantage of reducing the ability of the world's biomass to assimilate carbon. Other important so-called 'greenhouse gases' include methane and nitrous oxide, for which the primary source of emissions is agriculture.

In the atmosphere anthropogenic greenhouse gases increase the natural blanketing effect that moderates global temperature, which works by trapping a proportion of the Earth's re-emitted solar radiation inside the ionosphere. This increase in 'radiative forcing' was widely predicted and now is shown [3] to cause global temperatures to rise, with potentially destabilising effects on the environment. Although modelling the many diverse causing factors affecting global climate and temperature, both natural and human-induced, is a challenging task, a high level of confidence has been expressed in recent research conclusions. A scientific consensus [4] emerged in recent years, based on many disparate measurements, to show that anthropogenic climate change is already occurring. The most authoritative publication to date is the Intergovernmental Panel on Climate Change (IPCC) Fourth Assessment Report of 2007 [5], which addressed the scientific evidence for warming, its predicted impacts, and mitigation strategies. Among the potential consequences is a six-degree rise in mean global temperature over the next century, causing sea levels to rise; and a greater risk of flooding in low-lying areas including many of the world's major cities. Destruction of coastal habitats, extinctions and enforced migration of species to cooler latitudes, and a reduction in the productivity of agricultural regions will likely result, potentially engendering an unprecedented disruption of humanity's relationship with the natural world.

Direct atmospheric CO_2 measurements have been made since 1958 at Mauna Loa in Hawaii, to obtain a global average far from industrial regions (Fig. 2.2). They show an accelerating increase in concentration over the entire record,

subdivided into annual cycles with a minimum coinciding with spring in the northern hemisphere, as growing plants absorb CO_2. The carbon dioxide concentration rose from 319.98 parts per million (ppm) (per volume of dry air) as the mean annual concentration in 1959, to 377.38 ppm in 2004 [6]. Historical atmospheric CO_2 concentrations have been recovered from air trapped in ice layers in Antarctica [7, 8] and elsewhere. Fig. 2.3, combining data from three Law Dome (Antarctica) ice core analyses, shows that CO_2 concentrations remained within 10 ppm of 280 ppm over much of the last thousand years, but have shown rapid increase since c.1850, coinciding with industrialisation. It tracks the atmospheric readings from a South Polar measuring station and finds them in agreement with ice core samples for the years they were taken consecutively.

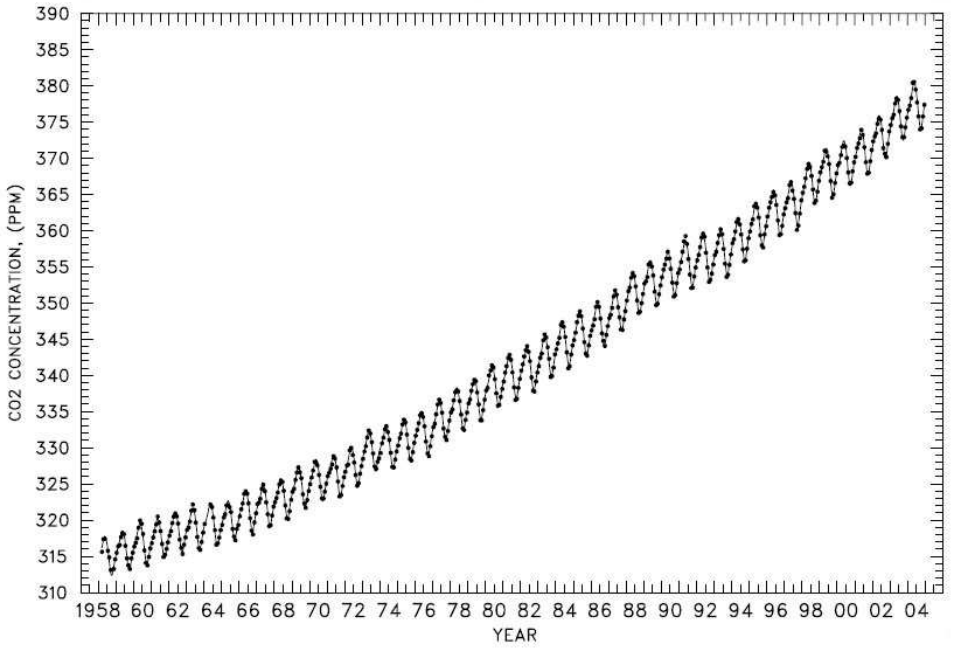

Figure 2.2: Monthly atmospheric CO_2 concentration, 1958-2004, measured at Mauna Loa observatory, Hawaii [6]

Ice core measurements dating back 420,000 years show the concentration of CO_2 and CH_4 in the atmosphere to be correlated closely with atmospheric

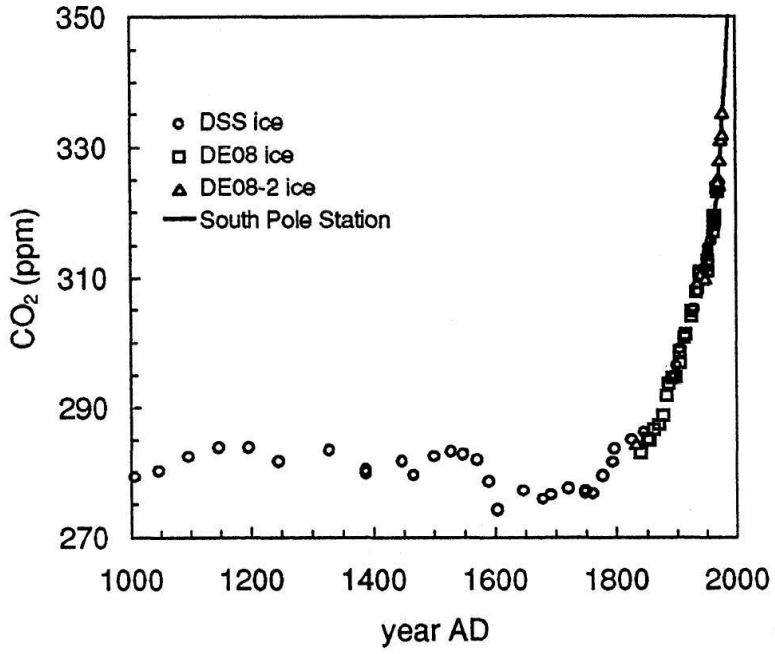

Figure 2.3: Concentration of atmospheric CO_2 over the last millennium, combining data from three ice core surveys in the Law Dome, Antarctica, and recent direct measurement at the South Pole, from [7].

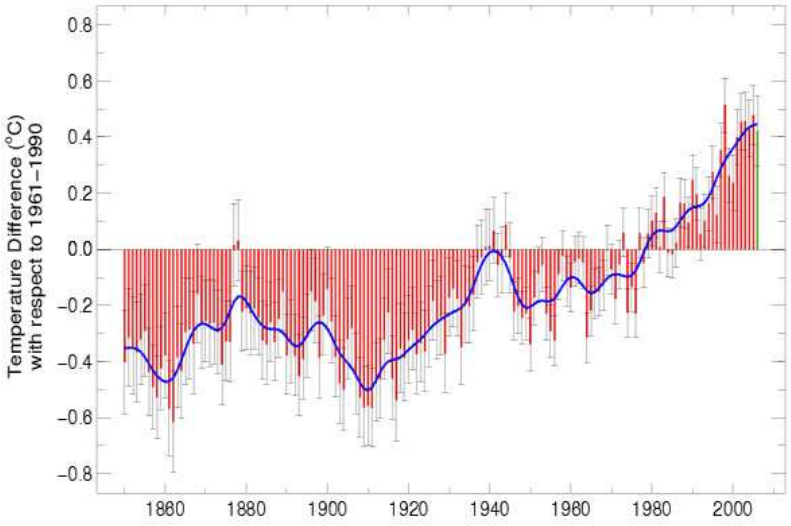

Figure 2.4: Global near-surface temperature annual anomalies 1850-2006. Adapted from [9]

temperature across ice ages and interglacial periods alike [8]. The 2005 measured CO_2 concentration of 379 ppm far exceeds any historical concentration in this period [3]. Natural variations in global temperatures are attributed to Earth-orbital variations, with short-timescale effects from vulcanism and asteroid impacts. Modelling of past increases in temperature show that higher greenhouse gas levels in the atmosphere are caused by and become driving factors for the temperature rises. This is due to a number of feedback loops; for example, the warming of oceans reduces their ability to absorb CO_2, increasing the proportion acting in the atmosphere. Melting of permafrost releases greenhouse gases from decaying biological matter. Expected decreases in growing ranges and irrigation of plants will reduce their removal of CO_2 from the atmosphere. A number of different proxy historical temperature records exist [10] and are used in modelling. Recent observations from many different disciplines confirm that warming is "unequivocal" [3]. In particular, average global air (Fig. 2.4) and ocean temperatures have risen, there is widespread melting of glacial ice, and a measured sea level rise estimated to be 0.17 ± 0.05 m over the 20th century. Due to the long time lag of climate change behind its forcing factors, a certain rise in temperature is already 'locked in' to the climate system, even if anthropogenic emissions were to cease immediately.

The causes and consequences of global climate change can be mitigated in a number of ways with favourable political, economic and social will. Greenhouse gas emissions would have to be cut considerably to stabilise their concentrations in the atmosphere. Adaptation will help to reduce negative impacts on human society and the natural world. Many of the more drastic approaches are unacceptable by current society as they would appear to entail a cut in the living standards and opportunities the developed world now takes for granted, and until it is generally understood that the potential costs of doing nothing far outweigh any short-to-mid term hardships, they will not be considered. As

more people across the world attain the lifestyle and energy consumption patterns enjoyed by the developed countries, often initially using cheaper, more polluting technology, this problem can only become exacerbated. Until very recently, political will seemed more bent to economic and social factors, and the full impetus to seek alternative power sources, limit energy consumption and redress environment damage may only come when it becomes obviously more costly to do nothing - when oil scarcity raises prices or when insurance against storms and floods becomes too expensive. The influential Stern Review [11], commissioned by the UK government and published in 2006, addressed the economic issues of climate change and concluded that preventative action investing 1 % of global GDP a year to mitigate the effects of climate change would save potential costs of 5 % GDP if no action were taken. The report was not the first to conclude that the risks and costs of untrammelled climate change outweighed those of the prophylaxis, but it has been the most high profile to date, authoritative by being a sober analysis conducted by a civil servant based on the most recent science. The report emphasises that international agreement is necessary to try and limit the total concentration of greenhouse gases to 450-550 ppm CO_2 equivalent, which would require global emissions to peak in the next 10-20 years and thereafter reduce at between 1 and 3 % a year at minimum. The scientific evidence suggests that this level is needed to prevent more than a 2° C rise in temperature. Any more than this, and the world is set onto a course of dangerous and less predictable warming with a real risk of serious economic decline and human suffering. Even if mitigation strategies were able to be implemented then, it would be wiser to search for them well ahead of time.

International governmental consensus on climate change is far from assured but is improving in a way not seen until very recently. The Kyoto agreement [12] on CO_2 emissions effectively stalled when some of the largest emitters failed

to ratify it. More recently, with growing acceptance of the scientific evidence among governments, and following several extreme weather events, such as the European heatwave (2003) and Hurricane Katrina (2005), which the IPCC predict to be more likely as warming continues, the level of public awareness is rising, leading to the possibility of a politically-favourable environment for targeting emissions. At the same time, funding by individual governments and non-governmental bodies, companies, development agencies and interested persons is resulting in a panoply of developing alternatives to fossil fuels and alleviations for environmental damage.

2.1.3 Hydrogen as energy carrier

A very promising potential replacement for petroleum spirits, coal and natural gas is hydrogen. It is referred to as an energy carrier rather than energy source because it is too volatile in its gaseous state to be obtainable naturally in any quantity. It must therefore be obtained from other materials and used as an energy-transferring intermediary.

Hydrogen can be obtained by several different synthesis routes. It is versatile, non-toxic, and combusts or otherwise oxidises to emit only water vapour and heat which makes it a potentially clean medium. It can be used to generate electricity in a fuel cell at a much greater efficiency than internal combustion. It has a high ratio of available energy to mass but, as a gas, a poor energy density as it takes up a large volume. It is particularly suited as a fuel concept for transport, mobile or off-grid electricity generation and emergency back-up power. But it can only be useful as part of an integrated solution to the energy supply problem.

Current industrial hydrogen production primarily involves petrochemical

processes, with hydrocarbons as feedstock. The steam reformation of natural gas, which produces CO_2, is a typical method. Others include partial oxidation and cracking. Hydrogen is also produced as a byproduct of other chemical processes. Most of the hydrogen produced currently is used to produce other materials such as ammonia and methanol, in steel production, the treatment of fats, and the manufacture of glass and electronics.

The simplest and cleanest way to obtain hydrogen in bulk is to electrolyse water. But if the electricity used comes from the combustion of fossil fuels, then the pollution problem has merely been transferred from the point of use — a car exhaust, for example — to a centralised generating point. Worse, because the hydrogen is a third generation fuel, efficiency losses make it much less polluting to burn the fossil fuel in the car instead.

Hence, only with a clean network of renewable electricity generators producing power surplus to the more modest electricity demands of power-efficient industry and homes does it become cleaner to run a car on hydrogen than petrol. There is a long way to go before that happens, irrespective of the development of hydrogen technology. Development of large amounts of renewable generating capacity is slow but accelerating. It is all the more imperative, then, that hydrogen technology is improved and tested in advance of that time so that it works well and safely when it can make a difference. Even removing pollution to further upstream in the energy chain would have a local benefit — if diesel exhaust emissions could be cut or abolished in cities then a substantial decrease in respiratory illnesses and cancers could reasonably be expected. Proving projects for zero-CO_2-emitting transport include the Clean Urban Transport for Europe (CUTE) trials, which ran hydrogen buses (Fig. 2.5) in nine European cities between 2003 and 2006, on standard routes using a variety of methods to generate, transport and store the hydrogen at refuelling sites [13]. Urban diesel buses are a significant producer of particu-

late pollution. Public transport constitutes an area where early adoption costs of the new technology can be borne by government, thus encouraging later uptake by private users.

Figure 2.5: Clean Urban Transport for Europe (CUTE) hydrogen fuel cell bus in London [14]

2.1.4 Hydrogen fuel cells

The hydrogen fuel cell incorporates a technology that has been understood since the early 19th century [15]. The process utilises a reverse electrolysis where the controlled recombination of hydrogen and oxygen produces an electric current and, as waste product, water. The first 5 kW device was demonstrated by Francis Thomas Bacon in 1959. The development of fuel cells was contracted by NASA for the space programme in the 1960s, and they proved suitable for spacecraft applications as a lightweight generator using available hydrogen and oxygen fuel to produce electricity and potable water.

A fuel cell consists of an electrolyte separating the fuel from the oxidant, in

the presence of which the two reactants combine, producing energy. The most common variant is the polymer electrolyte membrane (PEM), also known as the proton exchange membrane, fuel cell. Fig. 2.6 shows the cell in operation. The incoming hydrogen molecules diffuse to the anode, where they dissociate. An electrically-insulating solid polymer acts as electrolyte and conducts hydrogen protons from anode to cathode, while constraining the electrons to flow around the cell, driving a current. On the cathode side they are combined with oxygen atoms to form water, which is removed. The electrodes are usually of metal or carbon, sometimes nanotubes. They are backed with carbon paper to separate them from the electrolyte, and are impregnated with a catalyst, usually platinum.

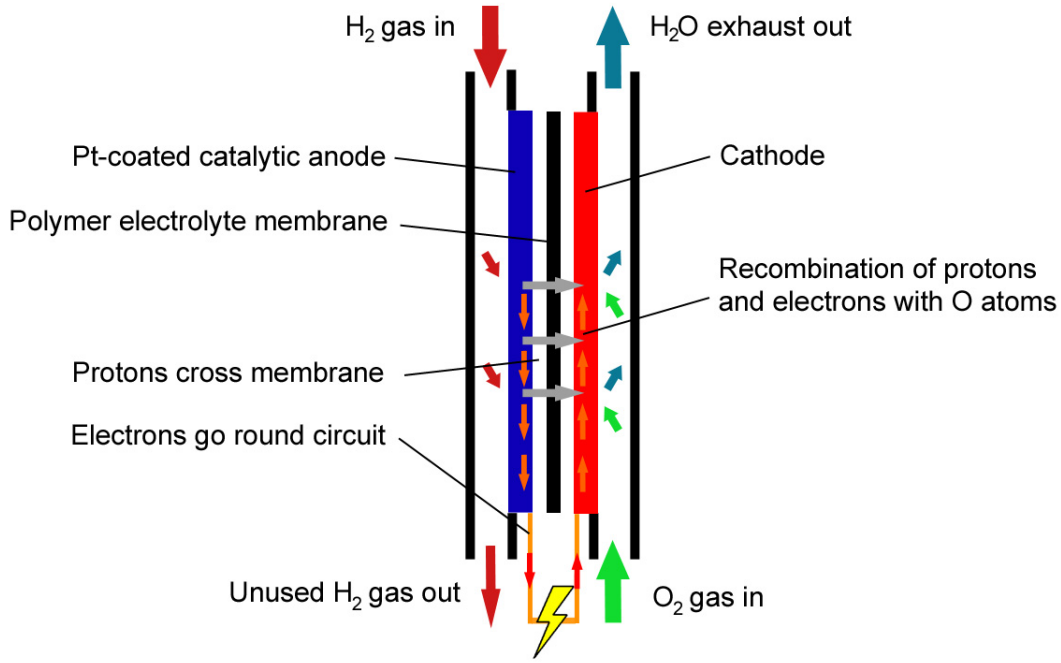

Figure 2.6: Operation of a polymer electrolyte membrane (PEM) fuel cell

A single fuel cell produces typically ∼1 V. To achieve greater potentials, cells are stacked in series. A typical energy conversion density required for a car is 2 kW/litre.

A fuel cell does not operate with a thermal cycle and is not constrained by the Carnot cycle's maximum efficiency. Thus fuel cells can be made more efficient than internal combustion engines (ICEs) burning hydrogen as a fuel. This is a significant advantage when looking at the overall system efficiency for powering a car, for example. In industry terminology this is known as the "well-to-wheel" efficiency. Using a fuel cell rather than ICE helps to counteract the efficiency penalty of synthesising the hydrogen from hydrocarbon feedstocks.

2.1.5 New hydrogen synthesis pathways

For fuel cells to successfully reduce the emission of carbon dioxide and other greenhouse gases, the hydrogen used as fuel needs to be derived from non-polluting sources. Utilising the electrolysis of water using cleanly-generated power will only make a large difference when all present electricity needs are met cleanly first. Another solution, suitable for areas with a surplus of growing land or agricultural waste, is to obtain hydrogen from biomass. Hydrogen production from sugars has been demonstrated [16], and from ethanol [17], for which a large manufacturing industry already exists, using rhodium-ceria catalysts. The energy availability quoted [17] by this study in a perfect system is 1.27 MJ per mol of ethanol (46 g or 58 cm^3). To match the energy available in 5 kg of H_2 (620 MJ) requires 22.4 kg or 28 litres of ethanol. Such a system might in a transport context be used for on-board reforming of hydrogen from a fuel tank filled with ethanol. Drawbacks include the extra complexity of the process compared with electrolysis, the large amount of potential food-producing land used to grow plants as feedstock for the ethanol manufacturing process, and the fact that carbon dioxide is still produced although as part of a reversible cycle with photosynthesis.

A similar synthesis process might be used to obtain hydrogen from domestic

or industrial organic waste, which currently decomposes emitting methane, another greenhouse gas.

2.1.6 The hydrogen economy

Hydrogen technology suits local-level energy generation. This is a concept which sees electricity generated in a decentralised, node-based energy network using a spread of different low-output renewable resources. This has numerous advantages, including security of generation: overcoming reliance on just one energy source, which in the case of oil may come from politically unstable regions, and empowering (as well as powering) local communities, as they take a personal stake in the provenance of their energy. It would be less vulnerable to terrorist attack or climate-induced problems, being less centralised than today's system of large power stations connected by a grid. Surplus energy generated from variable renewable sources such as solar or wind could be stored locally as hydrogen, where it would otherwise be wasted, and used to cover reductions in output. Such a setup, in conjunction with a transport infrastructure configured to run by oxidation of hydrogen in fuel cells, is colloquially known as 'the Hydrogen Economy'.

A hydrogen-based economy would theoretically be very close to carbon-neutral: with judicious use of carbon storage mechanisms such as vegetation and without large-scale emissions, atmospheric carbon dioxide levels would equilibrate and could be made to fall in the direction of pre-industrial ratios. Other greenhouse gases such as methane and nitrous oxides would be emitted in much reduced quantities; virtually none would come from surface transport. Methane emitted from agriculture and the decomposition of waste could be collected and either burned, producing some CO_2, or reformed to make hydrogen. Large-scale deforestation would have to be prevented. Energy from

photovoltaic cells, wind, waves and possibly nuclear fission and agricultural waste would generate electricity for industrial and domestic use, and manufacture hydrogen for use in the transport sector and for remote and emergency generating capacity. Hydrogen could be synthesised and used locally, or manufactured centrally and transported either by pipeline or tanker, with appropriate measures of safety, to local storage sites, fuelling stations and users. A network of fuelling stations similar to today's petroleum ones would disseminate hydrogen to the public and private vehicle user.

It is clear that the simple replacement of petrol-powered private cars by fuel-cell powered ones would not address other problems related to an over-reliance on motor transport such as congestion, accidents, personal unfitness through lack of exercise and urban sprawl. Such a change will be most effective as part of an integrated transport strategy giving more weight to electrified railways and human-powered transport. A large unknown in the equation is represented by air travel, which is a rapidly expanding source of pollution and for which current fuel cell technology is less suited. A large amount of experience has been accrued by the space industry in using liquid hydrogen to power rockets and this could be adapted. Here, a shift in public attitudes still mindful of accidents such as the Hindenburg disaster and the Challenger explosion will surely be required before it is accepted.

2.1.7 Hydrogen storage

We have seen that hydrogen is unlikely to be a complete panacea for the negative aspects of our oil-based economy. Its ability to reduce CO_2 emissions will be dependent on carbon-reduced (or carbon-free) generating capacity. And its most-heralded application, in motor transport, still requires a technological breakthrough, not to make it possible, but to make it practical; and, most

importantly perhaps, to make it marketable. That breakthrough must come in storage.

Hydrogen has to be stored, on board, in quantities sufficient to give a fuel cell vehicle the same range as a petrol-fuelled one.

Two methods of storing hydrogen that are technically well-understood, because they are already used, are high pressure compression of the gas and cryogenic storage of liquid hydrogen. The development of each chiefly requires evolution of existing technologies rather than the introduction and proving of wholly new methods. The third area of research involves storing hydrogen by absorbing it chemi-physically in metal or chemical hydrides, or adsorbing it onto the surfaces and into pores of a solid state matrix. This is where the most fundamental and interesting scientific investigation is being undertaken. Recent work has focused on porous nanofibres of carbon, including nanotubes, but many controversies remain to be disentangled in this area.

Storage methods for hydrogen gas need to fulfil several important criteria. For transport applications the most important involve safety, compactness and low weight. For the purposes of basic research into hydrogen adsorption and dynamics in condensed matter systems, aiming for low weight and volume storage materials is a more easily considered goal, but the safety implications can at least be acknowledged even at an early stage of investigation. A marketable storage system for transport must be crash-safe and not release hydrogen gas rapidly if damaged. Any release of hydrogen into atmosphere incurs a large risk of explosion or rapid combustion. This risk is increased if the storage container was containing some high pressure. Hydrogen's large buoyancy and diffusion properties do, however, mean the released gas will rapidly rise and disperse, unlike leaking petrol. And the minimum ignition concentration of hydrogen in air, 4 %, is four times higher than that of petrol vapour. Hydro-

gen's low density means that it is difficult to compact efficiently. But it has considerably higher energy density by weight than petroleum derivatives, at 124 MJ kg^{-1} against 44 MJ kg^{-1} [18]. This means the weight density of storage, usually expressed as the percentage of the storage system's total weight taken up by energy-yielding fuel, need not be so large for hydrogen as for fossil fuel systems. A typical weight proportion for a conventional car fuel tank is 18 wt.%, including the tank weight and crash protection installations; to store the same amount of energy in a hydrogen system requires approximately a third of this percentage. This would give a hydrogen powered vehicle a similar range — typically 480 km (300 miles) — and power output to modern petrol cars. The US Department of Energy has set a moving target for practical hydrogen storage of 6 % by weight based on this calculation and a volumetric density of 62 kg H_2 m^{-3} by 2010, increasing to 9 wt.% by 2015 [19]. The 6 wt.% target is frequently referred to in the literature and so far has not been reliably achieved with a reversible solid state storage system.

2.2 Hydrogen storage methods

What follows is a *précis* and evaluation of the current and foreseen hydrogen storage methods. The proposals range from the tried-and-tested to the outlandish-but-just-feasible (and, in fact, take in an unhealthy amount of the not-feasible too). Hydrogen is already stored in compressed gas and liquid forms, but increasing the storage density to that required for vehicular applications is a challenge [20]. Two main areas of solid state storage are under investigation; chemical sorption of hydrogen in hydrides, and physical sorption into micro- or nanoporous materials, chiefly based on carbon allotropes. Solid state storage has the potential for high-density storage at ambient or near-ambient pressures and temperatures. It is also less likely to vent gas

uncontrollably and dangerously if the storage unit is damaged.

2.2.1 Gas compression

Hydrogen is capable of being stored at high pressures in tanks. Standard lab supplies of hydrogen are stored in steel cylinders at 25 MPa (250 bar), and delivery is usually at some lower pressure via a regulator. This technology is well-developed, has been used for a long time, and requires little adaptation for stationary energy storage applications. Many of the fuel cell vehicle demonstration projects, for example the CUTE project [13], have used compressed gas storage of hydrogen. Hydrogen's major drawback is its large volume to energy ratio, with considerable tank volumes required to store a significant amount of hydrogen at 25 MPa. If the working pressure of the system is increased, the stored weight of hydrogen can be augmented, but the overall system weight increases as the tank has to be strengthened. Safety implications and, for real-world applications such as transport, public fears, set a *de facto* limit on the maximum pressure that can be used. A standard 24.5 MPa (245 bar) cylinder of size commensurate with installation in a private car would give a range of 200 km. Under development are 68 MPa storage tanks, for which a range of system geometries are being considered [21]. This would give the required vehicle range of 480 km but would impose a much greater explosion risk in the event of an accident.

The contemporary standard in tank design is the Type IV all-composite tank [22,23]. A working design by Quantum Technologies is shown in Fig. 2.7. It is constructed with a high density polyethylene thermoplastic liner, which is structurally overwrapped with carbon fibre bonded with epoxy resin. An outer, impact-resistant shell is structurally enhanced at vulnerable points with urethane foam. An internal regulator issues gas at low pressure, obviating the

need for a high-pressure gas transfer system.

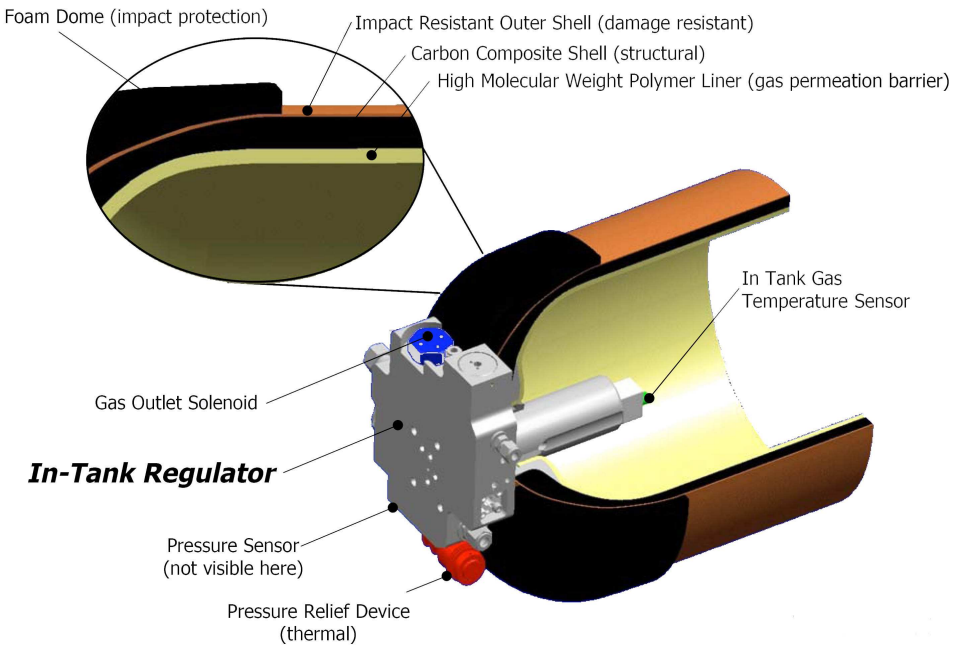

Figure 2.7: Design for Type IV high-pressure hydrogen tank by Quantum Technologies [23]

The use of composites rather than traditional high-strength steel decreases the required weight of material and reduces embrittlement problems associated with the high diffusion coefficient of molecular hydrogen, from which mild steels in particular suffer. The thermoplastic liner is designed to be impermeable to hydrogen. For safety certification the tank is subjected to rapid loading and unloading cycles, extreme variation in temperature, overpressure, physical shock and penetration, usually by a high velocity firearm round. In the event of a piercing of the tank fragmentation must not occur; instead the gas may be released in a controlled way.

The largest drawback with the Quantum Technologies tank is the high cost of aerospace-grade carbon fibres, which have the tensile strength required to make the tank weight viable. Reducing the quality of the carbon fibre used decreases the storage capacity. The current (2006) performance of the lower cost tank system against key targets is shown in Table 2.1.

Table 2.1: High pressure hydrogen gas storage system performance comparison with DoE targets. Reproduced from [24]

Storage parameter	Units	2007 target	2010 target	Quantum system (2006)
Specific energy	kWh/kg	1.5	2.0	1.3
Energy density	kWh/litre	1.2	1.5	0.8
System cost	US$/kWh	6	4	10

The theoretical energy cost associated with compression of hydrogen to 80 MPa is 2.21 kWh kg^{-1} [25] although in practice this would be higher.

2.2.2 Gas liquefaction

Hydrogen can be stored with a significantly more favourable density as a cryogenic liquid. The density of liquid hydrogen is 70.8 kg m^{-3} [26]. Significant losses of hydrogen are suffered from boil-off, which can be reduced by effective thermal insulation. The technique benefits from advanced technological developments gained from the aerospace industry and pilot projects in hydrogen refuelling stations. BMW demonstrated a tank system where evaporation losses were less than 1.5 wt.% per day, although any gradual loss would militate against long-term storage applications such as back-up power supplies or remote off-grid generation capabilities, unless regular re-supply were possible or space an important constraint.

Considering safety, in the event of damage to the tank or insulation there would be less overpressure until the liquid started to boil; thereafter the same risks that attend a release of compressed gas would apply. Cryogenic hydrogen would conceivably represent a risk of burns. Boil-off should diffuse rapidly

assuming well-designed ventilation.

The greatest drawback to liquid gas storage is the large energy input required to cool and condense the gas. At atmospheric pressure, the condensation temperature of H_2 is 20 K (-253°C) and the vaporisation enthalpy at the boiling point is 452 kJ kg^{-1}. The specific heat is 14.3 kJ kg^{-1} K^{-1}. To liquefy 5 kg of H_2 takes at least 2260 kJ at 20 K; to cool 5 kg from ambient temperatures (295 K) to 20 K means removing a further 19,660 kJ of heat. Assuming a 60 % efficient cooling engine means the input work required is 37 MJ, about 5% of the 620 MJ available from the 5 kg of hydrogen. Factor in boil-off losses and 'real' engineering and this proportion could rise considerably [25]. On the other hand, that 5 kg could be stored in only 0.07 m^3, making it a compact solution.

2.2.3 Metal hydrides

Hydrogen can be stored reversibly by reacting the gas with specific pure or alloyed metals to form metal hydrides. These decompose when heated, releasing hydrogen. Storage densities for some hydrides are considerably higher than standard compression or liquid storage, as Fig. 2.8 illustrates schematically. Magnesium hydride, MgH_2, by dint of structural simplicity and magnesium's relatively high position in the periodic table, has good weight storage of hydrogen, 7.6 %, which fulfils the DoE requirement for this property.

Absorption enthalpies for hydrides are favourable for gas uptake but often require a large endothermic input to release hydrogen. The available weight density of hydrogen is heavily dependent on the other species comprising the hydride. Alloys from lighter elements are advantageous for this reason, but require high temperatures for hydrogen delivery. Other considerations are the

bulk availability, toxicity and cost of the material.

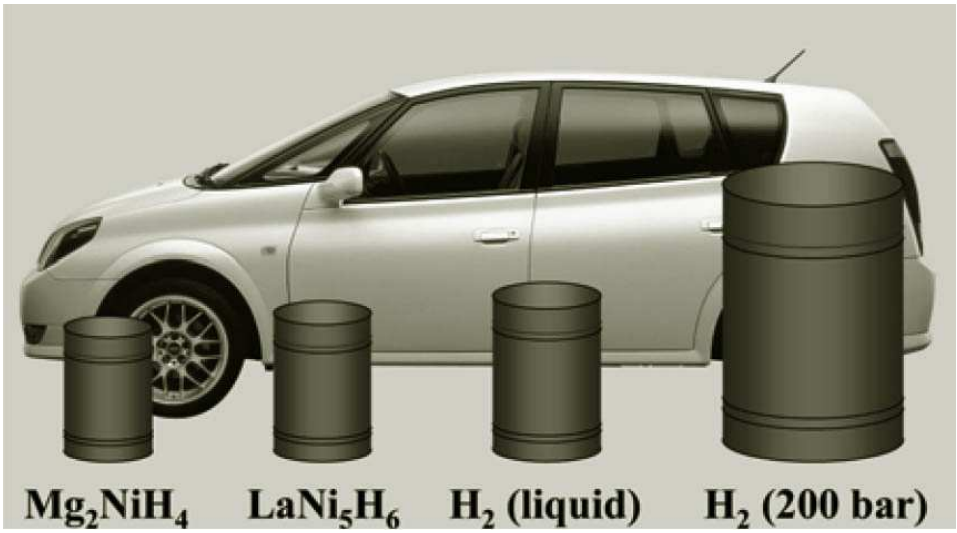

Figure 2.8: Volume comparisons for 5 kg H_2 stored in two metal hydrides, as liquid and compressed gas at 20 MPa. Graphic by Toyota

The process by which hydrogen is retained by a hydriding material is generally a dissociation of the molecule into H atoms which bond covalently with the host atoms. To retrieve the hydrogen in gas form, enough thermal energy must be supplied to break these bonds and allow the hydrogen molecules to reform. Release temperatures for higher-storage-density alloys such as MgH_2 are considerably higher than ambient ($\sim$300°C) but lower temperature materials such as $LaNi_5H_6$ have low storage density and considerable weight. Potential development hinges on finding higher density storage alloys with release temperatures little above ambient and suitable kinetic characteristics. Removing the exothermic heat from the storage material on loading is also problematic.

The breadth of investigation into hydride development is great [27,28], and many different candidate materials are known. Current research is focused on tailoring all the properties of the material to meet with storage targets. Current materials that are show strong potential include alanates and borohydrides. For example, the sodium alanate $NaAlH_4$ contains 7.9 wt.% hydrogen, of which

a maximum of 5.5 wt.% can be desorbed at 260°C. Mechanical grinding and chemical modification [29] can lower this value to 180°C for removal of 4.5-5 wt.%, but this is still higher than desired. Catalysing this system is beginning to allow desorption at temperatures close to ambient [30].

2.2.4 Physisorption systems

Hydrogen molecules are non-polar, but possess quadrupolar characteristics and can be adsorbed onto planar surfaces by means of weak van der Waals interactions. This is the basis for storage systems using physisorption as an entraining process. Many porous solid state systems are known to absorb gases, and these have applications, for example as purification filters in an airstream. Hydrogen is known to bond to surfaces such as graphene sheets, where the molecule rotates with a slightly reduced energy from a free hydrogen rotation [31]. The amount of hydrogen absorbed is suspected to increase with the surface area of the host, making meso- and nano-porous materials with high internal surface area most effective. As well as porous graphite-based materials [32], other good candidates for physisorption hosts include metal-organic frameworks [33], zeolites and clathrates.

The advantages of physically rather than chemically retaining hydrogen in a storage medium are principally two-fold; a low enthalpy of adsorption compared with a hydride reaction, and, related to that, fast and easily reversible sorption kinetics in relatively benign conditions. Further benefits may accrue if a plentiful and low-weight material such as carbon is the mainstay host material. The physisorption of hydrogen is considerably improved if its thermal energy is reduced from that available in ambient conditions to cryogenic temperatures. Doping materials with donor metal species can also improve sorption, by altering the charge properties to make hydrogen siting more

favourable.

A lot of recent interest has centred on nanotubes and other exotic carbon structures [34]. Carbon nanotubes are formed of cylindrically-rolled sheets of covalently bonded carbon atoms: essentially, a graphene sheet wrapped into a tube. At the meso-scale they are quasi-one-dimensional; varying in diameter on a nanometre scale but in length on a micron scale. If many tubes lie inside others with decreasing diameter, the overall structure is called a multi-walled nanotube (MWNT). A single rolled graphene sheet, most often capped at each end with half-fullerene domes, and empty of other material, is a single-walled nanotube (SWNT). A source of considerable excitement among researchers is that the physical properties of nanotubes vary widely depending on the diameter of the tube and the chiral angle at which the graphene hexagons are wrapped relative to the main body of the tube. A tube wrapped from a sheet at one angle may be a highly efficient conductor, transferring electrons ballistically along its length. A tube constructed with a different angle may be semi-metallic or even insulating, suggesting a potential for very small semiconductor devices to rival current integrated circuit technology. Already, nanotubes have been used as AFM and STM tips. A source of considerable frustration is that no method has yet succeeded in separating out in bulk the differently-characterised nanotubes which would be the first step to the large-scale study of their electronic properties.

The interest in nanotubes, as with other forms of carbon, as a hydrogen storage medium is predicated on the large surface area of carbon available for the physisorption of H_2 molecules. Some impressive results were announced — room temperature hydrogen capacities ranging from 4 to 13 wt.% in SWNTs. One claim, by Chambers *et al.* [35] for the related carbon nanofibres was as high as 67 wt.%. Ye *et al.* [36] were apparently able to achieve a maximum of $\sim$8 wt.% at cryogenic temperatures (80 K) and largely increased pressures (over

60 bar) which appeared inconsistent with the results for ambient temperature and pressure. Chen *et al.* [37] reported 14 and 20 wt.% hydrogen uptake in metal-doped nanotubes. Further studies on a variety of carbon structures suggested a maximum takeup of hydrogen of 0.7 wt.% at 105 bar at room temperature [38]. This introduced a dichotomy which with follow-up work [39] has led to a considerable lessening of confidence in the earlier claims. One potential source of error was in water content of the sample; another in the metal catalysts still present in nanotubes after synthesis.

Although the excess adsorption density correlates linearly with pore size and specific surface area [40], the adsorption capabilities of undoped carbon nanostructures do not approach the DoE targets. The curved walls of the SWNT define a volume into which is difficult to insert hydrogen. If the ends of the tube are capped it is virtually impossible to allow H_2 molecules inside the tube. Using MWNTs also reduces the weight percentage of hydrogen, yet a reliable large scale method of separation of single-walled from multiply-walled tubes is not yet known because they are difficult to dissolve. Technologically at least there are purification issues which need to be resolved but even so it seems unlikely that pure nanotubes can reversibly hold a suitable amount of hydrogen except possibly at low temperatures and high pressures. It seemed a more promising route to revisit an important group of compounds made by inserting host metals into graphite, where some work with hydrogen had already been done, and where the potential for storage seemed considerably higher: graphite intercalation compounds.

Chapter 3

Graphite intercalation compounds and hydrogen

3.1 Graphite intercalates

3.1.1 Structure and properties of graphite

Graphite is an allotrope of carbon constructed of stacked lamellar structures of single-atom thickness. Each sheet, known as graphene, contains carbon atoms bonded hexagonally, so each carbon has three bonds separated by 120°, one to each of its three nearest neighbours. The bonding between the sheets is weak, being composed of van der Waals interactions $\sim \frac{1}{300}$th of the C-C bond strength, and it is this difference between the in-plane graphene bonding and the out-of-plane interactions that cause the large anisotropic properties so characteristic of graphite and its more exotic cousins such as carbon nanotubes. For example, the electrical resistivity of pure graphite is approximately one thousand times greater across the interlayer spacings than it is in any di-

rection in the graphene planes [41], where free electrons have much greater mobility. Although in pure graphite the planes register regularly with an A-B-A (hexagonal), or more rarely A-B-C-A (rhombohedral), stacking pattern, very little lateral force is required to make the planes slip along one another, as the local energy minimum for each carbon atom to be in the centre of a hexagon in the layer above is not very deep. This makes graphite technologically applicable for uses such as lubrication, and is how graphite transfers from pencil 'lead' to paper. Graphite sheets can be used for thermal insulation as their thermal conductivity is poor in the interlayer direction; this is one of the principal marketable uses for exfoliated flexible graphite (see § 3.2.2), used in the project in somewhat smaller quantities!

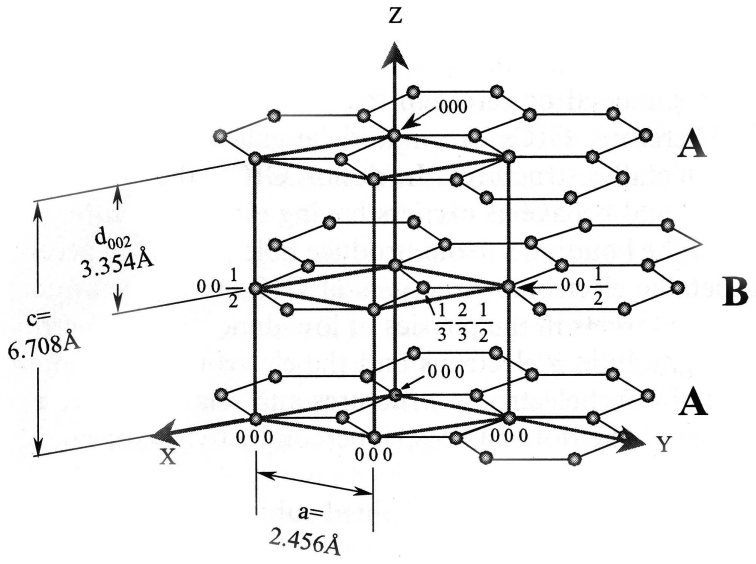

Figure 3.1: Structure and unit cell of graphite from [41]

The crystal structure of A-B-A graphite is $P6_3mmc$ and is shown with standard dimensions in Fig. 3.1. The C-C nearest neighbour distance is 1.42 Å.

A carbon atom has electronic shell configuration $1s^2 2s^2 2p^2$. Allowing each

carbon to bond with its three nearest neighbours gives rise to sp^2 hybridisation. Three electrons form covalent σ-bonds with the neighbouring C atoms and the fourth forms a delocalised π-bond: by analogy the graphene sheet can be interpreted as an interlocking set of aromatic rings. In the graphene plane the binding energy is 7 eV/atom [41]. Graphene is modelled as a zero band-gap semiconductor. The unit cell of 3D graphite has four atoms, and a weak overlapping of the π-bands leads to a 0.02 eV/atom binding energy between the planes and hence the semi-metallic nature of 3D graphite.

The loose, open structure of the interlamellar spacings, often referred to as 'galleries', is an environment that accepts guest species readily. Irregularly porous 'activated carbons' are frequently used as purifying filters for their willingness to accept impurities; graphite too accepts a great number of different examples. Many of these are stably absorbed under certain ranges of environment and remain inside the lattice in a process called intercalation. Such compounds, consisting of graphite 'host' and intercalated 'guest(s)', are collectively known as graphite intercalation compounds, shortened most often to GICs (Fig. 3.2).

3.1.2 Intercalation into graphite

Graphite is amphoteric: this means it accepts both positively and negatively charged intercalant species [42]. When readily-charged intercalants are accepted into the galleries, they may exchange charge with the π-bands in the graphene sheets above and below themselves, thus changing the fundamental electronic properties of the graphite superstructure. Simultaneously their presence between the layers often results in the layers being pushed apart, either as a charge effect or more simply by the physical size of the guest. This expands the c-lattice parameter (by crystallographic convention the a and b lattice vec-

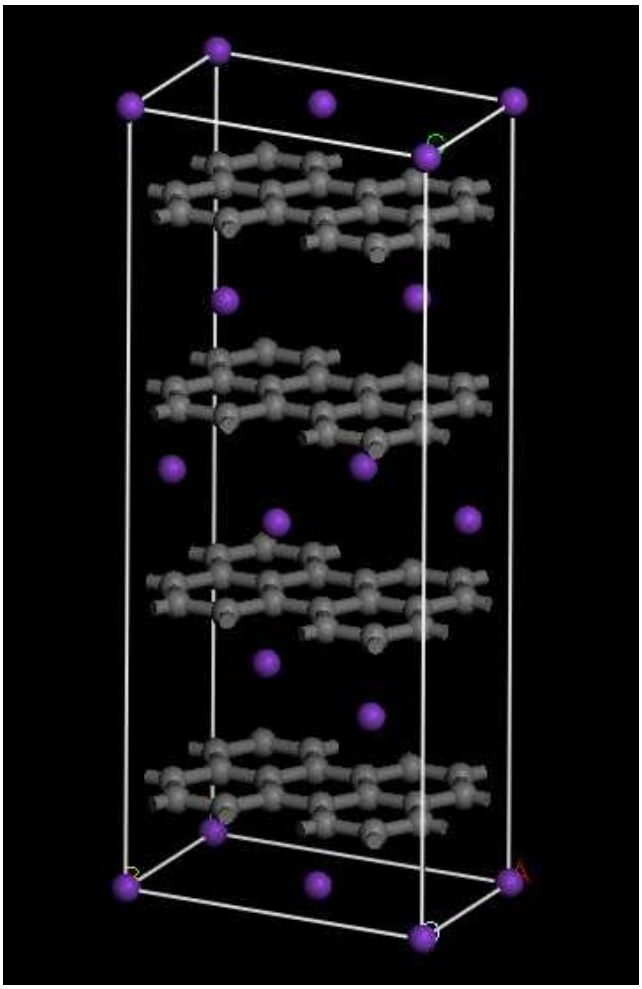

Figure 3.2: An intercalation compound (KC_8) of graphite, showing the guest species (purple) in the interlayer spaces. The graphene-graphene distance is increased from that of pure graphite, in this case from 3.35 to 5.35 Å.

tors are held to be in the graphite plane) and in a homogeneous intercalated sample this expansion of the third dimension will be readily apparent, even visible to the naked eye in many cases. Although many materials can form GICs, not all syntheses are energetically favourable and many are quite difficult to perform, especially if the intercalation is to be carried out homogeneously throughout a bulk sample rather than just in the surface layers. The direction of the charge transfer is evidently dependent on whether the intercalant is a donor or an acceptor species. Examples of donor intercalants include the alkali metals, alkaline earths (e.g. Ca, Sr) and rare earth metals such as Eu and Yb. Examples of acceptor compounds include Br_2, metal halides, and acids such as H_2SO_4 and HNO_3.

A particularly relevant example is GICs formed by the enticement of certain alkali metal species into graphite [41]. Alkali-metal graphite intercalation compounds (AM-GICs) have been studied extensively as they are extremely interesting materials. They demonstrate selective charging of the 2D graphene sheets based on the intercalant density. They have the beneficial attribute of long-distance homogeneity in the positioning of the intercalated metal ions in graphite galleries, denoted stage-n, where n is the integer of graphene planes between each intercalated layer. A stage-1 AM-GIC such as KC_8 (Fig. 3.3) contains metal ions between every graphene layer and is therefore the most densely intercalated compound possible, in the absence of added external stimuli such as pressurisation. By comparison, stage-2 KC_{24} has alternately filled and empty galleries, and as can be seen from the stoichiometry, each filled layer is only 2/3 as densely populated with K as a filled layer in the first stage. This fact holds for Cs- and Rb-GICs as well, which have the same carbon-relative composition as K-GICs. This contrasts with lithium-GICs, for example, where the stage-1 compound has the composition LiC_6 and the stage-2 composition is the expected LiC_{12}.

This staging property makes many GICs able to form well-characterised structures across large length scales, even up to stages as high as 12. Their electronic structure leads to high conductivity in the *a*-*b* plane, magnetic properties such as spin frustration, and several have been found to be superconducting [41]. In all, they are particularly useful test grounds for the study of systems confined to planar geometry and the 2D transport mechanisms resulting.

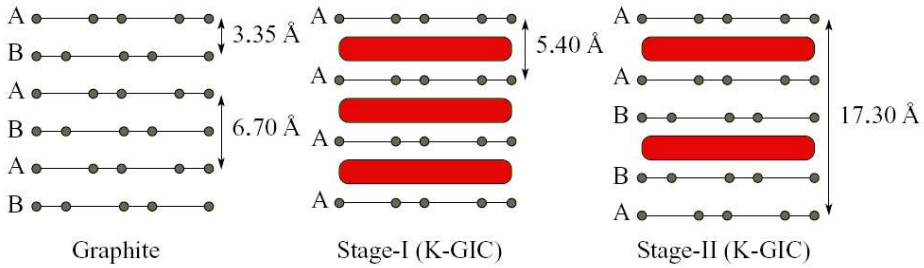

Figure 3.3: Graphite stacking and interlayer spacings for pure graphite, stage-1 and stage-2 potassium graphite intercalation compounds. Red bars denote metal layers. Adapted from [43]

The stage dependence of the c-axis lattice spacing I_c is trivially given by

$$I_c(\text{Å}) = d_s + 3.35(n-1) \tag{3.1}$$

where n is the stage number and d_s the interlayer distance of a fully-intercalated gallery.

Retaining our focus on the alkali-metal GICs, it is widely believed that by giving up some proportion of their single valence electron charge to the graphite lattice, alkali metal ions are pulled into the galleries and thence diffuse along them. Very quick changes of staging — for example from stage 1 to stage 2 — are observed under certain conditions in these compounds and

the exact mode for this is unclear. Metal atoms are unable to penetrate the graphene hexagons and thus change stage in a top-down or vertical way. The standard staging model, outlined by Daumas and Hérold [44], postulates a set of laterally shifting domains of intercalate held in the layers which line up periodically in the minimum energy configuration. GICs have the ability to accept further guest species, forming so-called ternary (or higher-order) GICs [42,45]. Of fundamental significance to the present work is that the uptake of these further species, particularly molecular hydrogen, is often much more energetically preferred in the GIC interlayer galleries than in pure samples of graphite. This makes graphite intercalations extremely promising as a base for absorption studies. The causes underlying this phenomenon shall be returned to shortly.

(a) KC_8

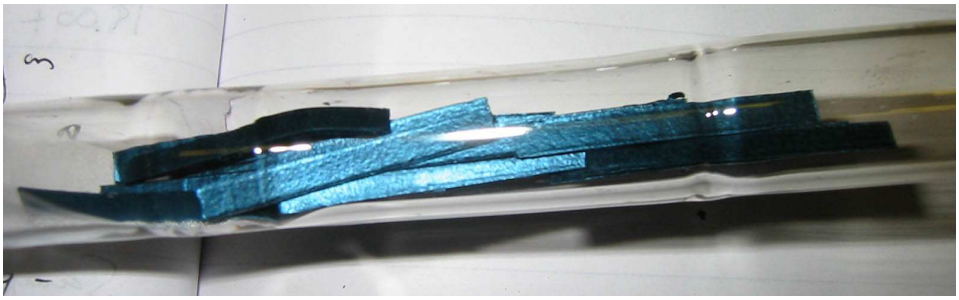

(b) KC_{24}

Figure 3.4: Characteristic colours of potassium GICs

The charge transfer to the graphite leads to characteristic colour properties of the intercalates by stage and intercalant type. These colours are intrinsically related to the band gap of the electronic interlayer states and thus related to the donated charge density. Pure KC_8, in common with RbC_8 and CsC_8, is a golden-orange colour and KC_{24} a metallic blue. Examples of both materials created according to the process outlined in § 5.1.2 are shown in Fig. 3.4. Higher stages are progressively greyer blues until indistinguishable from the grey of unadulterated graphite. The purity of the staging in a sample is easily identified by observing the sample colour. If it is homogenous then the sample has a high degree of purity. This method was used to select the best quality samples for experimentation. Mixed-phase samples, such as in Fig. 5.4, are omitted.

It is important to note that AM-GICs are in general very sensitive to oxygen, moisture and other impurities. Exposure to these results in rapid, irreversible degradation, sometimes demonstrating combustion if exposed to air. Even in atmospheres with a much lower proportion of oxygen, oxidation and desorption of the intercalant are observed to occur, resulting in a gradual return of the coloured sample to the grey of the original graphite, often with a layer of oxidised intercalant on the surface. Consequently, all sample synthesis and handling is done either under high vacuum ($< 1\times10^{-5}$ mbar) or an inert atmosphere such as high purity argon.

In the decades since the discovery and refinement of the synthesis of AM-GICs, considerable efforts have been made to characterise these materials, understand the processes by which they form and can decay, and their behaviour in conjunction with other materials. Work continues to construct more difficult intercalations; those that are much less energetically favourable or that are structurally discouraged, and so the panoply of materials suitable for adsorption studies of the present nature is increasing. Among the newer

materials are CaC_6 and YbC_6, under study for their magnetic properties in this research group. The bulk manufacture of these materials has been a recent breakthrough and they have been found to be superconducting, with transition temperatures T_c of 6.5 K for YbC_6 and 11.5 K for CaC_6 [46].

A wide-ranging review of literature published since the 1970s on the topics of graphitic compounds and exotic carbons, and their ability to accept hydrogen and other guest species internally, has been carried out and has isolated a number of potential research pathways of fundamental scientific and technological interest. Many of these have been relatively neglected hitherto, despite the unarguable topicality of hydrogen storage and the efforts that have been invested in attempts to store hydrogen in materials sharing close kinship, such as alkali-metal-doped carbon nanotubes. Certain GICs have been identified as materials with rich possibilities for development into a storage medium and the study has concentrated on these. Empirical analysis suggests that the available storage volume, dynamics and reversibility of loading in an open layered GIC system should be better than closed volume systems such as those involving fullerenes, also considered; and capped nanotubes. Technological benefits such as cheapness and relative environmental benignity also accrue with a graphite-based system. Other possible research areas involve studying hydrogen absorbed into liquid ammonia and C_{60}-graphite co-intercalation compounds, novel materials for which exist literature studies [47] and one synthesis claim, which the group is attempting to synthesise.

Original research into hydrogen uptake in GICs was carried out along with many other species to discover the sorption properties of the parent material and the novel characteristics displayed by the ternary or quaternary compounds thus created. Much of this research took a lower priority following the discovery of exotic graphitic structures; firstly fullerenes in 1985 and more recently nanotubes. When environmental concerns and developments in fuel cell

technology made hydrogen storage a research priority, much interest was shown in hydrogen in doped nanotubes and GICs, an area of considerable promise, were left largely untouched. A series of high profile claims [35, 36, 48] for extensive storage of hydrogen in undoped, and potassium and lithium-doped nanotubes [37] or microstructured carbons have been followed by embarrassing corrections or retractions [38, 39], leaving nanotube adsorption a controversial area for study, although work continues. Early studies of hydrogen in GICs were not carried out in general with the technological impetus of storage in mind, which implies that new research into these fascinating systems with the intention of evolving a successful storage system is timely and potentially very valuable. Furthermore, a number of issues relating even to the well-known GIC systems have never been fully resolved, and it has been worth defining these for the purposes of this study. More recent studies [32, 49] have raised the possibility of high-density storage at temperatures and pressures close to ambient in GIC-based structures with physical properties tuned to optimise hydrogen uptake.

All analyses of potential hydrogen storage materials must take into account one of the most important indicators of the suitability for storage: the percentage weight of hydrogen stored. Other factors such as the dynamics and reversibility of sorption, cost and availability are also considered but usually only after a material has shown sufficient hydrogen can be stored under experimental, time-invariant conditions. The 6 wt.% target of the US DoE, set for 2010, is a target that has been kept in mind throughout the project. For automobile use, however, reversibility under ambient conditions is vital, and this suits physisorbing materials such as those considered in this project, where the reversibility and sorption kinetics are good but it is difficult to store the required mass of hydrogen.

3.2 GIC synthesis

A number of different methods can be used to construct graphite intercalates [41]. The overriding objective is to bring the intercalant species in contact with the graphite and to mobilise it sufficiently to have it enter the inter-graphene galleries. For this it is usually necessary to have the intercalant in either a gaseous or liquid-like phase. The most common routes are vapour transport synthesis, liquid intercalation and cointercalation techniques. In the first method, the intercalant is sealed in a closed, typically evacuated, container with the graphite and heated to a carefully-regulated temperature to vaporise it partly or fully. The vapour is then taken up by the graphite. In general two variants of this method exist, the first denoted one-zone vapour transport (1ZVT), the second, two-zone vapour transport (2ZVT) (Fig. 3.5). For 1ZVT, the intercalant metal is sealed into the same space as the graphite and vaporised in contact or near-contact with it at a temperature T_{1Z}. The desired stage is selected by placing a stoichiometrically-accurate amount of the metal plus a small excess in at the start. In 2ZVT the graphite is placed in one part of the container and a narrow neck joins it to a zone with the metal inside. A well-characterised thermal gradient is placed over the two zones and the desired staging produced by the difference in vapour pressure over metal at temperature T_i and graphite at temperature T_g. Table 3.1 shows the zone temperatures used for some common alkali-metal intercalates.

An excess of intercalant can be used for 2ZVT as the vapour pressure gradient determines the maximum amount of intercalation and thus the staging of the sample. The time taken for intercalation to be completed depends very strongly on the intercalant species and the internal structure of the host graphite. Typical times range from a few seconds for easily-intercalated metals like potassium in graphite with a low degree of crystallinity, to many weeks

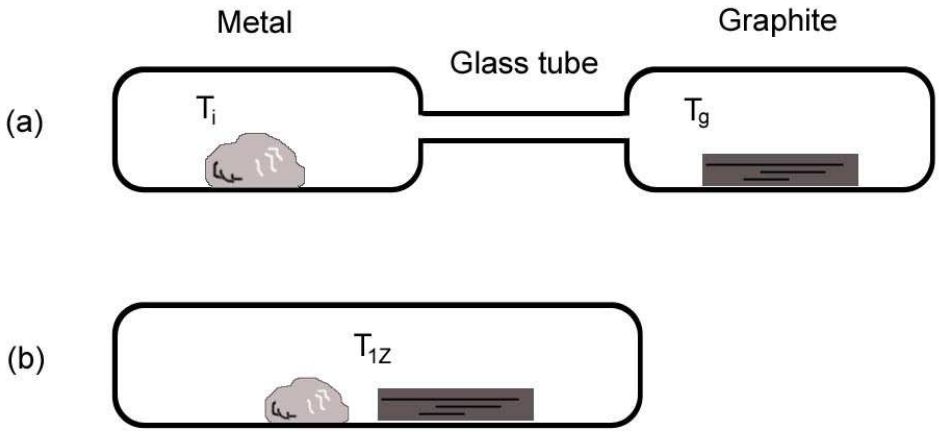

Figure 3.5: Vapour transport (VT) intercalation synthesis: (a) two-zone VT with excess metal, (b) one-zone VT with stoichiometrically exact weight of metal

Table 3.1: T_i and T_g for the preparation of some alkali-metal GICs by the two-zone vapour transport method. From Nixon (1966), reproduced in [41]

	K T_i=250°C	Rb T_i=208°C	Cs T_i=208°C
Stage	T_g(°C)	T_g(°C)	T_g(°C)
1	225-320	215-330	200-425
2	350-400	375-430	475-530
3	450-480	450-480	550

in the case of alkali-earth or rare-earth metals such as Yb in highly oriented graphite. Once inside the graphite, the intercalant must remain mobile to create a homogenised structure and so a process of annealing is used for a further period of time dependent on the temperature and the intercalated species. This allows the diffusion of intercalant ions through the material and the creation of a homogenised intercalation.

The temperature range of 200-550°C in which these reactions take place allow Pyrex glass to be used as a reaction chamber material. For Li-GIC synthesis however, stainless steel is used as Li vapour degrades the glass tube [42].

Melting the intercalant, if it is not already liquefied, enables intercalation of some species. Certain acid guest species are liquid at ambient temperature; lithium is a species that is intercalated well when the graphite is immersed in a metal melt. Co-intercalation is a process where two or more species are intercalated at the same time. Examples include using lithium alloys with other metals that do not intercalate alone. The alloy can enter the layer because the high mobility and donor properties of the Li bring in the other species with it; careful heating to remove the Li enables a stable binary compound to be formed with the other species. This route has been used successfully to synthesise CaC_6 [50, 51] and current studies are investigating it as a synthesis route for YbC_6 [52] and BaC_6 [51, 52] with success.

Alternatively a solvent can be utilised to mobilise the intercalant. Rüdorff [53,54] used liquid ammonia solutions of metals to intercalate the alkali metals Li, Na, K, Rb, Cs; also Co, Ca, Mg, Sr and Ba. Electrolysis of graphite in a metal-iodide-ammonia solution obtained compounds for Be, Mg, Al, Sc, Y, La, Sm, Gd among others [42]. Ammonia is a polar solvent with a strong affinity for donor metals, which undergo ionisation, releasing electrons into the solute.

The solutions penetrate graphite very well, with the electrons going to the carbon layers. It is very difficult to drive off the ammonia, although heating and pumping can remove some of it. In practice a ternary GIC results with residual ammonia distributed about the metal ions. Where the intercalated binary metal-GIC is synthesisable, it can be exposed to ammonia vapour to create the saturated metal-ammonia-GIC. For example, ammonia can be intercalated into second stage potassium-graphite to form a stage-1 compound of composition $K(NH_3)_{4.3}C_{24}$ at 8 bar of vapour pressure [55] and on removal of the ammonia to the greatest extent, a residual ammoniated compound with composition $K(NH_3)_{1.8}C_{24}$ is obtained [56]. Alternatively, a solution of a metal in ammonia can be made and then added to pure outgassed graphite to create an intercalation compound. The author utilised this technique to intercalate ytterbium into the lamellar material molybdenum disulphide in previous work [57]. This method was used for the synthesis of Ca-GICs in the present investigation (§ 5.1.4). The residual composition of Ca-NH_3-graphite resulting from this method is thought from literature to be $Ca(NH_3)_{2.2}C_{12.1}$ [54], while the saturated ammonia solution is thought to have 6 ammonia molecules arranged octahedrally around each Ca ion.

The pure metal-ammonia solutions have a series of colour transitions based on ammonia concentration, again resulting from the band gap properties of the dissolved electrons. The most concentrated solutions are golden-yellow, while the most dilute are a dark blue (see Fig. 5.9).

3.2.1 Graphite morphologies

Naturally-occurring graphite provides small single crystals often unsuitable for physical measurements. Typical dimensions for graphite flakes separated from limestone are ∼1 mm in-plane and a few hundredths of mm thick [41].

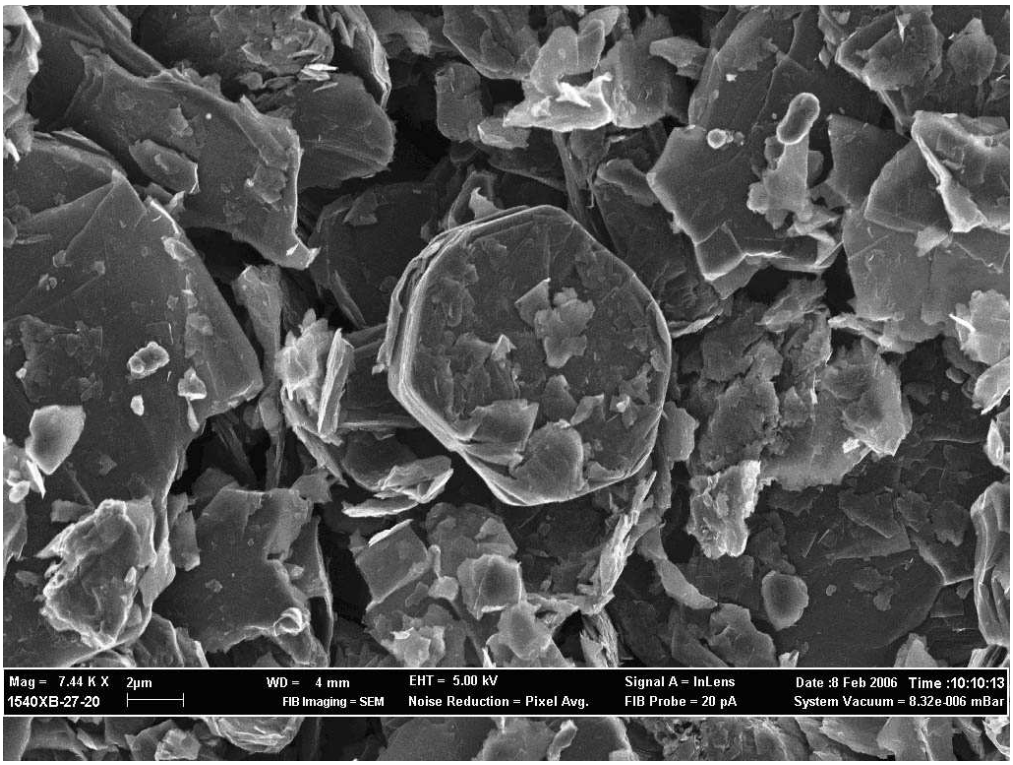

Figure 3.6: SEM micrograph of 1-2 μm mesh graphite powder supplied by Aldrich. From [58].

Artificially-created forms of graphite are more commonly used as a host for GICs. One such is highly-oriented pyrolytic graphite (HOPG), formed by cracking of hydrocarbons under heat and pressure. HOPG is well-oriented in the c-axis direction but contains $\sim$1 μm crystallites oriented randomly in the planar direction. This is less of a disadvantage than attempting to measure, for example, resistivity on a tiny natural graphite crystal, and HOPG has been a popular base for GIC research. Graphite powder formed by hydrocarbon cracking and then milling was used to create ammoniated calcium-GICs for the project. This power was supplied by Aldrich, product number 282863, and was nominally composed of 1-2 μm dimension platelets. SEM imaging (Fig. 3.6) showed the powder particles to have dimensions up to 20 μm.

Another form of graphite, less commonly used, is 'kish' graphite, obtained from crystallisation of carbon during the steel production process. This consists typically of large single crystals, more ordered than HOPG but less pure than natural graphite. They are however considerably bigger than natural crystals.

The type of graphite used primarily during the project was compressed-exfoliated or flexible graphite. This is produced by exposing natural graphite flakes to acid, often H_2SO_4, so that intercalation of the acid takes place, followed by rapid heating which causes swift expansion of the intercalant and explosive exfoliation of the graphite layers. The resulting expanded graphite is then rolled flat, creating a large laminate with a geometric density approximately half that of pure graphite and a corresponding increase in porosity and decrease in crystallinity. This resultant is quasi-amorphous, displaying little in-plane ordering but a strong preferred orientation of exfoliated platelets parallel to the plane of the sheet. Compressed-exfoliated graphite is manufactured on industrial scales because of its use in seals, batteries, and gaskets and as thermal insulation. Two products are widely used; Grafoil, supplied by Union

Carbide Co., and Papyex, supplied by Carbone Lorraine. Papyex was used for the samples studied in this project.

Exfoliated graphite was used in previous studies [59] to construct GICs and there is evidence [42] that intercalation and gas absorption kinetics are considerably quicker into powdered or power-like graphite than for more highly-crystalline forms, possibly because of the larger pore sizes and greater crystallite surface area. The samples also have higher homogeneity than other graphitic substrates [60]. A similar consideration resulted in the use of the 1-2 micron mesh powder [58]. This suggested that the adsorption-desorption kinetics of hydrogen into a GIC sample made from exfoliated graphite, or the powder, should be faster than from one made using HOPG, which would be advantageous. Exfoliated graphite has a lower density than graphite and the extra porosity might have an advantage in storing hydrogen. Secondarily, but of potentially huge benefit in the commercialisation of hydrogen storage technology, compressed-exfoliated graphite is far cheaper than HOPG. It was not possible to purchase Papyex in smaller units than rolls of several metres' width. An entire PhD's-worth of samples was constructed from two free samples — sheets smaller than A4 — requested from Carbone Lorraine's UK subsidiary.

3.2.2 Papyex exfoliated graphite properties

Papyex has been studied in some depth [60] with a number of techniques. Exposing the material to pressure, as during an adsorption measurement, can slow down the adsorption kinetics, but it has the effect of increasing the alignment of the (001) graphite planes, so improving the preferred orientation. These basal plane surfaces are thought to be where sorption takes place most readily.

The mosaic spread (Fig. 3.7) is a measure of the preferred orientation of

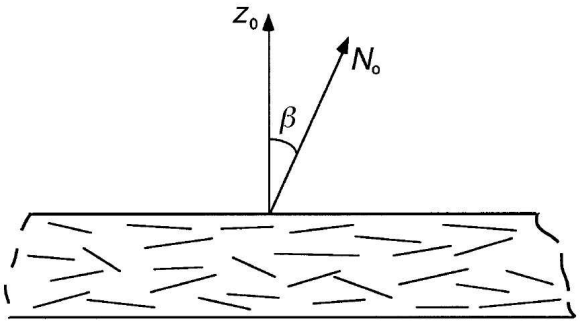

Figure 3.7: Crystallite alignments in compressed exfoliated graphite (e.g. Papyex) relative to the plane of rolling. z_0 is a vector normal to the graphite surface and N_0 a vector normal to the (001) plane of a crystallite. The distribution of planes as a function of the alignment angle β is symmetric about z_0 with a full-width half-maximum of about 30°. Reproduced from Gilbert *et al.* [60].

the sample, and equates to the angular distribution of crystallite alignments about an axis normal to the external plane surface of the material. It has been reported to be about 30° at full-width half maximum (FWHM), while 80 % of the available surface has been determined to be homogeneous (001) graphite surface suitable for adsorption. Through optical microscopy the Papyex surface appears with regular striations indicating large cavities separating graphite regions. Scanning electron microscopy (SEM) shows that the Papyex morphology consists of roughly circular graphite discs of radius μm stacked without order. The discs are thin, and the voids large, often of hundreds of μm.

Comparison of the (110) and (002)(hexagonal)/(003)(rhombohedral) peaks using X-ray scattering give a preferred orientation ratio of 900:1 in reflection geometry. It was found that a small but significant proportion of the crystallite planes are perpendicular to the rolling plane, i.e. are 90° from the average direction expressed by the preferred orientation. Papyex also appears to consist of a high proportion of rhombohedrally-stacked A-B-C-A graphite: 25-30 % is the estimated proportion, compared with 5-15 % in natural graphite. The

crystallite sizes are found to be ∼600 Å in their planes, and ∼300 Å out of their planes.

Nitrogen adsorption and desorption isotherms (See § 4.2.5) were measured at 77 K. The isotherm was of Type II (§ 4.9), suggesting a non-porous or macroporous sample (pores of dimension >500 Å). A BET analysis gave a c-parameter (Eqn. 4.59) of 65 and a monolayer adsorption capacity of 5.3×10^{-3} g g^{-1}. The surface area was calculated to be 18 m^2 g^{-1}, consistent with a macroporous morphology. The sample density was found to be 0.95 g cm^{-3}, which is 42 % that of ideal graphite (Table 6.1), suggesting that Papyex consists of ∼60 % void space. According to the authors, the voids were found to be interconnected.

3.3 Ternary GICs with hydrogen

A ternary GIC can be formed by co-intercalation of two species simultaneously, such as when using a Ca-Li alloy to synthesise CaC_6, or by selectively intercalating a second guest type into a pre-synthesised binary GIC. The focus of this project was on synthesising GIC-based materials to study their potential for hydrogen storage, and hence hydrogen was loaded onto GIC samples as a gas with the intention that it could be desorbed as a gas as well. This limitation followed from the ultimate technological aim of a storage material, as defined by foreseeable applications, government stipulation [19] and previous research: loading hydrogen gaseously from external sources into a vehicle, and delivering it gaseously to a fuel cell. In this case the storage material is seen somewhat analogously to a rechargeable electrical battery, with a 'charge' of hydrogen. All the alkali-metal GICs available have ternary versions with hydrogen which can be made by the direct method of intercalating the relevant metal hydride

into pristine graphite. Even a sodium-hydrogen-GIC can be made through intercalation of NaH though a binary stage 1 sodium-GIC cannot be made. These syntheses are clearly an unsuitable consideration for standard models of automotive refuelling processes — it would mean a long time at the pumps (The other problem is that the hydrogen remains chemically bound in the resulting ternary GIC and hence is difficult to get back).

The absorption capability of hydrogen in intercalates has been studied for a long time in GIC research [61]. Hydrogen absorption at room temperature in first-stage KC_8 was reported in 1977 [62] to result in a ternary compound of stoichiometry $KC_8H_{0.67}$ incorporating an unprecedented change of the compound structure to stage 2. While these sorption concentrations were too low to consider seriously for hydrogen storage, the process was interesting and the structural changes far from completely verified. They were therefore investigated as part of this project (Sections § 3.3.2, § 5.3.4, § 6.5, § 7.3) as they made a good counterpoint to the main thrust of the work on KC_{24}.

As with the synthesis properties of the binary GICs themselves, the reaction of hydrogen with the different alkali-metal intercalates varies considerably [42]. Hydrogen absorption into RbC_8 at room temperature gives $RbC_8H_{0.05}$, which can be increased to the same hydrogen concentration as $KC_8H_{0.67}$ only with the application of 100 bar of hydrogen. By contrast, CsC_8, Li and Na GICs do not adsorb hydrogen at ambient conditions. The direct intercalation of alkali-metal hydrides into graphite lead to a higher concentration of hydrogen taken up. Up to $KC_8H_{0.8}$ is possible if potassium hydride is intercalated into graphite; the Na-H-GIC approaches a hydrogen-to-sodium ratio of 1.

For the second stage AM-GICs the uptake is more promising. It was reported by several workers [45, 63, 64] that MC_{24} compounds, where M = K, Rb, Cs, reversibly physisorb up to $\sim$2 H_2 molecules per metal ion at cryogenic

temperatures below ∼200 K. Adsorption isotherms showed Langmuir-type saturation at monomolecular coverage. Above 200 K, the GICs act as catalysts to H and lead to H chemisorption as in the first stage compounds.

The inactivity of MC_8 GICs to hydrogen physisorption is explained by reference to the close-packed triangular 2D lattice of metal atoms between every layer: there is no room for hydrogen siting; by comparison, and disregarding the empty layers of graphite, the metal atoms in a stage-2 sample are only 2/3 as densely packed. They can move diffusively in the plane, like a 2D liquid. Higher stage compounds have a dilute matrix of alkali metal atoms. Hydrogen molecules absorbed at low temperatures are sited in the spaces between metal atoms. Hydrogen is not seen to enter the empty graphite galleries, and uptake is minimal in pure graphite. Significant hydrogen sorption has been seen in mid-stage compounds (e.g. KC_{12}) where there is a dilution of the metal intercalated layers [65], thus allowing hydrogen to sorb into empty metal sites. These compounds were synthesised from mesocarbon microbeads at high temperature.

Other small gas molecules are known to be physisorbed in higher-stage AM-GICs, but He and Ne are not, perhaps because they have a small polarisability.

In the next sections a detailed look is taken at the evidence from literature which informed the decisions taken at the outset of experimentation.

3.3.1 Structural properties of KC_8 and KC_{24}

Early crystallographic studies [62] of the pristine KC_8 structure determined that it was orthorhombic, of space group *Fddd*, but Trewern *et al.* [66] found a better fit to the lower-symmetry *Fdd2* with unit cell parameters $a = 4.92$ Å, $b = 8.59$ Å, $c = 21.4$ Å . The unit cell is shown in Fig. 3.2. The intercalated

metal ions are preferentially sited above (and below) the hexagon centres of the graphene structure. This maximises and equalises the distance between the ion and the six nearest carbon atoms. The graphite superlattice therefore takes on an A|A|A stacking, where | denotes a layer of intercalant.

The structure of KC_{24} has not been conclusively defined to date. Previous investigations [67, 68] found the graphite stacking to be AB|BC|CA|AB; thus graphene sheets either side of a filled gallery are aligned but empty galleries allow the pure graphite stacking to assert itself. The intralayer potassium structure was not ascertained by Nixon and Parry [68], although it was determined that the potassium sits above (below) hexagon centres in the graphite as for KC_8. Further work determined that the MC_{24} compounds undergo at least two phase changes on cooling, at two critical temperatures T_{cu} and T_{cl} ($T_{cu} > T_{cl}$) and that the metal ions are highly mobile above T_{cu}, diffusing rapidly through the layers as a 2D liquid [42, 69]. In the case of Cs- and RbC_{24}, the metal ions form domain structures commensurate with the graphite lattice below T_{cu}. A short-range c-axis stacking sequence is formed, which changes to one of longer periodicity below T_{cl} [70–72]. The domains are $\sqrt{7} \times \sqrt{7}R(19.1°)$ MC_{28} lattice regions. KC_{24} has c-axis stacking of AαABβBCγCA between T_{cu} (123 K) and T_{cl} (93 K), and a six-layer periodicity of AαABβBCγCAα'ABβ'BCγ'CA below that, where Roman letters denote graphite and Greek letters the potassium layers. Winokur and Clarke [72] identified a single domain structure existing above T_{cl} which fragments into four commensurate microphases below 93 K.

3.3.2 Hydrogen in KC_8

The chemisorption of hydrogen by the first stage potassium graphite intercalation compound was reported by numerous investigators [73, 74]. This process takes place at ambient temperature and above [73], giving compounds KC_8H_x

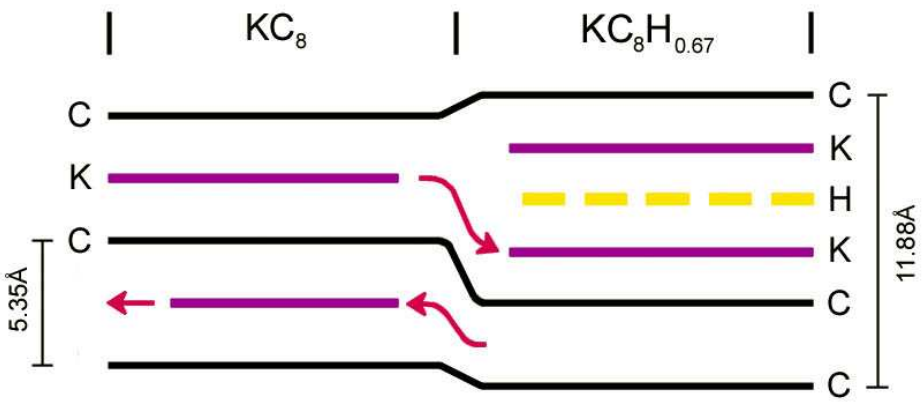

Figure 3.8: The stage transition associated with chemisorption of hydrogen in KC_8 at ambient temperature; every other layer empties of potassium forming a stage-2 compound with a trilayer K-H-K intercalation

up to a saturated value of $x = 0.67$. At 473 K this saturation is achieved at 133 mbar. A linear increase characterises H uptake for $0 < x < 0.1$, with a strong increase in sorption for $0.1 < x < 0.6$ and a levelling off to saturation above that. Characteristic of this process is a remarkable structural change of the compound from stage 1 to stage 2, as a result of potassium being entirely removed from alternate intercalated layers and combining with the dissociated hydrogen in remaining filled layers to form a triple layer of atomic planes, with a resulting c-axis sequence C-C-K-H-K-C, with the potassium electropositively and the hydrogen negatively charged. X-ray (00l) diffraction analysis [75] gives the $KC_8H_{0.67}$ repeat distance as 11.88 Å, composed of an empty graphite layer 3.35 Å and an 8.53 Å filled layer thickness, fundamentally different from the 5.3 Å repeat distance of a K-filled layer in KC_8. For concentrations $0.1 < x < 0.6$ the two phases coexist, the sample undergoing a metal to non-metal transition with the ongoing hydriding sequence, until the 5.35 Å phase disappears entirely in favour of the stage-2 compound. A probable route for the transition mechanism is suggested as a domain-model, shown in Fig. 3.8. The driving factor is not clear but is likely to be related to the dissociation enthalpy of the

hydrogen.

In the fully-hydrogenated phase, a difference Patterson synthesis placed the hydrogen midway between the potassium sheets. A 2×2 alternating potassium lattice structure was proposed, with hydride ions placed approximately in the tetrahedral vacancies between these layers. Three alternative models for the hydrogen-sorbed KC_8H_x structure were summarised by Miyajima *et al.* [76]: a $(2 \times \sqrt{3})R(0°, 30°)$, a $(2 \times 2)R(0°)$ and a $(2\sqrt{3} \times 5)R(0°, 30°)$ hydrogen superlattice. But the stoichiometry of these, with $x = 0.5$, meant that more work was required to determine not only the correct structure but the interstitial siting of hydrogen ions for concentrations between 0.5 and 0.67. The transition was not reportedly charted fully either in onset temperature or in time.

3.3.3 Hydrogen in KC_{24}

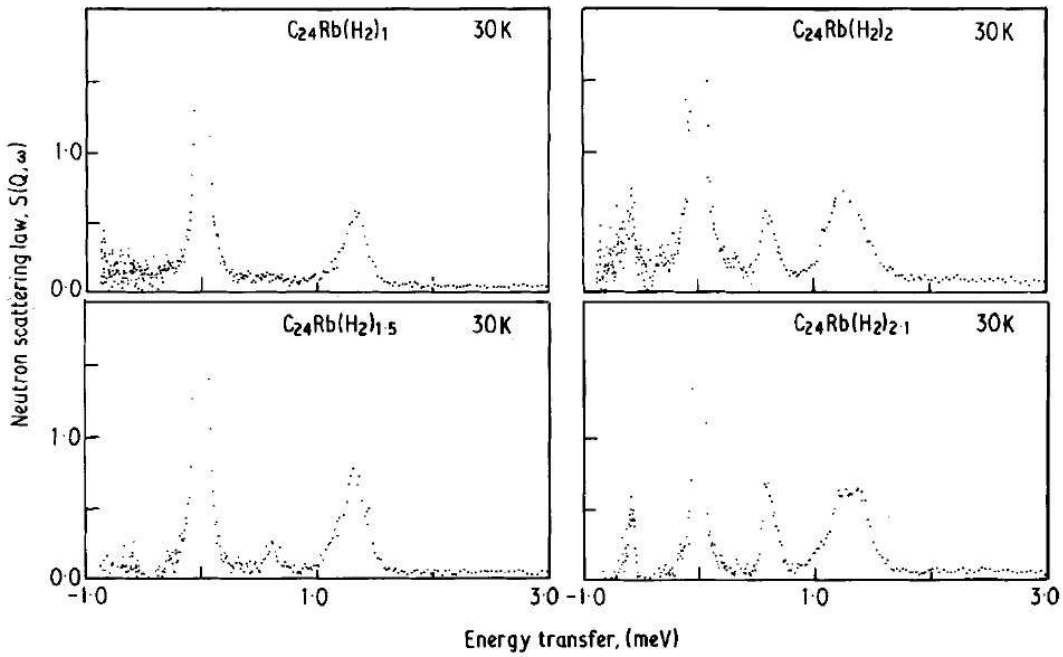

Figure 3.9: INS spectra of $RbC_{24}(H_2)_x$ for $x = 1.0$, 1.5, 2.0, 2.1. Taken on IN5 spectrometer (ILL) by Beaufils *et al.* [77]

The saturation uptake of H_2 in KC_{24} of ∼2.1 H_2 molecules/K ion was first reported by Watanabe *et al.* in 1971 [63]. A very similar saturation uptake is seen in RbC_{24} and CsC_{24}. The adsorption is accompanied by a ∼5 % *c*-axis swelling in KC_{24} and RbC_{24} [78], but not CsC_{24}, where it is assumed the layers are expanded enough to provide no hindering potential for hydrogen entry [42]. As X-ray and neutron diffraction proved inadequate to the task of locating and describing the hydrogen sites in the intercalate, investigators turned to inelastic neutron scattering in a bid to use the excitation characteristics of bound H_2 for this purpose. Beaufils *et al.* used $RbC_{24}(H_2)_x$ compounds with x up to the saturated maximum of 2.1 H_2/Rb, measured at 30 K [77]. At $x = 1.0$ they found an excitation peak at 1.34 meV; as the filling increased through $x = 1.5$ to $x = 2.1$, this peak acquired a growing shoulder at 1.17 meV while the original height remained roughly constant, and a new excitation appeared and grew at 0.60 meV (Fig. 3.9). The authors assumed this to be quantum tunnelling of the H_2 molecule in a hindering potential, and proposed two possible interpretations of the data: a model with two or more distinct sites for hydrogen in the GIC below 77 K, or a single site model with hydrogen-hydrogen interactions explaining the excitations that appear for $x > 1$. They continued by substituting D_2 or HD, and methane, for some of the sorbed H_2, to try using the molecular sieving effect [64] to determine which model was most likely. As HD and H_2 apparently were associated with different excitations, they concluded the two-site model was likely, with each isotope preferring a different site. The evidence for CH_4 blocking one of the sites is less compelling. As comparison they show the temperature dependence of $CsC_{24}(H_2)_2$ but no other concentrations. This has two areas of excitation as well; at 0.73 and 1.2 meV. The resolution (∼25, 36, 60 μeV) is not great enough for any data set to determine if there is finer structure within these excitations. This makes the experimenters' tentative conclusion that the single excitation 'A site' represents a site in a tetrahedral crystal field, and the double-peak 'B

site' represents one in an octahedral field, uncertain. It also appears that the hydrogen was not entirely converted to para-H_2 as intensity appears on the neutron energy gain side.

A similar study [59] carried out on $CsC_{28}(H_2)_x$ for $0.0 < x < 1.95$ benefited from 15 μeV resolution. The results show a single excitation for $0.0 < x < 1.0$ at 1.33 meV, joined by two others at 1.07 and 1.18 meV for $x = 1.0$, which drift outwards then inwards in energy as x increases. At $x = 0.65$ a new peak appears at 0.68 meV with a weak satellite at 0.77 meV, and both persist to the maximum x-value. The original peaks display fine structure which the authors attribute to H_2-molecule centre-of-mass modes.

Stead *et al.* [79] used inelastic neutron scattering at energy transfers of 10-200 meV to study corresponding librational transitions of H_2 in CsC_{24}. From this, the molecular barrier to rotation in the compound was calculated using a librational splitting model of H_2 in a $\cos^2\theta$ potential outlined by Silvera [31]. In an intercalate, their model suggests, the presence of a strong hindering potential causes the splitting into two of the first hydrogen $J = 1$ rotational level; the singly-degenerate $M = 0$ level is reduced in energy from the free molecular value of 14.7 meV and the two-fold degenerate $M = \pm 1$ state increased in energy. The former is manifest as the tunnelling spectra at $\sim$1 meV, the latter, librational excitations at $\sim$40 meV. These are seen to shift in energy as a function of coverage: the principal line from 37 meV in $CsC_{24}(H_2)_1$ to 35 meV in $CsC_{24}(H_2)_2$. This causes difficulties for the two-site model; the expected barrier to rotation of a tetrahedral 'A site' would be 25 kJ mol^{-1} instead of the 12 kJ mol^{-1} experimentally determined [64]. Their potential model assumes the hydrogen molecule is perpendicular to the graphite planes in a cylindrical potential, and they calculate the energy levels as a function of this potential

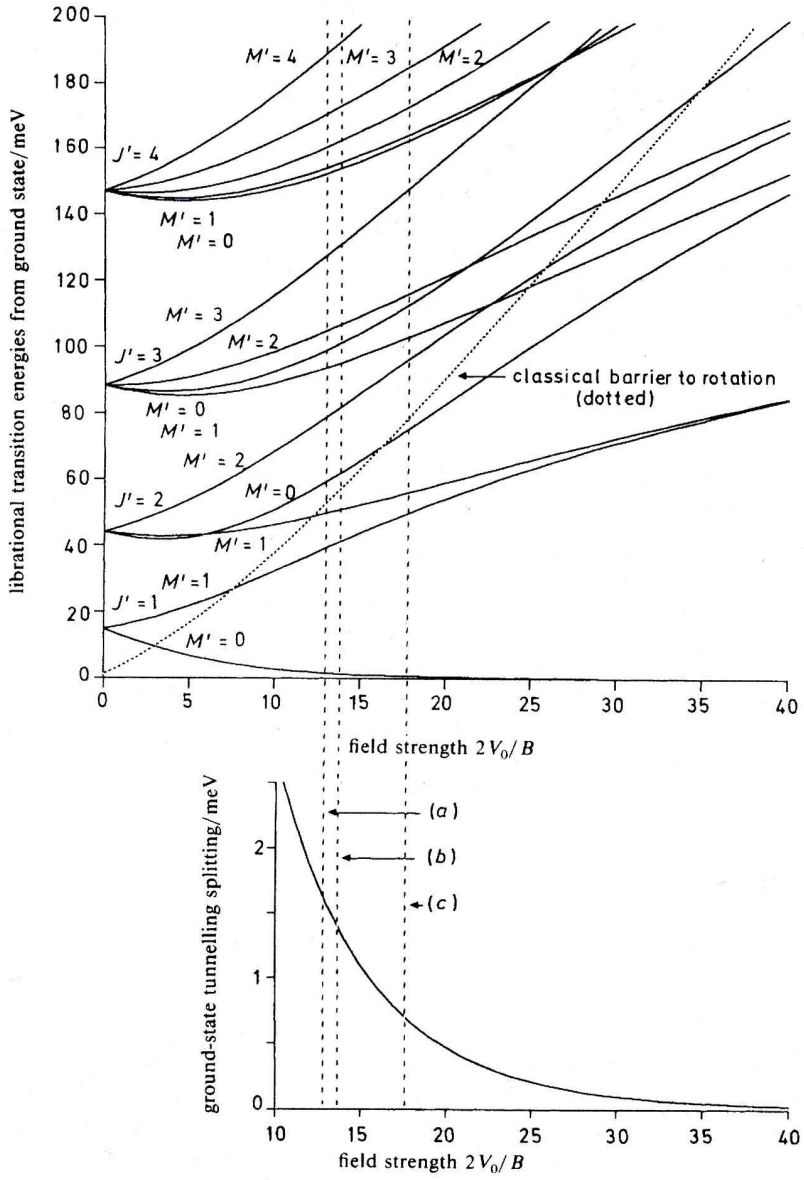

Figure 3.10: Splitting pattern for the rotational energy levels of a hydrogen molecule in a cylindrically symmetric $\cos 2\theta$ potential showing transition energies from the ground state in meV. Rotational transitions are depicted up to $J' = 4$. (a) is the 'A' site in $CsC_{24}(H_2)_x$, (b) is the 'A' site in $RbC_{24}(H_2)_x$, (c) is the B site in both compounds. Reproduced from Stead *et al.* [79]

$$V = V_0(1 - \cos 2\theta) \tag{3.2}$$

where $2V_0$ is the barrier constant and θ the angle to the preferred orientation. The splitting diagram is recalculated to show transition energies from the ground state as a function of the hindering potential (Fig. 3.10) in units of B, the molecular rotation constant (B_{H_2} for hydrogen is 7.35 meV [31]). They found good agreement for a model where 'A' and 'B' sites had the same symmetry but the latter had a deeper potential ($2V_0 = 13B$ for 'A' site and $18B$ for 'B' site). This did not explain mid-energy excitations at 13 meV in $CsC_{24}(H_2)_1$ and 18 meV in $CsC_{24}(H_2)_2$, which are concluded to be H_2 centre-of-mass vibrations, a possibility given added weight by the presence of weak bands in low temperature spectra assignable to overtones and combinations. Calculating relative intensities proved unworkable as the states do not correspond well to free rotation or harmonic oscillation; hydrogen modes being anharmonic. On substituting HD or D_2 for H_2 in the system, the barrier potential remained unchanged but B scaled accordingly. In a following paper [80], the same group presented equivalent tunnelling and librational spectra for $RbC_{24}(H_2)_x$. At 5 K for $x < 1$, a tunnelling peak is observed growing with coverage at 1.4 meV; for $x > 1$ is is joined by a peak at 0.7 meV which grows in the same manner. Each increases linearly with filling. Above $x = 1.2$, the peaks distort and show a shift to lower energies, suggesting several unresolved peaks. At $x = 2.0$, a new peak appears at 2.05 meV. Applying the rotational potential model to these data showed a reasonably good fit to the results. The 'A' and 'B' site barriers are found to be $14B$ and $18B$ respectively. Isotopic substition shows a downshift in the energies as expected for HD.

The H_2 molecule is a boson and so its overall symmetry must be symmetric. To achieve this, all even-J rotational levels must also have zero nuclear spin and all odd-J levels a spin of 1; these are the so-called para- and ortho-hydrogen

spin isomers respectively, of which the lowest are $J = 0$ and $J = 1$. A transition between these states requires a nuclear spin flip to change the spins from parallel (ortho) to anti-parallel (para), which is a very slow process in the absence of a magnetic moment, as provided by unpaired electronic charge density for example. At room temperature (the high-temperature limit) the para/ortho ratio is $\sim 1 : 3$, a result following from the degeneracy of the M nuclear spin states: $M = 0$ for para-H_2 and $M = 0,\pm1$ for ortho-H_2. At 5 K most of the atoms should be in the lower energy para-hydrogen state, but this conversion can take many hours. It is not clear from [79] and [80] if Stead *et al.* accounted for this; the existence of neutron energy gain intensity at 30 K in Fig. 3.9 to the left of the elastic line suggests that it was not accounted for by an earlier study [77]. This may be a consequence of the neutron spectrometer used.

The next phase reported was attempting to fit the sites to the domain model for the intercalate structures of the Cs and Rb-GICs. The authors identify two 'A sites' per metal ion in the $\sqrt{7} \times \sqrt{7}R(19.1°)$ structure, but in order to fit hydrogen up to a stoichiometry of $x = 2$ without a large number of possible sites in the domain walls (Fig. 3.11), they conclude by postulating that the $\sqrt{7} \times \sqrt{7}$ domains grow in size with coverage, reducing the number of domains, and that the higher energy 'B' site results from fitting a second molecule into an 'A' site next to an already occupied site. In the current work it became necessary to find a similar rationale for KC_{24} sorption sites.

Smith *et al.* [81] took up the baton; they were able to carry out higher-resolution INS on $RbC_{24}(H_2)_x$ for $x = 0.8$, 1.0 and more confidently assigned intermediate excitations between the tunnelling and the first librational peaks to whole-molecule centre-of-mass vibrations. Invoking the barrier splitting model, they noted that the first librational excitation was red-shifted to 32 meV rather than the expected 39 meV in a 100 meV well, and attributed

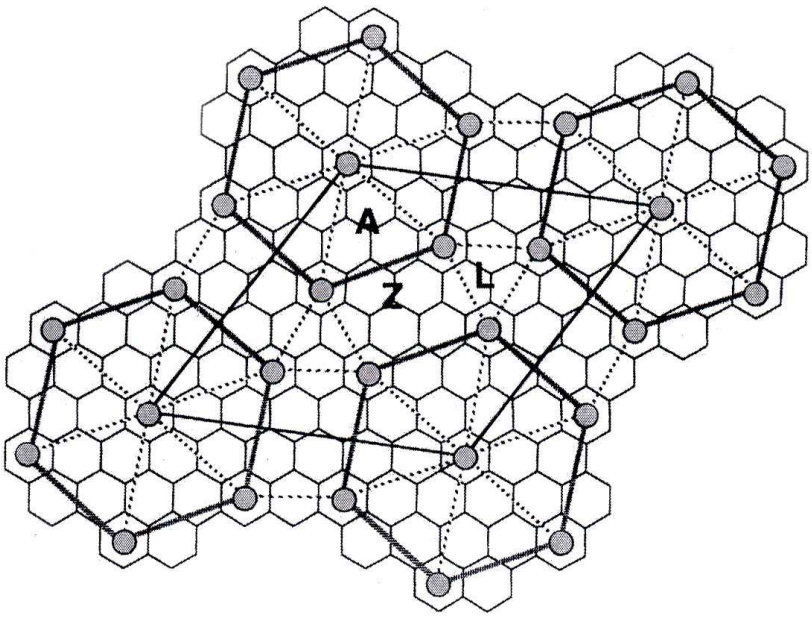

Figure 3.11: Domain structure of RbC_{24} at low temperature showing possible sites for hydrogen: inside the $\sqrt{7} \times \sqrt{7}R(19.1°)$ domain (A), in the domain wall (Z), and at domain corners (L). 'L' sites are equivalent in size to sites in the $(2 \times 2)R(0°)$ structure, for example in KC_8. Although two 'A' sites are available per ion in the bulk $\sqrt{7} \times \sqrt{7}R(19.1°)$ structure, it is not possible to get this many identical sites while a large part of the sample consists of interdomain spaces. Stead *et al.* theorised that the domains grow in size with hydrogen content, so that the sample approximates to bulk $RbC_{28}H_2$ at full hydrogen loading. Reproduced from Stead *et al.* [80]

this to non-sinusoidal contributions to the rotational barrier, or rotational-vibrational coupling. They carried out local density functional theory (LDFT) calculations to model the expected behaviour of hydrogen in the GIC using a $\sqrt{7} \times \sqrt{7}$ structure. The results were consistent with assignment of the 1.4 meV lowest energy peak to a tunnelling rotation and thus supported the Stead model.

More recently, Lindsell studied the in-plane structures of Rb- and KC_{25} with sorbed H_2 and D_2 using X-ray scattering [78]. They were not resolvable. As KC_{25} was hydrogenated, the structure apparently became less complex and a characteristic peak emerged at 5.15 Å for H_2 and 5.12 Å for D_2 sorption. Even at 90 K the in-plane ionic lattice was able to be restructured by H_2 and D_2 for concentrations above $x = 1$, suggesting that the model of increasing domain sizes may have validity, and that the ion-molecule interaction is relatively strong for physisorption. Lindsell concluded that the adsorbed hydrogen did not occupy sites in the existing metal lattice, but restructured the lattice into a solid solution without long range order.

3.4 Tuneability of GICs for hydrogen storage

The interaction of hydrogen with graphite intercalation compounds is a profitable area of study, because there are large numbers of open questions to be investigated. Much early work was carried out before the desirability of hydrogen storage was known, and many investigators turned their attentions from GICs to fullerenes and, later, nanotubes, leaving a comparative dearth of research in this area until recent years. As this chapter has shown, an overall model of hydrogen sorption is yet to be obtained, as the physical characteristics that govern uptake are not individually isolated. At the outset of this

work, we wished to explore the uptake behaviour of gaseous hydrogen in GICs, and the work has always kept a strong technological focus, so that the questions addressed were not only physics-related but targeted their applicability to the problem of hydrogen storage. It was concluded in the initial stages of research and review that the alkali-metal intercalates were a promising base material set for storage; more so than nanotubes and un-doped graphite. The doping with donor metals clearly plays an important role in increasing the storage potential in graphite; what was not known was, in particular, what role was played by the charge on the metal donated to the graphite sheets, and what role was played by the corresponding increase in available volume when the graphite lattice expanded on intercalation. These two factors seem to be the most crucial. If, for example, the hydrogen molecules physisorbed into stage-2 KC_{24} are bound to the metal ions rather than a true sorption on the internal surfaces of the graphite, and it is a true assumption that little physisorption takes place in undoped graphite because the layers are uncharged and the galleries too shallow, then half the graphite surface area in KC_{24} is unaccessible to hydrogen, being in the layers unfilled with metal. (A small amount of physisorption in empty galleries might account for the slight excess of hydrogen above $2H_2$/K reported). This suggests that the empty galleries could be primed to take up hydrogen, and if that could be done solely by a stage transition, retaining the KC_{24} stochiometry but filling all galleries with a dilute layer of potassium, then a significant increase in uptake might be possible as hydrogen fills the available volume at reasonably low pressures.

Based on literature and outline project discussions, it was thought that pillaring the inter-graphene galleries with large ions to increase the interlayer spacing to 5-6 Å might improve the uptake, as long as the pillars were relatively dilute. Deng *et al.* used Monte-Carlo (MC) simulation techniques in an investigation which suggested that pillared lithium-GICs with this separa-

tion are able to store 3-4 wt.% H_2 at ambient temperatures and pressures of 1 bar [49]. Fig. 3.12 shows the principal results. A force field for interlayer van der Waals interactions was determined using density functional theory, and then MC techniques were used to determine the likely hydrogen uptake in undoped graphite, undoped uncapped SWNTs (white markers in Fig. 3.12(a) and (b) respectively) for an artificial increase in the interlayer or intertube distance, at 300 K and various low-to-moderate pressure values. The same approach was then carried out for doped graphite and nanotubes (black markers in (a) and (b)) to the stoichiometric concentration LiC_6. This level of doping was chosen because it corresponds with the stage-1 Li-GIC.

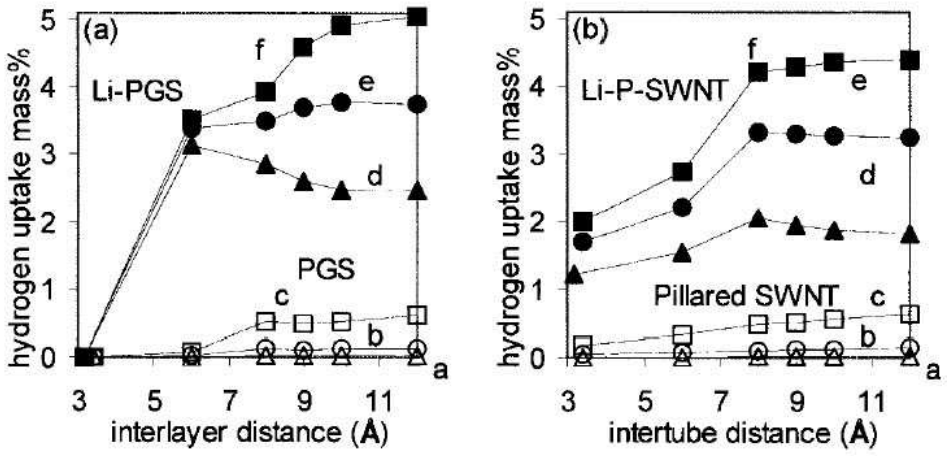

Figure 3.12: Theoretical dependence on the interlayer (intertube) distances of hydrogen uptake in (a) pillared graphite (white markers) and Li-GIC (black markers) and (b) (10,10) single-walled nanotubes (SWNTs) (white) and Li-pillared SWNTs (black) at 300 K. The doping concentration is 1:6 Li:C. The hydrogen pressures are 1 bar (triangle), 10 bar (circle) and 50 bar(square). From [49]

It can be seen that <1 % hydrogen by weight is taken up by pure graphite and pure nanotubes, irrespective of the interlayer or intertube distance. This corresponds well with the evidence by Pinkerton *et al.* [39] of negligible uptake in undoped graphites and SWNTs. Furthermore, no apparent H_2 uptake is observed in the graphite-based LiC_6 when the interlayer separation is the same

as that seen physically, i.e. 3.4 Å, again in agreement with literature [41, 42]. However, pillaring the layers of graphite further apart by unphysical means for the simulations showed a higher potential uptake at ambient conditions in the Li-GIC and the lithium-doped SWNTs. At 12 Å spacing, and 50 bar pressure, this surpassed 5 wt.%, although for 1 atmosphere of H_2 the amount was reduced from the value at 5 Å spacing. Thus for ambient conditions, the optimum appears to be 5-6 Å. The challenge would be to then either find a way of pillaring the structure further, or to find a dopant which opens the interlayer galleries more than Li, for which naïvely there are a good number of candidates (see Table 3.2). As has been noted earlier, the interlayer distance of KC_8 is 5.35 Å, but no hydrogen physisorption occurs even at cryogenic temperatures. This is most likely to be because the filled layer has too little free volume to accept hydrogen molecules.

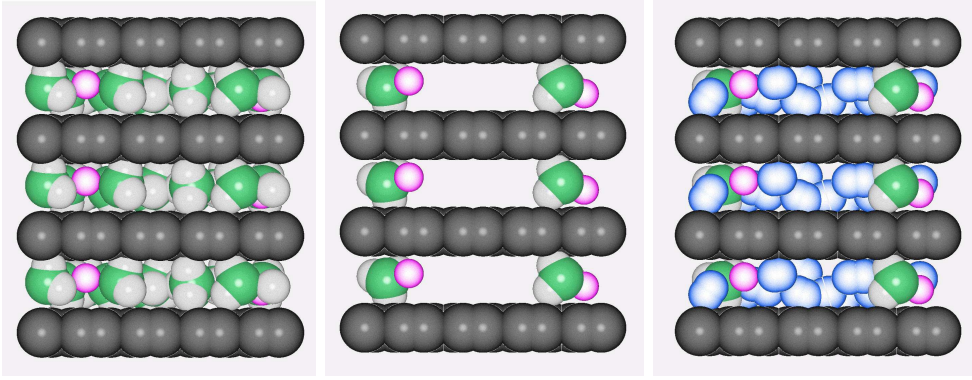

(a) (b) (c)

Figure 3.13: Pillaring graphite (grey) (a) using potassium-ammonia to open the layers, before removing ammonia (white and green) to leave (b) dilute stage-1 structure (K ions are pink) and then (c) filling with hydrogen (blue). Reproduced from [82]

Our proposal was to use ammonia in KC_{24}. The presence of ammonia drives a transition to a stage-1 compound, as mentioned in § 3.2, with the layers then being relatively dilute in metal, with only 1/3 of the intercalant density found in KC_8. The interlayer spacing is then a promising [49] 6.62 Å. The aim was

Table 3.2: Properties of graphite intercalation compounds used or considered for investigation in this research [42]. The filled interlayer spacing (ILS), d_s, is important for proposed pillaring species for maximising hydrogen sorption in graphite

Species	Composition	Stage	ILS, d_s (Å)
Graphite	C	-	3.35
Li	LiC_{6n}	n	3.706
K	KC_8	1	5.35
	KC_{24}	2	5.35
	$K(NH_3)_{4.33}C_{23.6}$	1	6.62
Rb	RbC_8	1	5.65
	RbC_{24}	2	5.65
Cs	CsC_8	1	5.94
	CsC_{24}	2	5.94
Mg	$Mg(NH_3)_{2-3}C_{32}$	4	15.95
Ca	CaC_6	1	4.60
	CaC_{12}	2	4.56
	$Ca(NH_3)_{2.2}\ C_{12.1}$	1	6.62
C_{60}	$C_{32}C_{60}$	1	12.530

to create the stage transition reported by York [56] and then remove as much of the ammonia as possible to free up internal volume for hydrogen. Fig. 3.13 shows the scheme. In this way, the alternate-layer gallery spaces could be levered open, which is an improvement on the accessible volume of the stage-2 compound. The question of how much hydrogen could be inserted given the residual concentration of ammonia was a very interesting one.

Even the intercalation of C_{60} molecules was considered. Although this C_{60}-graphite co-intercalation has been modelled [47], unequivocal evidence of its synthesis has yet to be presented. It is predicted to have a minimum *c*-lattice spacing of 12.530 Å, twice that found to be optimum by Deng *et al.* Potassium doping has been proposed to charge the graphite in order to allow the fullerenes inside, and it has been attempted, hitherto without success, by the author's research group, both using a metal-ammonia solution and a one-zone vapour transport method.

If the interlayer binding of hydrogen were a strong function of the charging of the graphite sheet, one would expect to see a large difference in the uptake if a monovalent intercalant such as K is replaced by a divalent element. If the enthalpy of sorption is a function of the van der Waals charge attraction, increasing the charging on the graphite sheets might well increase the binding energy of hydrogen and thus increase the temperature at which sorption can occur. Thus, varying the valency of the intercalated species is an important investigation. This is especially novel because very few lightweight divalent GICs have been synthesised to date, and their interaction with hydrogen has not been reported.

As a general target for minimising the weight of the storage material, and thus maximising its hydrogen uptake potential, host materials with low molecular weights are preferred. The relatively low weight of storage materials makes

carbon-based storage systems attractive compared with heavy metal hydrides (see § 2.2.3). Lithium and magnesium are the lightest mono- and divalent metals respectively. But Li-GICs do not increase graphite interlayer spacing significantly (see Table 3.2), which is a probable reason why hydrogen sorption is not reported in them. Pure Mg-GICs have not been synthesised; Mg is not readily dissolved by liquid ammonia either, and the resulting compounds are very dilute, with a minimum of stage 4 [54]. Mg-ammonia GICs have been created by electrochemical methods [83], but there was no experience of this in our research group. An attempt we made to use liquid ammonia to dissolve Mg was unsuccessful. So the two intercalants deemed most profitable for study were potassium (group I) and calcium (group II).

3.4.1 Project plan

Our immediate aim was to study the hydrogen dynamics in KC_{24} using inelastic neutron scattering, in a way directly analogous to work done in CsC_{24} and RbC_{24} [59, 77] and CsC_{28} [84]. The comparison would improve models of the hydrogen siting in these similar materials, and augment the understanding of the physics of the uptake. As the intercalated metal ions are of different sizes and weights, a idea of the sorption sensitivity to Z would be gained. KC_{24} has the best weight % storage potential as potassium is the lightest element of the three. If a saturated uptake of 2 H_2 molecules per K atom is assumed from literature, the maximal weight percentage of hydrogen in pure KC_{24} is 1.218 %; for RbC_{24}, it is 1.068 %, and for CsC_{24} it is 0.9488 %. The value for KC_{24} is approximately one fifth of the DoE target, but this is at low temperatures not at the specified ambient temperature.

The *c*-lattice structure of KC_{24} was known [66] but the in-plane structure had not been fully defined [78]; a complementary investigation of the structure

of the compound after adsorption of hydrogen required an investigation into this using neutron diffraction. Further, to evaluate the potential for ammoniated GICs as pillared hosts for hydrogen, it was planned to expose KC_{24} to ammonia to drive the stage transition [56], then remove as much as possible to leave a dilute stage-1 structure pinned apart by ammonia-metal complexes (Fig. 3.13) before testing the hydrogen uptake.

To investigate the chemisorption properties of K-GICs at ambient temperatures, a neutron diffraction experiment on the KC_8 - $KC_8H_{2/3}$ metal-insulator transition at room temperature was proposed. This was intended to provide high-resolution diffraction data in a time-resolved sequence over the phase transition, to try to model the phase growth and to gain good in-plane structural characterisation of the hydrogen-saturated stage-2 sample resulting.

To enable study of divalent ion intercalates, close collaboration was required with colleagues investigating synthesis routes for CaC_6, YbC_6 and BaC_6 GICs. The interlayer spacing of CaC_6 is 4.60 Å, which might not be wide enough to allow adsorption, but the ammoniated compound has an interlayer spacing of 6.62 Å. It was aimed to investigate both materials.

Measuring the hydrogen uptake of the different 'tuned' samples planned was an important consideration, so as the project got underway a thermogravimetric analyser was ordered. The commissioning process for this instrument took approximately one year and several upgrades proved necessary thereafter. This reduced the scope of the gravimetry investigation, though some interesting data were nevertheless acquired.

As a parallel investigation, it was intended to model the materials used by means of *ab initio* density functional theory (DFT), as implemented in the CASTEP code [85]. At least one similar study exists in literature [86]. This in theory enables analysis of geometry, forces, energies and electron density

in a system. There was not time to carry out this part of the plan during the project, however, an investigation using CASTEP to model the $KC_{24}(H_2)_x$ system was carried out in conjunction with the author during the writing of this thesis [87] and the results will be presented in Chapter 8 as part of discussion relating to a general model of the hydrogen sorption in this system.

Chapter 4

Theory of experimental techniques

The main experimental techniques used were neutron scattering and thermogravimetric analysis (TGA). Comprehensive descriptions of scattering theory exist elsewhere [88] [89] [43] [90] and the essential details will be considered here. The TGA theory is important for analysis of the reliability of the results and is described in somewhat fuller detail, accompanied by some consideration of the sorption properties of materials and models to describe this.

4.1 Neutron scattering

4.1.1 Introduction

Neutron scattering is an important probe for condensed matter systems, and has been developed to the point where it is an extremely versatile set of techniques, both in the types of systems that can be studied and the types of

information that can be extracted. It has several advantages over other scattering techniques and bulk matter probes which have informed its choice for this investigation. Table 4.1 shows some properties of the neutron. Neutrons have mass and are uncharged and so penetrate beyond the surface of a material, providing both structural and, as their mass allows them to scatter inelastically, dynamical data from the bulk material. The interaction of neutrons with matter is governed by the strong nuclear force. The probability of scattering depends on the proprietary spin state of the atomic nucleus and is independent of the atomic number Z of the scattering sample atom. Furthermore, this 'scattering length' is generally isotopically variant for each element, allowing scattering contrast between chemically-identical samples where one or more elements have been substituted for another isotope, and selective labelling of species of interest.

Table 4.1: Selected properties of the neutron. Reproduced from [91]

Mass	$m = 1.674928 \times 10^{-27}$ kg
Spin	$s = -\hbar/2$
Magnetic moment	$\mu = -9.64918 \times 10^{-27}$ JT^{-1}
β-decay lifetime	$\tau = 885.9 \pm 0.9$ s
Confinement radius	R=0.7 fm
Quark structure	udd

The electronic orbitals of the atom are virtually transparent to neutrons, so, unlike X-ray scattering, where photons interact with the electron cloud and where scattering length depends strongly on Z, smaller species like hydrogen are strongly visible to neutrons. As scattering takes place from the point nuclei, there is no interference from spatial variations of scattering across an electron cloud of finite width, unlike with X-rays, meaning that neutron intensity does not attenuate with increase in scattering angle. Neutrons can be

moderated to 'thermal' energies where their de Broglie wavelength is increased to the order of the interatomic distances in condensed matter systems, making diffraction interference possible. This enables the deduction of the crystal or non-crystalline structure of a material. This range of energies (5-100 meV) is similar to that of excitations inside materials, so the momentum change undergone by a neutron in the creation or destruction of an excitation in an inelastic neutron scattering (INS) event is a measurably large proportion of the neutron's incident momentum, making INS a powerful tool for observing the dynamics of materials: phonon states, diffusion and tunnelling can be measured. The thermal neutron scattering interaction is generally non-destructive, although certain materials are more vulnerable to undergoing ionisation and may remain active after removal from the neutron beam.

Neutrons, possessing a magnetic moment, can interact with unpaired spins in the sample and provide information on magnetic excitations. This makes them very useful in the examination of magnetic structures. A beam of spin-polarised neutrons can be created, to interact with the sample and after scattering can have the resultant spin change 'read' to determine the magnetic spins of the sample. Although the structures investigated for this thesis have in some cases noteworthy magnetic properties they were not the primary concern of the investigation and the neutron experiments were planned and executed without reference to these techniques; the theory of magnetic scattering therefore has no place here.

A moderated neutron has energy in a Maxwellian distribution about k_BT, where k_B is Boltzmann's constant (1.381×10^{-23} J K^{-1}) and T is the temperature of the moderator. A neutron emerging from a 300 K moderator with this mean should therefore have an energy of 4.14×10^{-21} J or 25.8 meV. The energy is low enough that the neutrons are treated non-relativistically; thus

$$E_n = \frac{\mathbf{p}^2}{2m_n}, \tag{4.1}$$

where E_n and m_n are the neutron's energy and mass, and $\mathbf{p}$ is the momentum. Using the de Broglie relationship

$$\mathbf{p} = \hbar\mathbf{k}, \tag{4.2}$$

where $\mathbf{k}$ is the wavevector, the magnitude of which is given by

$$|\mathbf{k}| = \frac{2\pi}{\lambda}, \tag{4.3}$$

it can be seen that the neutron of 25.8 meV has a wavelength of 1.8 Å. This is comparable to the interatomic spacings of solid state matter, being approximately half of the graphite interlayer spacing, for example.

4.1.2 The Q vector

A neutron travelling through space has a certain energy and momentum vector associated with it. If that neutron arrives at an atom and interacts with its nucleus, it will thenceforth have an altered momentum vector and, if the scattering event is inelastic, energy.

Overall conservation of energy and momentum requires that

$$\hbar\omega = E - E' = \frac{\hbar^2}{2m}(k^2 - k'^2) \tag{4.4}$$

and

$$\hbar\mathbf{Q} = \hbar\mathbf{k} - \hbar\mathbf{k'} \tag{4.5}$$

where E and E' are the initial and final energies of the neutron, **Q** the momentum transfer vector, m is the neutron mass, **k** and **k'** the incident and final neutron wavevectors and k and k' the magnitudes of these wavevectors. In such case as the scattering is elastic, no energy is transferred to the sample and the magnitude of **Q** is given by:

$$Q = \frac{4\pi \sin\theta}{\lambda}. \tag{4.6}$$

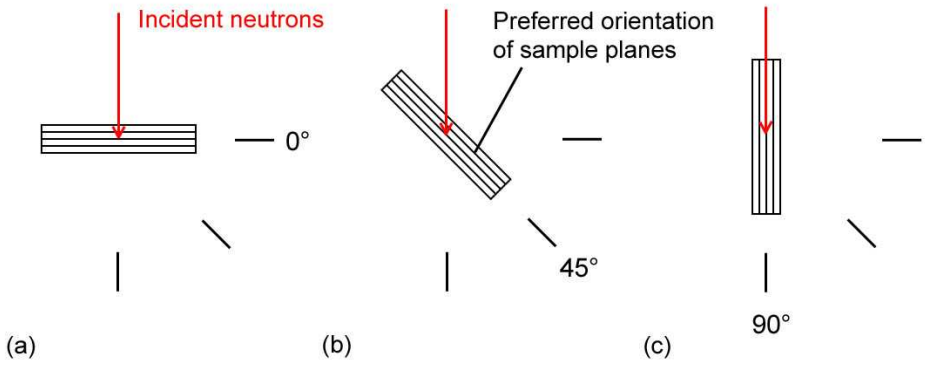

Figure 4.1: Definition of sample orientation angles used in neutron scattering experiments during the investigation; (a), with sample planes perpendicular to the incident beam, 0°, (b) 45° and (c) 90°

The direction **Q** takes in relation to the sample orientation is important for samples with preferred orientation. Information on structure is gathered along **Q**. If the momentum transfer vector is aligned with the out-of-plane axis of a graphite sample, the data gathered will describe the *c*-lattice direction. Fig. 4.1 shows the definition of the sample orientation relative to the incoming beam that was used in the experiments (135°, used in this investigation for INS measurements on IRIS in § 5.4, is perpendicular to the 45° setting).

4.1.3 The differential cross-sections

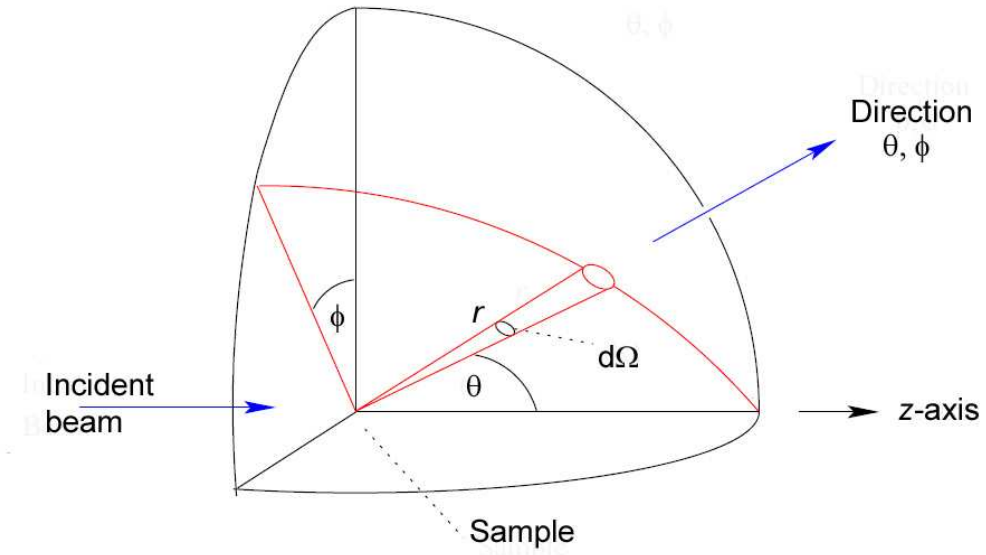

Figure 4.2: The geometry of a typical scattering experiment where a beam of thermal neutrons are incident on a target and are scattered into a small solid angle $d\Omega$ in the direction (θ, ϕ). Adapted from [43].

The quantity measured in a neutron scattering experiment is called the partial differential cross-section. This is defined as the fraction of neutrons of incident energy E scattered into a solid angle $d\Omega$ in direction θ, ϕ with a final energy between E' and $E' + dE'$. This is given by

$$\frac{d^2\sigma}{d\Omega dE'} = \frac{N_{d\Omega dE'}}{\Phi d\Omega dE'} \tag{4.7}$$

where $N_{d\Omega dE'}$ is the number of neutrons scattered per second into a solid angle $d\Omega$ in direction θ, ϕ with a final energy between E' and $E' + dE'$, and Φ is the incident neutron flux. Fig. 4.2 shows the geometry of a scattering event; a beam of thermal neutrons are incident on a sample and are scattered into a small solid angle $d\Omega$ in the direction (θ, ϕ).

The measured cross-section is termed the differential cross-section and is given by the integral of Eqn. 4.7 with respect to energy. The total scattering cross-section (TSCS) is obtained by integrating the differential cross-section over all angles. This quantity is given by

$$\sigma_{total} = \frac{\text{total no. of neutrons scattered per second}}{\Phi}. \tag{4.8}$$

4.1.4 Scattering from a fixed nucleus

A thermal neutron scattered by a fixed nucleus does so elastically. The wavelength is $\sim 10^5$ times greater than the nuclear diameter, so it can be treated as a point scatterer. The neutron incident and final wavefunctions can be approximated to spherically symmetric waves:

$$\psi_i = \exp(ikz) \tag{4.9}$$

$$\psi_f = -\frac{b}{r}\exp(ikr) \tag{4.10}$$

where k is the magnitude of the wavevector $\mathbf{k}$, z is the position of the incident wave on an axis in the $\mathbf{k}$ direction, r is the distance of the scattered wave at position $\mathbf{r}$ from the nucleus, and b is a constant representing the strength of the scattering interaction. This value is dependent on the type of nucleus in the scattering event and is called the scattering length of the nucleus. The TSCS is related to the scattering length by

$$\sigma_{total} = 4\pi b^2. \tag{4.11}$$

4.1.5 Scattering from a general system of particles

The differential cross-section (DCS) can be formulated to describe a system of scattering where the initial and final system states are λ and λ' respectively. The neutron has initial wavefunction $\psi_{\mathbf{k}}$ and final wavefunction $\psi_{\mathbf{k'}}$. This is expressed as

$$\left(\frac{d\sigma}{d\Omega}\right)_{\lambda\to\lambda'} = \frac{1}{\Phi}\frac{1}{d\Omega}\sum_{\mathbf{k'}\text{in } d\Omega} W_{\mathbf{k},\lambda} \to W_{\mathbf{k'},\lambda'}, \tag{4.12}$$

where $W_{\mathbf{k},\lambda} \to W_{\mathbf{k'},\lambda'}$ is the number of transitions per second from the state $\mathbf{k},\lambda$ to the state $\mathbf{k'},\lambda'$, and Φ is the incident neutron flux.

The sum is evaluated using Fermi's Golden Rule, a result from quantum mechanics taking into account the potential V between the neutron and the scattering system, which is assumed to be much weaker than the incident neutron energy, allowing the neutron wavefunctions to be represented by spherical S-waves. A formalism involving normalisation of the momentum states of the neutron is used to determine the following expression for the DCS:

$$\left(\frac{d\sigma}{d\Omega}\right)_{\lambda\to\lambda'} = \frac{k'}{k}\left|\int b_j e^{i\mathbf{Q}.\mathbf{r}_j} dr\right|^2, \tag{4.13}$$

where b_j is the scattering length of the jth nucleus located at position $\mathbf{r}_j$, and $\mathbf{Q}$ is the scattering vector.

The partial differential cross-section (PDCS) allows the possibility of inelastic scattering. It is formulated using the principle of conservation of energy between initial and final scattering states. The energy distribution of scattered neutrons is a delta function which can be integrated over time. The energy change of the neutron between initial and final states is $E - E'$ and is given

by

$$E - E' = \hbar\omega, \tag{4.14}$$

where the frequency ω is positive for neutron energy loss and negative for energy gain.

The resulting PDCS is given by

$$\frac{d^2\sigma}{d\Omega dE'} = \frac{k}{k'}\frac{1}{2\pi\hbar}\sum_{jj'} b_j b_{j'} \int_{-\infty}^{\infty} \left\langle e^{-i\mathbf{Q}.\mathbf{r}_{j'}(0)} e^{i\mathbf{Q}.\mathbf{r}_j(t)} \right\rangle e^{-i\omega t} dt, \tag{4.15}$$

for a system where the scattering length b varies from one nucleus to another. The angled parentheses denote an average over all starting times from 0 to t for observations of the system, equivalent to averaging over the system's thermodynamic states.

4.1.6 Coherent and incoherent scattering

Equation 4.15 may be rewritten as the sum of two contributions describing particle correlations:

$$\frac{d^2\sigma}{d\Omega dE'} = \frac{k}{k'}\frac{1}{2\pi\hbar}\left[\begin{array}{c} \bar{b}^2 \sum_{jj'} \int_{-\infty}^{\infty} \left\langle e^{-i\mathbf{Q}.\mathbf{r}_{j'}(0)} e^{i\mathbf{Q}.\mathbf{r}_j(t)} \right\rangle e^{-i\omega t} dt \\ \\ +(\overline{b^2} - \bar{b}^2) \sum_j \int_{-\infty}^{\infty} \left\langle e^{-i\mathbf{Q}.\mathbf{r}_j(0)} e^{i\mathbf{Q}.\mathbf{r}_j(t)} \right\rangle e^{-i\omega t} dt \end{array}\right], \tag{4.16}$$

The first term in the square parentheses depends on the correlation between the positions of the same nucleus and (more often because there are many of

them) different nuclei at varying times, giving rise to interference effects. This is called coherent scattering, which provides structural information about the sample, and is the term extracted in a diffraction experiment. The second term depends only on the correlation between the positions of the same nucleus at varying times, which does not cause interference effects; this is known as incoherent scattering. This is generally isotropic and in diffraction experiments it adds a featureless background to the coherent scattering. However, incoherent scattering can be used to probe the dynamics of a system and so it is the incoherent scattering length which is important in INS.

The scattering length pre-factor, $(\overline{b^2} - \bar{b}^2)$, represents random fluctuations of the scattering lengths from the average scattering length of the particles.

4.1.7 Neutron diffraction

In a theoretical diffraction experiment where no corrections apply to the data, the PDCS is equal to the total structure factor $F(Q, \omega)$ where Q is the magnitude of the momentum transfer $\mathbf{Q}$ and $\hbar\omega$ is the energy transferred to the sample. This contains both structural and dynamical information about the sample; only the first part is required. This represents the elastic scattering from the sample and is written $F(Q, 0)$. Energy transfer is liable to occur from nuclear recoil in the sample, but diffraction experiments are analysed only as a function of Q. The instrument is set up so the detectors integrate over all energy transfers. This means the diffraction picture is an ensemble average of the material for $t = 0$. As long as the energy transfer is small compared with the neutron energy, $F(Q, \omega)$ can be approximated to $F(Q, 0)$. This is termed the static approximation: it breaks down for liquid samples.

The total differential cross-section measured is given by

$$\frac{d\sigma}{d\Omega} = \int \frac{d^2\sigma}{d\Omega dE'} dE'. \tag{4.17}$$

The DCS can be formulated for an isotropic system as

$$\frac{d\sigma}{d\Omega} = \overline{b^2} - \bar{b}^2 \int 4\pi r^2 \rho_0 [g(r) - 1] \frac{\sin(Qr)}{Qr} dr, \tag{4.18}$$

where ρ_0 is the atomic number density and $g(r)$ the pair correlation function: this is the probability of finding an atom a distance r from another one. The measured diffraction pattern therefore consists of a featureless background combined with the coherent scattering: $\overline{b^2}$, the self term, which depends on correlations between the same atom at different times, and the interference or distinct term, the structure factor $F(Q)$, which contains the structural information of the sample. This last is a Fourier transform of $g(r)$.

This can be generalised to a system containing n chemical species. The measured DCS is the sum of the DCSs for individual species multiplied by an inter-species correlation factor (the static Faber-Ziman partial structure factor) and the relative abundance of each species. The total pair distribution function $G(r)$ and the total Faber-Ziman structure factor (FZSF) are related by a Fourier transform pair. The FZSF is in effect a weighted sum of all the individual partial structure factors and can be extracted from a diffraction experiment. To determine the contribution of individual species to this, isotopic substitution can be performed.

This technique is available because neutrons scatter from atomic nuclei independently of mass number, each type of nucleus having distinct values for coherent and incoherent scattering length, which can also be measured as coherent and incoherent cross-sectional area (the absorption cross-section σ_{abs} determines the probability of a neutron being absorbed by an atom). As σ_{total}

Table 4.2: Selected neutron scattering cross-sections for elements of interest to this research. σ_{inc} is the incoherent cross section, and σ_{coh} the coherent cross section. 1 barn = $10^{-28}\mathrm{m}^2$. Reproduced from [91]

Element	^{1}H	^{2}H (D)	C	K	Ca	V
σ_{inc} (barn)	80.27	2.05	0	0.25	0	5.0
σ_{coh} (barn)	1.7583	5.592	5.559	1.76	2.90	0.02

in Eqn. 4.11 is composed of the coherent and incoherent cross-sections

$$\sigma_{total} = \sigma_{inc} + \sigma_{coh}, \tag{4.19}$$

they are related to coherent and incoherent scattering lengths by

$$\sigma_{inc} = 4\pi b_{inc}^2, \quad \sigma_{coh} = 4\pi b_{coh}^2 \ . \tag{4.20}$$

Some cross-sections are shown in Table 4.2. Scattering cross-sections can vary considerably between isotopes of the same element, with one of the largest difference being between ^{1}H and ^{2}H (deuterium), allowing information to be obtained from isotopic substitution, where one isotope is selectively exchanged for another. This has proved a very useful technique to improve contrast between different species in a compound structure.

4.1.8 Scattering from crystals

If the scattering system is a single crystal, the cross-sections can be evaluated by considering a unit cell of a Bravais lattice with sides $\mathbf{a}_1$, $\mathbf{a}_2$, $\mathbf{a}_3$. It has a reciprocal unit cell in k-space with unit cell vectors $\boldsymbol{\tau}_1$, $\boldsymbol{\tau}_2$ and $\boldsymbol{\tau}_3$, where

$$\begin{aligned} \boldsymbol{\tau}_1 &= \tfrac{2\pi}{v_0}[\mathbf{a}_2 \times \mathbf{a}_3], \quad \boldsymbol{\tau}_2 = \tfrac{2\pi}{v_0}[\mathbf{a}_3 \times \mathbf{a}_1], \\ \boldsymbol{\tau}_3 &= \tfrac{2\pi}{v_0}[\mathbf{a}_1 \times \mathbf{a}_2]. \end{aligned} \tag{4.21}$$

The interatomic forces in the crystal are held to be harmonic. In this case displacements $\mathbf{u}_l$ of atoms from their mean positions $\mathbf{l}$ can be described as the sum of displacements due to a set of normal modes:

$$\mathbf{u}_l = \left(\frac{\hbar}{2MN}\right)^{1/2} \sum_s \frac{\mathbf{e}_s}{\sqrt{\omega_s}} \left[a_s e^{i\mathbf{q}.\mathbf{l}} + a_s^\dagger e^{-i\mathbf{q}.\mathbf{l}}\right], \tag{4.22}$$

where $\mathbf{q}$ is the wavevector of the mode and j its polarisation index, which can be 1, 2, or 3. s stands for the double index $\mathbf{q}$,j; ω_s is the angular frequency of the mode s, and $\mathbf{e}_s$ its polarisation vector. M is the mass of an atom (a monatomic crystal is being considered) and N the number of values of $\mathbf{q}$ in the first Brillouin zone, over the three values of j. a_s is the annihilation operator for the mode s, and $a_s^\dagger$ the creation operator. These are replaced with time-dependent operators to retrieve the time-dependent modes.

The probability function for a harmonic oscillator is derived from the Bloch theorem; the probability of finding a particle in an ensemble at temperature T in state n is expressed and its displacement probability is thermally averaged assuming it is a 1D harmonic oscillator, and is Gaussian in form.

A 3D crystal of N atoms has $3N$ normal modes. These modes are associated with $3N$ oscillators with quantum numbers n_1, n_2... n_{3N}. Following a scattering event, the system is in state λ' given by a second set of quantum numbers n_1', n_2'... n_{3N}'. These are changed according to the type of scattering process that occurred. In an elastic event, all the numbers remain unchanged. In a one-phonon process, all the numbers remain unchanged except one mode, which changes by ± 1. For two-phonon processes, two oscillators are changed

by ± 1, and so on. The coherent partial differential cross-section can be expanded to become a sum of the cross-sections of each p-phonon-process, where $0 < p < 3N$. For coherent elastic scattering we are concerned with the first term only, from which is obtained the differential coherent elastic cross-section

$$\left(\frac{d\sigma}{d\Omega}\right)_{coh\ el} = \frac{\sigma_{coh}}{4\pi} N \frac{(2\pi)^2}{v_0} e^{-2W} \sum_{\boldsymbol{\tau}} \delta(\mathbf{Q} - \boldsymbol{\tau}), \tag{4.23}$$

where v_0 is the unit cell volume of the crystal, $\boldsymbol{\tau}$ a vector in the reciprocal lattice, and $2W = \langle [\mathbf{Q}.\mathbf{u}_0(0)]^2 \rangle$ where $\mathbf{u}_0(0)$ is the displacement from the equilibrium position $\mathbf{l}$ at $t = 0$.

From this it can be seen that $\mathbf{Q} = \mathbf{k}$ - $\mathbf{k'} = \boldsymbol{\tau}$ which is the condition for Bragg scattering. Only when the momentum transfer is equivalent to a vector connecting points in the reciprocal lattice will there be scattering. This is made explicit using geometry in the reciprocal lattice. Bragg's Law is

$$n\lambda = 2d \sin\theta, \tag{4.24}$$

where n is an integer denoting the order of scattering, d the distance between successive crystal planes perpendicular to the scattering normal (represented in reciprocal space by $\boldsymbol{\tau}$), and θ half the scattering angle. A series of sharply-defined Bragg peaks are seen at particular angles where constructive interference takes place between the planes. The sharpness of the peaks diminishes as a structure becomes less ordered. For amorphous structures or liquids with no long range order the scattering pattern is more continuous, with short-range ordering or nearest-neighbour distances deducible from the relation between the first peaks of the pattern.

The exponential term in Eqn. 4.23 is known as the Debye-Waller factor

and causes an attenuation of scattering intensity as a function of temperature.

This formalism can be generalised to non-Bravais lattices. The intensity of a Bragg peak is evaluated by the Laue method, where neutrons with a continuous range of wavelengths are incident on a fixed crystal. An integration of the neutron flux with wavelengths between λ and $\lambda + d\lambda$, with the total cross-section $\sigma_{tot\ \boldsymbol{\tau}}$ for the value where the Bragg condition is satisfied gives

$$P = \frac{V}{v_0^2}\phi(\lambda)\frac{\lambda^4}{2\sin^2\theta}|F_N(\boldsymbol{\tau})|^2 \tag{4.25}$$

where P is the number of neutrons per second in the scattered beam, $V = Nv_0$ and is the volume of the crystal, $F_N(\boldsymbol{\tau})$ is the unit cell structure factor, λ the neutron wavelength, and $\phi(\lambda)$ the wavelength-dependent neutron flux. $F_N(\boldsymbol{\tau})$ is given by

$$F_N(\boldsymbol{\tau}) = \sum_j \bar{b}_j e^{i\mathbf{Q}\cdot\mathbf{r}_j} e^{-W_j}. \tag{4.26}$$

$\bar{b}_j$ is the mean value of scattering length and W_j the Debye-Waller factor for each nuclear position $\mathbf{r}_j$.

4.1.9 Inelastic neutron scattering

Inelastic neutron scattering is used to measure the dynamics of a system. In a measurement where the energy transfer is small, this is known as quasi-elastic neutron scattering (QENS). The correlation of a nucleus with itself at different times is therefore the property we consider, and the quantity extracted in the experiment is called the incoherent scattering function, $S_{inc}(\mathbf{Q}, \omega)$. To link these we define a correlation function $G(\mathbf{r}, t)$, which is the probability that,

given a particle at time $t = 0$ at the origin $\mathbf{r}= 0$, any particle is present at time t and position $\mathbf{r}$ in a volume element $d\mathbf{r}$. As this particle may be the same as the first, the resulting function has a self part, $G_S(\mathbf{r}, t)$, which measures the correlation between a particle and itself as a function of time, and a distinct part, $G_D(\mathbf{r}, t)$:

$$G(\mathbf{r}, t) = G_S(\mathbf{r}, t) + G_D(\mathbf{r}, t). \tag{4.27}$$

This is related to an intermediate scattering function $I(\mathbf{Q}, t)$ by a Fourier transformation in space, and this function can then be transformed into $S(\mathbf{Q}, \omega)$ by a Fourier transformation in time, thus:

$$G(\mathbf{r}, t) = \frac{\hbar}{(2\pi)^3} \int S(\mathbf{Q}, \omega) e^{-i(\mathbf{Q}.\mathbf{r}-\omega t)} d\mathbf{Q} d\omega \tag{4.28}$$

and

$$S(\mathbf{Q}, \omega) = \frac{1}{2\pi\hbar} \int G(\mathbf{r}, t) e^{i(\mathbf{Q}.\mathbf{r}-\omega t)} d\mathbf{r} dt. \tag{4.29}$$

$G_S(\mathbf{r}, t)$ is related to the incoherent structure factor $S_{inc}(\mathbf{Q}, \omega)$ by

$$G_S(\mathbf{r}, t) = \frac{\hbar}{(2\pi)^3} \int S_{inc}(\mathbf{Q}, \omega) e^{-i(\mathbf{Q}.\mathbf{r}-\omega t)} d\mathbf{Q} d\omega \tag{4.30}$$

and

$$S_{inc}(\mathbf{Q}, \omega) = \frac{1}{2\pi\hbar} \int G_S(\mathbf{r}, t) e^{i(\mathbf{Q}.\mathbf{r}-\omega t)} d\mathbf{r} dt. \tag{4.31}$$

The coherent partial differential cross-section is given by

$$\left(\frac{d^2\sigma}{d\Omega dE'}\right)_{coh} = \frac{\sigma_{coh}}{4\pi}\frac{k'}{k}NS(\mathbf{Q},\omega) \tag{4.32}$$

and the incoherent PDCS is related to $S_{inc}(\mathbf{Q},\omega)$ by

$$\left(\frac{d^2\sigma}{d\Omega dE'}\right)_{inc} = \frac{\sigma_{inc}}{4\pi}\frac{k'}{k}NS_{inc}(\mathbf{Q},\omega) \tag{4.33}$$

where N is the number of nuclei in the scattering system, k and k' the magnitude of the incident and scattering vector respectively.

Both the incoherent and coherent PDCS contribute to the experimental measurements, but only the incoherent component is wanted, as it relates the correlations of the same nucleus across time. Thus elements with a large ratio of incoherent to coherent scattering lengths are most useful to ensure the incoherent term dominates: ^{1}H is one of these. The one-phonon incoherent cross-section is the term for a simple incoherent scattering event, and is derived as

$$\left(\frac{d^2\sigma}{d\Omega dE'}\right)_{inc\ 1\ ph} = \begin{array}{c}\frac{\sigma_{inc}}{4\pi}\frac{k'}{k}\frac{1}{2M}e^{-2W}\sum_s \frac{(\mathbf{Q}.\mathbf{e}_s)^2}{\omega_s} \\ \times\{\langle n_s+1\rangle\delta(\omega-\omega_s)+\langle n_s\rangle\delta(\omega+\omega_s)\}\end{array} \tag{4.34}$$

where, as in Eqn. 4.22, ω_s is the angular frequency of the mode s, and $\mathbf{e}_s$ its polarisation vector. M is the mass of an atom, $2W$ an expression of the Debye-Waller factor, and n_s the quantum number of the oscillator in the scattering event. The first δ-function term refers to phonon emission and the second to phonon absorption. There is no interference condition as for coherent scattering, and so incoherent one-phonon scattering occurs for a continuous range of k' values. Thus the cross-section depends on the number of modes with the correct frequency.

In an INS event, the neutron gains or loses an amount of energy which is transferred from or to the scattering nucleus. The energy transfer is characteristic of the motion of the nucleus; thus, for systems where the energies are quantised into allowed states, discrete peaks are seen in the INS spectra which relate to fundamental dynamic modes of the sample such as vibrations, librations or quantum tunnelling in a potential well, as proposed for H_2 in MC_{24} materials (§ 3.3.3). In the case of KC_{24}, the small incoherent cross-section of both C and K compared with H (Fig. 4.2), means that the H_2 dynamics are by far the most visible characteristic of the scattering, and this is improved by subtracting a background measurement of INS from the pure sample without H_2 to remove any contribution from the lattice (for the purpose of the experiment it is assumed that the graphene sheets are rigid). Diffusion of a species such as H_2 through a structure produces QENS events, as the diffusive motion is of low energy and long timescales compared with vibrational excitations. As outlined in the previous chapter, the local potential environment of the H_2 is accessible through INS.

Other correction factors which often apply to both diffraction and INS data include multiple scattering, instrument and sample cell contributions, and absorption in the sample.

4.1.10 Experimental techniques

The high visibility of hydrogen with respect to heavier elements makes neutron scattering methods ideal for studying hydrogen interactions and bonding within host compounds, and dynamics such as diffusion, molecular rotations and dissociation. Molecules containing hydrogen can be 'labelled' with H or D. Hydrogen is a largely incoherent scatterer which makes it unsuitable for diffraction experiments but useful for dynamical studies, and so for structural

studies it is wiser to use deuterium which is a better coherent scatterer.

Two main methods exist for producing neutrons at thermal energies for scattering. A reactor source, such as that at the Institute Laue-Langevin in Grenoble, France, produces high-flux continuous neutron radiation from fission reactions. The neutrons are moderated to thermal energy and a required wavelength is selected using a monochromator. The neutrons are collimated into a beam in the path of which is placed the sample. At measured angles around the sample position neutron detectors register arriving neutrons. A diffraction pattern from neutrons scattered from the sample is built up, forming Bragg peaks or continuous spectra depending on the crystallinity of the sample.

A pulsed neutron source, such as the ISIS facility (Fig. 4.3) at the Rutherford Appleton Laboratory in Oxfordshire, UK, generally uses a particle accelerator to produce a high-energy pulsed beam of protons which are fired at a heavy metal target such as tantalum or mercury. The target atoms slough off neutrons with a spherically-symmetric distribution in a process known as 'spallation' from the geological term for chipping away at a rock sample. A 'white beam' of energy-variant thermal neutrons is produced, passes through a moderator to reduce its energies, is collimated, passes through the sample and is scattered into detectors at fixed angles. Both the energy and wavelength are proportional to a neutron's speed and this is measured on detection by the time elapsed since the last neutron pulse was produced at the target. This is called 'time-of-flight' scattering analysis. In this way neutrons of all wavelengths are utilised to construct the scattering pattern. The complete pattern across the entire range of neutron momentum transfer, $\mathbf{Q}$, is detected from the first pulse. Pulsed or spallation neutron sources usually operate at 50 Hz pulse frequency; ultra-fast or ultra-slow neutrons from previous pulses which would interfere with the pattern are eliminated by a system of guides, choppers and neutron-absorbing beam stops. Although reactor sources have

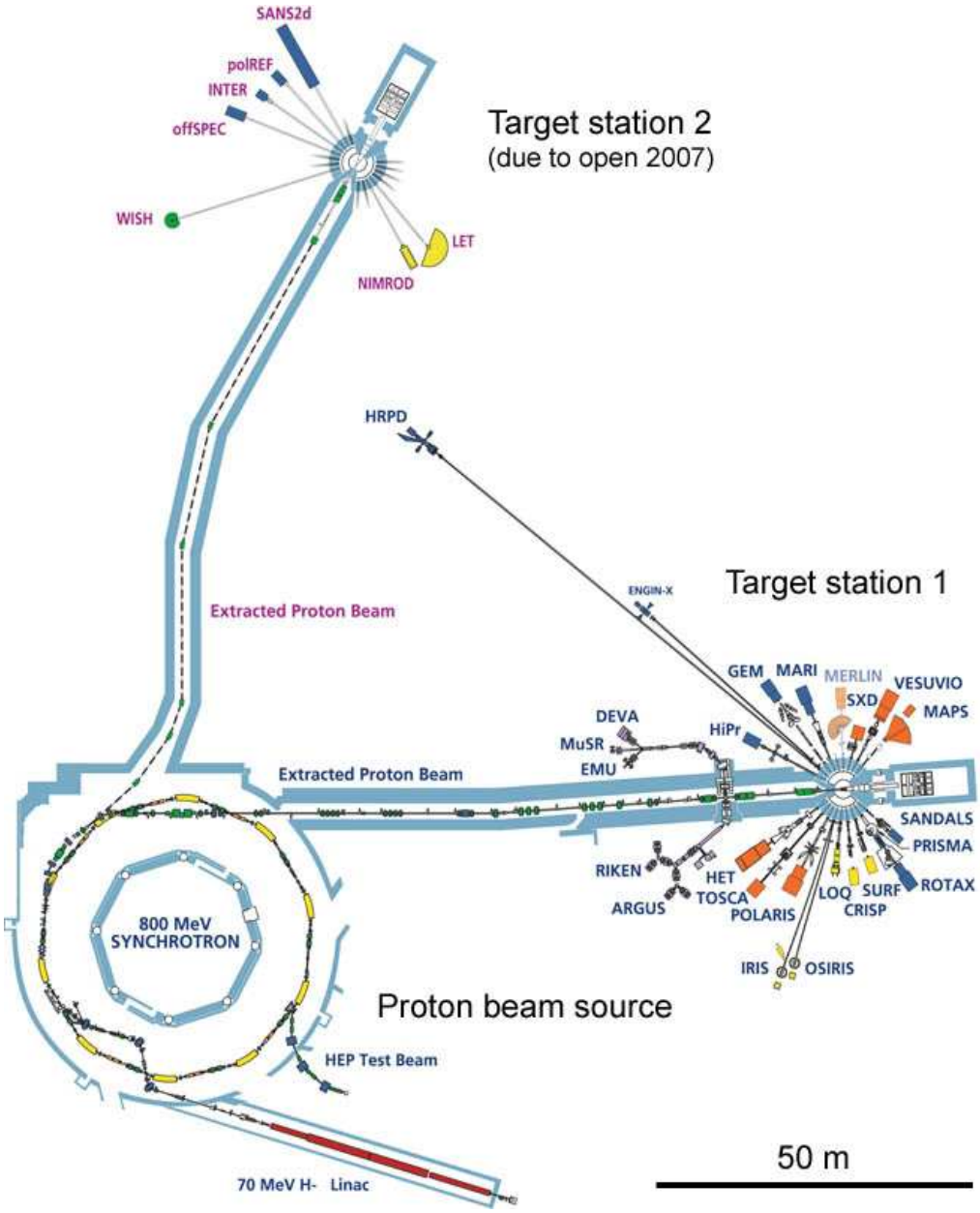

Figure 4.3: The ISIS neutron scattering facility at the Rutherford Appleton Laboratory, as at September 2005, showing the proton beam source, synchrotron accelerator and original target station (1) surrounded by instrument beamlines. A second target station (2) is due to open in late 2007. Adapted from [92]

a higher average flux, spallation sources are more intense. Reactor neutron sources produce MW of thermal energy; the heat dissipation in the ISIS target is 160 kW [93] and it is cooled by water.

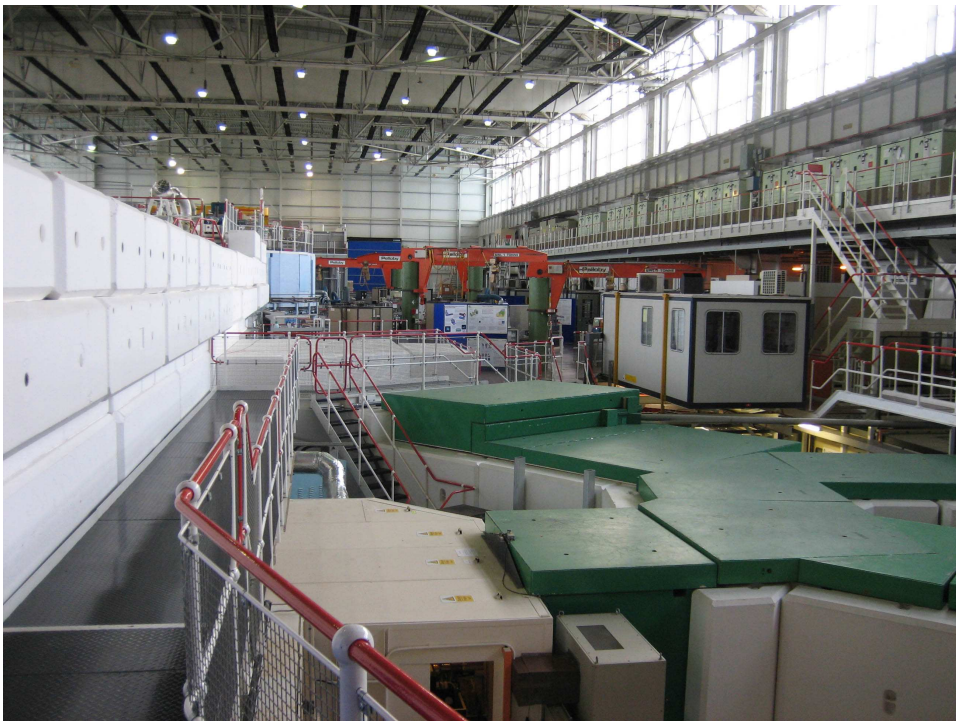

Figure 4.4: The ISIS experimental hall

Neutron experiments were planned using complementary diffraction and INS instruments to gain the most comprehensive data on the sample being studied. They were proposed and accepted using a peer-reviewed proposal system. All the experiments were performed at the ISIS facility (Fig. 4.4). Each accepted experiment is given a unique identifier called an RB number, and these are noted in the experimental sections.

4.1.11 Neutron instruments

A general diffractometer layout is shown in Fig. 4.5. A beam of neutrons from the moderator is selected to remove unwanted energies, and then, after

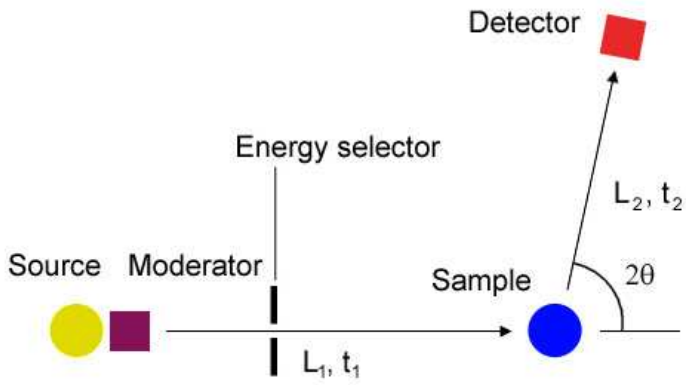

Figure 4.5: Schematic layout of a time-of-flight neutron diffractometer. Incident neutrons are collimated and selected by energy. They scatter elastically from the sample at an angle 2θ. They arrive at the detector with a distribution of times related directly to their energy, which can be calculated from the total time-of-flight $t_1 + t_2$ using the total flightpath $L_1 + L_2$ to determine the scattering properties of the sample.

a flightpath of typically some metres, is incident on the sample. The neutrons diffract through an angle 2θ to a detector. They arrive at a distribution of times after the initial pulse left the moderator and as the scattering was elastic, their energies can be worked out from the time-of-flight taken, $t_1 + t_2$, over the entire flightpath $L_1 + L_2$. Only those neutrons with wavelengths satisfying Bragg's law for one set of planes in the crystal will arrive in the detector, allowing a complete diffraction pattern to be assembled from the different wavelengths arriving.

Spectroscopic (INS) measurements are made by scattering neutrons inelastically from the sample. The neutron's kinetic energy as well as momentum vector is changed on collision with a dynamic nucleus, and as long as the incident neutron energy is known, the energy gain or loss ΔE can be calculated from measuring the final energy. This enables probing of excitations and thermal motions in the sample. Neutrons may lose or gain excitation-characteristic amounts of energy on scattering from the sample. The technique can record

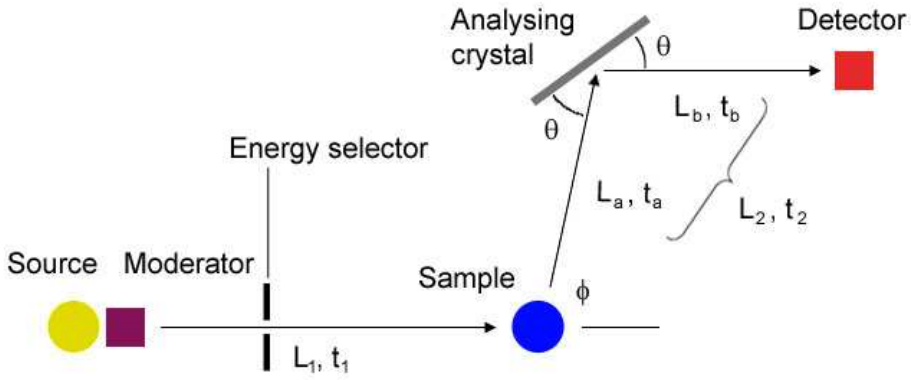

Figure 4.6: Schematic showing the layout of a time-of-flight neutron spectrometer. Incident neutrons are generally selected by energy before the sample, and scatter inelastically from the sample. Only those with wavelengths allowing Bragg scattering from the analyser into the detector are selected; i.e. the detector collects neutrons at constant energy and their time of arrival is used to determine the energy loss ΔE in the sample. The primary flightpath $L_1 >> L_2$, the secondary flightpath.

spectra up to energy transfers of several hundred meV, depending on the source and instrument setup. Quasi-elastic neutron scattering (QENS) looks at excitations very close to the elastic peak, a feature of INS spectra given by the large majority of neutrons which scatter elastically and so are detected at $E = 0$. Thermal processes lead to broadening of this peak which can be qualitatively analysed to find coefficients of diffusion of species through a sample, a very useful tool for studying hydrogen which in general has large diffusion rates.

A schematic of a time-of-flight neutron spectrometer is outlined in Fig. 4.6. Neutrons moderated from the source are further selected by energy using a chopper system to select an energy range, and then are incident on the sample. They are scattered through an angle ϕ and one monochromatic energy is selected by the crystal analyser using Bragg scattering (see previous section). The single-energy neutrons are detected with a distribution of arrival times which are compared with the time since the initial neutron pulse left the

source. The time-of-flight, t_2, of each neutron over the secondary flightpath, L_2, is known; from this the primary flightpath time-of-flight t_1 is calculated and hence the energy transfer in the sample. Neutron energy loss (that is, energies given by the neutron to phonons or other dynamic processes in the sample) appears on the positive energy transfer scale, and energy gain (energies transferred from dynamic processes to the scattering neutron) appears on the negative energy transfer scale.

4.1.12 Diffraction data refinement

To analyse diffraction data comprehensively it is necessary to correlate it with a sample structure. If the structure is known, the diffraction pattern peaks can be assigned to interference reflections from the characteristic dimensions of the sample or, in a liquid, short-range order between molecules. If, as is more usual in experiment, the structure is not known, a refinement of a trial structure is carried out. This can be done manually or using a fitting technique. For some of the diffraction data collected during this project, the refinement program GSAS [94] was used, with updated graphical front-end EXPGUI [95]. This uses Rietveld refinement techniques [96]. A proposed structure is inserted and its diffraction pattern calculated and refined incrementally to the real data using least-squares calculation. Fitting was made more complicated by the necessity to account for the sample's preferred orientation. This was attempted using a March-Dollase function [97] implemented in EXPGUI.

4.2 Gravimetric analysis

4.2.1 Introduction

This is a direct method of measurement of gas absorption in bulk materials. A sample of the host material is hung on a precisely-calibrated balance in a vacuum-sealed, temperature-controlled chamber. Purified gas is pressured into the chamber and into the sample, engendering a measurable weight change in the sample which is logged by the balance. As the pressure and temperature are independently controllable to high levels of precision, it is very straightforward to obtain isotherms of gas uptake as a function of applied gas pressure. The extrinsic value of the weight change can be converted to a storage factor in weight percentage as long as the base weight and density of the sample is known: this is a non-trivial procedure as a buoyancy correction must be made to counterbalance the upthrust on the sample by any gas pressure greater than vacuum.

Measuring gas uptake in bulk samples is essential to characterise hydrogen storage potential. A gravimetric mode of analysis is advantageous through relative ease of data collection and gathering of bulk data through the measurement of all the gas uptake in a macroscopic sample. The sensitivity of the technique is sufficient for good precision but care must be taken to ensure correct calibration and avoid any introduction of impurities.

For these measurements, an Intelligent Gravimetric Analyser (IGA 001) system was purchased from Hiden Isochema.

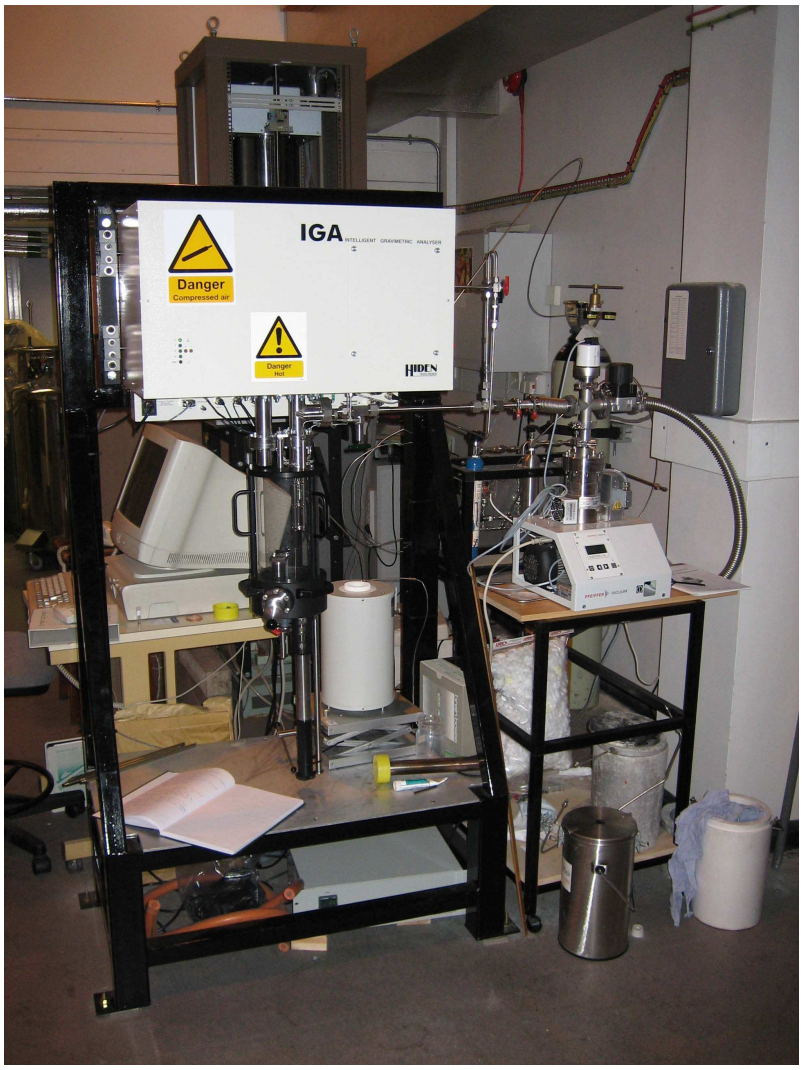

Figure 4.7: Intelligent Gravimetric Analyser (IGA) setup with dry loader attached.

4.2.2 The Intelligent Gravimetric Analyser

This system has a specified precision [98] of 1 μg for a maximum sample weight of 1 g. Software control from a dedicated PC allows simultaneous recording of 12 variables and fully-automatic accumulation of data across pressure ranges of 0 (vacuum) to 21 bar. Control of mass variables allows the automatic application of buoyancy corrections meaning that the uptake in weight percent can be plotted as a function of pressure. A furnace system linked to the software can attain stabilised sample temperatures of up to 500°C. The system has the capability of measuring at low temperatures but cryogenic apparatus was not initially supplied. A dry loader, designed to enable the successful transfer of air-sensitive material from glove-box storage to the IGA in inert conditions, was supplied.

The balance head, sample hangdown and counterweight are enclosed in a 2 litre stainless steel vacuum chamber, with the sample hangdown terminating in a stainless steel reaction tube, removable for loading, which is connected to the main balance chamber by a seal where a copper gasket is pressed between two CF flanges. In dynamic mode, the IGA constantly adjusts pressure, opening the admit valve as the pressure drops and the exhaust valve if it increases above the set point. The balance head is kept under a constant temperature set by the manufacturers at 55°C. The 500°C furnace has high thermal mass, with good thermal stabilisation. Temperature is measured at the sample, the balance head and externally. The pressure resolution of the system is $\sim$12 mbar - this can resolve 1 mbar $\pm$6 mbar.

4.2.3 Buoyancy correction

Buoyancy corrections are essential for pressure isotherms because of the upthrust of the gas about the sample. As the entire balance assembly is contained within the pressure chamber, a separate buoyancy value is required for each element within the apparatus. Those for components on the sample side of the balance contribute negatively to the recorded weight — the upthrust makes the sample seem lighter with increasing pressure — and those on the counterweight side contribute positively. The raw weight recorded during an isotherm run inevitably incorporates these buoyancy effects to give a set of readings strongly altered from the 'correct' uptake values. These correct readings are hard to estimate intuitively, especially where the buoyancy leads to an offset so negative as to counteract any increase in weight through sample absorption of gas. Small positive linear trends in uptake often appear to be negative, suggesting the sample might be losing mass as absorption gas pressure increases around it! The sample itself contributes significantly to the buoyancy error and to correct this accurately its density must be determined. This is achieved either using the IGA in density determination mode, or using some external measuring system such as a pycnometer (see § 6.1).

In gravimetric gas-sorption analysis the value to be measured is the mass of interacted gas or vapour, m_a, found from the weight force under gravitational acceleration. All other forces must be corrected for. The principal correction is that of buoyancy, caused by the upthrust on the sample and sample holder by the surrounding pressure of gas. The buoyancy upthrust force for an object in a gas of density ρ_g is given by

$$C_b = m_s g \frac{\rho_g}{\rho_s}, \tag{4.35}$$

where m_s is the mass of the object and ρ_s its density.

The total force including this buoyancy contribution, F_t, is given by

$$F_t = m_s g - C_b = (1 - \frac{\rho_g}{\rho_s}). \tag{4.36}$$

The gas density ρ_g is expressed as

$$\rho_g = \frac{MP}{Z(P,T)RT} \tag{4.37}$$

where M is the gas molar mass, P the gas pressure, T the gas temperature and Z the gas compressibility factor. R is the universal gas constant.

The IGA setup can be simulated simply as a beam balance with a reference mass m_1 of density ρ_1, which, when all forces are in equilibrium, can be expressed as

$$m_1(1 - \frac{\rho_{air}}{\rho_1})g = m_s(1 - \frac{\rho_{air}}{\rho_s})g, \tag{4.38}$$

where ρ_{air} is the air density.

The correction increases for samples with a density low compared with that of the reference mass. The Earth's gravitational acceleration is considered to be constant over the small spatial separation of the balance ends and so is ignored in subsequent expressions. The sample mass m_s for an ideal balance is therefore calculated to be

$$m_s = \frac{(1 - \frac{\rho_{air}}{\rho_1})}{(1 - \frac{\rho_{air}}{\rho_s})}. \tag{4.39}$$

In the case that the densities of the reference mass and the sample are identical, called *compensated loading*, the buoyancy correction is unnecessary and m_s=m_1.

The IGA incorporates an electronic beam balance (EBB) which measures an output, ϕ, proportional to the difference in weight between the sample and the reference arms. The reference mass is typically a counterweight fashioned from stainless steel. When the balance is completely unloaded, ϕ is not zero but is arbitrarily set to a null position approximately in the middle of the measurement range. Excess force on the balance gives a positive or negative output depending on whether the sample or the reference arm is loaded. The exact null position, ϕ_0, depends on the balance alignment. The perfected balanced condition where $\phi = \phi_0$ is called *balanced loading*. For mass uptake measurements ϕ_0 is not a required quantity because uptake is measured from force changes with respect to a sample's 'dry' mass and not the null position.

ϕ_0 can be found if an object of mass m and density ρ is added to the balance in an atmosphere of density ρ_{air}. The resulting force, $\delta\rho_m$, is used to find ρ_0:

$$\rho_0 = \delta\rho_m - m(1 - \frac{\rho_{air}}{\rho}) = \delta\rho_m - w \tag{4.40}$$

where w is defined as the equivalent object weight at the same air density.

The buoyancy correction is important in a sensitive balance, where the registered weight increase in a sample is small compared with the upthrust in a high-pressure atmosphere, or where the density of a sample is not significantly greater than the surrounding gas. Even where the correction is not significant, however, the data added to the buoyancy table is a useful record of the system setup and can be used to derive ϕ.

Any object may be hung on the balance and be used in buoyancy calculations as long as its properties are inserted into the calculator by means of the table.

Table 4.3: IGA buoyancy calculation variables

Object	Description	Weight	Density	Temperature
s	Dry sample	m_s	ρ_s	T_s
a	Interacted gas/vapour	m_a	ρ_a	T_s
i_1	Sample container	$w_{i=1}$	$\rho_{i=1}$	$T_{i=1}$
i_2	Sample ballast	$w_{i=2}$	$\rho_{i=2}$	$T_{i=2}$
i_3	Upper sample hangdown	$w_{i=3}$	$\rho_{i=3}$	$T_{i=3}$
i_4	Lower sample hangdown	$w_{i=4}$	$\rho_{i=4}$	$T_{i=4}$
j_1	Counterweight	$w_{j=1}$	$\rho_{j=1}$	$T_{j=1}$
j_2	Counterweight container	$w_{j=2}$	$\rho_{j=2}$	$T_{j=2}$
j_3	Upper counterweight hangdown	$w_{j=3}$	$\rho_{j=3}$	$T_{j=3}$
j_4	Lower counterweight hangdown	$w_{j=4}$	$\rho_{j=4}$	$T_{j=4}$

The buoyancy calculator in the IGA software has capacity for 10 objects, the variables for which are defined in table 4.3. Objects labelled s, a and i_x are defined in the sense of increasing weight on the sample side of the balance, and those labelled j_x are in the sense of increasing weight on the reference (or counterweight) arm. Not all of these items are necessarily present at any time. Included is a contribution for the interacted, or absorbed, phase, m_a, possessing density ρ_a.

To find the total buoyancy correction, C_b, in a gas of density $\rho_{g'}$, it is necessary to sum all the terms for gas displacement arriving from each object present:

$$C_b = \Sigma_{i=1,4} m_i \frac{\rho_{gi'}}{\rho_i} - \Sigma_{j=1,4} m_j \frac{\rho_{gj'}}{\rho_j} + m_s \frac{\rho_{gs'}}{\rho_s} + m_a \frac{\rho_{gs'}}{\rho_a} \tag{4.41}$$

It is expected generally that the largest contribution to the buoyancy correction will come from the sample, because reference objects, including the counterweight and hangdowns, are normally made from dense materials to avoid contributing largely to the buoyancy. The buoyancy arising from the interacted mass of gas or vapour is low, except where the gas density in the chamber is high, in conditions of high pressure or low temperature.

The real sample mass is usually unknown at time of loading, because the sample has been weighed in air or is not completely dry or free from impurities. This is why m_s is entered under 'weight' in table 4.3; effectively that is what the IGA measures and so the buoyancy calculator specifies all the items as weights not masses. It can make corrections for air density based on the value of ρ_{air} entered in the buoyancy setup dialogue box. It also registers the air density automatically on loading.

An object with index i in Table 4.3 has a correction in terms of its weight w_i as follows:

$$C_b = m_i \frac{\rho_{gi'}}{\rho_i} \tag{4.42}$$

where

$$m_i = \frac{w_i}{(1 - \frac{\rho_{air}}{\rho_i})} \tag{4.43}$$

thus

$$C_b = w_i \frac{\rho_{gi'}}{(\rho_i - \rho_{air})} \tag{4.44}$$

When measured in vacuum, m_i=w_i as there is no air buoyancy to account for. The final expression for the buoyancy correction takes into account the weights of the reference materials:

$$C_b = \Sigma_{i=1,4} w_i \frac{\rho_{gi'}}{\rho_i - \rho_{air}} - \Sigma_{j=1,4} w_j \frac{\rho_{gj'}}{\rho_j - \rho_{air}} + m_s \frac{\rho_{gs'}}{\rho_s} + m_a \frac{\rho_{gs'}}{\rho_a} \tag{4.45}$$

When the sample is loaded it is not considered to be 'dry' by the system. The first operation carried out on a sample is typically an outgas. In the case of the intercalate samples, made using outgassed graphite and metal in a dry inert atmosphere, little outgassing should be necessary in theory, but the dry loading system in practice turned out not to be foolproof, and with the possibility of atmospheric contamination in the loaded samples a significant concern, outgassing was carried out at temperatures dependent on sample type and in conditions of high vacuum ($4 \times 10^{-7} > p > 2 \times 10^{-6}$ mbar), with the sample chamber directly connected to the TMP. These outgassings were typically carried out until no more weight loss was registered by the IGA data collection.

The 'wet' weight of a newly-loaded sample is called the 'load' by the IGA software and is the difference between the total weight with the sample loaded, ϕ_I and the unloaded value, ϕ_U. In practice it does not matter if the weight is changing on loading of the sample, because m_s cannot be calculated without bringing the sample to some 'dry' state, vital for adsorption experiments. The dry mass, ϕ_D, is defined as

$$\phi_D = \Sigma_{i=1,4} w_i \frac{\rho_i - \rho_{gi'}}{\rho_i - \rho_{air}} - \Sigma_{j=1,4} w_j \frac{\rho_j - \rho_{gj'}}{\rho_j - \rho_{air}} + m_s \frac{1 - \rho_{gs'}}{\rho_s} + \phi_0 \tag{4.46}$$

which includes the correction for the change in buoyancy between the loaded state in air and the end state in gas density ρ_g. In favour of m_s,

$$m_s = \frac{\phi_D - \phi_U + \Sigma_{i=1,4} w_i \frac{\rho_{gi} - \rho_{air}}{\rho_i - \rho_{air}} - \Sigma_{j=1,4} w_j \frac{\rho_{gj} - \rho_{air}}{\rho_j - \rho_{air}}}{\frac{1 - \rho_{gs'}}{\rho_s}} \tag{4.47}$$

where ρ_g are densities corresponding with the force measurement of ϕ_D and are zero if the dry mass is in vacuum. In this case, there is no buoyancy correction, and formula 4.47 reduces to

$$m_s = \phi_D - \phi_U. \tag{4.48}$$

For calculating the mass of interacted gas, m_a, one accounts for buoyancy after a force reading, ϕ_s, is taken after the dry sample is allowed to react with gas or vapour of density $\rho_{g'}$.

$$\phi_s = \Sigma_{i=1,4} w_i \frac{\rho_i - \rho_{gi'}}{\rho_i - \rho_{air}} - \Sigma_{j=1,4} w_j \frac{\rho_j - \rho_{gj'}}{\rho_j - \rho_{air}} + m_s \frac{1 - \rho_{gs'}}{\rho_s} + m_a \frac{1 - \rho_{gs'}}{\rho_a} + \phi_0 \tag{4.49}$$

and m_a is expressed using ϕ_D as

$$m_a = \frac{\phi_s - \phi_U + \Sigma_{i=1,4} w_i \frac{\rho_{gi'} - \rho_{air}}{\rho_i - \rho_{air}} - \Sigma_{j=1,4} w_j \frac{\rho_{gj'} - \rho_{air}}{\rho_j - \rho_{air}} - m_s \frac{1 - \rho_{gs'}}{\rho_s}}{\frac{1 - \rho_{gs'}}{\rho_a}}. \tag{4.50}$$

The mass percentage uptake is calculated from

$$\%Mass = 100 \times m_a/m_s. \tag{4.51}$$

4.2.4 IGA Density determination

Obtaining accurate measurements of sample density is important for use in calculating the error due to sample buoyancy and hence correcting to give an accurate value of the weight uptake. The IGA is able to carry out density determination measurements on porous samples. A sample is loaded and then its weight determined under a number of different pressures of a known inert gas. The gas by definition must not interact with the sample; in that case, Equation 4.50 can be used with $m_a = 0$ and the term $\frac{1-\rho_{gs'}}{\rho_a}$ does not apply. If the expression is rearranged in favour of the sample volume $V_s = m_s/\rho_s$, one can plot

$$y = \phi_s - \phi_U + \Sigma_{i=1,4} w_i \frac{\rho_{gi'} - \rho_{air}}{\rho_i - \rho_{air}} - \Sigma_{j=1,4} w_j \frac{\rho_{gj'} - \rho_{air}}{\rho_j - \rho_{air}} - m_s \tag{4.52}$$

against $x = \rho_{gs'}$, which gives a gradient of $-V_s$. The displaced volume is found by a least squares fit to the rescaled straight line. A new value of m_s is found by rearranging Equation 4.47 as

$$m_s = \phi_D - \phi_U + \Sigma_{i=1,4} w_i \frac{\rho_{gi} - \rho_{air}}{\rho_i - \rho_{air}} - \Sigma_{j=1,4} w_j \frac{\rho_{gj} - \rho_{air}}{\rho_j - \rho_{air}} + V_s \rho_{gs}, \tag{4.53}$$

which includes the buoyancy of the sample directly as $V_s \rho_{gs}$.

The new effective sample density is then

$$\rho_s = \frac{m_s}{V_s}. \tag{4.54}$$

This fit can be performed from the uptake data in the IGASWIN software.

4.2.5 Adsorption theory

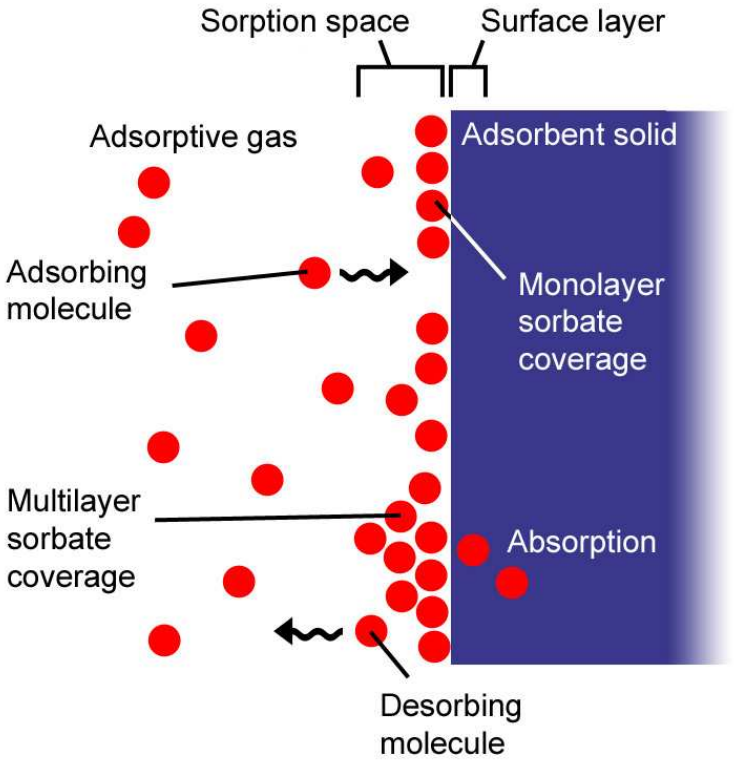

Figure 4.8: Properties of gas adsorption on a solid surface

Gas molecules that approach a solid surface may adsorb; that is to say, may associate with the surface such that the solid-gas interface demonstrates an enrichment of the proportion of that gas compared with the bulk [99]. In general the interface can be divided into the surface layer of the adsorbing solid, or adsorbent, and a region in which the adsorption of the adsorptive gas

occurs (Fig. 4.8). The material in this sorption space is known as the adsorbate to distinguish it from the unadsorbed gas. If the adsorbate penetrates the solid surface and moves into the bulk solid, the term *ab*sorption is strictly speaking used. Where it is difficult to distinguish a difference between ad- and absorption, the terms sorption, sorbent, sorptive and sorbate are often used. Desorption is the process by which the concentration of sorbate atoms or molecules is reduced. The relation between the equilibrium pressure of the gas, at constant temperature, and the amount adsorbed, is defined as the adsorption isotherm. Any difference between the adsorption and desorption curve demonstrates adsorption hysteresis. As many sorbent materials of high surface area are porous, characteristic pore sizes can be defined and the sorption behaviour can vary with this, as well as the sorbent-sorptive interaction. Macropores are those with widths greater than about 50 nm; mesopores are those with widths between 2 and 50 nm, and micropores have dimensions of 2 nm or below. Any volume accessible by an adsorbate may be regarded as adsorption space; this is likely to vary with the adsorbing gas molecules' size and shape, leading to a molecular sieve effect. Gas adsorption measurements can be used for determining the pore size distribution and internal surface area of many materials.

Physisorption is the general case of sorption where the adsorbing molecules interact with the solid with the same forces that govern condensation; generally these are van der Waals-type interactions which are 2-3 orders of magnitude weaker than the binding energy of particles in the solid and the intramolecular bonds of the adsorbing gas, if it is not monatomic. The enthalpy of adsorption for hydrogen in graphite is 4-7 kJ mol^{-1}. The micropore filling process can be described as primary physisorption, while sorption on the internal surfaces of meso- and macropores can proceed from monolayer to multilayer coverage (Fig. 4.8) and thence by capillary condensation. Monolayer coverage is defined

as that situation where every adsorbed molecule is in direct contact with the solid surface. Multilayer coverage has one or more layers of sorbate molecules on top of the monolayer. Capillary condensation is where any left-over pore space after multilayer adsorption has occurred is filled with liquid-like bulk adsorbate separated from the gas phase by a meniscus. This generally occurs at pressures and temperatures similar to that at which the bulk gas condenses.

The monolayer capacity is defined as the quantity of adsorbed gas needed to cover the surface of the sorbent entirely with a monomolecular layer. The surface coverage is then the ratio of the actual adsorbed quantity to the monolayer capacity; if greater than unity then multilayer sorption is occurring.

4.2.6 Isotherm types

Six characteristic isotherms are generally defined; they are illustrated in Fig. 4.9 and the majority of physisorption isotherms can be grouped into one of these. At low surface coverage isotherms are likely to display a linear form of uptake directly proportional to pressure.

Type I isotherms are reversible and known as Langmuir isotherms after the model advanced by Langmuir in 1916 [100]. They describe a surface where coverage is limited to a monomolecular layer, which leads to saturation as the monolayer capacity is reached. They are characteristic of microporous solids (where multilayer coverage is not possible) such as activated carbons and molecular sieve zeolites.

Type II isotherms are reversible, and shaped sigmoidally. They demonstrate unrestricted transition from mono- to multilayer adsorption. The point marked ‘B’ in Fig. 4.9 is taken to indicate the point at which monolayer coverage is complete and multilayers are beginning to form. A model to describe the

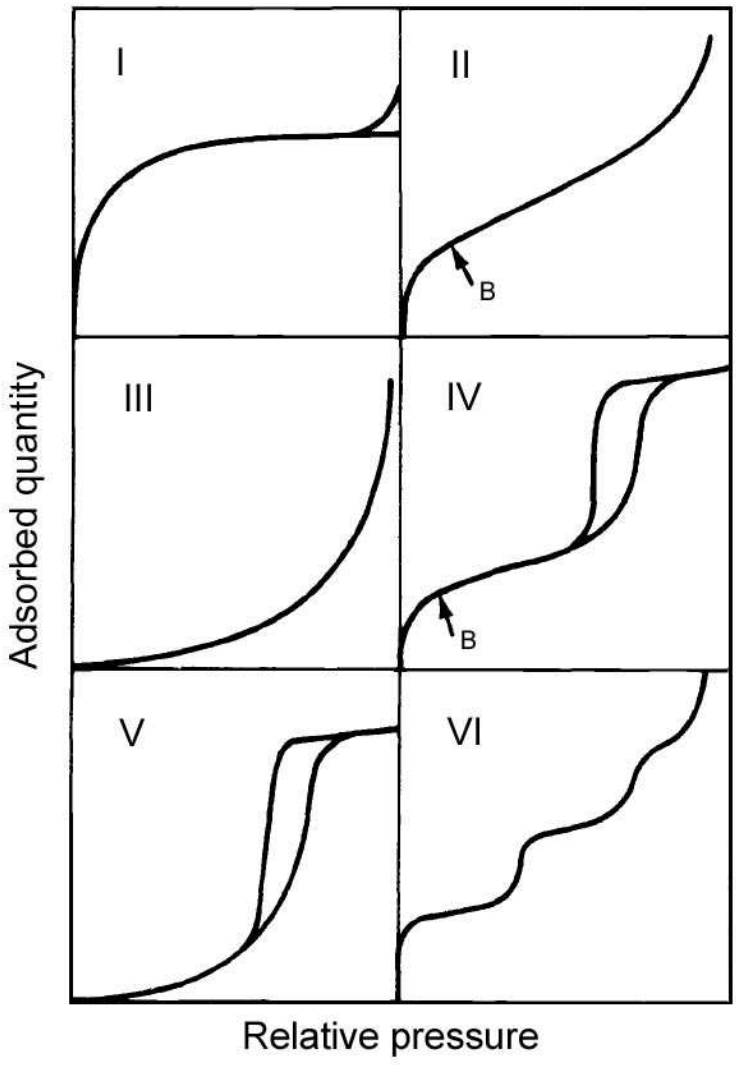

Figure 4.9: Types of adsorption isotherm, labelled I to VI and described in the main text

process was formulated by Brunauer, Emmett and Teller in 1938 [101] and so this type are known as BET isotherms. They are common and are associated with non- or macroporous materials.

Type III isotherms are convex to the pressure axis and are not common; some associated processes include water vapour adsorbed on non-porous carbons.

Type IV isotherms are similar to Type II in that the initial path is attributed to mono- to multilayer adsorption, with an analogous point 'B'; they have a hysteresis loop associated with capillary condensation in mesopores, and have a limiting uptake at high pressures.

Type V isotherms are related to Type III isotherms, but are symptomatic of porous adsorbents, with attendant hysteresis. The adsorbate-adsorbent interaction is weaker than the intra-adsorbate bonding.

Type VI isotherms demonstrate incremental additions of adsorbate layers to a non-porous surface, resulting in a step-like characteristic. They can be obtained by adsorption of krypton or argon on graphitised carbon at $\sim$77 K.

4.2.7 The Langmuir model

The Langmuir isotherm rests on three assumptions: firstly, that coverage cannot increase beyond the monolayer capacity; secondly, that all sites on the surface that can accommodate one molecule are equivalent; and thirdly, that the probability of a molecule adsorbing at a given site is independent of the occupancies of surrounding sites. At equilibrium, the adsorption equilibrium can be represented as

$$S + G \rightleftharpoons S - G, \tag{4.55}$$

where S is the number of surface sites, G the unadsorbed molecules in the gas, and $S - G$ the adsorbed molecules on the surface.

An equilibrium constant K can be determined as

$$K = \frac{[S - G]}{[S][G]}, \tag{4.56}$$

noting furthermore that $[S - G]$ is proportional to the surface coverage of adsorbed molecules, θ; $[S]$ is proportional to the number of vacant sites $1 - \theta$, and $[G]$ is proportional to the gas pressure P.

A second equilibrium constant b is therefore defined as

$$b = \frac{\theta}{(1 - \theta)P}, \tag{4.57}$$

which is more normally rearranged to give

$$\theta = \frac{bP}{1 + bP}. \tag{4.58}$$

This, the Langmuir isotherm, is only a constant if the enthalpy of adsorption is independent of coverage. b is temperature dependent and related to the enthalpy change.

4.2.8 The BET isotherm

The BET isotherm analysis treats multilayer coverage starting from these assumptions: there is no limit to the number of layers that can be adsorbed; the interaction between layers is constant; each layer can be described using the Langmuir model. The enthalpy of sorption of each layer above the first is treated as for condensation of the gas as liquid. At the saturation pressure of the gas, p_0, infinite condensation can take place. The isotherm is described by

$$\frac{1}{v[(p_0/p)-1]} = \frac{c-1}{v_m c}(\frac{p}{p_0}) + \frac{1}{v_m c}, \tag{4.59}$$

where p is the equilibrium pressure of the gas, v the adsorbed gas quantity, v_m the monolayer adsorbed gas quantity, and c the BET constant, which is given by

$$c = \exp(\frac{E_1 - E_L}{RT}), \tag{4.60}$$

where E_1 is the heat of adsorption for the first layer, and E_L the heat of adsorption for all subsequent layers, and equivalent to the heat of liquefaction in the gas. R is the ideal gas constant and T the isotherm temperature.

If the possible coverage is restrained so v/v_m cannot exceed 1, the Langmuir isotherm is obtained. Further developments of the theory by Brunauer, Deming, Deming and Teller provided a general model of adsorption, able to describe the first five types of isotherm as special cases [102].

4.2.9 Isotherm analysis using the IGA

An isotherm is measured by recording the equilibrium uptake (on the IGA, by registering the raw weight) in a sample after a change in chemical potential. This is usually obtained by varying the gas pressure; other examples are concentration, or humidity. A certain equilibration time is associated with each data point, and the magnitude of this varies strongly with sample and is intimately related to the diffusability of the sorbed gas in the sample and its concentration. If the sample undergoes a phase transition, the nucleation rate of the new phase will affect the timescale too.

If the relaxation to equilibrium is rapid (< 1 s) then direct measurement of the uptake within the system accuracy is possible. In the long time limit of diffusion the uptake trend tends to $e^{-t/k}$ where k is a time constant for the set of conditions under scrutiny. As the time scale increases it becomes inefficient to wait for equilibrium within the system accuracy; in this case the trend is analysed to determine the asymptote of the exponential. The IGA software has a real-time processor (RTP) which by least-squares regression on one of two fitting models can extrapolate an asymptotic value. It can adjust the length of time of each isotherm measurement and provides additional kinetic data.

If the relaxation time is so long that the maximum collection time is reached, the analysis software will either use the predicted asymptote, or if no asymptote is predicted, will use the last value of the uptake recorded. After some experimenting a 30 minute timeout was set for all isotherms. Analysis of the kinetic data showed that even where the timeout was reached, the uptake measurement was close enough to the asymptote to be inside the estimated instrument error.

The least-squares fitting program performs an iterative process until values converge to the fit minimum. Two models of the uptake variation with time are incorporated into the RTP; a linear driving force (LDF) model and an Avrami model.

The LDF model of the relaxation, $u(t)$, is given by

$$u(t) = u_0 + \Delta u(1 - \exp(-\frac{(t - t'_0}{k}), \tag{4.61}$$

where u_0 is the uptake at the arbitrary time origin t'_0, k is the exponential time constant, and Δu the change in uptake. The asymptotic uptake is $u_0 + \Delta u$. According to the IGA manual [98], the model is "identical" with the response of the microbalance control system. It is a simple model, with three model parameters. This is because u_0 and Δu are refined separately. It is applicable to a range of processes, including diffusion.

The Avrami model [103] [104] of the relaxation, $u(t)$, is given by

$$u(t) = u_0 + \Delta u(1 - \exp(-\frac{[t - t'_0]^x}{k}), \tag{4.62}$$

where again u_0 is the uptake at the arbitrary time origin t'_0, k is the exponential time constant, and Δu the change in uptake. x is a variable power. The asymptotic uptake equal to $u_0 + \Delta u$.

This model is suited to fitting phase transitions, including nucleation and growth of the new phase, for which generally $x > 1$. If $x < 1$, a good fit is obtained for many non-LDF sorption curves. When $x = 1$ the model is identical to the LDF model. The four adjustable parameters can describe many types of uptake/time relationships.

The LDF model was used to govern data collection on the IGA during the experimental work. The Avrami model was used to attempt fitting of the phase transition in KC_8 (§ 7.3).

Chapter 5

Experimental Work

The experimental work fell naturally into three major segments: firstly, the synthesis of the various intercalation compounds investigated; secondly, investigations of both structure and dynamics of hydrogen adsorbed into the materials using neutron scattering; thirdly, investigations into the hydrogen uptake capabilities of the GICs using thermogravimetry. These results will be presented in the three following chapters with the thermogravimetry first.

5.1 Synthesis of GICs

A large number of samples were synthesised during the course of the experimental work. The focus was initially on stage-1 and stage-2 potassium-GICs KC_8 and KC_{24}, and later moved to CaC_6. For each compound, macroscopic quantities ($\sim$1 g) were required for the two principal investigation techniques, neutron scattering and thermogravimetry. A set of synthesis techniques were accumulated from literature and previous work [43]; inevitably, early synthesis methods were superseded by later ones until an efficient procedure evolved for

making well-staged homogenous K-GICs which is outlined in the next sections. CaC_6 synthesis in bulk is a very recent achievement [50] and requires a more complicated co-intercalation technique or (for ternary Ca-GICs) the use of a liquid ammonia solution; our development of these methods has been successful but there is still opportunity for improving on them. Material characterisation has been able to determine the success rate of the synthesis methods.

5.1.1 Preparation of Graphite

The preparation of graphite prior to intercalation was undertaken with two objectives; firstly, to select the size and morphology of the eventual finished sample, as this is far more dependent on the graphite properties than the intercalant; and second, to remove as many of the impurities from the graphite as possible by heating and submitting the material to high vacuum for an extended period of time. Aside from any catalytic impurities such as copper or chlorine in the graphite, there may well be air impurities, specifically oxygen, attached to graphite edges and within the layers. These need to be removed to be able to make well-characterised samples. Oxygen bound to graphite surfaces and edges hinders the intercalation process by preventing the physical movement of intercalant into the interlayer spaces, and by providing potential sites for oxidation reactions of the air-sensitive metal intercalant species. This preparation is valid no matter what the morphology and size of the graphite used.

As discussed in § 3.2.2, exfoliated graphite was generally used as a base for K-GIC samples, and a mixture of exfoliated graphite and micron-sized graphite powder for Ca-GIC samples. The exfoliated graphite samples were made from Papyex flexible graphite, carbon content 99.8% by the manufacturer's data, supplied by Le Carbone (GB). The grade was N998SR ('nuclear grade') and

the sheet thickness a rolled 0.5 mm. As the sheet supplied was readily cut into integral strips the samples were generally created in strip form, with convenient dimensions for loading into the neutron scattering sample cans. This made a requirement to use flat-plate cans, the dimensions of which in the plane of the neutron beam's cross-section were 20×40 mm, with sample depth either 1 or 2 mm. Hence, strips were cut of dimensions 5×40×0.5 mm so that four of these side-by-side would fill the full width of the can. As the Papyex displays preferred orientation in the *c*-axis direction with this axis of the smaller exfoliated crystals pointing out of the plane of the sheet, the majority of the sample swelling due to intercalation was expected in this direction, the sheet thickness.

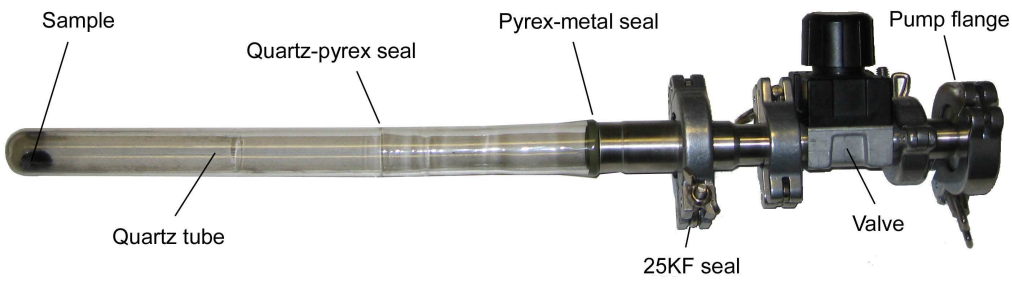

Figure 5.1: Quartz sample tube with valve for vapour transport synthesis

Strips of Papyex were cut, marked for identification and weighed in air. They were then inserted into a clean quartz glass tube with a glass-metal seal and KF-type vacuum flange. These tubes, manufactured by the UCL MAPS faculty workshop and glassblower during the course of the project, were used to make all the K-GIC samples. Where graphite powder was used instead, the procedure following was identical; a quantity of powder was weighed out in air, on a foil dish, before placing in the tube. The tube was sealed with a valve (Fig. 5.1), and the whole assembly moved to a tube furnace. Here, the valve was connected to a turbomolecular pumping station.

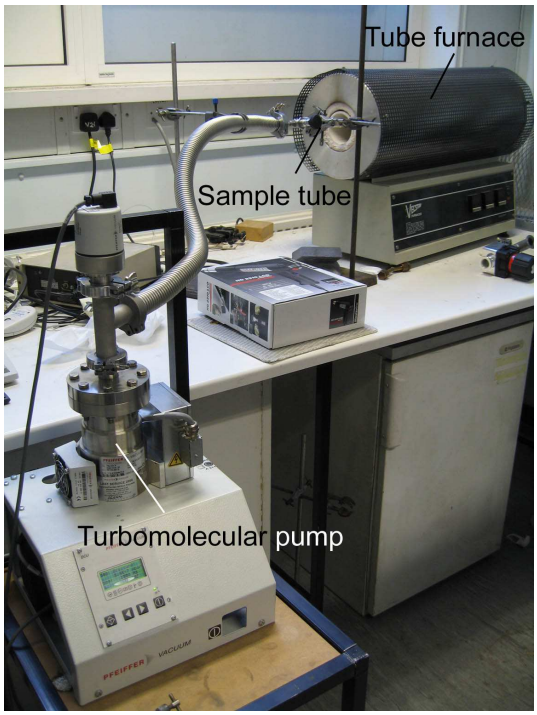

Figure 5.2: Equipment layout for graphite outgassing and vapour transport (1ZVT) GIC synthesis. The sample tube is connected to the pump while the end is inserted into the furnace. For outgassing, the valve is open to the pump; for 1ZVT the valve is closed.

The pump would be switched on and the closed valve on the tube opened gradually to prevent a rush of pumped air disturbing the graphite — more important if the graphite was fine powder rather than exfoliated strips. The tube end with the graphite was inserted into the furnace and the furnace temperature raised in steady increments, generally of 100°C, to 500°C, a temperature chosen to be higher than any used in the intercalation synthesis following but not high enough to cause thermal decomposition of the graphite (Fig. 5.2). As the temperature increased, often the pressure in the tube as read at the turbopump would be seen to increase as well, demonstrating the extra mobility given to the outgassing impurities by the heat. This whole procedure is known as 'graphite outgassing'.

As a general procedure the graphite was left to outgas at the selected temperature for more than 24 hours, the length depending on how rapidly the outgas pressure attained an acceptably low value. This was taken to be around 1-1.5$\times 10^{-6}$ mbar and could take up to 72 hours, with outgassing occasionally continuing for a week or more. From this point onwards in the synthesis process it was critical not to allow the sample to be exposed to air, moisture, or other reactants. Consequently the tube valve was shut firmly before the pump was deactivated, leaving the graphite sealed under vacuum. After cooling naturally, the tube assembly was placed in an argon glovebox of high purity atmosphere (containing H_2O, O_2 concentrations of less than 10 ppm; the ideal value was less than 1 ppm). The graphite was weighed again to determine the weight loss during outgassing. The graphite was then ready to be used in synthesis.

5.1.2 Synthesis of KC_8 and KC_{24}

These two compounds accounted for the largest proportion of samples created in the course of the experimental work. After the first syntheses, the methods

were evaluated and altered to improve the yield of well-staged, homogenous samples, and this process continued throughout the project. The intercalation method used was one-zone vapour transport (§ 3.2), modified slightly to include an element of liquid intercalation. Using a one-zone method proved perfectly adequate and was far simpler than using a two-zone method requiring a known temperature profile of the three-element tube furnace and some specialist glassblowing to separate the graphite and the potassium.

Samples of outgassed Papyex graphite of known mass were placed in the end of a tube of the type discussed in the previous section. Even after a long period of outgassing it could not be guaranteed that more impurities would leave the graphite, so a trick was used to remove them without reacting with the metal about to be added. A sacrificial lump of potassium was placed on a specially-designed spatula and moved down the tube to rest near the graphite. If the graphite was still outgassing the oxidising process would be seen to occur; the potassium's shiny surface would dull, then turn by degrees grey and mauve as the impurities were absorbed. As this was held to be suboptimal for intercalating, this potassium was then discarded, and a new amount weighed out and inserted in the tube. Potassium is not easily tractable because it is very sticky, so weighing it and delivering the resulting quantity to the closed end of the tube was often problematic. Minimising the surface area of the loading spatula in contact with the metal was the best way of ensuring the loading went smoothly.

The amount of potassium used for each sample was swiftly harmonised at the stoichiometric value for the stage required based on the graphite mass, plus a 20 % excess by weight. The rationale for this was based on observed formation of a mirror layer of solidified potassium on the inside of the tube where it came out of the furnace; while excess would be expected to be rejected by the saturated first-stage KC_8, the 'mirror' was seen to form when creating

KC_{24} as well; evidently a proportion of the vapour did not enter the graphite even if there was room for it: if this unintercalated amount did not represent an excess then the sample was less than the stoichiometrically-desired stage-2. Adding an excess to the potassium resulted in a similar mirror, suggesting a certain proportion of the intercalant was always unintercalated. When the excess entered the graphite, a mixed stage-1 and stage-2 sample was observed to form, but this was not always the case. It is possible that the extra potassium entered the forming intercalate but was forced out during the annealing process because a singly-staged sample was energetically preferred, though this does not seem likely given the more amorphous character of the Papyex structure compared with a highly-oriented graphite, in which in all probability could co-exist many different phases.

Figure 5.3: Quartz ampoule with KC_8 sample

When the potassium had been loaded in the glovebox, the valve was reconnected to the end of the tube and closed again, sealing the tube. The tube assembly was then removed from the glovebox and reconnected to the pump, and the pump was activated. Once a vacuum of at least 10^{-4} mbar was attained in the pump hose up to the valve, the tube valve was very slowly

opened. This procedure allowed the argon to be pumped off without risk of air entering the tube, or of the exiting gas damaging the pump. The tube was left to outgas with the valve fully open, and then the valve was sealed when the pressure was low enough, i.e. below 5×10^{-6} mbar. In early syntheses, the end of the tube with the metal and graphite was necked off and then broken retaining the vacuum inside to leave an ampoule (Fig. 5.3) which was inserted completely inside the furnace for intercalation but this was difficult to break controllably to retrieve the sample and proved to be unnecessary to ensure complete intercalation. In later syntheses, the tube valve was simply closed and the pump switched off and when it had vented, removed. The tube and closed valve were then able to be moved into and out of the furnace which enabled observations to be made of the beginning of the intercalation process.

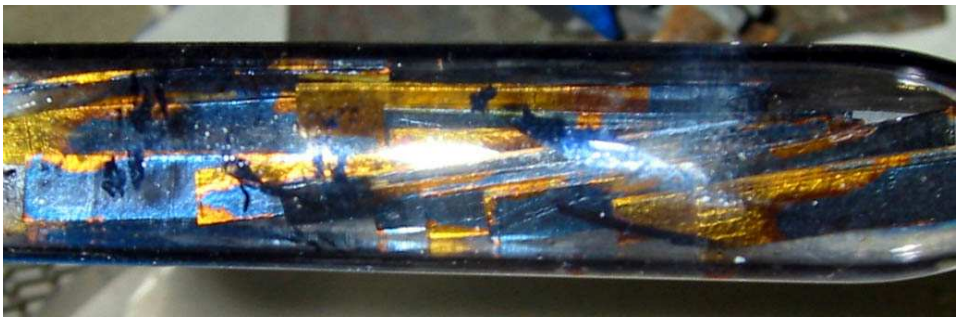

Figure 5.4: Mixed stage-1 and stage-2 batch of K-GIC

The temperature of intercalation used for the one-zone method was 250°C for KC_{24} and 300°C for KC_8. The modified one-zone method that evolved was carried out by holding the tube inside the heated furnace manually until the metal had melted completely into a globule. The melting point of potassium is 63.38°C [105] so the metal liquefied rapidly. The molten metal was then tipped onto the graphite, leaving a silver runnel where it ran over the glass of the tube. It was less important for metal to be taken up initially by the graphite than for the molten potassium to be in close proximity to it. Where metal entered the Papyex, a golden colour characteristic of KC_8 was

Figure 5.5: Melted potassium begins to intercalate immediately into graphite; a golden orange colour shows areas of stage-1 intercalation

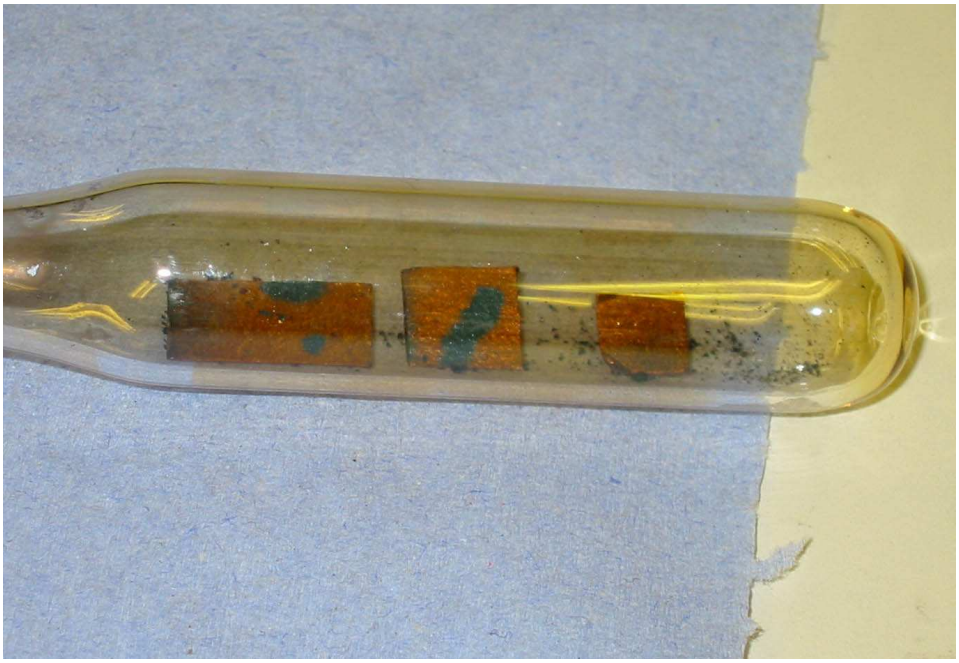

Figure 5.6: Stage-1 K-GIC with admixture of stage-2 domains

seen immediately. When the metal had been mixed with the graphite strips, the tube was re-inserted into the furnace and left there at 300°C; from experience this temperature was required to provide enough mobility to the metal to homogenise the sample, for both KC_8 and KC_{24}. This annealing process took in the region of 48 hours; the sample was taken out and observed periodically to ensure a uniform colour was achieved across the graphite. Early annealing attempts at lower temperatures for KC_{24} synthesis led to mixed phase samples, where certain parts were stage-1 (gold) and other parts appeared to have stage higher than the desired second (blue grey shading to the grey of pure graphite), as in Fig 5.4. Using an annealing temperature of 300°C meant that golden stage-1 areas and metal runnels on the tube disappeared as the vapour transport continued and the intercalation equilibrated to stage-2. As discussed in § 3.1.2, the colour of the sample is a direct indicator of its stage, and before other characterisation techniques were used, the colour was used as a guide to determine when intercalation was complete.

An illustration of the immediate appearance of golden intercalated elements on liquefaction of the potassium is shown in Fig. 5.5, during a test synthesis where the potassium was melted in contact with graphite outside the furnace using a hot-air gun for demonstration purposes. As Fig. 5.6 shows, the final intercalated sample was not completely stage-1; there are obvious domains of KC_{24}.

At that point, the sample tube was removed from the furnace and left to cool for a short time, before being returned to the glovebox through the port cycle. All handling of the sample inside the glovebox was done with clean tweezers, spatulas and scalpels on baked-out foil. The tube valve was opened to let in argon and then the tube was disconnected and the sample retrieved and stored in a clean glass vial, with plastic stopped wrapped around with Parafilm to guard against any contamination of the glovebox atmosphere before it was

needed.

5.1.3 CaC_6 synthesis by Li alloy co-intercalation

This is a technique developed by the Nancy group [50]. Only a very small amount of surface intercalation of calcium has ever been achieved in graphite using a pure vapour transport method, and the temperature of this procedure is limited to be lower than the formation temperature of calcium carbide (about 500°C). As alloyed with the more-easily intercalated lithium, calcium can be inserted into graphite, and the synthesis proceeds at the expense of the lithium until the calcium is entirely intercalated and no detectable fraction of intercalated Li remains.

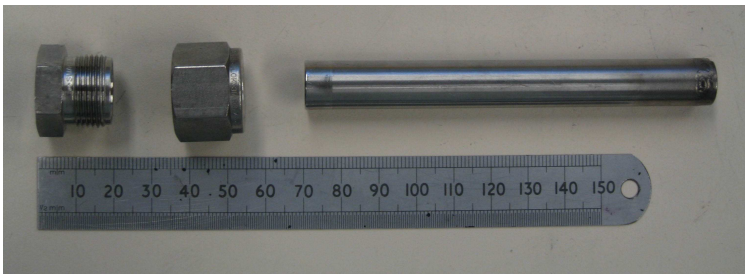

Figure 5.7: 1/2" stainless steel Swagelok tube with blanking unit for Li-alloy synthesis

The procedure is carried out as follows: reaction tubes are constructed from 10-20 cm lengths of 1/2" Swagelok stainless steel tubing with a stainless steel cap welded across one end (Fig. 5.7). The Li-Ca alloy is constructed with composition ratio of 4 Li per Ca: by weight this equates to 0.6928 g Li per gram of calcium due to the relative atomic weights. Approximately 0.3 g of calcium is measured into a reaction tube in the glovebox and is followed by the correct weight of lithium to obtain this composition ratio. The tube is then capped with a nut and blanking unit and sealed. It is removed from the glovebox and placed inside a tube furnace with the reaction tube at a

shallow angle to the horizontal. To control the rate of melting, a standard temperature raising sequence is followed which allows homogeneous mixing of the metals, with a long period at 175°C, just above the melting temperature of the lithium. This sequence is reproduced in Table 5.1. The final temperature is 350°C. The melt is left at this temperature for about 72 hours and is then cooled gradually back to ambient temperature by turning the tube furnace off. The tube is extracted when cool and placed back in the glovebox. It would be convenient if the blanking piece could be simply loosened and removed using a spanner to gain access to the tube but the alloying process generally prevents this from happening, wedging the Swagelok connection fast. Instead, this end of the tube is removed by cutting through the tube bore with a cutting tool. The alloy is solidified on the tube inner walls but the shallow angle at which the tube was held allows graphite to be slipped down above the alloy to almost the base of the tube; to facilitate the intercalation process, when there is evidence that the graphite floats on the alloy melt and resists the necessary immersion, the tube is rotated so that the alloy is above the graphite and a new Swagelok nut and blanking unit connected to the now-shorter tube. The graphite used for the CaC_6 samples made as part of this project was Papyex exfoliated graphite, outgassed as before and cut into pieces small enough to fit inside the space about the alloy. A stoichiometric ratio sufficient for a calcium excess of 2:1 (thus 1 Ca: 3 C) was used to calculate the weight of graphite required. The new blanking piece was tightened to seal the graphite and alloy inside the tube, which was then removed from the glovebox. The tube was then placed in the tube furnace at the same shallow angle with the furnace floor and with the alloy above the graphite. This was designed to ensure that the melting alloy fell onto the graphite and intercalated.

The temperature was then raised in 20° increments every 10 minutes to 350°C, with a pause of two hours at the melting temperature of the alloy

Table 5.1: Temperature raises for Ca-Li alloy formation

Elapsed time hr:min	Temperature °C
0:00	100
0:45	150
1:10	175
3:10	200
3:40	230
4:10	260
4:40	300
5:10	350

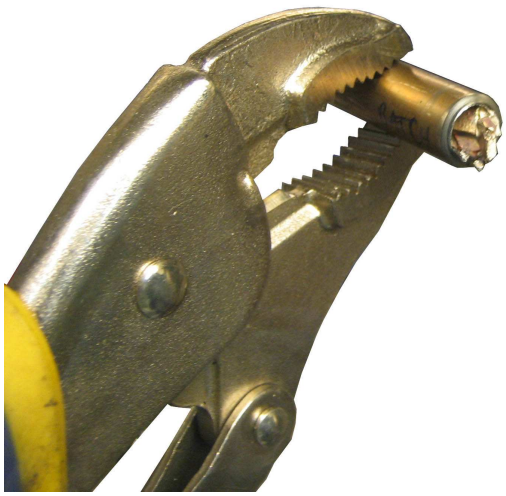

Figure 5.8: Finished CaC_6 samples embedded in the Li alloy in a freshly-opened reaction tube

(∼210°C) and held constant for 10 days, over which time the intercalation took place. Although not explicitly stated in [50], it is important that the final cooling takes place rapidly to quench the sample, otherwise deintercalation of Ca takes place. This is done by removing the sample tube from the furnace hot and cooling rapidly in air.

The tube was then placed cool inside the glovebox and cut open in the same way as before. The graphite intercalate and remains of the alloy, made primarily of Li metal, had hardened together into a mass (Fig. 5.8). To retrieve the sample, it was necessary to melt it out of the alloy using a hot-air gun inside the argon atmosphere. The maximum allowable temperature for doing this was 350°C; above that, there is a risk of forming calcium carbide (CaC_2). Melting and then scraping off the alloy from the graphite was difficult.

5.1.4 Ca-GIC using a metal-ammonia solution

Liquid ammonia is a well-known solvent for metals, producing highly-reactive solutions of metal ions in an electron soup. Solutions of Li, Na and K in liquid ammonia have been used to intercalate these metals into graphite. The method works for sodium, which does not intercalate further than the surface layers by vapour transport, as the solution is much easier to intercalate than the metal alone. This is also the case for metals outside of group 1; Eu, Ba, Yb metals have all been intercalated with ammonia. This method is not useful for creating binary metal-intercalated graphite compounds, however, as the ammonia remains an integral part of the final structure. A series of ternary compounds of metal, graphite and residual ammonia are formed after most of the ammonia has been driven off by heating under vacuum.

A known weight of previously-outgassed graphite powder was placed into a

thin glass tube inside the glovebox, together with an amount of clean calcium calculated to give the desired CaC_6 stoichiometry, and the tube was connected using a rubber 'O'-ring screw seal to a valve, which was shut so that the airtight tube assembly could be removed from the glovebox. The valve was then connected to an eighth-inch Swagelok stainless steel capillary tube of approximately 2 m length which was attached to the distributing connection on the gas-handling rig. The rig had supply bottles of ammonia gas, a 300 cm^3 buffer volume, and could be evacuated by a connection to a turbomolecular pumping station. The rig was carefully tested for leaks before any ammonia was transferred from the supply bottles. Firstly, the tube was opened to the pump via the rig to evacuate the argon atmosphere inside. The rig's buffer volume was evacuated as well. This dynamic vacuum was kept in place overnight. Then, a bath of acetone or isopropanol inside an open dewar was prepared using dry ice as cooling agent to bring the temperature down as far as 195 K. The tube was suspended in the bath inside a fume hood with the glass screen kept down as far as possible to guard against possible ammonia leaks. The gas rig valves to the pump and the sample tube were then shut, isolating the rig and tube assembly separately.

Ammonia condenses at 240 K and freezes at 195 K [105]. Thus the bath is held at ∼220 K to be in the middle of the liquid phase. For some of the samples, the ammonia used was deuterated (ND_3), which does not affect the chemistry but will have a small effect on the sample weight after synthesis.

The valve over the ammonia storage bottle on the rig was then opened, allowing a quantity of gas into the rig tubing and the buffer volume. This was measured on the rig pressure gauge. The ammonia bottle valve was shut when approximately 2 bar of ammonia was in the rig. As the volume of the gas rig buffer and tubing was known, the mass of ammonia available for condensation could be calculated. This pressure was noted.

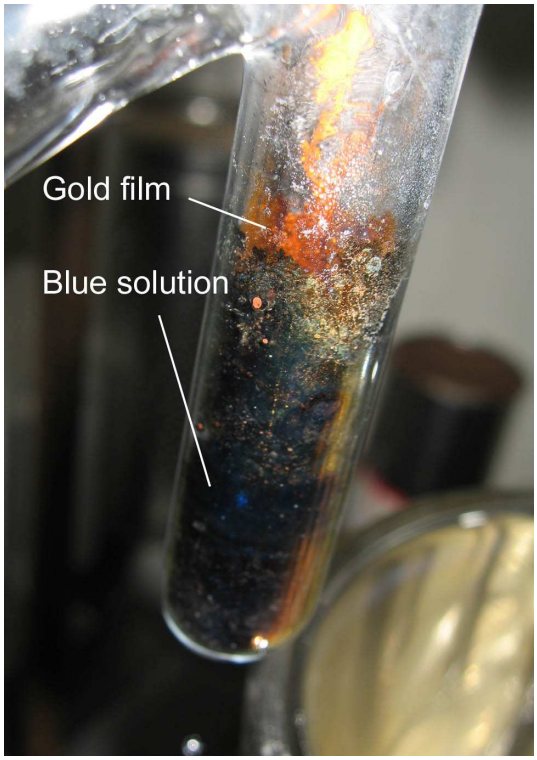

Figure 5.9: GIC synthesis using metal-ammonia solutions: the tube contains calcium-ammonia solution and graphite. The solution intercalates more readily than pure calcium. The rich blue colour is a highly solvated solution; a gold film coating the tube walls above the meniscus consists of more metal-concentrated Ca-ND_3. The sample tube is viewed temporarily out of the 220 K isopropanol bath before the ammonia begins to evaporate.

The gas rig valve to the sample capillary was then slowly opened part way, and ammonia began to condense onto the cooled sample with a corresponding drop in pressure measured on the rig. The ammonia condenses as clear liquid but in dissolving the calcium, a blue solution is formed. This is illustrated in Fig. 5.9. After a while the pressure differential between the rig and the condensed solution on the sample was not large enough to continue a fast condensation, so the rig valve to the sample was shut again, and the equilibrated pressure on the rig readout noted. The difference between the pressure noted when the valve was opened and this one allows the amount of ammonia condensed to be calculated. Often when making ammonia solutions, a specific concentration of solute in ammonia is required; this allows a precisely quantified amount of ammonia to be added to a known weight of metal, for example. In this case, however, a very weak solution was desired to facilitate the intercalation process and provide enough solution to submerge the graphite entirely.

The ammonia supply bottle was opened again, and a new pressure of ammonia recorded in the buffer and rig after it was closed. Then the valve to the capillary was opened again and the new ammonia condensed onto the sample, until the pressure differential was low again. The preceding steps were repeated a number of times until a large amount of liquid was present on the sample in the tube. The solution has very low viscosity and a thin layer of it very often creeps up the inside tube wall.

The mobility of the solution was expected to take calcium inside the powder without extra encouragement such as agitation. The solution was kept on the graphite for a number of hours, with the valve to the gas rig kept open to monitor the vapour pressure above the solution, before the ammonia was removed. This procedure was carried out extremely slowly to prevent damage to the intercalated sample by evaporating ammonia leaving the layers. Firstly,

Table 5.2: Ca-GIC samples synthesised using the metal-ammonia method. t_s is the synthesis time, during which the sample was in liquid ammonia. t_a is the time for which the sample was annealed under vacuum at 423 K.

Sample label	Starting Ca:C ratio	t_s hours	t_a days	IGA sample (see § 6.7)
A	1:6	6	0	-
B	1:6	12	10	1
C	1:6	9	5	2, 3
D	1:12	9.5	10	4

the valve to the gas rig was shut, after first making sure the acetone bath was cool enough to avoid a possibly dangerous rise in vapour pressure over the sample. A dewar of liquid nitrogen was placed under the ammonia storage bottle so the ammonia inside froze, leaving a vacuum above the solid. Next, the valve above that bottle was opened, condensing all the ammonia retained in the gas rig onto the frozen ammonia. Then that valve was shut, leaving a cryopumped vacuum in the gas rig. At that point, the gas rig valve to the sample was opened very slightly so that ammonia began to evaporate from the sample solution into the gas rig vacuum, but was not seeing the stronger vacuum in the storage bottle. This procedure was carried out at a rate of increase of pressure in the gas rig of <0.0001 bar s^{-1} for 75 minutes, with the valve being opened at regular intervals as the pressure built up to maintain the removal rate. This removed all the remaining liquid from around the sample and began outgassing ammonia from inside the graphite. The storage bottle acting as cryopump was reopened with the sample tube isolated, to condense all this ammonia, then reclosed. Caution was needed to prevent outgassing from the sample exfoliating the graphite and so the sample was left overnight to warm gradually to room temperature, with the evaporated ammonia being

collected in the rig. The next day this too was cryopumped off using the same technique. Any remaining pressure in the rig that isn't cryopumped is likely to be hydrogen formed from the decomposition of ammonia into amines. This can be safely removed through the turbopump. As it is expected that ammonia will remain inside the graphite even after direct pumping on the room temperature sample, further annealing was carried out at 150°C using a hot air gun and tube furnace. The sample was then unloaded from the tube in the glove box and stored under argon.

The list of samples made using this method is shown in Table 5.2. The resulting composition and structure was not able to be determined although X-ray diffraction was attempted for samples from A, B and C condensations [58]. No evidence was found for a 6.62 Å interlayer distance, suggesting that the samples were further exfoliated on deammoniation into an amorphous structure. Post-annealing, the composition was possibly similar to that found by Rüdorff (see Table 3.2). Whether this held true for the D sample, which started with a ratio of 1:12 Ca:C, was not determined but seems likely as 1:12 is about the ratio in the literature composition: sample D was made with no excess metal.

5.2 Thermogravimetry using the IGA

5.2.1 Introduction

The Hiden IGA was purchased and installed over the course of the project, and a large amount of time was spent on its setup and testing. Once operational, active testing was done using samples relevant to the research. Constant evolution of the techniques and operating procedures enabled results to improve

in both accuracy and confidence through later stages of data accrual. In the initial stages of the IGA operation, many of the data had limitations which will be considered here but analysed separately in the results section. An overview of the evolutionary process and the IGA operation is offered here, together with generic procedures, including sample loading and unloading, outgassing and setting of the dry mass, operation of the IGA in isotherm mode and data correction.

As the GIC samples under consideration are, without exception, sensitive to air, the dry loading apparatus supplied with the balance was a vital piece of equipment. The dry loader had only recently been developed by Hiden and was intended to provide airtight transfer of samples from a glove box to the IGA sample chamber. This turned out to be a little optimistic and early samples that were loaded suffered from oxidation damage - "went off", as we say. As it happens, the feedback given to the company helped them to improve the original loading process, which was eventually changed quite considerably and thereby improved to a large degree. It will be necessary for the purposes of this thesis to report the best loading techniques in high detail; firstly, so that the difficulties encountered and thus possible sources of error in the thermogravimetric data presented later are clear, and secondly to provide a useful reference for others who wish to use the same technique. The supplying company has not yet formulated a written user guide for the dry loading system so any notes on its use run the risk of being helpful to a wider audience of users!

5.2.2 Sample loading

If the sample is not air sensitive, the loading system is relatively straightforward: a loading sequence is initiated in the IGASWIN control software, which

checks that the sample chamber is at atmospheric pressure. If not, a vent valve must be opened to let air into the chamber: in practice this is unlikely to be necessary as the sample reaction tube will not be sealed if no sample is present. Generally an unloading of a previous sample takes place and the new sample is loaded directly afterwards. The reaction tube is removed from around the sample hangdown. The buoyancy table appears on screen, into which are entered appropriate known weights and densities for all the items on the balance (see Table 4.3). Most of these weights and densities were entered during the IGA installation and do not change unless the components of the balance setup are altered. For the first samples, the sample holder used was a stainless steel mesh cone with wire handle, of mass 85.4 mg and density 7.9 g/cc (7900 kg m^{-2}). The counterweight used with this was a stainless steel wire loop, of mass 287 mg and identical density. This placed the equilibrium point of the unloaded balance towards the lower end of the 200 mg weighing range. The cone allowed easy loading of solid samples such as those based on Papyex, which could be cut up to fit in the mesh 'basket' but was unsuitable for powder or liquid samples. When a powder sample was loaded, this sample holder was exchanged for a Pyrex bulb with glass hook and a hole in the upper hemisphere for loading and unloading sample (Fig. 5.10). The stable, non-leaking confinement of powders and liquids could be carried out in this, or rather these, as more than one was used. The masses of these were 312.6 and 296.5 mg and the density 2.23 g/cc. Because of the increased weight on the sample side of the balance, a new heavier counterweight had to be made and installed in its sealed compartment so that the equilibrium position remained within the weighing range. This new counterweight had mass 497 mg, and the changeover was sufficiently inconvenient to ensure the Pyrex bulb holder was retained for all subsequent samples, powdered or solid. For Papyex-based samples, the loading technique was to cut the sample into pieces small enough to enter the bulb and then push them inside with tweezers. This had the

further advantage of avoiding sample pieces being spilled when using the dry loading stick in the glovebox and transferring this to the IGA; the cone holder was susceptible to this problem.

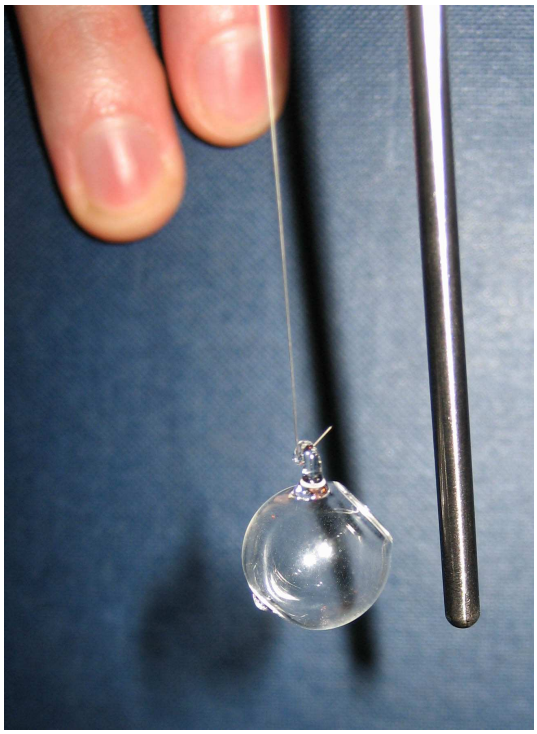

Figure 5.10: Pyrex bulb sample holder on IGA sample hangdown

Once the buoyancy correction table is filled in, and the loading table completed with the sample title and description, the loading screen appears. For samples loaded in air, a 'small sample' loading procedure is invoked (see Section § 4.2.3) and the empty sample container placed on the lower sample hangdown using a Swagelok (or other) 1/4" tube fitting nut as a support so that no extra weight is imposed on the hangdown to risk damaging the balance head. The reaction tube is reattached lightly with two or more bolts to act as a draught-excluder while the balance is steadied with the sample holder. This sets the sample null reading which is then accepted by the user. Following this, the reaction tube is uncoupled again, the sample holder removed by the same technique, and a pre-weighed sample placed inside. Weighing the sample

before loading is not strictly required, because the weight will almost certainly change as the sample is outgassed after loading, and can be measured with far greater precision using the IGA itself. It provides a useful guide nevertheless, and is important to prevent too large a sample for the IGA measurement range being loaded.

The sample in its holder is placed on the IGA hangdown, shielded once again from air movements, and then its weight is set in the software, which retains it as the 'Load' value. The reactor tube is then sealed using a copper gasket and the sample can be outgassed.

The pressure setpoint and the turbomolecular pump (TMP) are controlled from the software. When the pressure has reached a minimum using the automatic 'Exhaust' valve, the valve PIV1 is manually opened and the TMP pumps harder on the IGA vacuum chamber.

The furnace is engaged and set to a temperature suitable for outgassing the sample. With the sample in the outgassed tube suspended in near-vacuum, there is very poor thermal connection between the furnace and the sample, with the result that the sample temperature is considerably lower than the furnace when the system is in equilibrium at temperatures greater than 100°C. It is generally wise to set the furnace temperature about 30 K higher than the desired sample temperature in this situation. Conversely, and as shall be seen, the sample temperature when outgassing at cryogenic temperatures is considerably higher than the cryogen.

For air-sensitive samples, the above procedure is altered only by the need to use the dry loading chamber, which is shown in operating position in Fig. 5.11. A new Cu gasket is placed on the reaction tube flange, which is bolted to the IGA flange but not tightly. The dry loading chamber is inserted over the seal and bolted in place. A handle is inserted into the base of the loading chamber,

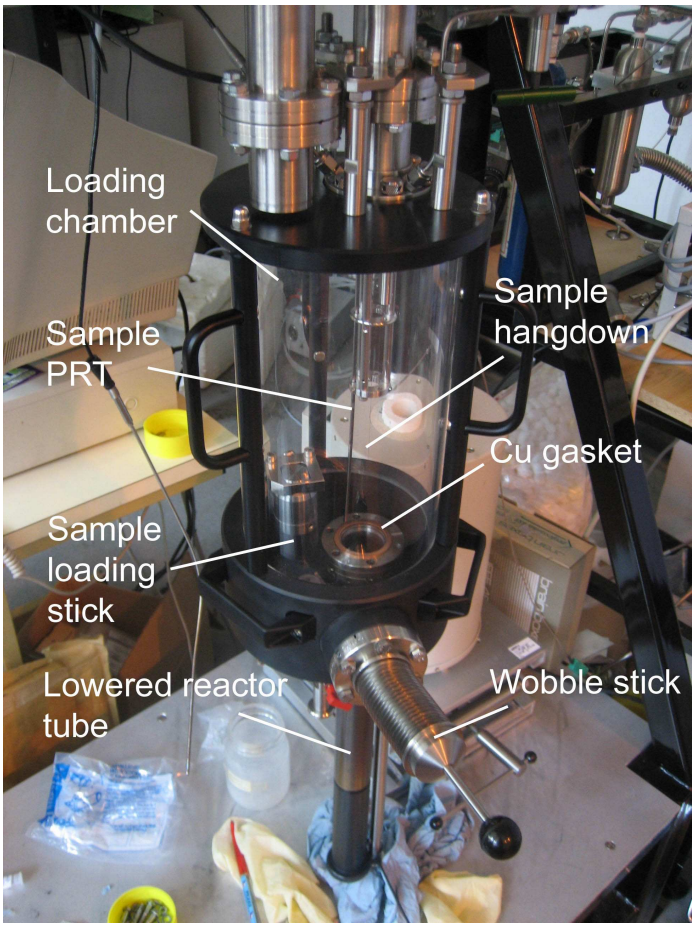

Figure 5.11: IGA dry loader

sealed with 'O'-rings, and secured to the reaction tube which is then brought down so the flange is resting on the floor of the chamber as in the picture. The sample loading stick is loaded with the air-sensitive sample placed in the sample holder in a 'top hat' unit, in the glovebox, and a lid is screwed tightly on to engage another 'O'-ring. The stick is then removed upright from the glovebox and inserted into the correct aperture in the bottom of the loading chamber, as seen in Fig. 5.11. The loader is then purged with the IGA purge gas species; originally by adding an overpressure from 1000 to 1250 mbar and then pumping out to 1000 mbar, repeated over 50 cycles. In this way the air in the chamber was to be diluted until negligible levels of oxygen and moisture remained. This often proved ineffective at preventing contamination, and so a new purge system was provided by the manufacturers. In this one, a constant flow of purge gas through the IGA chamber and dryloader is initiated, with an overpressure of 300 mbar preventing any backflow of air from the outlet hose. This made a better loading environment. The dry loader was not airtight to the tolerance normally required for handling GICs. Pumping directly on the chamber resulted in a dynamic vacuum of only 1×10^{-2} mbar. To improve this as far as possible, liberal quantities of vacuum grease were applied to every 'O'-ring seal on the chamber, as well as the seal on the sample loading stick lid. When loading the sample in the glovebox, often some sacrificial alkali metal was placed inside the lid to remove any low levels of impurities that might damage the sample. As far as possible, the chamber was kept at positive pressure using the purge gas throughout the loading sequence.

When the purging cycle is complete, the sample loading stick lid is unscrewed and left in its clamp, and the stick lowered to expose the sample (Fig. 5.12). The 'wobble stick' manipulator is then used to lift the 'top hat' holder off the loading stick, and to hang the sample holder onto the hooked end of the lower sample hangdown. Then the reaction tube is pushed carefully

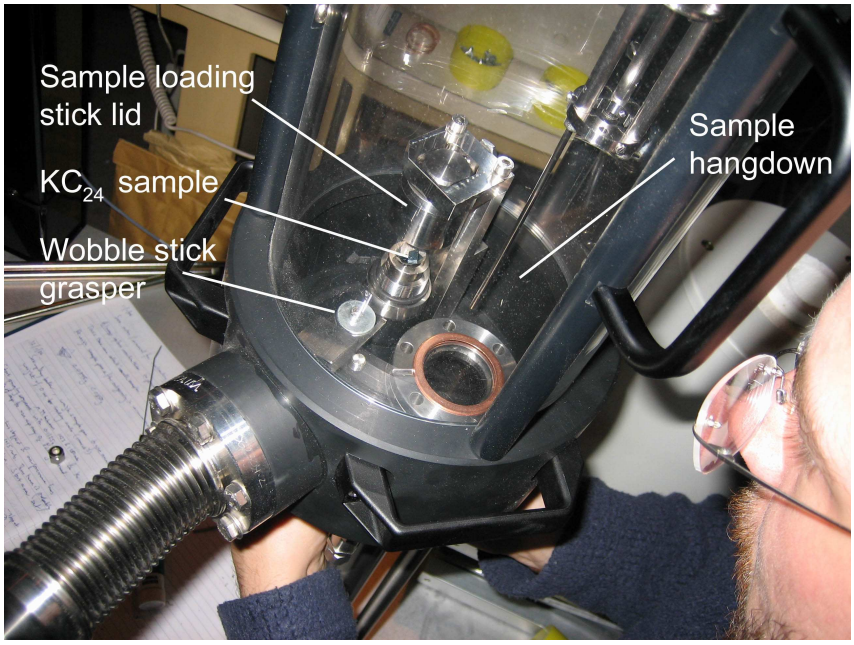

Figure 5.12: Unscrewing the IGA sample loading stick lid after purging, ready to load the sample holder onto the hangdown

up to engage with the IGA flange, and the gasket is sealed. At this point the new sample reading is noted on the software, and then an outgas procedure may be commenced.

5.2.3 Measuring uptake using the IGA

Following the first outgas procedure after every sample, a dry mass was recorded for use in the buoyancy corrections. To measure an isotherm, the sample temperature had to be set and kept constant. For cryogenic temperatures this was achieved using a bath of liquid nitrogen in a dewar surrounding the reaction tube, as shown in Fig. 5.13. Later, a cryofurnace was available with constant temperatures from 88-773 K, allowing the collection of data at more temperatures.

The individual experimental details are expounded in the IGA results chap-

Figure 5.13: 77 K liquid nitrogen bath for IGA

ter. As the exact method used varied perforcely with sample the details were more conveniently explained there.

5.3 Neutron diffraction on Polaris

Polaris is a time-of-flight neutron powder diffractometer at ISIS. It has four detector banks ranged from low angles to backscattering, allowing the coverage of a **Q** range from 0.3 to 31.4 $Å^{-1}$. The neutrons are moderated by an ambient temperature (316 K) water moderator. The sample cell is 12.0 m from the spallation source. The beamline contains a nimonic alloy chopper with B_4C tailcutting strip. It spins at 50 Hz, the ISIS pulse frequency, and cuts down detection of both 'fast' neutrons produced in the pulse and slow neutrons that might be detected into the next pulse, preventing frame overlap. The incident and transmitted neutron flux is measured by two scintillator detectors 4 m up-beam of the sample position and 2.5 m after it. The maximum beam

dimensions at the sample position are 20 × 40 mm although two collimators driven by motors in the beamline can reduce this to match the sample size or to reduce background [106].

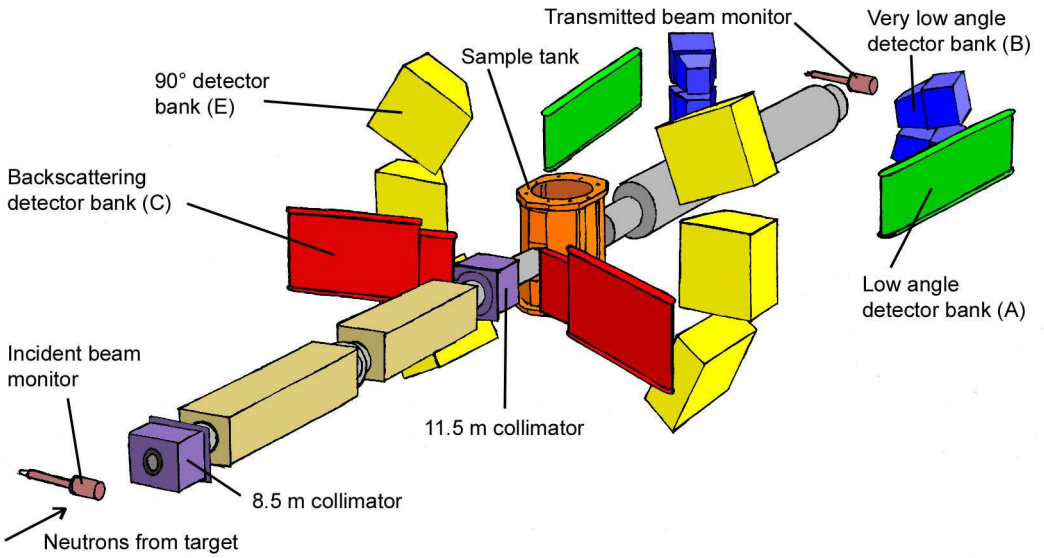

Figure 5.14: POLARIS neutron diffractometer diagram

The instrument layout is illustrated in Fig. 5.14. Each detector bank has units symmetrically matched on either side of the beam. The detector specifications are outlined in Table 5.3.

The sample tank enables the use of a standard He cryostat which has a temperature range between a base of ∼1.5 K to slightly above ambient temperature at 320 K. The sample container is attached to a long probe 'centre stick', which may contain a gas line capillary, temperature sensors and heating coils depending on the experimental requirements.

Table 5.3: POLARIS detector bank configuration [106]

Bank position (label)	V. low angle (B)	Low angle (A)	90° (E)	Backscattering (C)
Detector type	ZnS	^{3}He	ZnS	^{3}He
No. of elements	4×20=80	2×40=80	6×36=216	2×29=58
Sample dist. (m)	∼2.2	1.72 - 2.65	∼0.80	0.65 - 1.35
2θ range	13°-15°	28°-42°	83° - 97°	130° - 160°
Δd/d	$\sim 3\times10^{-2}$	$\sim 1\times10^{-2}$	$\sim 7\times10^{-3}$	$\sim 5\times10^{-3}$
d-range (Å)	0.5 - 21.6	0.5 - 8.3	0.2 - 4.0	0.2 - 3.2
Q-range (Å^{-1})	0.3 - 12.6	0.75 - 12.6	1.5 - 31.4	2.0 - 31.4

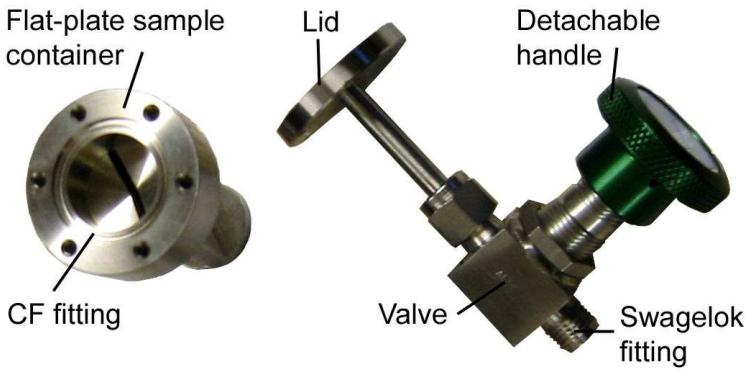

Figure 5.15: Flat plate sample container and valved lid used for neutron experiments

5.3.1 General experimental details

The standard procedure for the experiments on Polaris was to load the samples in the argon (later helium) glove box on site in the ISIS facility. The stainless steel sample container lids were manufactured so that an air-sensitive sample could be loaded and sealed in the glovebox. To this end they incorporated a bellows valve with unscrewable handle so the assembly could fit into the cryostat bore. Two lids were made, as well as two stainless steel sample containers for inelastic neutron experiments. The sample container and lid are illustrated in Fig. 5.15. All the samples had a Papyex base and were manufactured in the standard strips described in § 5.1.1. The container, or can, used on Polaris was of null-scattering titanium-zirconium (TiZr) alloy, pressure tested to 10 bar, and had a flat-plate geometry of 20×40×1 mm volume. The strips were slipped inside this space. The can was then sealed using indium wire in the CF fitting to effect an airtight barrier between container and lid. The valve on the lid was ensured closed. The sample container was then removed from the glovebox and attached to the Swagelok fitting on the bottom of the centre stick capillary, and the capillary first evacuated using a turbomolecular pump, before the sample lid valve was slowly opened to evacuate the Ar or He from around the sample and prepare it for hydrogenation. When fully open, the sample lid valve handle was removed so that the centre stick assembly could fit into the cryostat. At this point the required temperature sensors and heating units were taped to the can, using aluminium tape.

The hydrogen used was of 99.999 % purity, the deuterium was of 99.9 % and was pre-cryopumped to liquid nitrogen temperatures to remove impurities such as moisture.

The TiZr alloy is designed to avoid coherent scattering by combining the two metals in a proportion to give an overall coherent scattering length of 0,

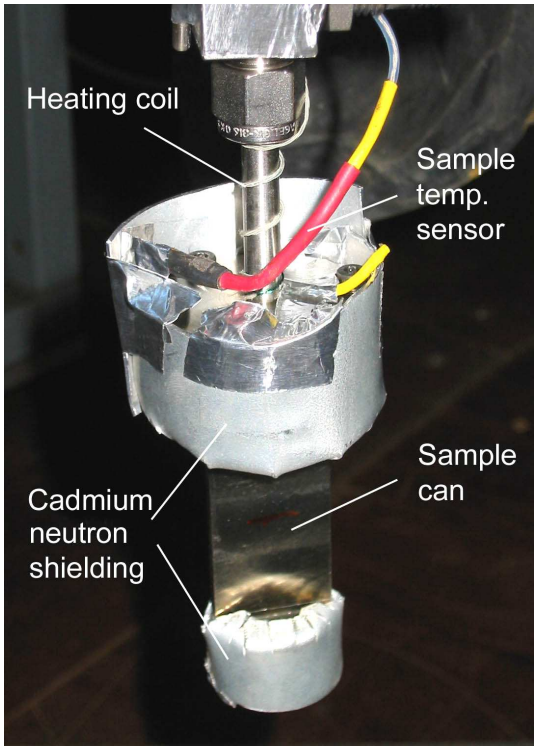

Figure 5.16: POLARIS sample can setup prior to installation on the beamline

and thus does not contribute Bragg peaks to the background. The chance of unwanted diffraction from the walls of the cell was diminished by surrounding the sample container's mixing volume and base with cadmium metal, as shown in Fig. 5.16. Cadmium has a large absorption cross-section (2520 barn: for comparison, $\sigma_{abs} = 0.03$ barn for H and 0.0005 barn for D) so is a good mask of neutrons. When ready, the centre stick was lowered into the cryostat bore and an airtight seal made with the cryostat so that the stick chamber could be purged with vacuum and flushed with helium gas before being evacuated again. After that it was usual to put a small amount of He into that space to effect a good heat transfer.

The Papyex-based sample has preferred orientation as the small crystallites of graphite tend to be arranged with the c-axis out of the plane of the sheet. In the a-b plane there is no ordering and the crystallites are powderlike in

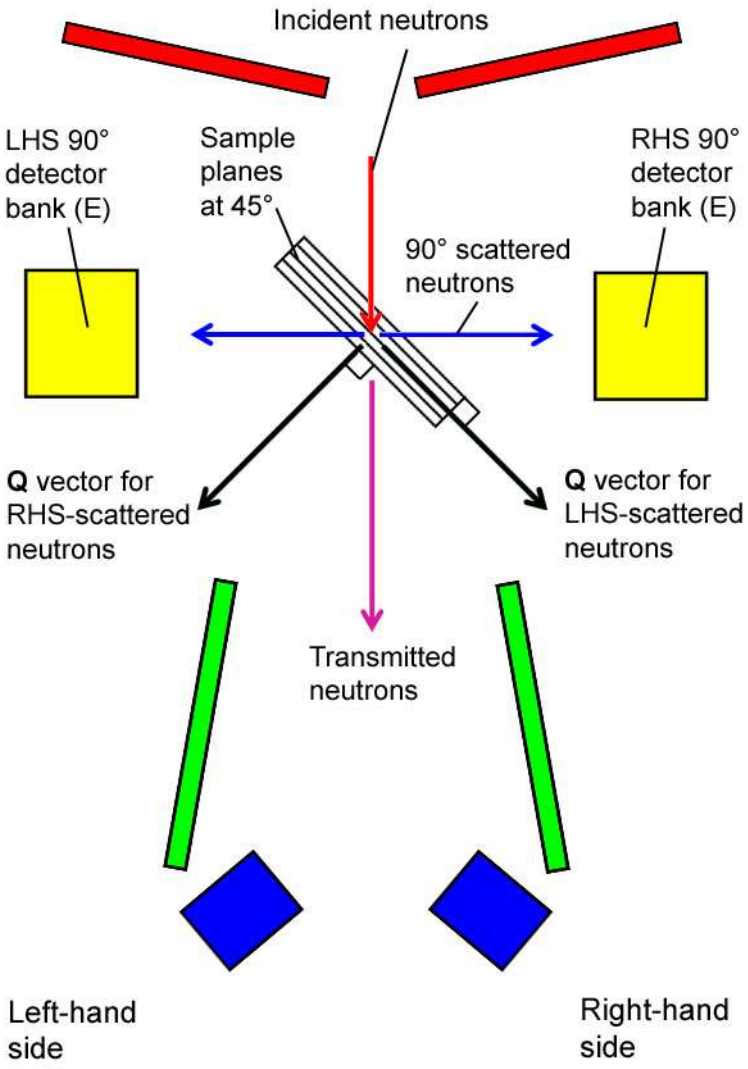

Figure 5.17: POLARIS instrument setup with sample at 45° alignment with incident beam (see Fig. 4.1). This orientation allows momentum transfer from scattering into the 90° detector banks to be aligned with sample in-plane, to the left-hand side (LHS) and out-of-plane, to the right-hand side (RHS), sample directions. Diffraction information for the sample a-b plane and c-direction is therefore decoupled allowing easier refinement.

two dimensions. If the angle of the sample to the beam is set with care, the **Q** vectors representing scattering to detectors on left and right of the instrument convey different information. In this way the in-plane and out-of-plane structure of the intercalates might be separately resolved. Fig. 5.17 shows this setup with the sample at 45° to the incoming beam. Left and right are defined from a plan view of the instrument with the neutron source at the top. In this way, the **Q** vector for neutrons scattered into the left-hand side (LHS) 90° bank represents a cut through the in-plane structure of the sample, and the **Q** vector for the neutrons scattered into the right-hand side (RHS) 90° bank represents the out-of-plane structure of the material. The limitations to this view are that the sample is not the single crystal at a perfectly defined angle implied.

A sample orientation of 90° was also used. In this case, the diffraction was intended to be symmetric on both sides of the instrument. One advantage for this arrangement is that a large component of the in-plane scattering is seen in both forward scattering and backscattering positions, while a large component of the *c*-axis scattering is detected in the 90° banks.

5.3.2 Polaris data analysis

Data collected during the course of a neutron experiment in each Polaris detector are stored in histograms of neutron counts against time-of-flight (ToF). The ToF axes are subdivided into bins of finite width based on the time channel boundaries. Histograms, once present in the data acquisition electronics and subsumed into the RAW files at the end of each data collection run, are known as 'spectra'. Spectra can be manipulated in the GENIE analysis and plotting program to compare, sum, convert in units or correct the data. The resolution of each Polaris detector bank, $\Delta d/d$, varies with scattering angle

2θ, and so each bank is considered separately during data normalisation. Each detector in a single bank is considered approximately to have the same resolution, which allows all the detectors in a bank to be summed ('focused') into a single workspace in GENIE. The larger numbers of counts improve the counting statistics.

Polaris data normalisation is generally carried out in three separate stages, run using a separate GENIE command file for each detector bank. The spectra from all the detectors in a particular bank are focused and held in a software memory unit known as a workspace, where they are divided by the counts on the incident beam monitor to normalise to counting time. An instrument background spectrum is subtracted and then the data are normalised by dividing by a vanadium spectrum which has been corrected for absorption and multiple scattering. This normalises the data to the energy distribution of the incident neutrons, thus accounting for differences in detector efficiency across the neutron energy range. The background and vanadium spectra are updated every instrument cycle.

All the experiments carried out on POLARIS utilised adapted focusing routines that considered the right and left-hand detector banks separately. This enabled scattering runs to be split by their Q-vector relative to the sample's preferred orientation.

The data are retrieved from the ISIS server system and can be viewed remotely on emulation software before being converted into ASCII format files, which can be read into graphing and fitting packages.

5.3.3 Polaris experiment on deuterium and ammonia in KC_{24}

This experiment was numbered 20181. The aim of this experiment was to chart the structural changes in KC_{24} upon the sorption of deuterium to the saturated limit $KC_{24}(D_2)_2$.

As a separate part of the experiment, we planned to expose the GIC to ammonia to drive the stage-2 to -1 phase transition seen by York *et al.* [56], to create a dilutely pillared porous material. This was firstly to chart the structural changes in unprecedented resolution, both in **Q** and time, and secondly to study the uptake of deuterium in the system afterwards to assess its storage capability.

0.218 g (in two strips) of well-staged KC_{24} was selected and loaded into the TiZr can in the ISIS glovebox under argon. The sample was loaded into the cryostat as described above, and the capillary connected to the gas handling rig. The equipment setup on the beamline is shown in Fig. 5.18.

Data were collected from the pure sample at 45 and 90° to the beam at 80 K as a background, before doping with deuterium. Measurements were performed at these two angles on KC_{24} $(D_2)_1$ at 50, 20 and 2 K and on KC_{24} $(D_2)_2$ at 50K. The deuterium was then removed by heating and pumping. The KC_{24} was then subjected to room temperature doping with deuterated ammonia (ND_3) and the resulting transition was observed by time-resolved diffraction. The ammonia was then partially removed but as previously, a residual amount of ammonia remained in the GIC after heating to 260K. An overpressure of D_2 gas was added at 50 K and data were collected on the ammonia-residual system at 20 and 1.7 K before the D_2 was removed and replaced with an overpressure of H_2. Data were collected at 20 K for KC_{24}

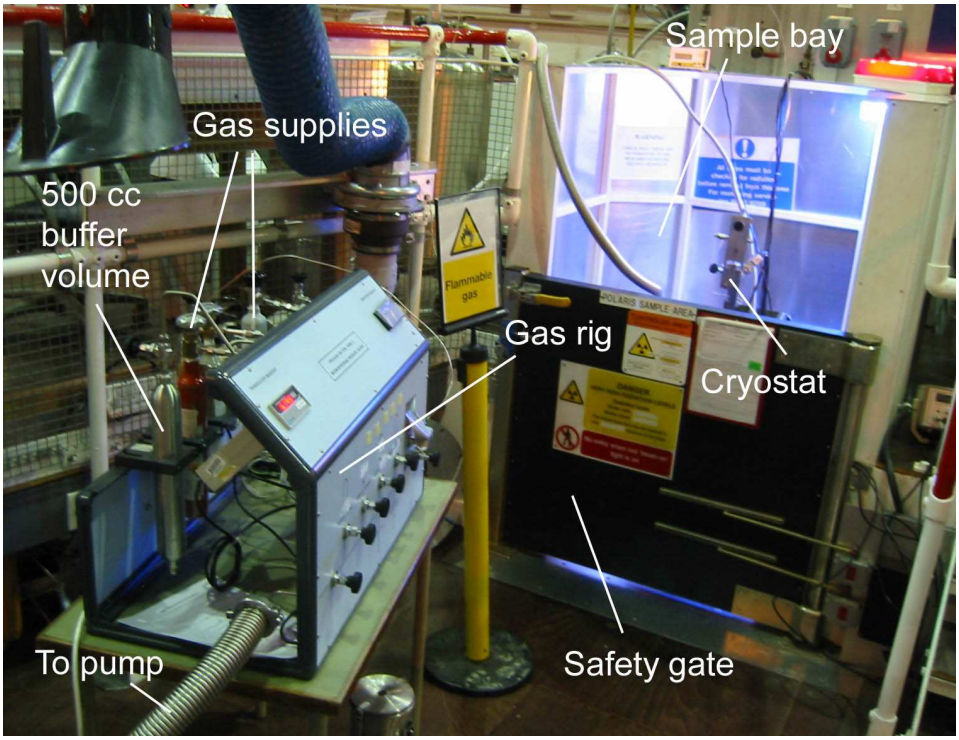

Figure 5.18: POLARIS beamline equipment used on experiment RB20181. The gas rig supplies and measures the volumes of gases used. The safety gate must be closed and locked before the beam shutter can be opened. A capillary connects the gas rig to the centre stick inside the crystat

$(ND_3)_{1.8}$ H_2.

To quantify the background contributed by the instrument and the sample container, scattering runs were performed on an empty sample can in the beamline at 70 K at the two beam-referenced angles used in the experiment. These data had low statistical error.

5.3.4 Polaris experiment on hydrogen in KC_8

The aim of this experiment was to explore the sorption of hydrogen in the first stage potassium-GIC over the temperature range where physisorption changes to chemisorption. The advantage of using Polaris was that it has high incident neutron flux, allowing time-resolved diffraction scans to be taken with sufficiently good statistical resolution. A standard orange cryostat was used for temperature control. Hydrogen was used as the sorbent rather than deuterium despite its higher incoherent scattering properties to try to increase the detectability of changes in the graphene spacing and because it was purer than the D_2 available.

0.3557 g of KC_8, selected by homogeneity of colouring, was loaded into the flat plate 1 mm depth TiZr sample cell as described in Section § 5.3.1, and the sealed cell outgassed and loaded onto the beamline in the standard manner. Angular variation of the plane of the sample with respect to the incoming neutron beam was used as for the previous experiment. Data were collected on the pristine KC_8 sample at 50 K with the sample (preferred-orientation) *c*-axis aligned at 45 and 90° to the incident beam. At this temperature, pre-cryopumped H_2 was added to the sample. No structural change was observed on loading and physisorption uptake was expected to be negligible even at this temperature. An overpressure of 3 bar was placed on the sample can. While

this remained, the sample temperature was raised to trace any physisorption and find the onset of the stage-1 to stage-2 metal-insulator phase transition. Measurements of the hydrogenated sample were taken at 50, 100, 150 and 200 K without seeing any structural changes in the compound.

The staging transition was observed to begin at 250 K but its rate was very low so the temperature was raised further. The largest transition rate was measured between 300 and 314 K and the sample was fully stable in the new phase after 11.5 hours for a final temperature of 316 K, which was very close to the maximum possible with the cryostat. Data were collected at c orientations of 90 and 45° to the incident beam on $KC_8H_{0.67}$. Short time-resolved data runs were taken over the transition. Pumping and cooling the sample was not seen to remove hydrogen; thus the transition appeared irreversible within the limits of the timescale and temperature environment available.

5.3.5 Polaris experiment on hydrogen in CaC_6

Following the apparent observation of irreversible H_2 uptake in CaC_6 synthesised using ammonia at ambient temperatures using thermogravimetry (see § 6.7), an experiment was planned to chart structural changes in a CaC_6 sample constructed using Papyex and Li-Ca alloy as it was supposed that a structural change accompanied the chemisorption of hydrogen. This was postulated to have a similar form to the staging transition in KC_8. Thus the experimental procedure was planned to follow closely that of the previous experiment.

Alloy-method CaC_6 was synthesised as described in Section § 5.1.3. On melting the sample out of the excess alloy after intercalation in the glovebox, the hot air gun malfunctioned and operated at its full 650° temperature. This was a result of the gun's lack of durability when operating under argon. It

meant there was a probability that CaC_2 formed in the sample.

The sample surfaces were scraped to remove the thickness of alloy attached to them to allow hydrogen to enter the intercalate. It was considered that sufficient alloy had been removed to achieve that; the exposed surface, although silver in colour, showed a texture like that of Papyex and of the Papyex-based potassium-GICs rather than smooth metal.

The experiment was given the identifier RB620361. 0.3470 g of CaC_6 in small strip form was loaded in the He glovebox at ISIS into the TiZr can. The can was set up with Cd shielding, outgassed and loaded into the beamline in a standard cryostat.

The sample was cooled to 50 K and a background run was collected at 90°, then another at 45° alignment with the beam. The latter alignment was kept through the next stages of the experiment.

Para-hydrogen from the ortho-para hydrogen converter rig used on TOSCA and described in § 5.5.1 was loaded at 40 K. The rig was being used elsewhere so the hydrogen was transferred in a small pressure bottle which limited the overpressure of hydrogen available to drive the proposed transition. The first sorption was to attain a nominal stoichiometry of $CaC_6H_{0.25}$, and short-timescale runs were taken while this stabilised. Then more was added, to obtain $CaC_6H_{0.37}$. No structural change was seen so the temperature was raised to 50 K to provide direct isothermal comparison with the KC_8 experiment. A 500 mbar overpressure was retained on the sample container. With no transition expected until close to ambient temperature, 600 μAh runs were carried out at 100 and 150 K, and thereafter short time-resolved runs during the heating process to 200 K, where significant intensity was recorded with the temperature stable, then the same short runs recorded the rise in temperature to 250 K. From 250 K to the cryostat maximum temperature of 320 K, time-

resolved runs were taken. No transition appeared to take place, though a peak shift congruent with thermal expansion was visible. Using another source of hydrogen enabled an overpressure of 3.7 bar to be placed on the sample, but this did not drive any change of phase. The sample was then cooled to look for any physisorption below 50 K, then with the hydrogen removed and after outgassing, cooled still further to see if any structure change related to the onset of superconductivity at 11 K [46] was visible. It wasn't.

5.4 Inelastic neutron scattering on IRIS

IRIS is a high-resolution chopper neutron spectrometer situated on beamline N6(A) at ISIS. It is designed for low energy transfer spectroscopy and with good resolution about the elastic line is well-suited for quasi- and inelastic scattering [107]. The sample tank is a 2 m diameter vacuum chamber lined with crystal analysers. The beamline is moderated by a liquid hydrogen moderator kept at a temperature of 25 K. The sample site is 36.41 m from the moderator. Two beam choppers at 6.3 and 10.0 m from the moderator select appropriate neutron energies from the incident white beam and a curved neutron guide and focusing supermirror deliver them to the sample position in a 21×32 mm beam, thus filtering out fast neutrons and preventing frame overlap (§ 5.19). The width of the wavelength band defined by the choppers implicitly selects both energy resolution and transfer range accessed during an experiment.

The spectrometer is shown in Fig. 5.19.

Neutrons scattered from the sample are analysed by energy using either cooled pyrolytic graphite (PG) or muscovite mica with a variety of reflections available. Neutrons are then counted in a set of ZnS detectors, 51 for each semicircle of analysers. Additionally, there are 10 ^{3}He diffraction detectors in

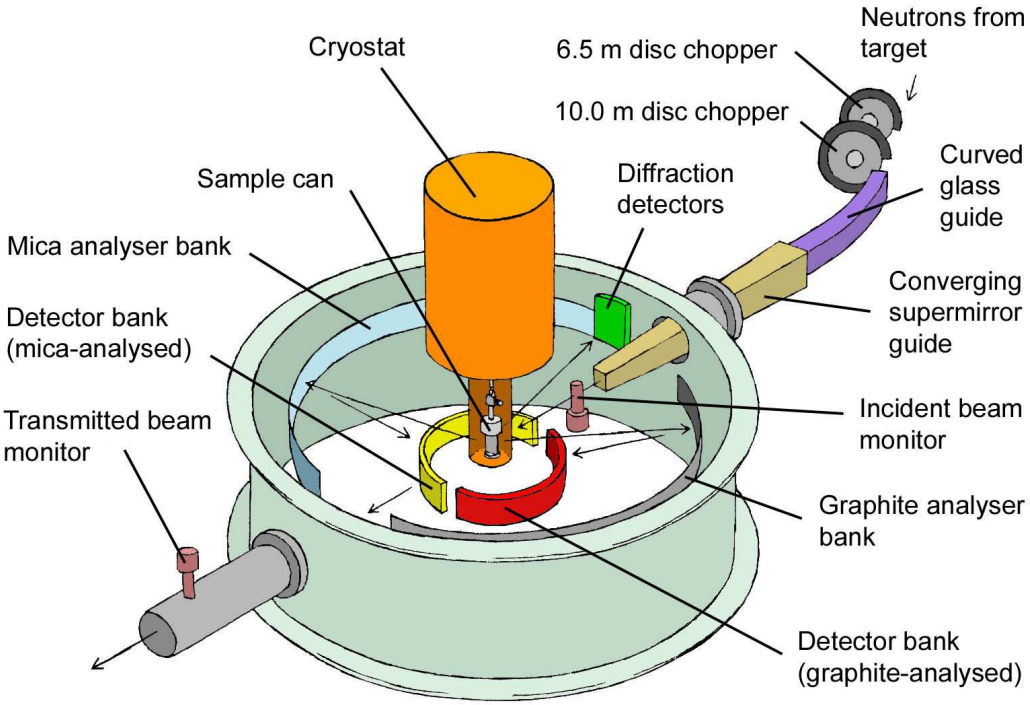

Figure 5.19: Schematic of the IRIS neutron spectrometer

the backscattering position around 170° 2θ. Depending on the selected incident energy, the diffraction range available runs from 1-12 Å. The diffraction capability of the instrument allows sample structure to be studied *in situ* and even for simultaneous collection of dynamical and structural data.

The PG analyser is cooled to reduce thermal motion in the crystal which would affect the resolution of the selected energy and contribute background from thermal diffuse scattering. Additionally, a 25 K beryllium filter is available to extend the energy range available using the PG analyser.

The sample tank takes the standard sample environment equipment including the orange cryostat (§ 5.3).

5.4.1 General experimental details

Two experiments were carried out on IRIS, both on the KC_{24}-H_2 system. The first experiment did not answer all the questions raised and the second was proposed to address that. The experimental aims and methods are outlined below.

Sample loading took place exactly as for the diffraction experiments outlined in § 5.3.1. The sample can used was made from stainless steel, with a sample space 20×40×2 mm and was constructed at the same time as the stainless steel valved lids used on POLARIS. Stainless steel was used instead of a material like aluminium because it was intended to allow the condensation of liquid ammonia into the sample space. Stainless steel does not react with metal-ammonia solutions. This exposure to liquid ammonia was not carried out in this project. Stainless steel has quite large unwanted coherent scattering and contributes Bragg peaks which must be identified and subtracted.

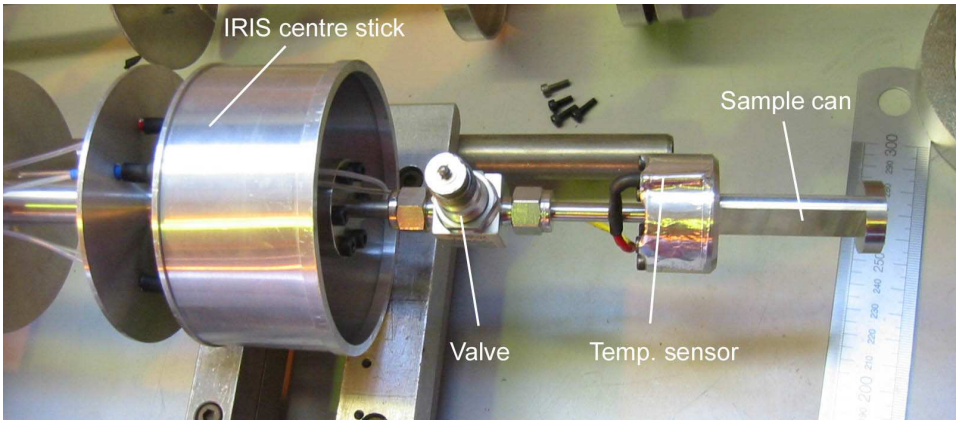

Figure 5.20: The IRIS sample can attached to the cryostat centre stick prior to placement on the beamline

The sealed can was attached to the centre stick and a temperature sensor was connected. When the helium had been pumped out of the sample space using the turbopump (TMP), the green valve handle was removed as shown in Fig. 5.20. The centre stick was then inserted into the cryostat and the sample space pumped out to leave about 100 mbar of He as thermal exchange gas.

The sample orientation was 135° to the incoming beam (see Fig. 4.1 for definition of the 0° orientation). This had the effect of limiting structural contamination from Bragg diffraction to the unused left-hand side of the instrument; the graphite analysers are situated on the right-hand side.

5.4.2 First experiment: INS on H_2 and ND_3 in KC_{24}

This experiment was given the identifier 20259 and was chronologically the first neutron experiment to be carried out in the investigation. The intention was to obtain data for hydrogen sites in the second stage K-GIC analogous to the studies on Cs- and $RbKC_{24}$ (§ 3.4.1). It was proposed in conjunction with the first POLARIS experiment (§ 5.3.3).

In previous work it had not been possible to refine the hydrogen sites from diffraction data with any confidence. But it appeared possible to get information on the number of sites and some information on the site symmetry from inelastic neutron scattering by measuring the crystal field splitting of the hydrogen's first rotation excitation. So this neutron experiment was designed to match the INS energy window used by Carlile *et al.* [59] and Beaufils *et al.* [77] and the hydrogen loading was intended to allow quantitative analysis of the site excitations and their interactions, to compare the system with the other two. For hydrogen storage purposes, the stage-2 potassium GIC has an advantage over the others in that potassium is lighter, but it also has a smaller diameter and so opens up the graphite galleries less.

After measuring on the saturated $KC_{24}(H_2)_2$ material, the sample was to be exposed to ammonia gas to drive the stage-2 to dilute stage-1 transition, increasing internal volume and surface area, before being loaded with hydrogen a second time. This was a direct comparison with the first POLARIS experiment (§ 5.3.3).

The sample was synthesised as in § 5.1.2. 0.821 g of sample was inserted into the sample container which was loaded on to the beamline as detailed in the previous section. A gas rig with the standard buffer volume and cryopump capability was connected between the centre stick top valve and the TMP. This gas rig had available lecture bottle supplies of pure H_2 and anhydrous deuterated ammonia (ND_3).

The PG 002 analyser was used, which with a chopper frequency of 25Hz gave an energy resolution of 15 μeV and an energy transfer window of between -0.8 and 2.2 meV. High-purity hydrogen gas was transferred to the sample cell *in situ* using the gas rig buffer volume to measure the amount required at 55 K before the temperature was lowered. Measurements were taken on $KC_{24}(H_2)_1$

at 1.5 K, and on the saturated H_2 concentration $KC_{24}(H_2)_{1.5}$ at 1.5, 10 and 20 K to observe the quasi-elastic excitations of hydrogen diffusion through the sample. For each additional loading of hydrogen, the cryostat temperature had to be raised to 55 K before being cooled again. Some measurements were taken up to 30 meV by using a 16.7 Hz chopper setting to look for intensity at the free rotor energy (14.7 meV). The hydrogen excitations were isolated by subtracting a pure KC_{24} background, this being collected after the hydrogenation when the hydrogen was pumped off completely. The sample was then exposed to deuterated ammonia gas at 280 K to drive a transition to stage-1 to increase internal volume, which was observed by diffraction, and the ammonia removed leaving a residual compound of $KC_{24}(ND_3)_{1.8}$, as expected from the literature [56] [108].

Following the ammoniation of the sample, and subsequent phase change and removal of the maximum possible ammonia, the sample was doped with hydrogen at 55 K. An amount of hydrogen equivalent to 0.25 H_2/K was seen to enter the sample cell readily, though this may have been simply the system equilibrating with the extra volume represented by the sample cell at 55 K being filled. With an amount still left in the 300 cm^3 buffer volume, the sample was cooled to 1.5 K. All this hydrogen was subsequently condensed into the sample can, an amount equivalent to $x = 1.08 \pm 0.09$ as before. No low-energy peaks were seen, but a subsequent 16.7 Hz chopper setting had been used to survey the energy transfer window from -0.5 to 30 meV. The sample was warmed to remove hydrogen, and then more hydrogen was applied under a pressure of 7307 mbar: a reduction in pressure of 860 mbar was observed when opened to the sample cell. Proportionally this was less than the preceding uptake, and reconcilable with the extra volume represented by the cell rather than physisorption, though not ruled out. The reservoir was closed, and the temperature was lowered to 1.5 K, so that the total H_2 concentration condensed

on the sample was $x = 4.2 \pm 0.4$. A second set of data at the wider energy window setting was taken.

Diffraction measurements over 1 - 10 Å in d-space were taken in stages using different instrument settings to get the full range. The idea was to chart the structural changes during the experiment. The separate runs were then convoluted to give the diffraction patterns shown in Fig. 8.1. The measurements and sample orientation varied and are detailed fully in § 8.1.

At the end of this time the sample was removed and stored until its radioactivity was reduced.

A statistically acceptable set of data consisted of over 1000 μAh collected current.

5.4.3 Second experiment: INS on low coverage H_2 in KC_{24}

This experiment was proposed to look at low coverage of hydrogen in KC_{24} following from the first experiment, as no preferential filling had been seen at an H_2 to K ratio of 1. It was designed to complement the analogous TOSCA experiment (§ 5.5.1) and was carried out just before. The KC_{24} sample mass was 0.6767, consisting of six strips, and was loaded into the same stainless steel can as reported in the previous section. The same instrument settings were used (PG 002 and the Be filter); the energy transfer ranges used were from -0.8 to 2.2 meV and 5 to 30 meV as before. For this experiment the hydrogen was not converted from ortho- to para-H_2 before dosing; a combination of the low temperature and catalytic action of the host lattice allowed this conversion to take place over a period of hours after each new concentration was attained. When conversion was complete, all the intensity transferred from the neutron

energy gain to loss side, as expected if the hydrogen was in the ground state. It therefore behoved us to revisit the concentrations studied in the previous experiment where the conversion had not always had time to complete. The concentrations studied in this experiment were harmonic, starting with the lowest amount of hydrogen it was thought would be visible on the instrument. The background run on pure KC_{24} was taken before hydrogenation. The nominal concentrations of hydrogen studied were $KC_{24}(H_2)_x$, where $x = 0.25$, 0.5, 1, 2 and 2+ (later determined to be 6, see § 8.2). For each concentration, statistically good measurements were taken in both energy windows. These consisted of at least 1500 μAh collected current, usually split into 500 μAh runs. As 1500 μAh took approximately 17 hours to increment, splitting the runs was advantageous in case the sample environment stability was disturbed, and to allow comparisons between the beginning and end of the data collection to look for long period changes in the sample.

The $(H_2)_{2+}$ concentration was obtained by letting on as much hydrogen as would come from the buffer under a pressure of 4630 mbar, then closing the valve to the sample on the rig, and cooling the cryostat down to base temperature. Any hydrogen that had not been sorbed into the sample, including in the capillary, centre stick and mixing chamber, was liable to liquefy on the sample surfaces. This also made it hard to determine the exact concentration *in situ*.

5.4.4 IRIS data analysis

Data from the IRIS experiments was corrected for detector efficiency using a detector calibration file in the software package MODES for OpenGenie. The raw INS data files can be summed by all detectors or any combination of them to observe the variation in the scattering with **Q**. A background can be

subtracted and the S($\mathbf{Q}$) intensity normalised to a vanadium pattern collected at the beginning of each beam cycle. From there, data can be exported in ASCII format to a graph program where peak fitting is done.

5.5 Inelastic neutron scattering on TOSCA

TOSCA is an indirect geometry INS spectrometer at ISIS, situated 17 m from the 300 K water moderator. It is optimal in the energy transfer range 0 - 500 meV with best resolution below 250 meV [109]. A Nimonic chopper at 9.5 m reduces the fast neutron background and a tailcutting absorber on the leading edge suppresses slow neutrons and prevents frame overlap. There are two banks of detectors arranged annularly, that detect neutrons scattered both forward and backwards from the sample. Neutrons deflected from the sample through angles of 45 and 135° are incident on a graphite analyser, which selects certain wavelengths and passes them through a cooled beryllium filter to ^{3}He detector tubes.

The instrument layout is shown in Fig. 5.21. The path of the neutrons through the symmetrical analysers is shown in Fig. 5.22.

The beam size at the sample position is 40×40 mm. Sample cryogenic cooling is provided by a closed-cycle refrigerator (CCR).

5.5.1 Medium energy INS on H_2 in KC_{24}

One experiment was carried out on TOSCA. It was given the identifier 502408. It was complementary to the low energy spectometry carried out on H_2 in KC_{24} on IRIS, and was designed to provide evidence for the crystal field splitting

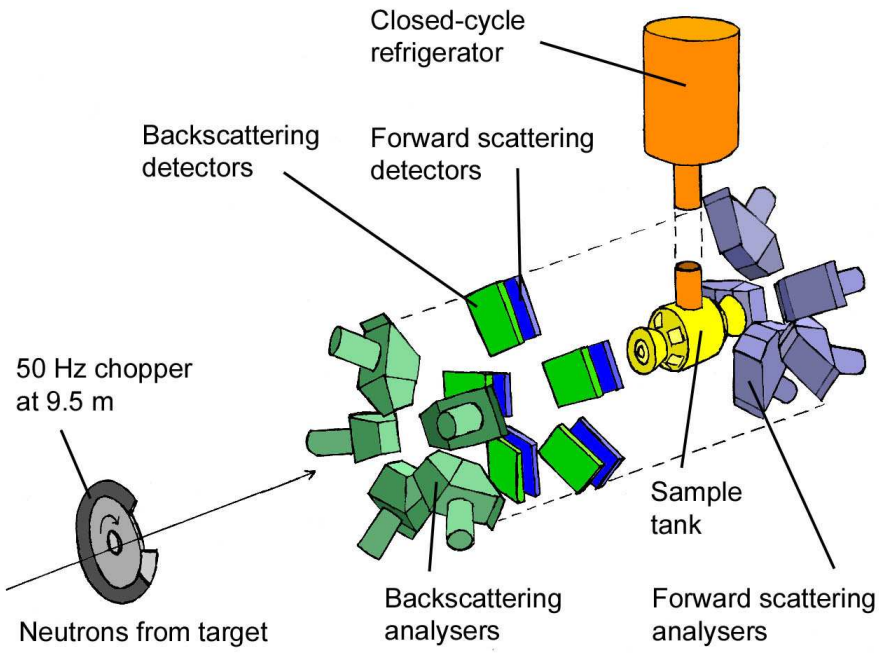

Figure 5.21: Exploded diagram of TOSCA layout

of the hydrogen excitations in the same system by seeking the upper energy splitting at ∼50 meV, and any higher order energy levels. As on IRIS, a stainless steel valve-lidded flat plate can was used to contain the KC_{24} sample, which was of mass 0.7681 g, from the same batch as that used for the second IRIS experiment (§ 5.4.3). It was loaded in the familiar way (see § 5.3.1), placed on the CCR centre stick and the glovebox helium outgassed and the valve handle removed. It was quenched by immersion in liquid nitrogen to speed up the CCR cooling process, then loaded into the sample chamber on the TOSCA beamline. The orientational angle was 0° to the incoming beam; the beam was normal to the preferred orientation planes. This had been planned to maximise the cross-section of the beam incident on the sample, but the lack of an angular dependence had implications for the visibility of excitations parallel to the planes (described in § 8.4.1).

High-purity hydrogen was provided this time from an ortho-para conversion

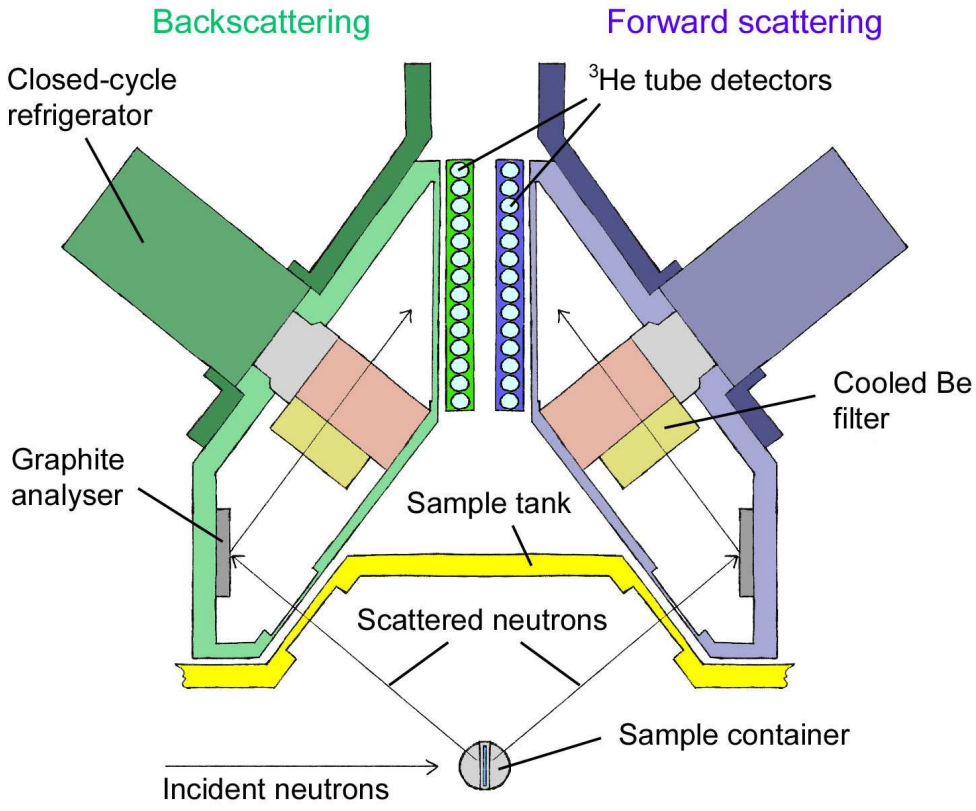

Figure 5.22: Schematic of TOSCA analyser and detector operation.

rig, utilising a cryostat-cooled chamber with iron catalyst to encourage the transition to the H_2 ground state. This could be setup to convert overnight; the temperature of the cryostat was set to 20 K to liquefy the hydrogen, then a small temperature inversion between an upper heater and a lower one in the chamber was set so convection currents in the liquid would enable thorough mixing and contact with the catalyst. A general view of the visible parts of the beamline prior to the loading of the sample is in Fig. 5.23.

Figure 5.23: The TOSCA beamline with ortho-para hydrogen conversion rig and CCR centre stick before sample loading

The CCR was cooled to its base temperature, which was ∼12.5 K. A background run of KC_{24} alone was collected overnight, for 2500 μAh. Then the sample can was warmed to 50 K to load hydrogen, and cooled again to base temperature to collect INS spectra. This process was repeated with the proceeding concentrations. The nominal concentrations of hydrogen studied were $KC_{24}(H_2)_x$, where x = 0.25, 0.5, 1, and 2 ; i.e. the equivalent of the second

IRIS experiment without the highest concentration. This was omitted because of limited experimental time. As the IRIS sample was still on the beamline at this point it was not possible to use the same sample for both experiments but this would have been the ideal situation.

Chapter 6

Thermogravimetry results

6.1 Density measurements

It is critically important for thermogravimetric analysis that the sample density is well-characterised (§ 4.2.4). Most elements of the balance system; the hangdowns and the counterweight, for example, are made of metal of density greater than 7 g/cc. The samples, based on graphite, are much less dense than this and their buoyancy corrections are correspondingly much larger.

Nuclear-grade Papyex graphite comes in thin rolled sheets of constant thickness. The manufacturers claim the density is 1.1 g/cc [110]. A simple (and, it transpired, naïve) density calculation was performed by cutting a 100 × 100 mm sheet of 0.5 mm thickness, calculating the volume and weighing it to determine the density. The density was measured to be 0.976±0.051 g/cc, in reasonable agreement with this claim.

Samples with solid Papyex as base material could be measured in this way. Samples made using micrometre-mesh powdered graphite could not have their

volume measured geometrically; instead, pycnometry was employed. This was carried out on a selection of the samples using two pycnometers to try and gain an appreciation of the factors needed to account for density. A third way of measuring density was to use the IGA as detailed in § 4.2.4. The theoretical density value could be calculated where the molecular structure was known, by dividing the combined mass of the atoms in a unit cell by that cell's volume. No one method was able to be used for all samples, which was a disadvantage.

6.1.1 Pycnometry and IGA density determination

The first set of density measurements was carried out at Imperial College, London (ICL). A pre-weighed sample of the μm graphite powder was placed in a Micromeritics Accupyc 1330 and He gas was let into a known volume including the sample space. From the volume of gas let in at a known pressure, the volume and hence density of the powder sample could be determined. For each analysis the pycnometer took ten measurements, and averaged them with a standard deviation (which is the quoted error value in Table 6.1).

As the pycnometer was not in a controlled or inert atmosphere, the samples were unavoidably exposed to air on loading. This adds a large potential problem to the density measurement of air sensitive samples; the weight may not be stable because the sample is oxidising, and the volume measured by the instrument may be different from the unoxidised sample.

The first analysis for the graphite powder was discarded because the sample did not seem to be stable, but the second and third were in good agreement with much reduced variation in their measurements. The procedure was repeated with an ammoniated calcium graphite sample, the last one measured in the IGA. Two sets of measurements were taken on this sample.

Table 6.1: Sample density measurements by material. Pycnometer 1 is the Imperial College Accupyc, pycnometer 2 the Micropycnometer at Rutherford Appleton Laboratory

Material	Determination method	Weight	Density	Average
Units		mg	g/cc	g/cc
Graphite	Theoretical		2.26	
Papyex	Geometrical	4881.7±0.4	0.976±0.051	
	IGA	126.4665	2.4430	
	Pycnometer 2	1128.6	2.035±0.037	
KC_{24}	Geometrical	53.5±0.1	0.96±0.10	0.949±0.070
	Geometrical	100.9±0.1	0.942±0.098	
	Pycnometer 2	611.6	2.00±0.05	
KC_8	Theoretical		1.968	
	Geometrical	99.0±0.1	1.00±0.10	1.004±0.074
	Geometrical	108.6±0.1	1.01±0.11	
CaC_6	Theoretical		2.527	
(Li alloy)	Geometrical	131.3±0.1	1.38±0.14	
	Geometrical	157.9±0.1	1.57±0.16	
	IGA	95.8105	1.6715	
	Pycnometer 2	289.6	1.734±0.074	
1-2 μm	Pycnometer 1	106.8±0.1	2.82±0.08	
graphite			2.74±0.10	
	Pycnometer 2	750.6	2.33±0.05	
CaC_{12} (NH_3)	Pycnometer 1	41.4±0.1	3.17±0.42	
			2.87±0.38	

The second set of pycnometry measurements were carried out at the Rutherford Appleton Laboratory on a Quantachrome Micropycnometer. Each volume measurement using He was carried out manually and a graph of the data points plotted until a nearly-constant value within error bars associated with the smallest digit of the pressure readout was obtained. Density values were obtained for pure Papyex, to compare with the geometrically-measured value; μm graphite powder; Papyex-based CaC_6, which appeared to oxidise slowly enough to give meaningful results; and Papyex-based KC_{24}, which oxidised too rapidly to be reliably measured.

The IGA was used in density determination mode on pure Papyex and the Li-alloy CaC_6 sample, using nitrogen as the cycling gas. It was assumed to be inert with respect to the samples.

The results for the density measurements are shown in Table 6.1, arranged by material and method. They are compared with theoretical densities, which set an upper limit for the possible density.

6.1.2 Conclusions and discussion of errors

The search for a meaningful definition of density highlights some of the limitations of sorption experiments. Measurements that utilise a gas to measure the sample volume are likely to find higher readings than simple geometrical calculations, because the gas penetrates pores, reducing the effective volume taken up by the sample. As intercalates are well-known to act as molecular sieves [64], the measurement gas is liable to be sorbed to a greater or lesser degree depending on the size of the gas molecules. To determine the density "seen" by the hydrogen, it would be theoretically necessary to find a non-interacting gas of the same size. A perfectly penetrating gas would measure a

density approaching the theoretical value, as long as it did not intercalate into the graphite layers. The van der Waals (vdW) radius of He is comparable to the interlayer graphite spacing (∼3.4 Å), suggesting that He in general cannot intercalate. Measurements that exceed the theoretical limit are probably ascribable to experimental error rather than He intercalation.

As expected, the IGA and pycnometric density measurements were higher than those established by other means. The measurements associated with Pycnometer 1 exceed theoretical values and were not used. The geometrical measurements used for early analysis were too low and, when applied to the data, showed a puzzling linear uptake after H_2 'saturation' had occurred. Those from Pycnometer 2 fitted the Langmuir model for KC_{24} and Papyex and so were used universally, the exceptions being for KC_8 and the ammoniated calcium-graphite samples. There were two main contributions to the experimental uncertainty: error in the zero weight of the sample, with a constant value over all data points, and error in the density, which had an effect proportional to the uptake. The latter was more significant for samples with large uptakes (>1 wt.%). Larger offsets in the uptake for some isotherms were sometimes attributable to instrumental drift and sometimes to prior irreversible uptake. In the case of the former where a vacuum reading was available, the offset was adjusted using the new dry weight in the buoyancy calculator.

6.2 Temperature stability

Many of the first isotherms suffered from poor temperature stability, especially those conducted at room temperature. This was a direct result of variations in the ambient temperature in the laboratory being transferred to the sample

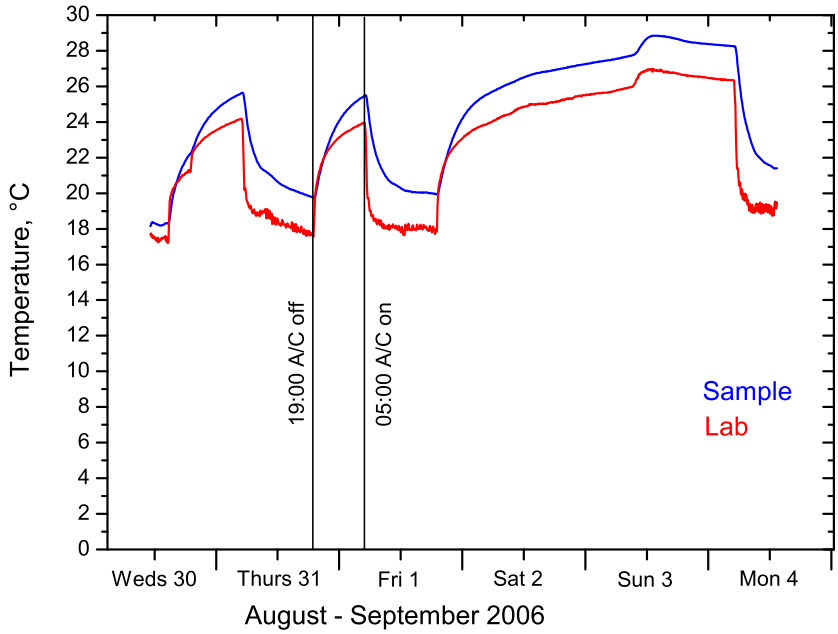

Figure 6.1: Temperature of lab and sample from 'External' and 'Sample' PRTs over period 30 August to 4 September 2006

tube. The principal variation came from the air-conditioning being switched automatically on every morning and off at night. Fig. 6.1 shows a typical summer variation in the lab temperature, and shows how the unshielded sample tube transmits this to the sample PRT even though that is under vacuum. Radiative forcing from the top of the cabinet and the lack of an exchange medium under outgas probably accounts for the sample being warmer than the outside air. The lab air-conditioning operated from 5 am to 7 pm every day bar weekends and the total temperature range could be nearly 10 K.

The reaction tube required insulating to minimise the temperature variation affecting the sample PRT. As the furnace has high thermal mass, it was used as a shield at the beginning. It was replaced for a while with an expanded polystyrene container filled with paper towels to stop air motion over the tube. Later still, a container of water, possessing high thermal mass, was used to immerse the sample tube. For cryogenic measurements, a dewar

of liquid nitrogen was used to provide stable temperatures of 77-78 K, though thermal drift occurred when the nitrogen levels were too low, as in an overnight run. Under outgas conditions the sample temperature decoupled considerably from the cryogenic temperature as there was no exchange gas, leading to large temperature, and sometimes weight, anomalies at vacuum readings. Many isotherms suffering from insufficiently stable temperatures had to be omitted from this chapter. More fundamentally, it was not possible to obtain isotherms at intermediate temperatures between 77 and 295 K by the above methods, frustrating the possibility of obtaining adsorption enthalpies for the samples. Although one attempt was made, for 200 K, using dry ice in a dewar about the sample tube, the results were not encouraging. As the CO_2 was in solid pieces, there was no even thermal contact; the dewar could not be refilled, and the data were not publishable.

To alleviate this problem, a cryostat was obtained on loan to open up the temperature range and allow the IGA to be run overnight with reliable temperature control. The cryostat was supplied by Hiden and was designed to work with the IGA model. It was certified for a range of 123-773 K. In operation it pumped liquid nitrogen from a 35 l reservoir through coils in good thermal contact with the sample reaction tube, and in combination with a heating coil could be adjusted in practice to hold any temperature in that range and down to 88 K, for a period of at least 18 hours without refilling. By the time it was set up, it was only in use for the last two samples investigated, and these did not have enough uptake to be able to determine the adsorption enthalpies. The cryofurnace did not prevent the temperatures at low pressure rising due to inadequate thermal exchange.

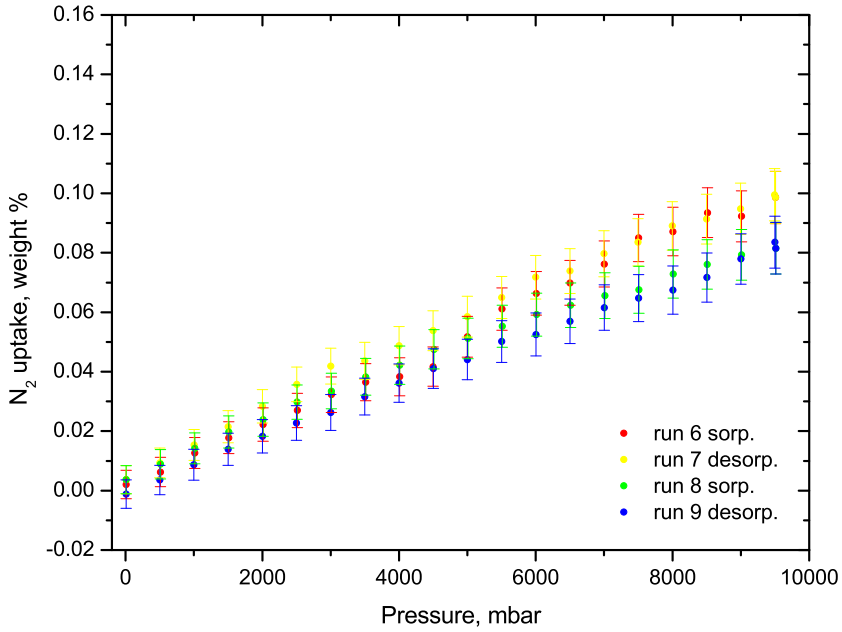

Figure 6.2: Uptake of nitrogen gas in outgassed Papyex graphite at room temperature. Although the N_2 is not completely inactive, the uptake is less than 0.1 wt.%.

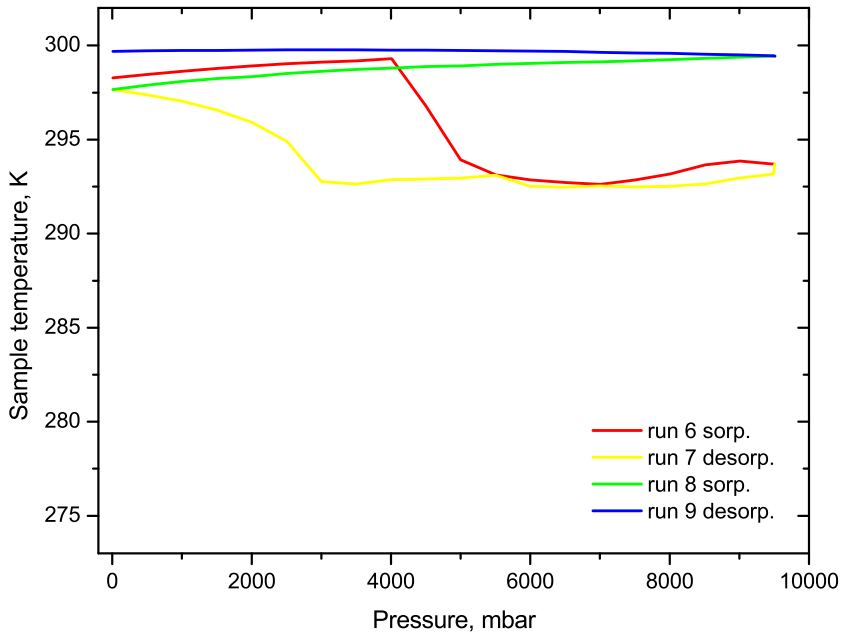

Figure 6.3: Papyex sample temperature during nitrogen loading

6.3 Papyex graphite

Loading graphite into the IGA has the advantage that it is not air sensitive, and thus the dry loading procedure does not need to be used. Instead, the graphite is loaded in air, a loading weight is recorded, and then the IGA furnace is used to outgas the graphite at 500°C, before a dry weight is fixed.

The first sample loaded was Papyex. The sample container was the stainless steel gauze cone. The weight on loading was 104.77 mg. The outgas temperature was 300°C for the first three days followed by 500°C for 1 day, at the end of which the sample weight was 104.066 mg, signifying an outgassing weight loss of 0.67 %.

The first set of measurements were to see if any N_2 uptake occurred in the outgassed Papyex. An isotherm run was set up in the IGA software: the pressure values chosen were in 500 mbar steps from the lowest value pressure the machine could allow to 10,000 mbar as a sorption run, and the same in reverse for desorption. The software does not allow a positive pressure lower than 12.1755 mbar to be set, so this was the lowest chosen. It was for later samples that the first point in the sequence was set to be an outgas ('zero' mbar) which gives a dry outgas weight to begin with on the isotherm playback graph. The lack of this vacuum point means that the automatic dry mass setting facility in the software could not be used. For these early runs the dry mass was recorded manually by outgassing each sample and then recording the minimum weight attained under vacuum.

Fig. 6.2 shows the uptake of nitrogen in the first Papyex sample at room temperature, in mass %. Two complete sorption/desorption scans are shown, described by run number. The earlier runs were insufficiently isothermal to include. Even here, there was a range of 7 K in the sample temperatures

measured, as shown in Fig. 6.3 . This deviation in temperature for runs 6 and 7 is matched in Fig. 6.2 by their divergence in uptake from runs 8 and 9 for high pressures. The uptake is small but non-zero, implying that N_2 adsorbs in graphite to a tiny extent. It also appears linear with pressure up to 10,000 mbar, where it is <0.1 wt.%, or <1 molecule of nitrogen for 2300 carbon atoms.

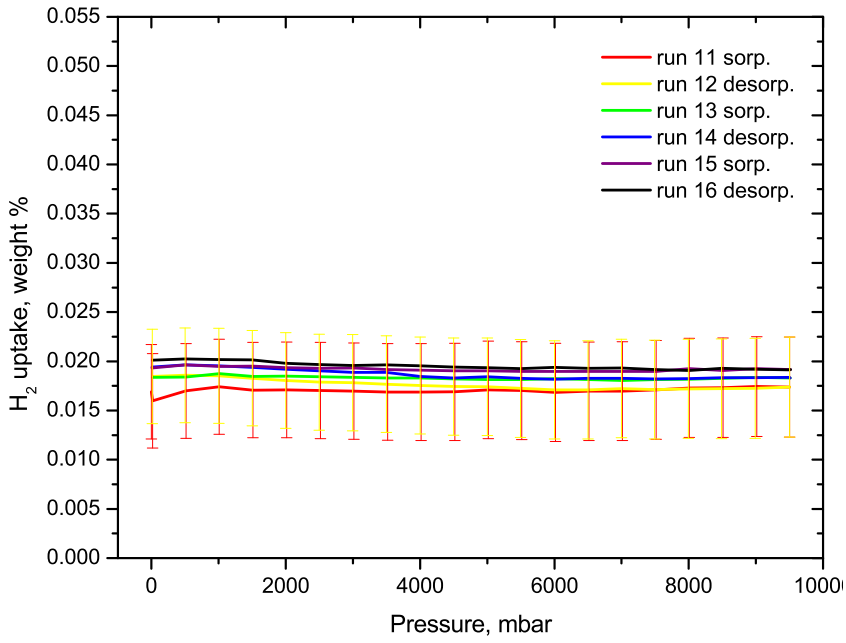

Figure 6.4: Corrected weight uptake for three room-temperature adsorption/desorption isotherms of H_2 in Papyex; runs 11-16

After outgassing at 400°C, the working gas was switched to hydrogen. The first set of runs were taken at room temperature as for the nitrogen sorption. The same isotherm template was used. The first eight runs were not suitable for inclusion; Fig. 6.4 shows the final six of the set, comprising three complete isotherms. Although there is an offset of 0.015-0.020 wt.%, which may be attributable to a small irreversible uptake from the previous runs, there is no apparent uptake of H_2 in Papyex at room temperature; the isotherms are flat lines within the error. As the internal surface area of Papyex is low, this is not a surprising result. The variation in temperature for these results is plotted in

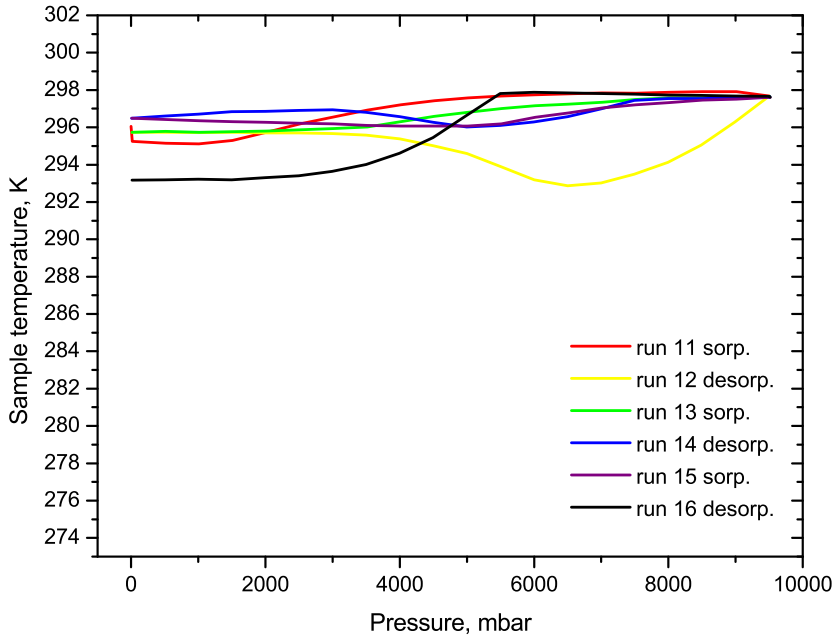

Figure 6.5: Sample temperature for three room-temperature isotherms of H_2 in Papyex; runs 11-16. The temperature variation is 6 K

Fig. 6.5.

The next set of isotherms were taken at 77 K using a liquid nitrogen bath. Two are shown in Fig. 6.6, with fits to the sorption data superposed. The isotherm temperature records are in Fig. 6.7; they show less variation than the room temperature measurements but gradual rises during desorption betray the difficulty of keeping the nitrogen bath full to maintain a steady temperature. The saturated hydrogen uptake was found by a Langmuir-type analysis to be 0.088±0.002 wt.% for run 2 with an offset of 0.032 and 0.084±0.002 wt.% for run 5 with an offset of 0.038. If the offset is assumed to be constant the uptake values are closer. This magnitude for cryogenic H_2 uptake is consistent with the literature.

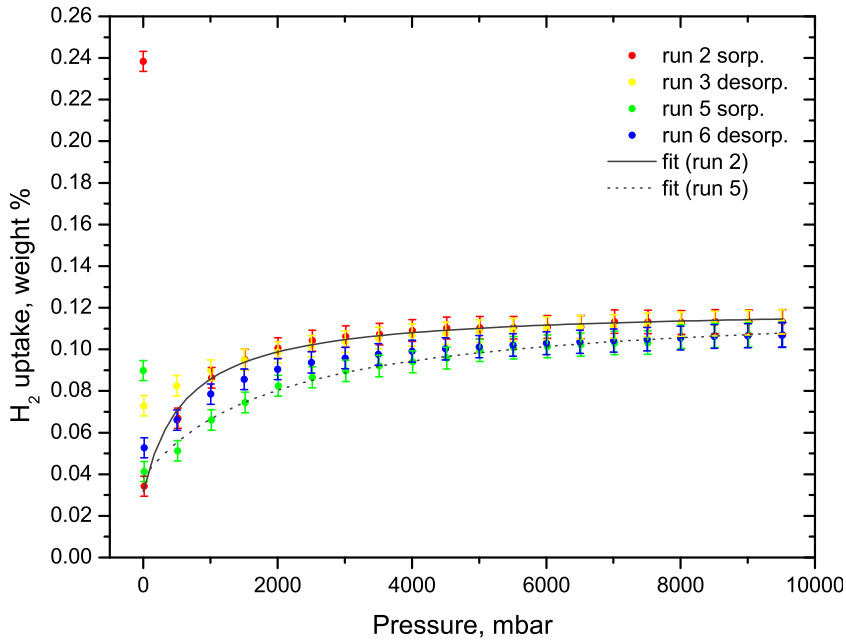

Figure 6.6: Corrected weight uptake for two 77 K adsorption/desorption isotherms of H_2 in Papyex; runs 2-3, 5-6. Langmuir fits to two datasets are shown

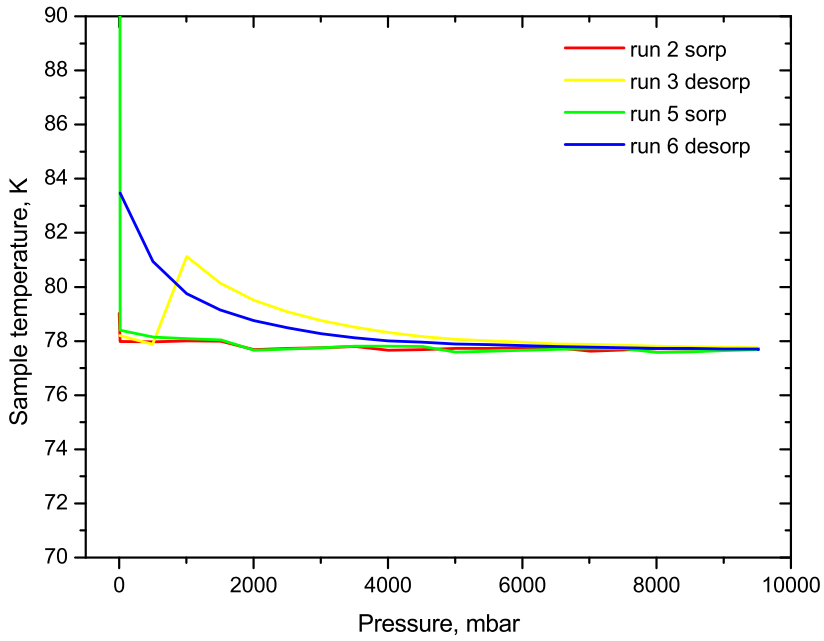

Figure 6.7: Sample temperature for two 77 K isotherms of H_2 in Papyex; runs 2-3, 5-6

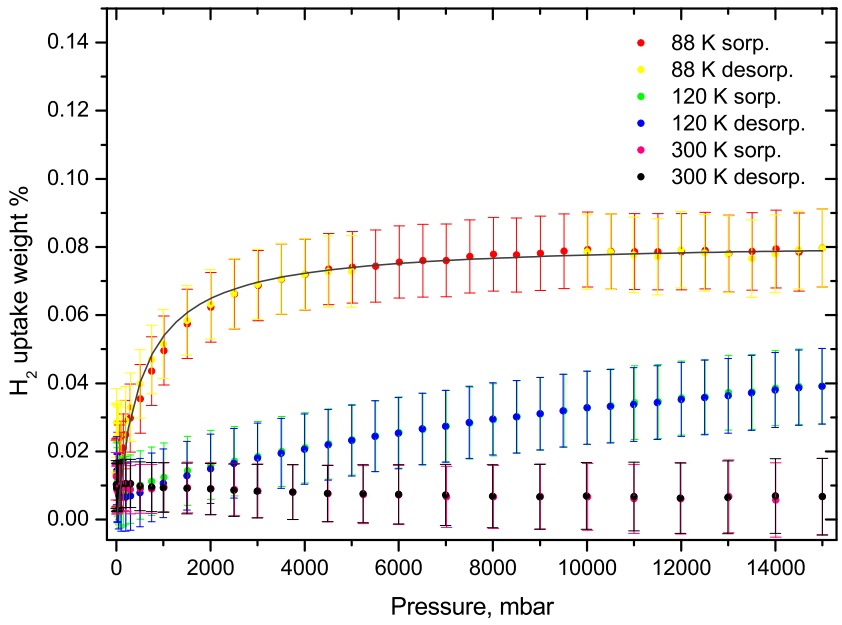

Figure 6.8: Corrected weight uptake for H_2 in Papyex sample 2 for 88 K, 120 K and 300 K runs. Certain points in the 88 K desorption run were omitted as the temperature was not stable. The negative gradient of the 300 K isotherm suggests that the sample density is slightly less than 2.035 g/cc. Temperatures are quoted to the nearest degree

6.3.1 Papyex sample 2

A second Papyex sample was investigated after the quality of IGA data had improved through experience and optimised operation. The sample's outgassed weight was 126.4665 mg. The newly-installed IGA cryofurnace was used to control the sample temperature, and the sequence of runs went from low to high temperatures, to minimise irreversible uptake over the course of the experiment. Selected data are shown in Fig. 6.8. The 88 K and 120 K sorption isotherms are fitted. The saturated uptake at 88 K was found to be 0.0726±0.0004 wt.% with an offset of 0.012, and that for 120 K was 0.070±0.006 wt.% with an offset of 0.009. These values are generally consistent with the previous sample, with the total uptake reducing as the temperature is increased. A slight negative uptake for H_2 at 295 K implies that the density value used (2.035 g/cc, as for the previous sample) was an overestimate, though the potential variation of this value was included in the error calculation (The alternative possibility is that the density reduces significantly as a function of hydrogen pressure; this is considered unlikely given the generally low response of pure exfoliated graphite to hydrogen). As previously, there is a slight offset. Not shown for clarity are isotherms at 220 and 350 K; neither showed any evidence for sorption.

6.4 KC_{24}

The second stage potassium-GIC was investigated for its uptake to complement the neutron scattering studies carried out on the system with hydrogen. It was the first air-sensitive sample, and thus the first in which the dry loading system was used to preserve the sample during the loading process. Two separate samples were loaded in this initial case; later, when various improvements to

the loading and measuring technique had been made, a third KC_{24} sample was studied.

6.4.1 KC_{24} sample 1

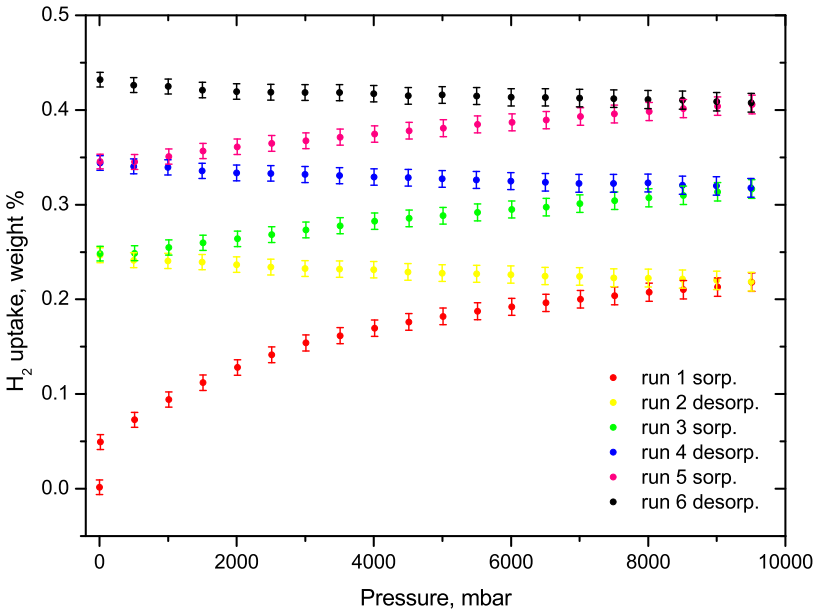

Figure 6.9: Corrected weight uptake for three 295.5±1.5 K adsorption/desorption isotherms of H_2 in KC_{24}, sample 1. The adsorption is characteristic of constant and irreversible uptake under hydrogen loading. The total loading recorded here is 0.43 wt.%, though it is apparently not saturated. This equates to $0.7H_2$/K ion.

This sample was selected from well-characterised blue strips, which were cut into pieces approximately 5 × 10 mm and placed in the stainless steel mesh sample holder. This was loaded into the IGA using the dry loading procedure outlined in § 5.2.2. After outgassing the weight was 32.2774 mg which was taken as the dry weight for the buoyancy calculations. This was the first 'successful' use of the dry loader (where the sample was not completely ruined); this notwithstanding, significant oxidising of the sample was seen to take place. Measurements of H_2 adsorption at room temperature showed

irreversible weight gain as predicted by the literature [42]. The first three sorption/desorption runs are shown in Fig. 6.9; starting with non-linear adsorption the first time hydrogen is pressured onto the sample, the uptake after that shows a constant increase whether the pressure is increasing or decreasing, making a zig-zag characteristic of chemisorption. As the set of runs were performed back-to-back we can surmise that the uptake is more-or-less linear with time exposed to the hydrogen. No significant quantity of hydrogen was removed even under outgas. The sample temperature was 295.5±1.5 K across the set of runs.

The sample was then cooled by a liquid nitrogen bath to a nominal 77 K and a further set of isotherms measured. These showed much higher values of adsorption but when corrected for sample density showed poor data quality. The uptake for the first isotherm was ∼0.9 % wt, and 0.7 % wt. for the second. As the irreversible H_2 uptake from the room temperature measurements had a high likelihood of influencing these results, and as good quality isotherms were obtained with further KC_{24} samples (below), these data are not presented here.

What effect did the irreversible uptake of hydrogen during the room temperature runs have on later uptake? To prevent any irreversible uptake affecting later sample runs, as well as increasing the base weight of the sample for physisorption, it is better to carry out the lowest temperature measurements before the ambient temperature ones. This was a salutary lesson carried over to later samples.

6.4.2 KC_{24} sample 2

The second sample of KC_{24} was taken from the batch labelled TOSCA 1. Good, well-staged blue strips were selected and cut into smaller pieces, before being weighed (0.0909 g) and placed in the glass bulb, which was placed on the IGA loading stage in the glovebox. The dry-loading procedure was very intricate and possessed no easy way of retrieving a sample undamaged if the procedure was not successful. During the loading process the balance was accidentally zeroed with the sample loaded, causing the weight to be under-read by a constant amount for all measurements taken with this sample. This under-read amount was noted. The IGA software was not always reliable and, when loading in an inert atmosphere of precarious purity, it was better to continue rapidly with the loading rather than reset the software. Thus all buoyancy calculations for this and some later samples were done 'manually' in a spreadsheet and not by the software, so that the weight could be corrected. See § 6.7.

The dry weight of the sample, after outgassing on the IGA, was found to be 95.4652 mg. Three 77 K adsorption/desorption isotherms were run, and the latter two are displayed in Fig. 6.10, with attendant temperature measurements in Fig. 6.11. They were discontinuous scans, where the hydrogen pressure was maintained at the end of the sorption run, and the desorption run started some time later once the nitrogen bath had been refilled. This led to some slight differences between the highest weight in the sorption cycle and the highest weight in the desorption cycle, probably attributable to long-period uptake in the sample. The two sorption runs show a large increase in uptake at low pressure, followed by a quasi-saturation, where the weight increases very slightly in a linear fashion to the maximum pressure, as would be seen if there was a very slow uptake mechanism working.

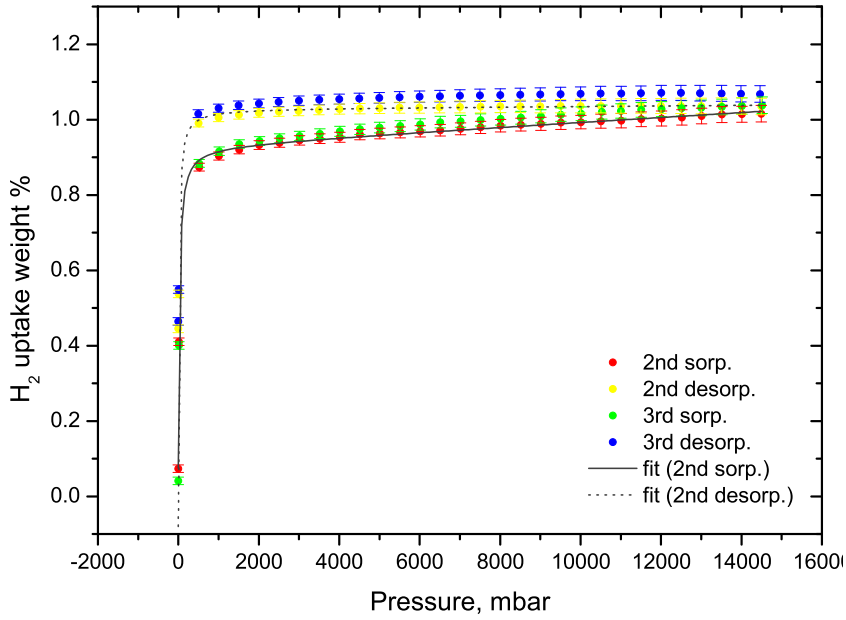

Figure 6.10: Corrected weight uptake for two 77 K adsorption/desorption isotherms of H_2 in KC_{24}, sample 2. The grey lines denote Langmuir fits to selected datasets

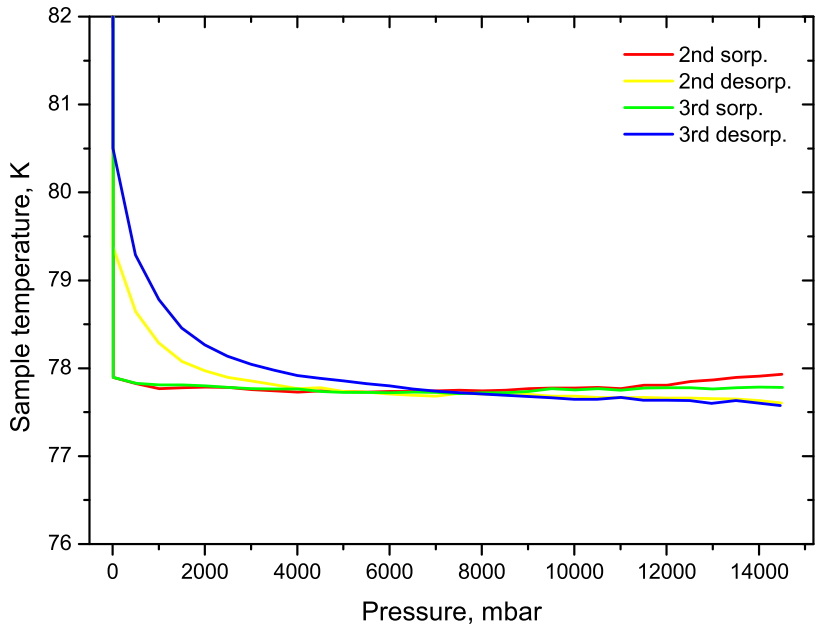

Figure 6.11: Sample temperature for two 77 K adsorption/desorption isotherms of H_2 in KC_{24}, sample 2

A hysteresis is seen for both isotherms, where the desorbing uptake is higher than that seen during the sorption. It also appears to be a constant value until desorption begins below 2000 mbar. This may be because the secondary slow absorption is complete by the time the desorption run is begun, a number of hours after the sorption run ended. The desorption run thus shows the sample completely saturated until the pressure is reduced far enough to permit desorption.

Table 6.2: Langmuir fits to KC_{24} sample 2 77 K isotherm runs. n = saturated uptake, d = Langmuir equilibrium constant, m = gradient of linear uptake contribution, c = offset constant, s = saturated H_2 concentration in $KC_{24}(H_2)_s$.

Run	n wt.%	d	m wt.%/mbar	c wt.%	s H_2/K
2nd sorp.	0.939±0.003	0.046	7.9×10^{-6}	0	1.52
2nd desorp.	1.03±0.04	0.065	$6.8e\times10^{-7}$	0	1.67
3rd sorp.	0.941±0.005	0.043	7.4×10^{-6}	0	1.53
3rd desorp.	1.05±0.04	0.08	1.6×10^{-6}	0	1.70

The curves were fitted using a Langmuir model. The results are shown in Table 6.2. The desorption runs fit to a higher saturation because they show no linear desorption; they were taken after the slow adsorption was complete. The sorptive saturation would be the limit with these kinetics if a quick sorption was required. The offset between the isotherms is likely to be systematic and probably associated with drift on the IGA measurements. The calculated H_2 saturation concentration is somewhat less than the 2 H_2/K stemming from the literature. It is possible that the sample was damaged on loading, hence limiting its uptake. Equally, there may be a hidden offset in the IGA data. This issue will be addressed at greater length in a later chapter, because it has bearing on the neutron scattering results.

6.4.3 KC_{24} sample 3

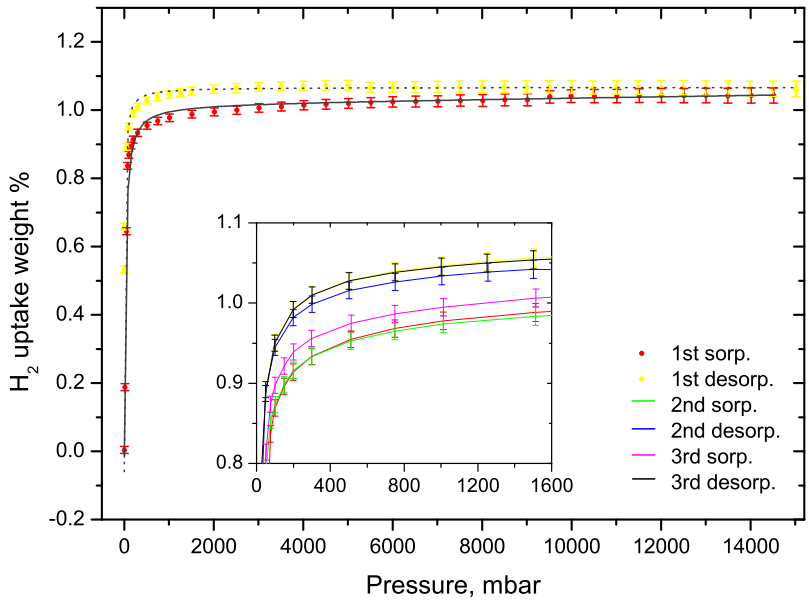

Figure 6.12: Corrected weight uptake for three 77 K adsorption/desorption isotherms of H_2 in KC_{24}, sample 3. The second and third are shown in the inset compared with the first. The grey lines illustrate Langmuir fits of the first isotherm runs.

The third sample of KC_{24} was measured upon some months after the previous one. It was intended to check the reliability of the earlier data and to sample the initial uptake of gas below 500 mbar external pressure at better resolution. The sample dry loading process had been improved considerably by this time too; the purging cycles had been replaced by a simpler constant flow of purge gas through the chamber (see § 5.2.2) and initial tests were favourable that the sample would be far less contaminated by air or moisture during the loading process.

0.1328 g of homogenously-blue KC_{24} was weighed in the glovebox and loaded into the IGA by the revised dry-loading method. The sample was outgassed for 16 hours at 94°C and then at 113°C for a further 21 hours, after which the measured sample weight was 133.5499 mg. A liquid nitrogen bath

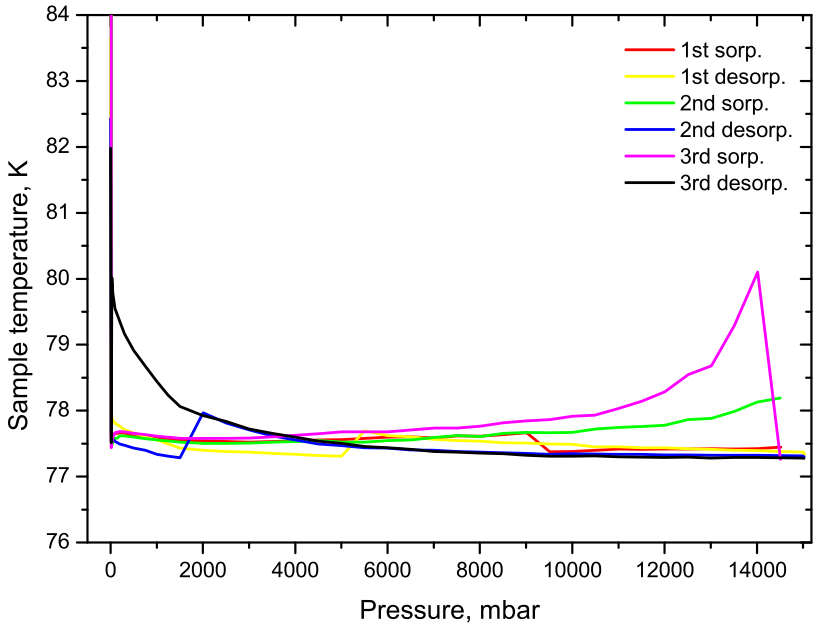

Figure 6.13: Sample temperature for three 77 K adsorption/desorption isotherms of H_2 in KC_{24}, sample 3.

was placed around the sample tube. Three sorption/desorption isotherms to 15,000 mbar applied H_2 pressure at 77 K were successfully run. Variability or perhaps non-reversible uptake during the initial cycles meant the stable zero weight for these isotherms was 133.6129 mg. Before each isotherm the sample was outgassed at 400 K for ∼24 hours. The H_2 uptake is shown in Fig. 6.12. Importantly, a higher density of points at low pressures allows a better fitting of the uptake characteristic. It can be seen that all the isotherms are in good relative agreement, with some spread in uptake of magnitude 0.1 weight %. The magnitude of the sorption agrees well with isotherms at the same temperature on samples 1 and 2. The fit parameters are shown in Table 6.4. Again, it transpires that the highest saturation concentration of H_2 according to these data is approximately 1.75 H_2/K, in good agreement with the previous sample but under-performing by the literature.

The corresponding sample temperatures for these isotherms are shown in

Table 6.3: Langmuir fits to KC_{24} sample 3 77 K isotherm runs. n = saturated uptake, d = Langmuir equilibrium constant, m = gradient of linear uptake contribution, c = offset constant, s = saturated H_2 concentration in $KC_{24}(H_2)_s$.

Run	n wt.%	d	m wt.%/mbar	c wt.%	s H_2/K
1st sorp.	1.02±0.01	0.036	1.8×10^{-6}	0	1.66
1st desorp.	1.07±0.02	0.093	0	0	1.74
2nd sorp.	1.017±0.007	0.043	8.4×10^{-7}	0	1.65
2nd desorp.	1.05±0.03	0.099	2.0×10^{-7}	0	1.70
3rd sorp.	1.04±0.01	0.046	9.6×10^{-7}	0	1.68
3rd desorp.	1.07±0.02	0.11	0	0	1.73

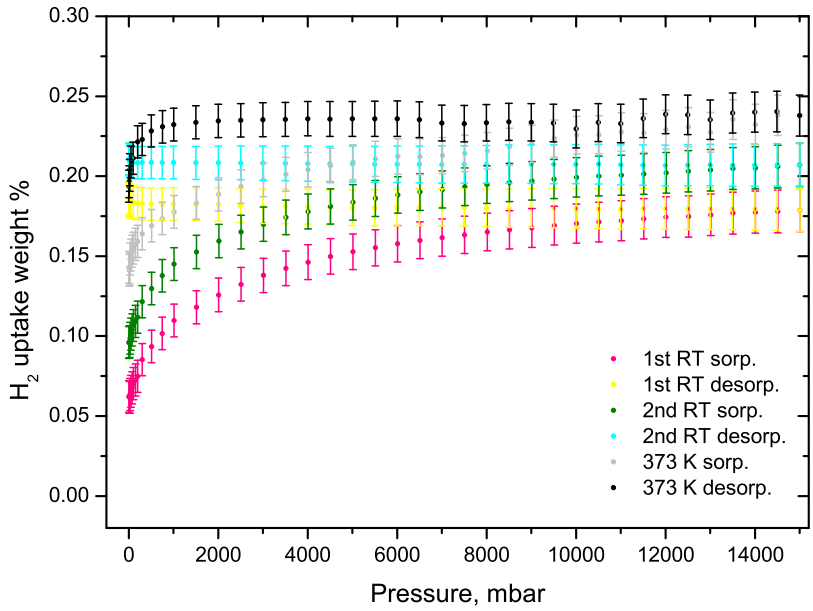

Figure 6.14: Corrected weight uptake for two room temperature adsorption/desorption isotherms and one at 373 K, of H_2 in KC_{24}, sample 3

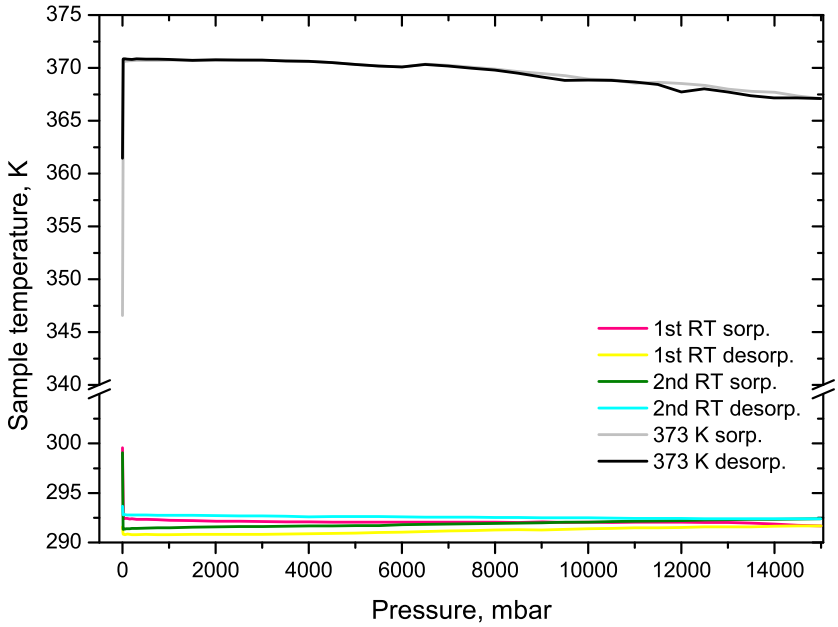

Figure 6.15: Sample temperature for two room temperature adsorption/desorption isotherms and one at 373 K, of H_2 in KC_{24}, sample 3

Fig. 6.13. It can be seen that the temperatures were not always stable, particularly for the third isotherm towards the end of both the sorption and the desorption cycle. As the gas was removed from the IGA balance chamber, in conjunction with a reduced level of N_2 in the bath, the sample temperature crept up. This may be why the desorption runs do not seem to desorb back to the original pre-sorption weight without being outgassed under vacuum: the temperature is not stable for them. The outgassing valve PIV1 was opened to pump thoroughly on the sample between isotherms, and the starting weight for all three isotherms was comparable, if slightly higher for the third.

With solid CO_2 in a dewar as a cold 'bath', an experiment was carried out at c. 200 K in an attempt to get data at intermediate temperatures between liquid nitrogen and ambient air. The isotherm was shortened so it ended at 2500 mbar, but even so the temperature was unstable and the data not reliable enough to be analysed.

Two isotherms were run at ambient temperature, with outgassing periods of at least 24 hours at 400 K between each one. Following them, an isotherm was run at 373 K (set at 100°C on the furnace). The uptake was small and appeared semi-irreversible. All three isotherms are shown in Fig. 6.14. The temperature characteristics are shown in Fig. 6.15. The uptake is irreversible as the desorption uptake is constant; however, outgassing the sample at elevated temperature drives out a proportion of the hydrogen before the next isotherm is started, implying that the uptake is not entirely chemisorbed.

6.5 KC_8

One sample of KC_8 was investigated on the IGA, but only one 77 K H_2 isotherm was carried out before a lab power failure let air into the sample chamber and oxidised the sample. The sample then had to be discarded (after a speculative second isotherm on the oxidised sample) and time constraints prevented further investigation of this compound. The intention had been to check whether sorption took place at cryogenic temperatures, unreported in the literature, and then to chart the irreversible weight gain expected from forcing hydrogen into the sample at room temperature to determine the final composition of the samples similar to the one used to chart this chemisorbing transition using neutron diffraction.

0.1350 g of KC_8 was selected and loaded into the IGA using the dry loader's original purging sequence. After outgassing at 94°C for 18 hours and 120°C for a further 10 days, the sample weight stabilised at 124.8036 mg.

On beginning the uptake measurements, the weight was 124.7729 mg and this was used as the dry mass value. The analysis of the uptake proved difficult as only a geometric estimate of the sample density was obtained, 1.004

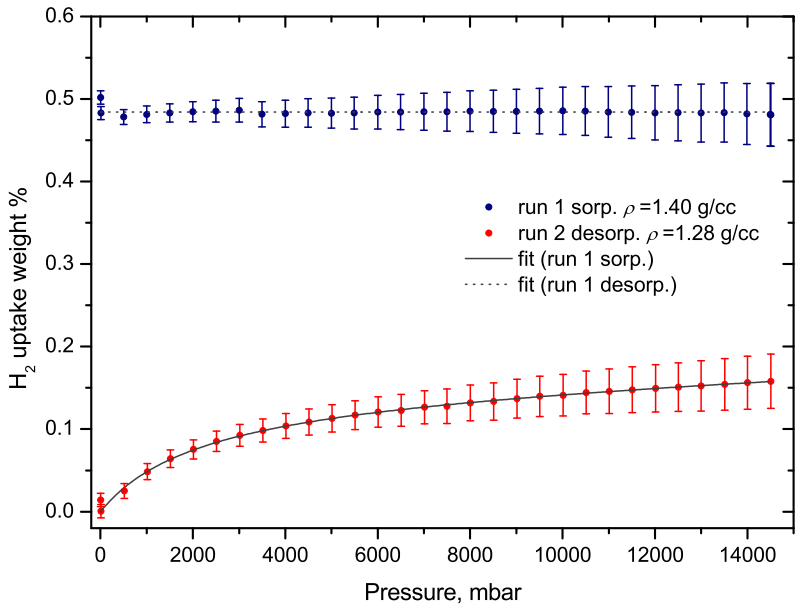

Figure 6.16: Corrected weight uptake for one 77 K adsorption/desorption isotherm of H_2 in KC_8. The temperature was 78±1 K. There was a pause of 82 hours between sorption and desorption measurements, during which time the hydriding phase change presumably occurred. The hydrogenated sample density ρ_h was extrapolated by setting the desorption points to a constant uptake. The grey dotted line shows the fit: $y = 0.4841 \pm 0.0001$. The sorption density ρ_s was extrapolated from this using the ratio of the theoretical densities of KC_8 and $KC_8H_{0.5}$ as a guide. The grey line shows a fit to the modified Langmuir model.

g/cc. This was considerably less (∼half) than the density values used for other Papyex-based materials, as well as the KC_8 theoretical density of 1.97 g/cc, and did not account for sample porosity. Was it possible to gain a more reliable value?

A significant pause of 82 hours existed between the sorption and desorption measurements, in which time the weight of adsorbed H_2 increased considerably. Although the sample had been at liquid nitrogen temperature while the measurements were underway, it was not possible to prevent the temperature rising to ambient in this hiatus while the sample was still under a hydrogen pressure, thus presumably forcing the H_2 uptake. As the time required to saturate KC_8 at room temperature was known to be about 14 hours, it was possible to assume that all uptake took place before the desorption run began, and that it was irreversible, in which case the desorption data could be fitted to a constant, equivalent to the uptake of the saturated KC_8H_s. The extrapolated density was 1.28±0.10 g/cc, and this was used to plot the desorption plot, in Fig. 6.16. The desorption data was fitted to 0.4841±0.0007 % wt., the grey line shown on the plot. This uptake is equivalent to $s = 0.648 \pm 0.001$, which is close to the saturated H concentration of 0.67 from the literature. Thus the density derivation appears justified. Applying this density value to the sorption curve gave a Langmuir-type increase at low pressure followed by a positive linear trend, which is not expected at 77 K. As the sample composition changed between sorption and desorption, so would the density. The ratio between the theoretical density of KC_8 and $KC_8H_{0.5}$ was found to be 1.094; applying this to the extrapolated density of the hydrogenated sample suggested the KC_8 density in this sample might have been 1.40 g/cc. This value was applied to reduce the positive linear uptake, and a Langmuir fit applied. This gave a saturated Langmuir uptake of 0.148±0.009 wt.% for an equilibrium constant, d, of 0.00045. The addition linear uptake was 2.02×10^{-6} wt.%/mbar.

Analysing the uptake gives a saturated compound at 77 K of $KC_8H_{0.20}$, in moderate agreement with the $KC_8H_{0.1}$ limit reported in literature (§ 3.3.2).

A similar extrapolation suggests that the density of the oxidised sample is about 1.1 g/cc and that the total irreversible uptake is approximately 1.65 wt.% (including the oxidation). A small sorption/desorption cycle of H_2 was apparent in this case but the data were of sub-optimal quality and will not be included.

In this experiment, it was not possible to prevent the room temperature chemisorption of H_2 into the sample as intended as no automatic cryostat was available. This does allow a good estimate of the true sample density. After long exposure to hydrogen at room temperature, the weight uptake attains close to the expected saturation concentration of $H_{0.67}$. The sorption of hydrogen at 77 K, shows a Langmuir-type increase to a concentration higher than reported, followed by a positive linear trend. The large errors reflect the uncertainty in the sample density, which will vary as the hydrogen adsorbs. It seems unlikely that this is all physisorption as there is a lack of available interlayer volume for H_2 siting. If chemisorption, it is taking place at temperatures much lower than expected, although the driver for the sorption and thus the structural transition seen using diffraction may be the high pressure. This area is not well-explored so there is scope for an investigation of the transition onset under high hydrogen pressure.

6.6 Stainless steel

This sample was loaded as a calibration test for the IGA and to determine a confidence level for the data collected from adsorbing samples. As stainless steel wire is resistive and non-porous, one does not expect to observe any H_2

uptake at all. This is why the material is used for other elements in the balance train, notably the counterweight. In early analysis of Papyex-based samples a constant increase in uptake with pressure was observed after the hydrogen content appeared to saturate. This was due to inaccurate geometric density measurements, later superseded. If for any reason it had been a systematic error associated with the balance operation, it would likely manifest itself in the isotherms of the stainless steel.

320.4 mg of steel wire, identical to that used for the counterweight (which for that sample weighed 497 mg) was cut, fashioned into a hooked loop and loaded onto the IGA hangdown in air. The reactor tube was sealed and the sample outgassed at 420°C for 20.5 hrs, after which the dry mass was recorded as 319.4354 mg. Next, two complete isotherms were measured at ambient temperature, as shown after correction in Fig. 6.17, with the corresponding sample temperature runs shown in Fig. 6.18.

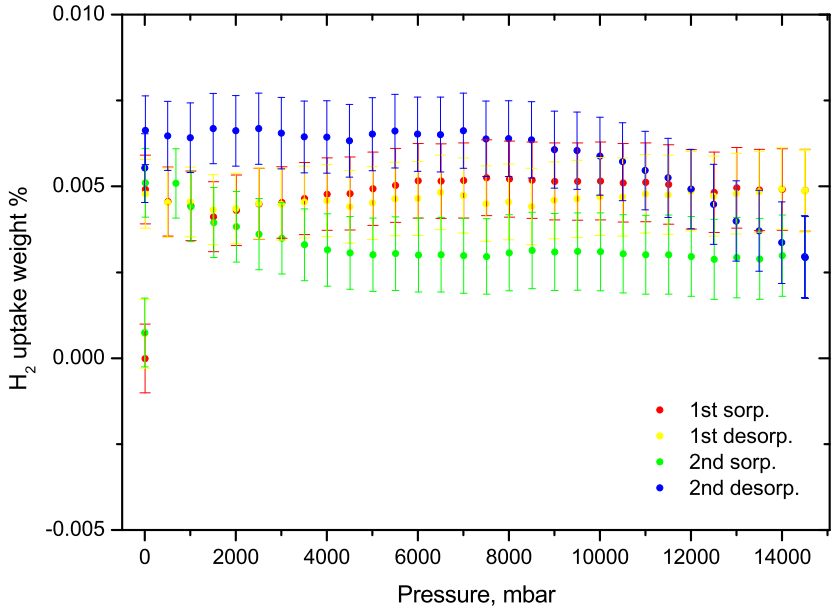

Figure 6.17: Corrected weight uptake for two room temperature adsorption/desorption isotherms of H_2 in stainless steel

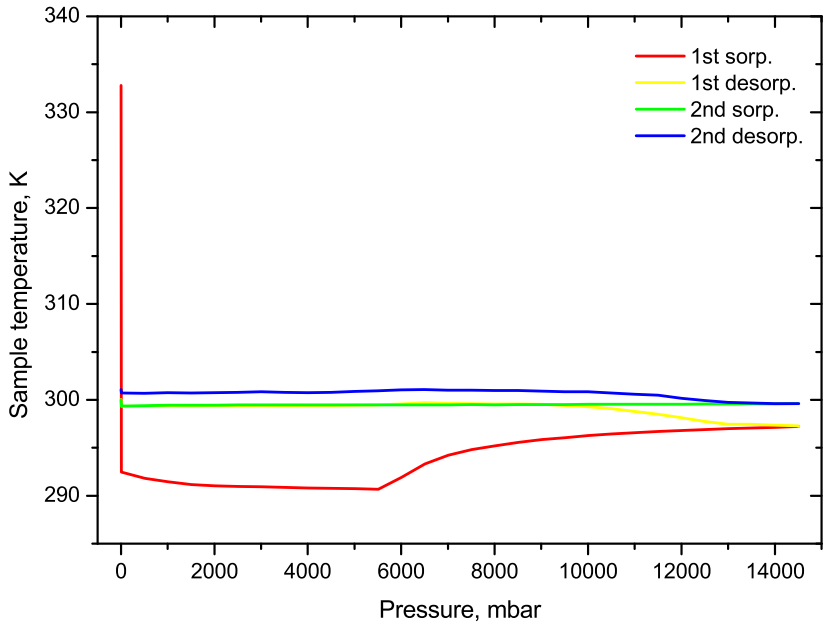

Figure 6.18: Sample temperature for two room temperature adsorption/desorption isotherms of H_2 in stainless steel

The amount of adsorbed hydrogen is very small - between 0.002 and 0.007 wt. % for all non-vacuum readings. Though there is variation in the uptake characteristics, they can be seen not to show any collective trend of increase or decrease in sample uptake with pressure. The second sorption curve appears to lose mass initially and the second desorption curve to gain mass as the pressure falls. It can also be noted once again that the first reading of the first sorption run, taken under vacuum, was not taken in a stable temperature region.

After the room temperature data were acquired, another outgas was performed, during which the sample base weight decreased to 319.4182 mg. The reason for this is not clear. 3 complete isotherm cycles were measured at liquid nitrogen temperatures, and a fourth that only collected four points on the desorption run. Of these, four had sample temperatures sufficiently stable for selection: the first and the third isotherms. The corrected weight uptake using

319.4182 as a dry mass is shown in Fig. 6.19 and the sample temperature in Fig. 6.20.

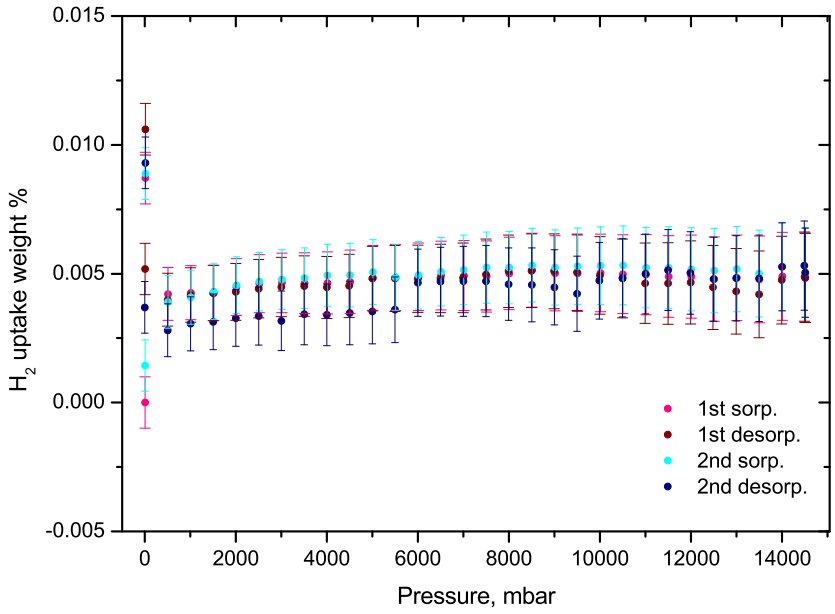

Figure 6.19: Corrected weight uptake for two 77 K adsorption/desorption isotherms of H_2 in stainless steel

It can be seen that a very similar level of uptake to the room temperature runs is observed, with all the runs at greater than the lowest pressures showing uptake in a band between 0.0025 and 0.0050 wt.%. Some sort of 'bounce' characteristic when the first gas is added results in isolated low pressure points for both sorption runs and the second desorption run at c. 0.010 wt.%, which are unlikely to be real. In the case of the second desorption run this may be a result of the rising sample temperature (off the second graph at 155 K). The two important properties of the uptake are that it is very small, and generally flat-lined. A comparison with even the lowest-sorbing graphite-based sample shows that the weight uptake is minimal. As stainless steel is not porous to hydrogen at pressures such as the IGA sustains, this is the predicted result. Such variance from a flat line of zero uptake as exists may suggest a magnitude for instrumental error, but other evidence implies it is bigger than the offset

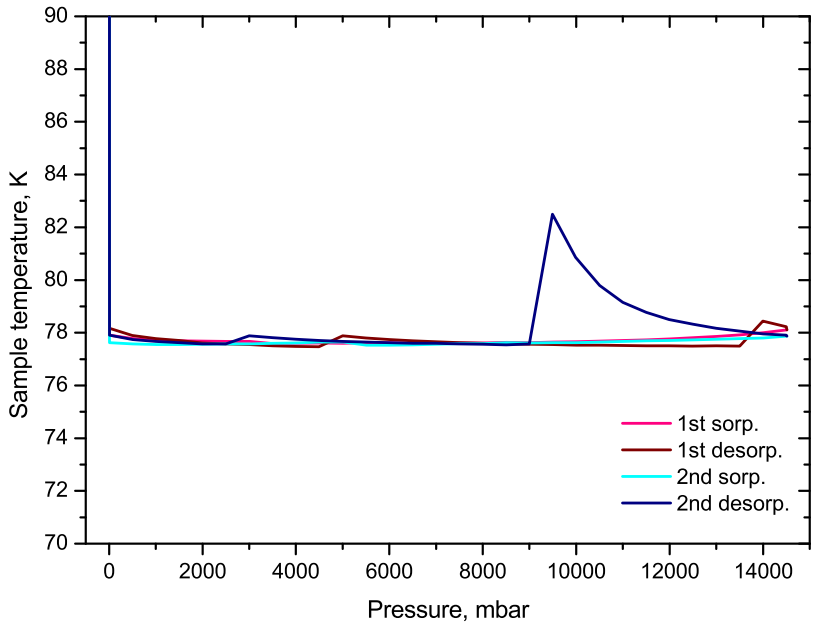

Figure 6.20: Sample temperature for two 77 K adsorption/desorption isotherms of H_2 in stainless steel

from zero uptake here (∼0.005 wt.%).

6.7 Ammoniated Ca-graphite

Three samples of calcium graphite synthesised using the liquid ammonia route were investigated to begin with. The stoichiometry was not known exactly although the target had been CaC_6. This work was carried out as part of an MSci masters project by Steven Leake and a preliminary report of the results was made in [58]. Table 5.2 shows the complete list of samples made using this route.

The first two samples for this section were loaded with an accidental offset in the weight registered on the IGA of -200.1296 mg. As the 'real' weight of the sample was measured in the loading window at the same time as the weight

including the erroneous offset, a correction factor could be applied to all the weights thus measured; obviously the weight *difference* would not be affected. However, inaccurate weight measurements severely affect the buoyancy correction routine. As the weights could not be corrected inside the IGASWIN software, it was necessary to construct a buoyancy correction table outside the program, which allowed investigations into the sensitivity of the buoyancy correction to, for example, the assumed density of the sample, later extended to all the IGA data.

6.7.1 Ca-GIC sample 1

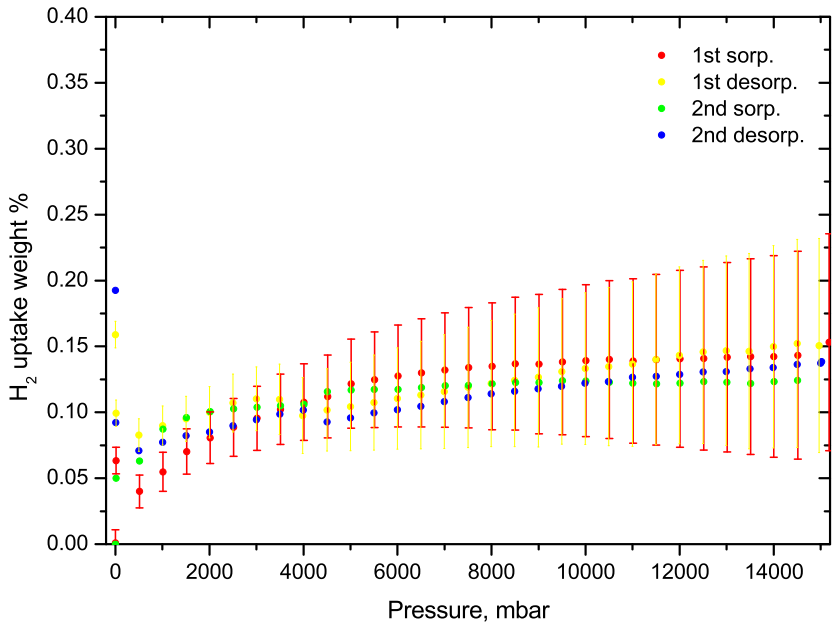

Figure 6.21: Corrected weight uptake for first two 77 K adsorption/desorption isotherms of H_2 in ammoniated CaC_6 sample 1. Error bars are not shown for the second isotherm for clarity

This sample had an outgassed weight of 39.106 mg. As it was a powder, it was loaded into the IGA in a pyrex bulb rather than the steel mesh cone, which had a greater contribution to the buoyancy correction. This bulb was

retained for all following samples. The 77 K isotherms are shown in Fig. 6.21. The maximum uptake is approximately 0.14 wt.%. within proportionally large errors. The room temperature isotherms are shown in Fig. 6.22. They show a very small linear sorption effect in the sample, up to 0.05 wt.% within the error bounds and an experimental offset.

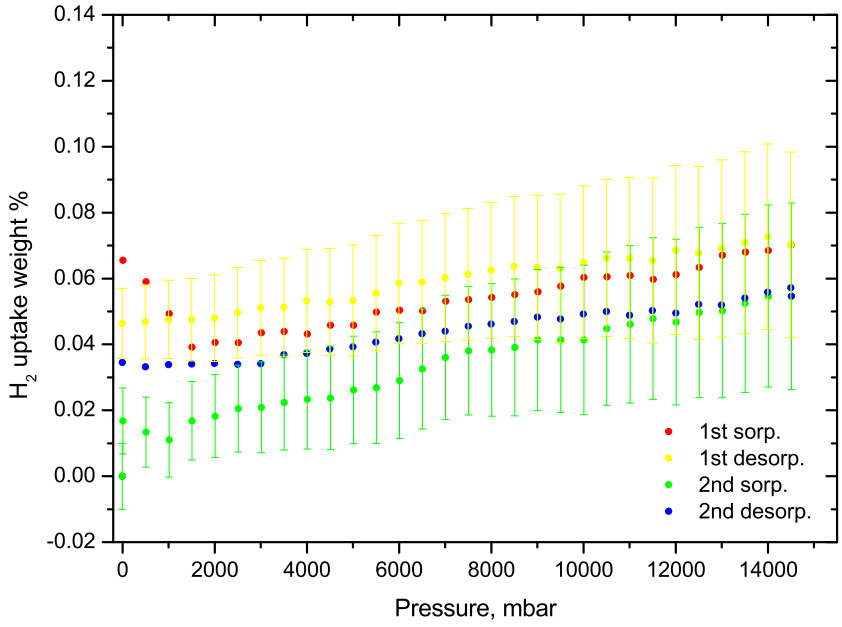

Figure 6.22: Corrected weight uptake for two room temperature (295 K) adsorption/desorption isotherms of H_2 in ammoniated CaC_6 sample 1. Error bars are not shown for two runs for clarity

There was no precedent for hydrogen uptake in this sample, and as the first intercalation made with a divalent metal, the hydrogen sorption was liable to provide a good indication of whether it would be suitable for consideration as a storage medium. On this basis it appeared to be a poor adsorber, comparable to Papyex at this temperature.

6.7.2 Ca-GIC sample 2

A second sample was taken from a different condensation batch. It had been outgassed after synthesis, and on loading into the IGA was outgassed some more, at 403 K for 2 days, to drive out as much NH_3 as possible. The outgassed weight was 104.698 mg. An isotherm was completed at 77 K, with uptake similar to the first sample, following which the sample was outgassed at 405 K for 2 days. A second isotherm was completed and showed an entirely different, and promisingly larger, uptake. Following this and another outgas for three days at 405 K, a third isotherm was completed, showing very similar results to the second. These first three isotherms are reproduced in Fig. 6.23. As can be seen, the second and third plots show an uptake of >3 wt.%. This is the most significant result from the thermogravimetric investigation, hinting as it does that a storage capacity in excess of any binary GICs exists in this ammoniated divalent-ion GIC. It is not clear why the first isotherm, carried out under identical circumstances, shows a different uptake characteristic. Perhaps the combination of the outgas with the remaining hydrogen reconfigured the sample to improve the sorption prior to the second isotherm. Of interest equally is the unexpected desorption characteristic; the hydrogen appears to desorb more rapidly as the pressure is reduced, indicating that the binding is weak. There was a large wait between each sorption and desorption run where the pressure remained at its maximum value. The sample temperature records are in Fig. 6.24 but show nothing unusual.

Following these results, it was decided to continue with room temperature isotherms, before returning to 77 K to see how the uptake might have changed. First, the sample was outgassed at 415 K for 24 hours. Three 295 K isotherms were carried out as a batch, followed by one more 77 K isotherm. These are plotted in Fig. 6.25. The room temperature plots show an offset of 0.4

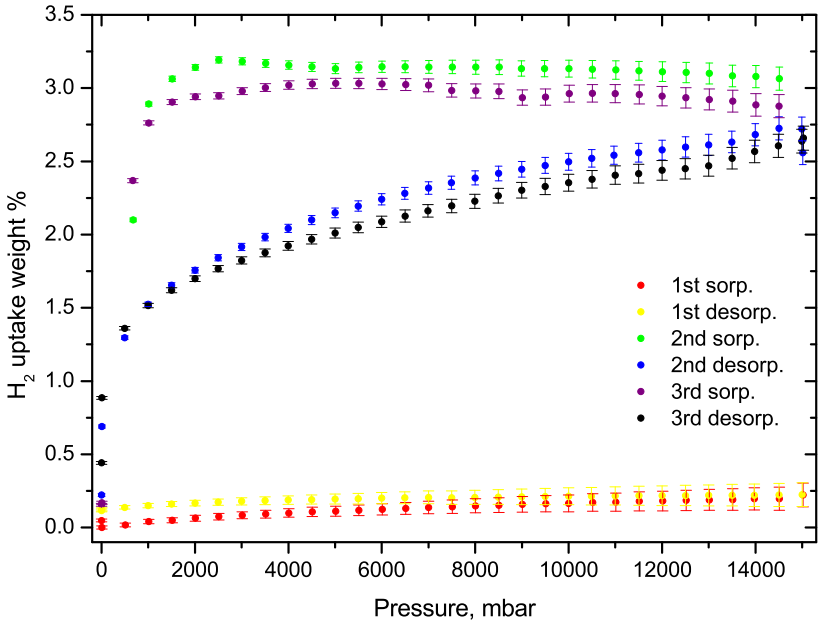

Figure 6.23: Corrected weight uptake for first three 77 K adsorption/desorption isotherms of H_2 in ammoniated CaC_6 sample 2

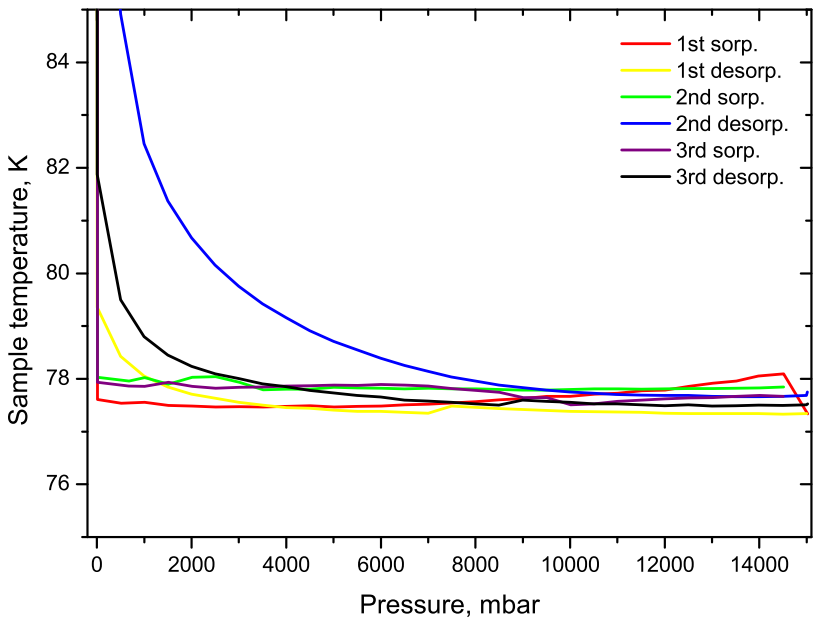

Figure 6.24: Sample temperature for first three 77 K adsorption/desorption isotherms of H_2 in ammoniated CaC_6 sample 2

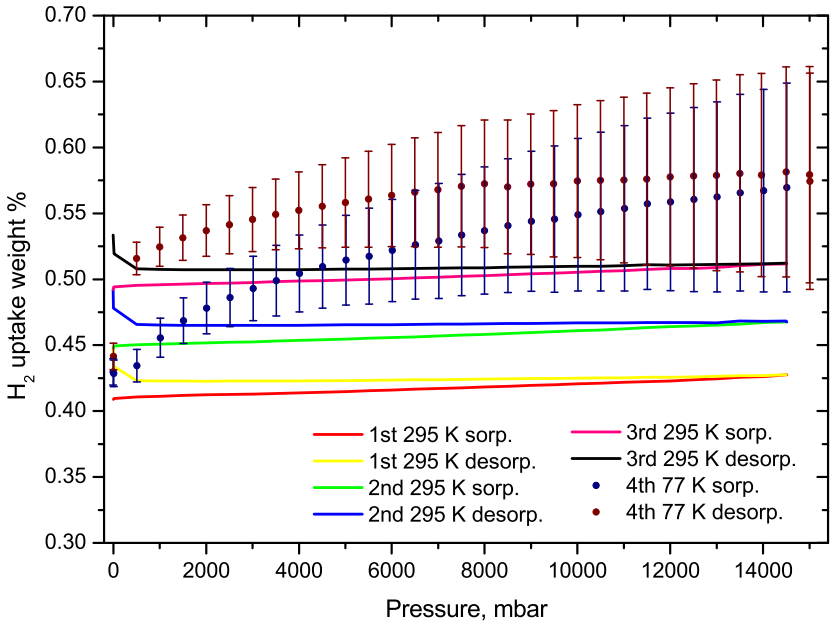

Figure 6.25: Corrected weight uptake for three 295 K isotherms, followed by one 77 K isotherm, of H_2 in ammoniated CaC_6 sample 2

Table 6.4: Langmuir fits to ammoniated Ca-GIC sample 2 77 K isotherm runs 2-3. n = saturated uptake, d = Langmuir equilibrium constant, m = gradient of linear uptake contribution.

Run	n wt.%	d	m wt.%/mbar
2nd sorp.	3.25±0.06	0.0073	8×10^{-6}
2nd desorp.	2.01±0.11	0.03	0
3rd sorp.	3.29±0.04	0.0046	-3×10^{-5}
3rd desorp.	1.59±0.05	0.097	7×10^{-5}

wt.% and irreversible uptake. The 77 K isotherm shows an offset uptake of 0.15±0.01 wt.%, comparable to the first 77 K isotherm for this sample and the 77 K isotherms for ammoniated Ca-GIC sample 1. Some part of the intervening room temperature measurements 'turned off' the remarkable 3.2 wt.% sorption. It is possible that chemisorption is occurring at 295 K, as suggested by the irreversible gain in weight over these three isotherms, which were not separated by heated outgas periods. It was suspected that a H_2-driven structural change might be occurring in the manner of the KC_8H_x system, which led to a neutron diffraction experiment on CaC_6H_x (§ 7.4).

6.7.3 Ca-GIC sample 3

This sample was taken from the same batch as the previous one. It was outgassed at 418 K for 33 hours and at 475 K for a further 20 hours. The outgassed weight was 103.680 mg. Three isotherms at 77 K were taken, with outgassing between each one for 48 hours at 415 K. The maximum uptake was 0.37±0.02 wt.%, and the average was 0.28±0.02 wt.%. Some irreversible uptake occurred, but these results were very similar to those for ammoniated Ca-GIC sample 1 and did not show the noteworthy sorption of sample 2.

6.7.4 Ca-GIC sample 4

This sample was made using a lower Ca ratio of 1:12 (see Table 5.2). It was intended to produce a more dilutely-pillared compound to try and improve the sorption uptake beyond that of the second sample. The ammonia was thought to remove some of the Ca from the CaC_6 stoichiometry while synthesising the earlier samples, because there would be no space for ammonia in a pure CaC_6 crystal. This was intended to provide that dilute stoichiometry, which might

in practice be as low as CaC_{24}.

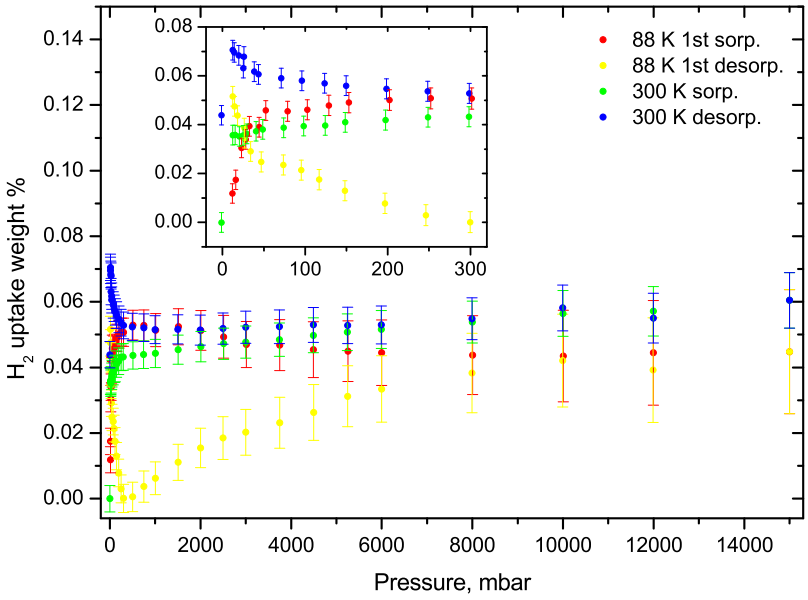

Figure 6.26: Corrected weight uptake for 88 K and 300 K adsorption/desorption isotherms of H_2 in ammoniated Ca-GIC, sample 4

Altogether six isotherms were collected; three at 88 K, and one each at 150, 220 and 300 K. The initial dry weight was 47.5634 but this had to be adjusted by isotherm as drift occurred between each one. The sample appeared to lose weight between the first and second 88 K isotherms. At low pressures some anomalies were seen, particularly in the desorption stages. An example is shown in the graph, Fig. 6.26, which shows one the first 88 K and the 300 K isotherms. The other temperature isotherms were omitted as they showed no uptake in excess of that shown. Both desorption curves appear to gain weight below 300 mbar as illustrated by the inset. Examination of the temperature record, shown in Fig. 6.27, shows the temperatures to become unstable at low pressures, due to the difficulty of cooling the sample when there is little gas to effect thermal exchange, as noted before. It is not certain why this should have this counter-physical effect on the sample weight. This and the unavoidable drift in the IGA base weight measured call the reliability

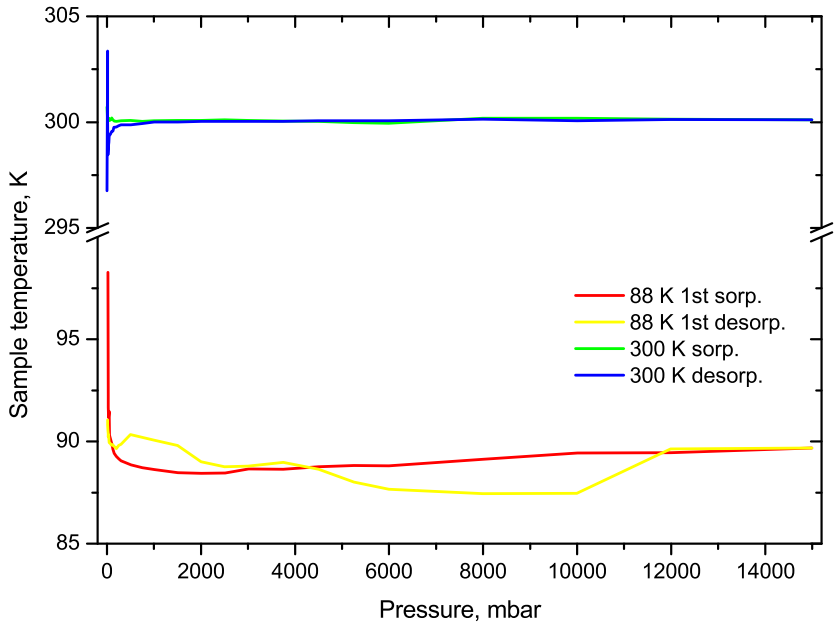

Figure 6.27: Sample temperature for 88 K and 300 K adsorption/desorption isotherms of H_2 in ammoniated Ca-GIC, sample 4

of the results into question. Furthermore, the hydrogen sorption recorded is at maximum 0.055±0.008 wt.%, and the uptake magnitude is comparable across the isotherms, irrespective of temperature. This is lower than the equivalent uptake in Ca-GIC samples 1 and 3, not to mention 2! There are many question marks over these data which the experiments were unable to resolve. As a priority, reproducing the 3.2 wt.% results should be addressed, by synthesising another sample using the same parameters. It may seem perverse that the fourth sample used half the starting ratio of calcium, but sample 3 had attempted to reproduce the notable physisorption using a sample from the same batch as sample 2, without success. The key to optimising the raw sample for storage appears to lie in outgassing it after exposure to hydrogen. It is thought that the ammoniated calcium sample must needs be less concentrated in calcium than CaC_6 and so this excess was not required, but this does not have to be the case.

6.8 CaC_6 from Li alloy synthesis

The neutron diffraction experiment carried out on H_2 in alloy-synthesised CaC_6 had not seen any hydrogen uptake at all, at any temperature from 1.5 K up to 320 K (§ 7.4). Corroborating evidence was acquired by IGA measurements on one sample, at 77, 295 and 473 K. These data are shown in Fig. 6.28.

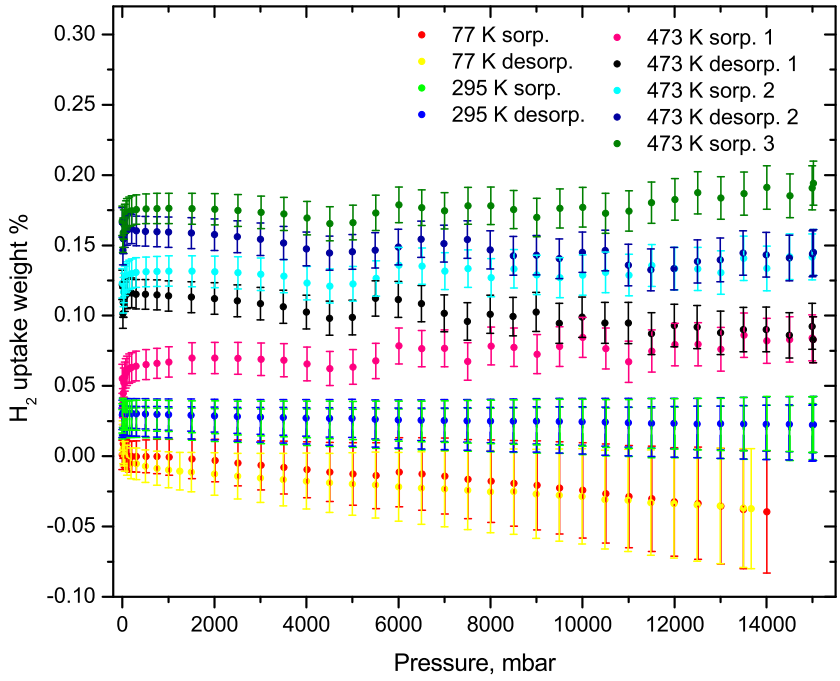

Figure 6.28: Corrected weight uptake for isotherms at 77, 295 and 473 K, of H_2 in CaC_6 made using Li-Ca alloy

The sample was outgassed for 48 hours at 415 K. The sample dry weight was 95.8089 mg. Three 77 K isotherms were completed with outgassing at 440 K between each. This temperature was much lower than the synthesis temperature so no decomposition was expected. Only one 77 K isotherm is shown on the graph, for clarity. They showed no uptake (the negative gradient of the graph is likely to be a density error).

One 295 K isotherm out of three is shown in the graph, again for clarity.

There is a slight offset of ∼0.03 wt.% symptomatic of irreversible uptake so perhaps a slow hydride reaction takes place; however, there appears to be no fast uptake. Only for the 473 K isotherm does an apparent irreversible sorption occur, over three cycles. If this is evidence for a phase transition, it takes place at temperatures higher than were available on the neutron experiment. The total uptake registered over the three runs is 0.14±0.03 wt.%, which equates to a compound $CaC_6H_{0.15}$. This is probably too small an amount to be capable of driving a structural change, though it may not be the saturation value. In conclusion, the purer CaC_6 available by the Li-alloy synthesis route appears less capable of sorption than the ammoniated Ca-GIC equivalent. This is self-consistently attributable to the lack of available volume in the CaC_6 structure to host H_2 molecules.

Chapter 7

Neutron diffraction results

7.1 Data analysis and refinement

Three diffraction measurements were carried out on Polaris as detailed in § 5.3. The diffraction data were analysed where possible using Rietveld methods [96]. Data fitting was performed in these cases using the GSAS package [94], incorporating the EXPGUI interface [95]. The optimum fitting was performed on data from the 45° *c*-axis sample orientation from neutrons scattered into the 90° detector banks, which were decoupled so that left and right banks summed independently. As explained in § 5.3.1, with this configuration, the scattering vector **Q** for these banks lay parallel to the *c*-axis on the right side of the instrument, as seen facing the neutron source; hence within the variation given by the mosaic spread of the graphite, all the scattering was out-of-plane in the right-side 90° detectors. On the left side **Q** lay perpendicular to the *c*-axis, hence there was predominantly in-plane scattering recorded in the left side 90° detectors. Separate fits were made for the in-plane and out-of-plane scattering. Preferred-orientation analysis was carried out by refining the data to a March-

Dollase function [97] within EXPGUI. Background measurements run on an identical sample cell setup showed a quasi-continuum of scattering without Bragg peaks, due to the null-coherent-scattering Ti-Zr cell and Cd shielding. This allowed the background to be fitted to an n-variable Chebyschev polynomial function and subtracted within the fit. Where fitting was not used, the collected empty cell scattering data was scaled to fit and then subtracted.

The GSAS fits were not able to be refined to a high degree of accuracy, because of uncertainties in the potential in-plane structure. In particular, the peak broadening and intensities do not refine well, possibly because of strain broadening and crystallite size in the Papyex base material, although a measure of confidence exists for the c-axis unit cell parameters because the out-of-plane structures are well known. The uncertainty on these values is greater than the number of significant figures quoted by GSAS because of the poverty of the fits. In this chapter fitted lattice parameters are quoted with an implicit uncertainty of ± 0.01 Å which is similar to the uncertainty associated with estimating the peak positions by eye from the graphs. The issues with the fits necessitated a more manual approach to the analysis, indexing the peaks, again in the c-direction primarily. The in-plane structure appears difficult to obtain from the diffraction, as evidenced by the literature [41] [78].

7.2 H_2 and ND_3 in KC_{24}

Time-resolved diffraction data for D_2 adsorbing into KC_{24} were obtained on Polaris. First, data were collected on the undosed KC_{24} sample at 80 K with the sample oriented at 45° to the beam so that $\mathbf{Q}$ was oriented along the sample in-plane direction in the left-hand 90° detector bank, and along the sample c-axis on the right-hand 90° bank. The results were fitted using GSAS. Two

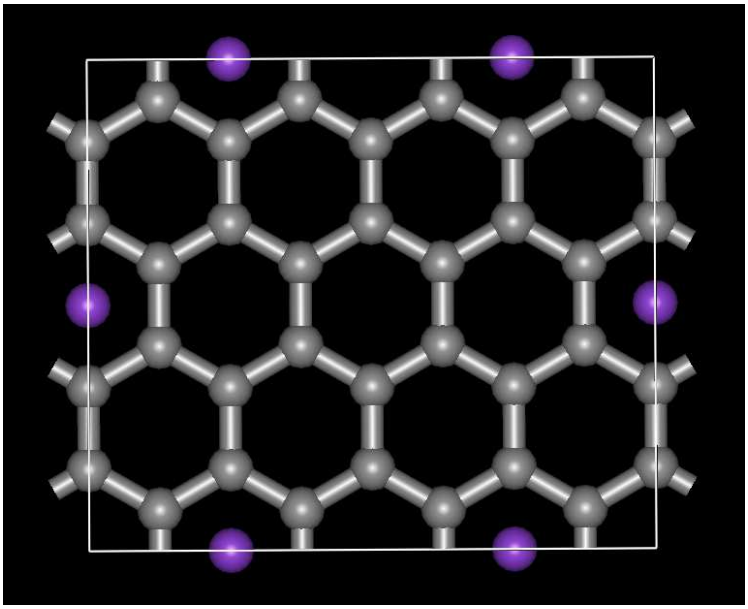

Figure 7.1: Proposed in-plane potassium (purple) structure for KC_{24} [67]. The effective stoichiometry is $KC_{21.33}$ and the unit cell parameters are $a = 9.84$ Å, $b = 8.52$ Å, $c = 8.70$ Å.

potential structures were fitted independently. Both were potential component phases of a KC_{24} multiphase structure. These two were KC_{28}, a stage-2 structure where the potassium in the filled layers is distributed in a $\sqrt{7}\times\sqrt{7}R(19.1°)$ superlattice as detailed in § 3.3.3, and KC_{16}, a stage-2 analogue of KC_8 with the same $(2 \times 2)R(0°)$ K lattice but only half the layers filled. It was reasonably supposed that they would give very similar *c*-axis structures as the interlayer spacings are identical. There was an attempt to build a "KC_{24} stoichiometry" structure, the one of symmetry *Pmmm* presented by Rüdorff and Schultze [67](Fig. 7.1) but fitting was not successful, perhaps because of the large number of atoms (12) in the primitive unit cell taking into account the symmetry. In fact the (conventional) unit cell illustrated contains K_3C_{64} making the effective compound $KC_{21.33}$.

All the structures fitted were of AAA graphite stacking, because to add an *c*-axis stacking sequence reduces the symmetry thus increasing the size of the

unit cell, and hence increases the difficulty of fitting. The KC_{28} proposed unit cell is described by the crystal space group *P6/m* and contains four atoms. The KC_{16} proposed unit cell is *P6/mmm* and contains three atoms. The structures were fitted by refining the unit cell parameters, the preferred orientation and a peak profile function

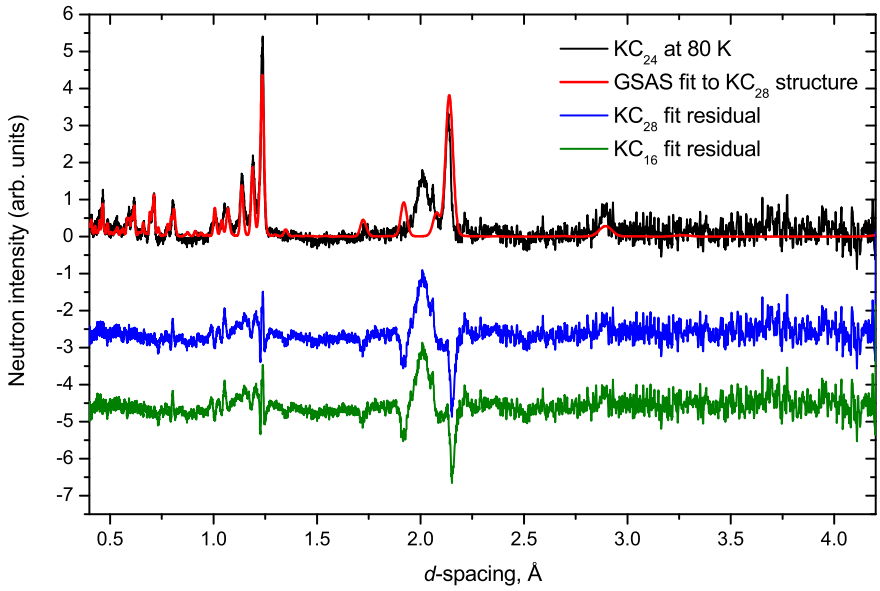

Figure 7.2: Diffraction pattern showing the in-plane scattering of KC_{24} at 80 K. The background was fitted to a 12-term Chebyschev function and subtracted in GSAS. The GSAS fit to a KC_{28} structure is shown, with its residual pattern and another from a KC_{16} structure fit, which was omitted because it was so similar to the first fit.

The in-plane diffraction of KC_{24} at 80 K is shown in Fig. 7.2 and the out-of-plane diffraction in Fig. 7.3; each together with the fit to the KC_{28} structure and the fit difference (residuals) from this and the KC_{16} structure fit are shown offset by constant values below $y = 0$. The KC_{16} fit was not added to the data set because, as the residuals suggest, it almost entirely overlaid the KC_{28} fit for both patterns. The implications of this are profound because they imply that the trial structures are indistinguishable in terms of the expected scattering, even though the in-plane K lattices are different. A look at both structures confirms that the K superlattice is overlaid by a graphite repeat distance in

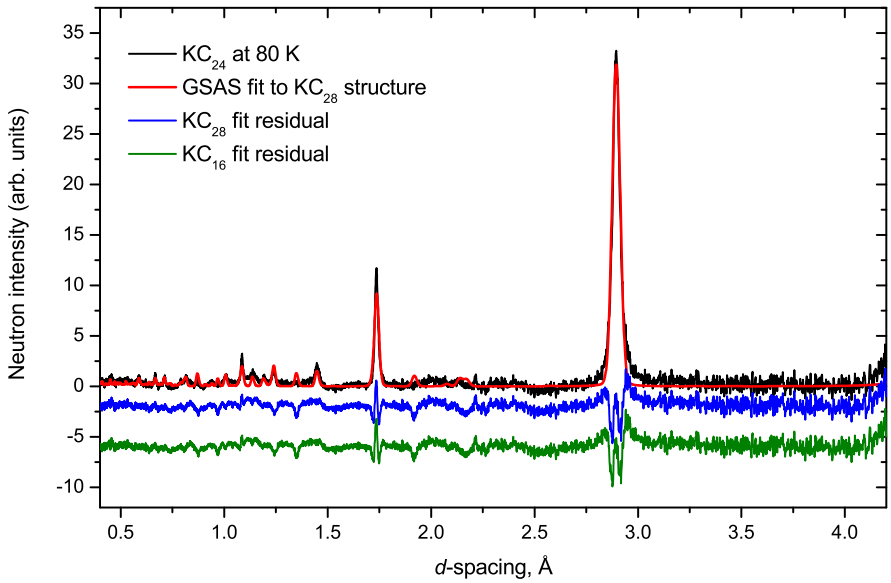

Figure 7.3: Diffraction pattern showing the c-axis scattering of KC_{24} at 80 K. The background was fitted to a 12-term Chebyschev function and subtracted in GSAS. The GSAS fit to a KC_{28} structure is shown, with its residual pattern and another from a KC_{16} structure fit, which was omitted because it was so similar to the first fit.

Table 7.1: Selected fit parameters from 80 K KC_{24} diffraction data GSAS fits. a, b and c are lattice parameters. ρ is the calculated sample density (cf. 2.00±0.05 g/cc by pycnometry from Table 6.1)

Structure	KC_{28}	KC_{16}
Space group	$P6/m$	$P6/mmm$
Fit χ^2	3.379	3.343
a,b (±0.01 Å)	6.54	4.93
c (±0.01 Å)	8.67	8.67
ρ (±0.01 g/cc)	1.95	2.10

each case, so graphite and potassium in-plane peaks are superposed. The $\sqrt{7} \times \sqrt{7}R(19.1°)$ and $(2 \times 2)R(0°)$ superlattice d-spacings do not overlap directly and so the K reflections would contribute to different peaks in the in-plane pattern for each structure, but there is little evidence of this.

The above being the case, there is a high probability that the 'true' in-plane structure, were it to be known, would fit in a very similar way. This is interesting: if the K-ion distribution is disordered in the sample at low temperature, as is the case above T_{cu} (see § 3.3.1), then no Bragg peaks resulting from K-K interference would be seen in the pattern. But the simpler seed structures for the refinement have an ordered K lattice and yet there is scant difference between them to denote their heterogenous intercalant structure, even in the fitted peak intensities. It is difficult to draw firm conclusions as the peak profile did not fit well, but it does imply that the in-plane K structure is not being recognised in the fit, or that it is cancelled out. The results of the fits are shown in Table 7.1. The c-axis spacing of 8.67 Å implies a good out-of-plane scattering fit as it is close to the literature value of 8.7 Å and agreed by both fits. This is seen in the data, although the fitted intensities and peak shapes do not match the data set. The (003) peak at 2.89 Å in Fig. 7.3 is as expected. The in-plane peaks that are fitted are identical for each structure (and they remain rigid on hydrogenation when this is performed later) suggesting they are a result of the graphite in-plane structure rather than potassium. In short, it is unlikely to be possible to use the fits except to extract the already well-established c-axis structure. Yet in terms of the number of peaks viewed and expected in the refinement, there is a good correlation. There is a peak in the in-plane scattering at 2.05 Å which is not fitted by either structure. The in-plane peaks are indexed to the KC_{28} structure in Table 7.2.

The dosing took place in two stages: deuterium intended to obtain stoichiometry $KC_{24}(D_2)_1$ was allowed into the sample cell at a sample orientation

Table 7.2: Selected KC_{28} peak (hkl) index assignments from GSAS REFLIST using fit in Table 7.1

in-plane		*c*-axis	
d-spacing Å	index (hkl)	*d*-spacing Å	index (hkl)
2.89	(003)	2.89	(003)
2.14	(120)	1.73	(005)
”	(210)	1.45	(006)
1.24	(410)	1.24	(007)
1.19	(412)	1.20	(126)
1.14	(413)	1.14	(413)
1.07	(240)	1.09	(008)
0.71	(360)	1.00	(415)

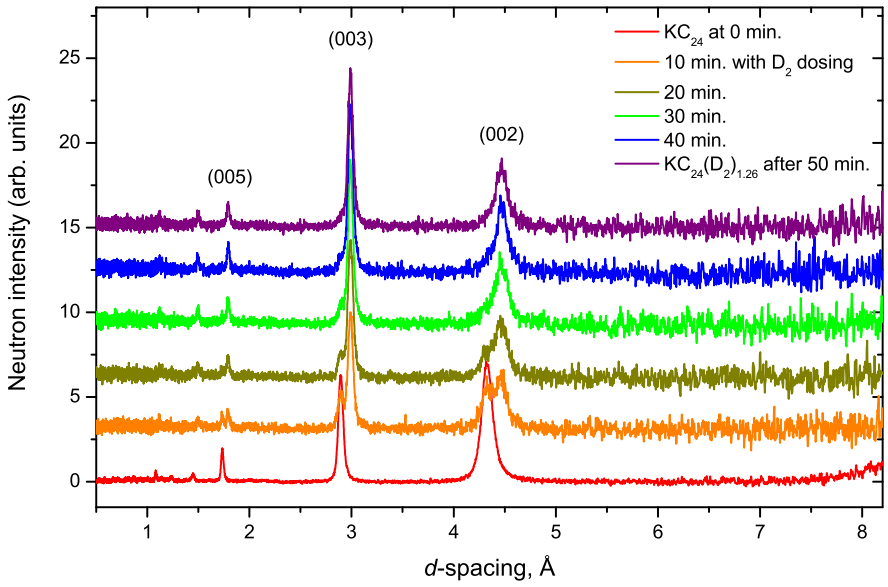

Figure 7.4: Time-resolved diffraction patterns of KC_{24} sample at 50 K showing *c*-axis expansion through D_2 adsorption (offset for clarity). The time resolution is 10 minutes.

of 90°, and allowed to equilibrate while repeated 30 μAh runs were collected, each lasting approximately 10 minutes, depending on the proton beam current (hence, the neutron flux). The *c*-axis diffraction was available in the low angle scattering banks, so Fig. 7.4 shows the expansion of the graphite layers with the ingress of the D_2 in this first dosing. This was followed by data acquisition at 20 and 2 K before the sample was rotated to a 45° angle. An empty can run at both angles of interest was performed at the end of the experiment and used to subtract background from the results.

Due to uncertainties in the volumetric measurement of the D_2 amount, there was a slight overdosing: the real value of the sorbed deuterium was $1.26\pm0.07(D_2)_1$. If we assume a single layer unit cell, with *c*-parameter a combination of the unfilled and filled layer spacing, 3.35 + 5.35 Å, the two largest peaks are the (003) at 2.89 Å and (002) at 4.33 Å in KC_{24}. The sample appears well-staged, with no sign of KC_8 peaks. As deuterium is put on, the KC_{24} peaks diminish and hydrogenated peaks appear and increase at a slightly expanded *d*-spacing. By the time the full amount of D_2 is present, the original peaks are less than a faint shoulder on the new ones. The *c*-axis repeat distance increases (apparently by way of D_2-filled domain structures) from 8.66±0.03 Å to 8.94±0.03 Å. If one accepts that the empty gallery in the KC_{24} unit does not change spacing significantly, then the results can be quantified by a change in the filled layer spacing from 5.35 to 5.63 Å. This is consistent with the literature, for less than the reported saturation value of $(D_2)_2$. The interlayer spacing was found to be 5.69 Å for $(H_2)_2$ [42]; D_2 enters the GIC more readily and for a concentration of $KC_{24}(D_2)_x$ for $x = 1.25$, a 0.29 Å increase in the lattice parameter is expected. The experimental result is 0.28±0.03 Å.

With the sample orientation at 45°, data were collected at 50 K. The results are shown in Fig. 7.5 and Fig. 7.6. The data were again fitted to a KC_{28}

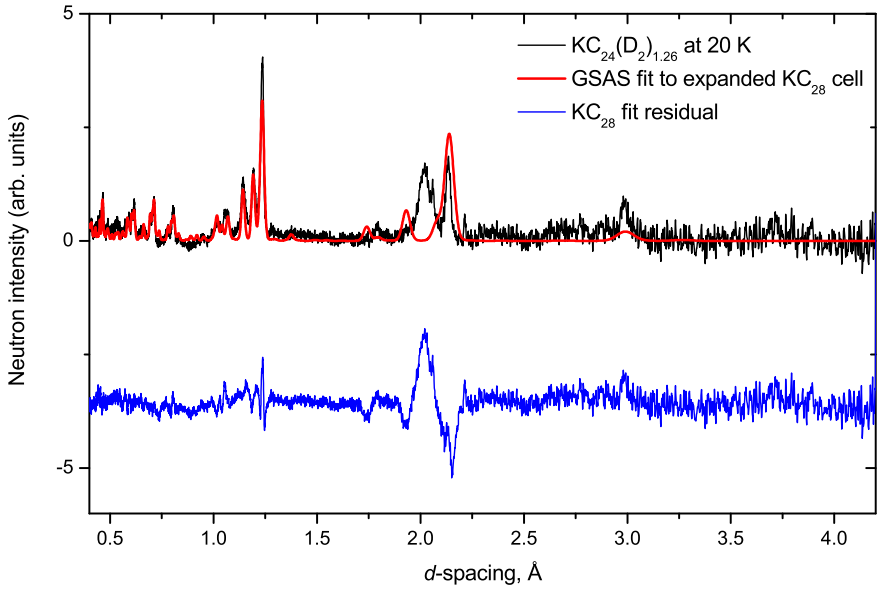

Figure 7.5: Diffraction pattern showing in-plane scattering of $KC_{24}(D_2)_{1.26}$ sample at 50 K.

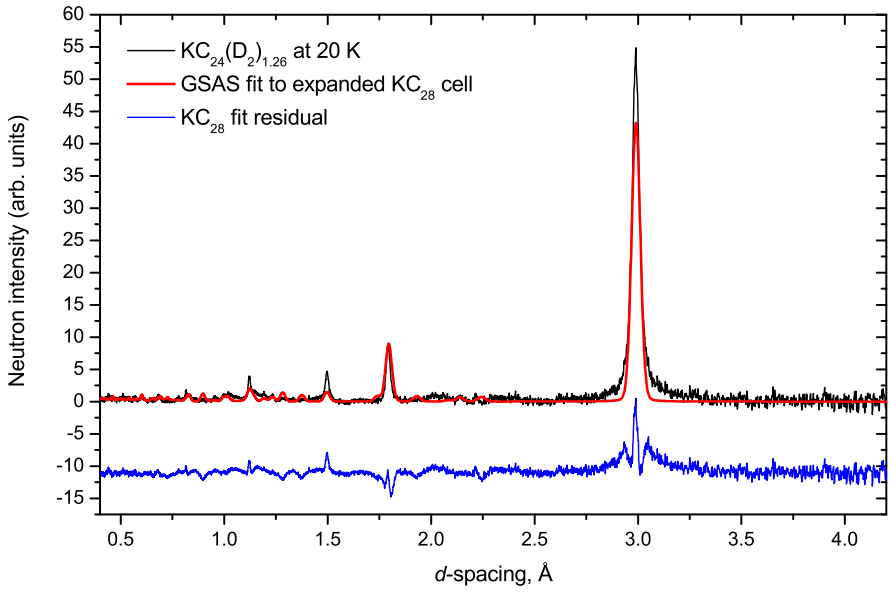

Figure 7.6: Diffraction pattern showing c-axis scattering of $KC_{24}(D_2)_{1.26}$ sample at 50 K. The fit begins to converge for $c = 8.96$ Å, showing that the deuterium has driven an expansion of the graphite.

structure with the intention of at least finding the c-axis expansion under the intercalation of D_2. Compounds containing dihydrogen were not of low enough symmetry to fit. It can be seen that the peak shape and intensity fittings are rudimentary despite relaxation of the peak profile parameters. The unit cell refinement extracts fitted cell parameters of $a = b = 6.53(\pm 0.01$ as noted in the § 7.1) Å and $c = 8.96$ Å. This is in keeping with prediction: all the H_2-driven expansion is seen in the c-direction, and the new c-parameter implies an expanded filled layer spacing of 5.61 Å, as compared to 5.63 Å determined above.

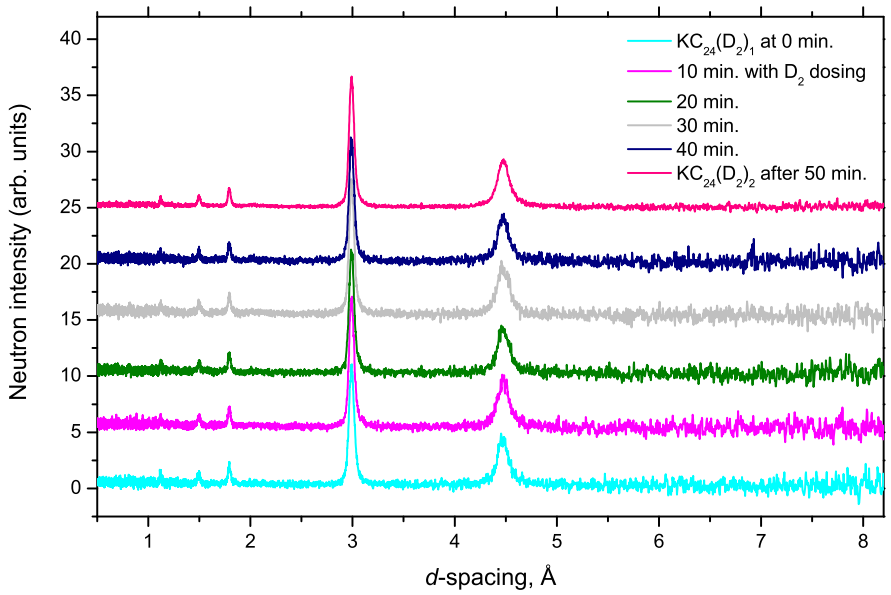

Figure 7.7: Time-resolved diffraction patterns of $KC_{24}(D_2)_{1.26}$ sample at 50 K showing further D_2 adsorption to a stoichiometry of KC_{24} $(D_2)_2$ (offset for clarity). The time resolution is 10 minutes.

A second amount of D_2 ($x = 1$) was then placed onto the sample and time-resolved data collected at a 90° sample orientation. The resulting sequence is shown in Fig. 7.7. There is no structural change visible; the (003) peak remains at 2.989±0.005 Å through all six patterns. Furthermore, the ratio of the (002) to (003) peaks remains broadly similar, with no variation of intensity resulting from extra D_2 in the layers. This suggests that the sample was

already saturated, or nearly so, and that $x = 1.26$ is close to the maximum uptake in the sample. This is a puzzle that may be attributable to sample characterisation, or potentially an error on the measured uptake. A later, more carefully characterised uptake of H_2 in KC_{24} observing the same (003) diffraction peak concluded that the unhydrogenated peak should still be visible at $x = 1$, but disappears somewhere between that concentration and $x = 2$ (§ 8.2, Fig. 8.5). This may well suggest that the hydrogen uptake in the first sequence was closer to saturation than was realised. A more accurate way of determining the dosage is required for future experiments; this entails using a gas handling rig with well-defined volumes and controlling the ambient temperature so true volumetric measurements can be made.

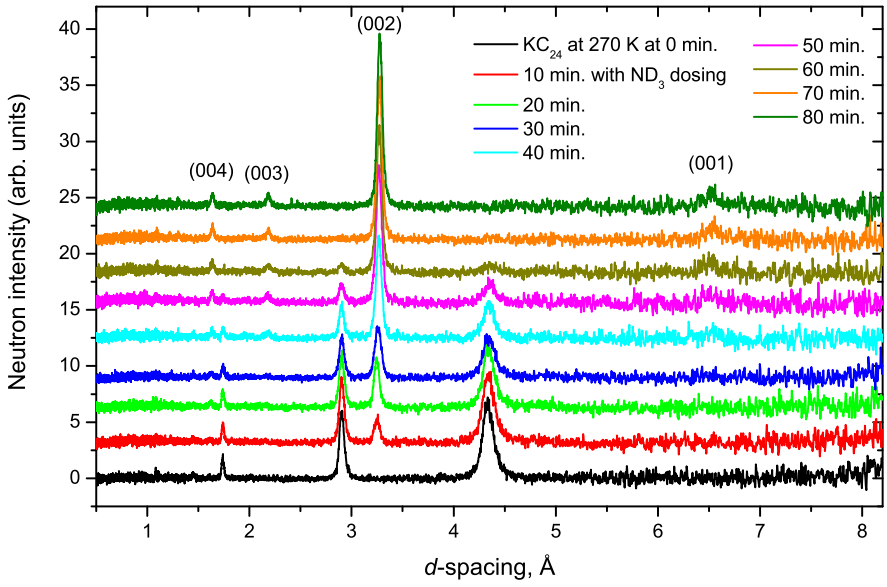

Figure 7.8: Time-resolved diffraction patterns of KC_{24} sample at 270 K on exposure to ND_3 gas. A transition to an ammoniated stage-1 compound with layer spacing 6.56±0.02 Åis visible (offset for clarity). The time resolution is 10 minutes.

Following this section, the deuterium was removed by pumping on the sample while warming it to ambient temperature. The original *d*-spacing returned, showing the reversibility of the physisorption. The next sequence (Fig. 7.8)

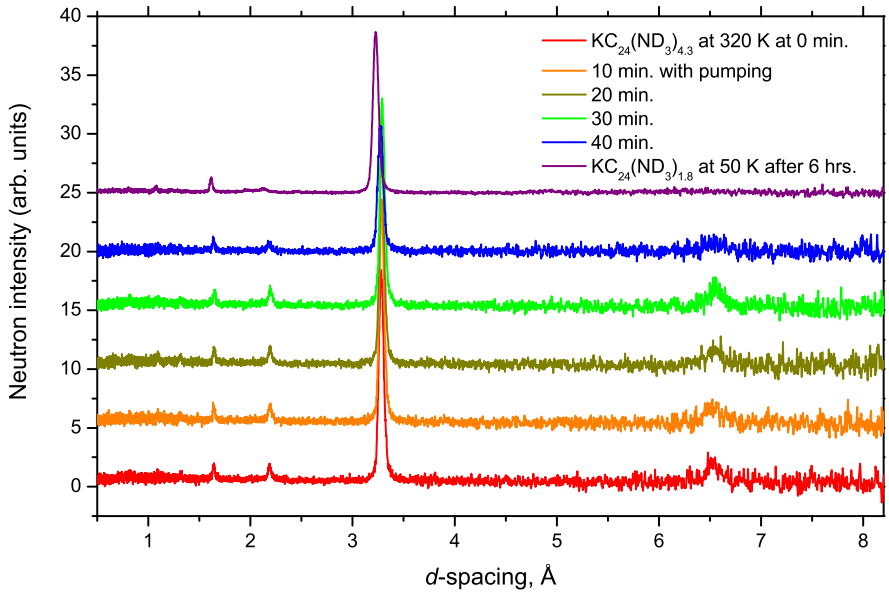

Figure 7.9: Time-resolved diffraction patterns of $KC_{24}(ND_3)_{4.3}$ sample at 320 K while ND_3 is removed by cryopumping and then direct pumping on the sample. The intensity of the (002) peak diminishes as ammonia is removed, but enough remains to pin the stage-1 structure (offset for clarity). The time resolution is 10 minutes.

shows the sample under gaseous anhydrous ND_3 at 270 K. Upon exposure, a stage-2 to stage-1 phase transition is observable. The ammoniated compound has c-lattice parameter 6.56±0.02 Å. After 80 minutes of exposure the original structure has disappeared from the pattern. The (001) peak of the new phase is weak, but the (002), (003) and (004) peaks are visible. This phase represents an expanded stage-1 structure with dilute metal concentration, each ion being surrounded by ammonia molecules. Following a period of equilibration of 80 minutes at 320 K, the ammonia gas was removed by cryopumping into a liquid nitrogen-cooled buffer. The time-resolved sequence taken during this period is shown in Fig. 7.9. There is little change to the diffraction pattern until after 40 minutes have elapsed, and then the peaks diminish in intensity and the (002) peak begins to shift to lower d-spacing. This can be attributed to ND_3 being pulled out of the interlayer galleries which contract slightly. After cooling to 50 K, the (002) peak has shifted to 3.23±0.01 Å, implying a gallery

spacing of 6.46±0.01 Å, a 1.5 % shift in this value. While some of this may be a result of thermal contraction, it is a good indicator that significant amounts of ammonia have been removed. The residual ammonia concentration from literature [56] is $KC_{24}(ND_3)_{\sim 1.8}$. Data on this system were taken for a 45° sample orientation (Fig. 7.12 and Fig. 7.13)

The guiding hypothesis of this part of the experiment was that hydrogen might be taken up more readily in the dilute stage-1 K-ND_3-GIC sample resulting. To this end, D_2 was allowed onto the sample at 50 K. An overpressure of deuterium up to 6470 mbar was created. The time-resolved sequence showing this is in Fig. 7.10.

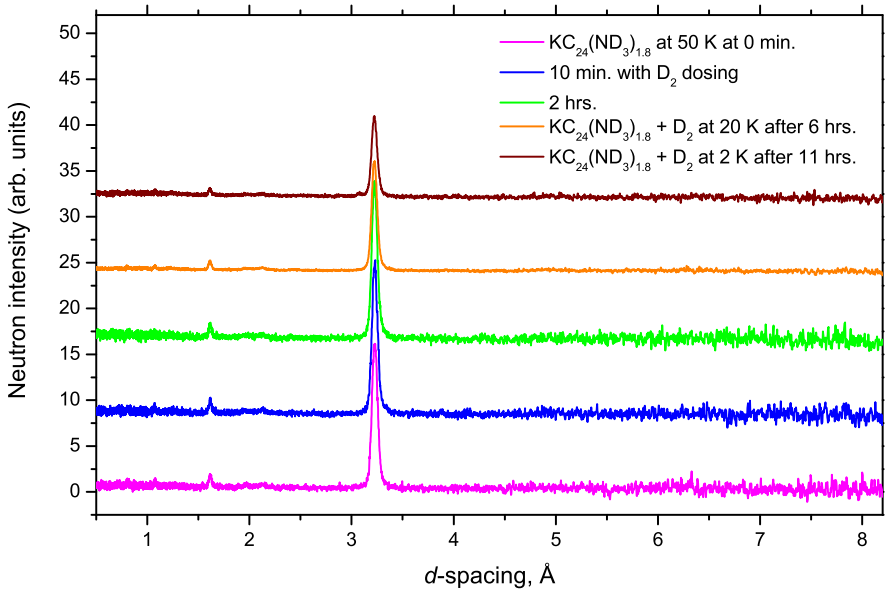

Figure 7.10: Time-resolved diffraction patterns of $KC_{24}(ND_3)_{1.8}$ sample at 50 K under D_2 to 6470 mbar pressure. As deuterium is forced onto the sample the diffraction peaks lose intensity, though do not change position. (Patterns offset for clarity).

Although no peaks change position, there is intensity change in the peaks as the deuterium goes in. The ratio of (002)/(004) intensities does not change significantly with dosing, implying no structural change, though as no (001) peak is visible it is not possible to conclude for certain. The valve to the gas

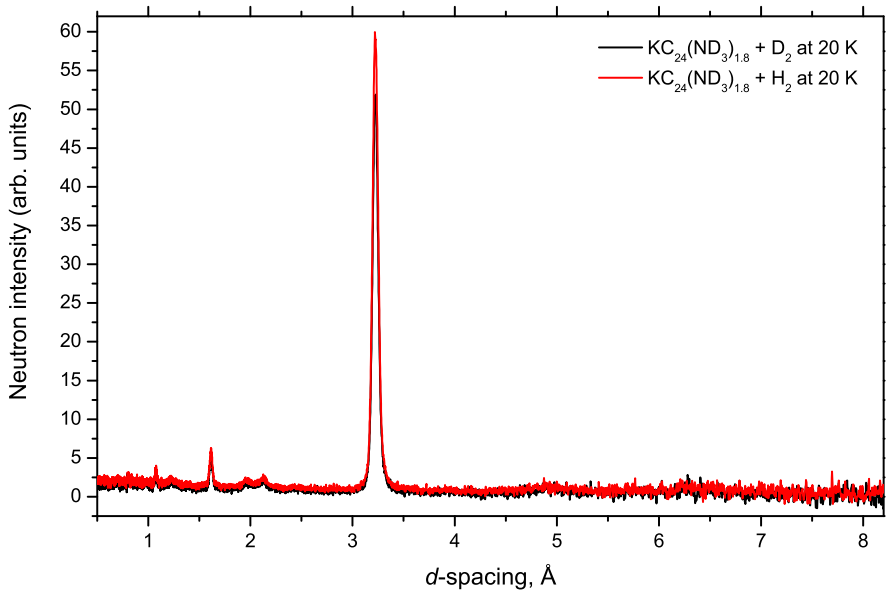

Figure 7.11: Comparison of $KC_{24}(ND_3)_{1.8}$ under D_2 and H_2 loading at 20 K and 6.5 bar. A higher incoherent background is visible on the hydrogen pattern (red)

reservoir was shut before the temperature was lowered so that all the D_2 did not condense into the cell. After cooling to 2 K after 11 hours, the (002) peak has moved from 3.227 to 3.223 Å, corresponding to a layer spacing contraction from 6.454±0.002 to 6.446±0.002 Å. This is a 0.1 % change probably ascribable to thermal contraction. The intensity of this peak is 0.723±0.025 that of the initial peak prior to deuteration. Deuterium did not appear be sorbed readily by the sample: there was no significant fall in the pressure on the sample. A likely explanation is that the deuterium was resident gaseously in pores of the sample at 50 K, probably within the graphite galleries as well, but did not possess significant enthalpy of adsorption to allow uptake. On cooling to 20 K and then 2 K under pressure, this D_2 would have condensed in and around the sample, forming solid layers but not physisorption *per se*.

After data were collected at 2 K, the sample was warmed to 50 K and the D_2 removed by pumping. In an attempt to provide isotopic contrast, H_2 was allowed onto the sample at a maximum pressure of 6560 mbar and a matching

run performed at 20 K. The patterns of H_2 and D_2 in the residual ammoniated GIC at 20 K are shown in Fig. 7.11. There is a greater signal from H_2, expected because of its higher incoherent cross-section.

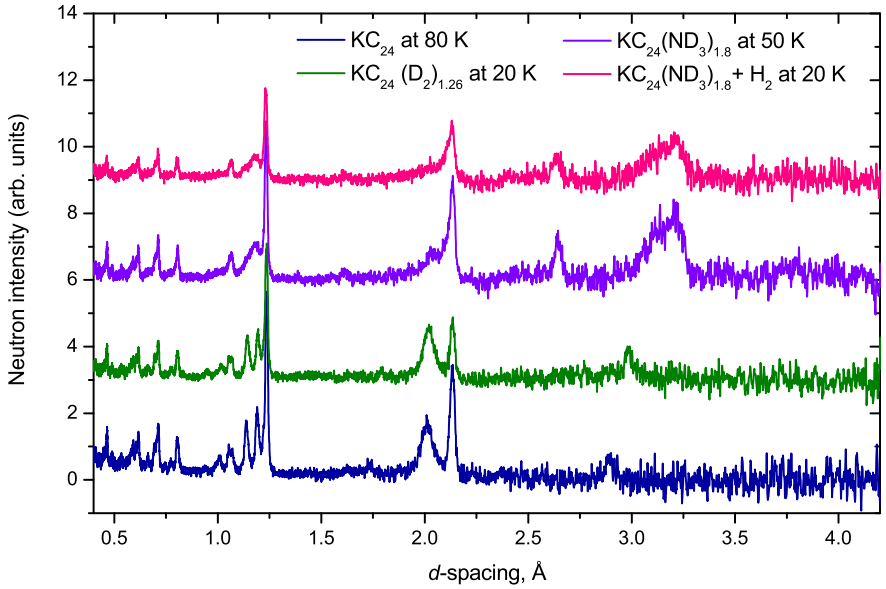

Figure 7.12: Comparison of in-plane scattering in four diffraction patterns taken at a 45° sample orientation during the experiment. A scaled empty cell background has been subtracted.

The sample was oriented at 45° to decouple the in-plane and out-of-plane scattering. These data are in Fig. 7.12 and Fig. 7.13 with the patterns from pure KC_{24}, $KC_{24}(D_2)_{1.26}$ and $KC_{24}(ND_3)_{1.8}$ for comparison. The *c*-axis patterns vary as described above on ammoniation, resulting in a compound with a (002) peak at 3.228±0.002 Å. A small fraction of the *c*-axis scattering can be seen in Fig. 7.12, as evident by the weak (003) peak for KC_{24} and $KC_{24}(D_2)_{1.26}$ and the weak (002) peak in the ammoniated patterns which is combined with new intensity at approx. 3.10 Å. The stage-1 ammoniated structure has a peak at 2.64±0.01 Å. Furthermore, the peaks at 1.14 and 1.19 Å in the in-plane structure of KC_{24} appear to coalesce to a single broad peak after ammoniation. The interlayer structure of ammoniated KC_{24} has been studied [108] by isotopic substitution using neutron diffraction, and the ammonia molecules were

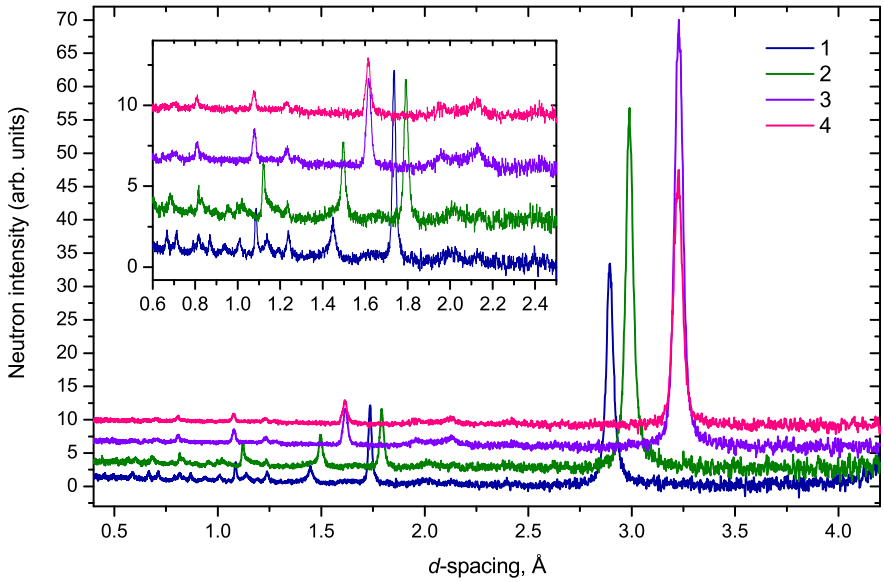

Figure 7.13: Comparison of c-axis scattering in four diffraction patterns taken at a 45° sample orientation during the experiment with inset enlargement: (1) pure KC_{24} at 80 K, (2) $KC_{24}(D_2)_{1.26}$ at 20 K, (3) $KC_{24}(ND_3)_{1.8}$ at 50 K and (4) $KC_{24}(ND_3)_{1.8}$ + 6560 mbar pressure of H_2. A scaled empty cell background has been subtracted.

located to the mid-plane. The results showed that the K ions were displaced to two layers, one either side of the midplane. The in-plane structure is a 2D liquid at room temperature [55] and there was not great evidence of crystallinity at the low temperatures surveyed here. A seed structure for GSAS was not known and so no useful fit could be performed.

The data collected here show that good time-resolved diffraction measurements exist to chart the stage transitions in KC_{24} with D_2 and ND_3, and as the (00l) reflections are well-defined, the c-axis spacing could be determined. The transitions were as expected from literature. The in-plane structures are not trivial, either to model or to fit. Useful analysis of these data awaits better evidence for the in-plane structure to enable a fit to take place. What can be said is that the potassium signature is not clear in the pattern, and thus siting of deuterium and hydrogen cannot be with confidence expressed. As the inelastic

neutron scattering measurements are more sensitive to the local environment of the sorbed molecules, they proved the route to a consistent model of the H_2 sites and this will be elaborated on in future chapters. The effectiveness of diffraction is in this case limited by the apparent lack of long-range order in the in-plane structure, and the limitations of the GSAS refinement program for turbostratically-disordered structures, so evident above, imply that a more suitable refinement method is needed.

7.3 H_2 in KC_8

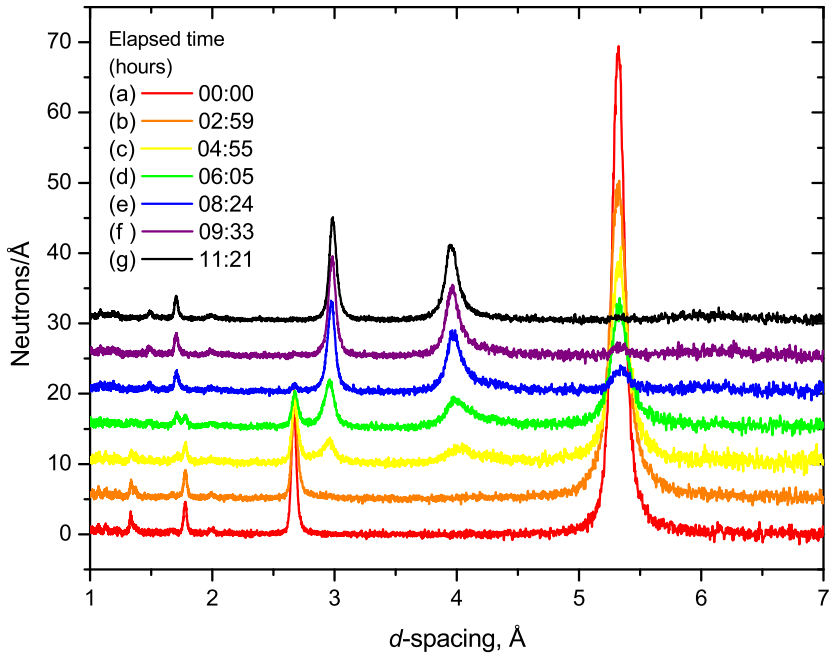

Figure 7.14: Time-resolved diffraction patterns of the KC_8 phase change with hydrogen. Data taken between 250 and 316 K. The labels (a) to (g) refer to time slices of the phase proportion plot in Fig. 7.15.

Good time-resolved data were acquired for the KC_8H_x phase transition (Fig. 7.14). The minimum temperature for the phase change in KC_8 on sorp-

tion of hydrogen, and hence the critical temperature for the physisorptive-to-chemisorptive transition at this pressure, was found to be 250 K, though the hydrogen overpressure reduced very slightly from 2.940 to 2.938 bar between 210 and 250 K. Analysis of the phase change shows a two-stage process. Firstly, there is a broadening of the KC_8 peaks without significant structural change, incorporating a reduction in peak intensity. Second, an augmentation of the lattice parameter is followed by the progressive generation of the new phase and extinction of the first. Following [111], this provides evidence for hydrogen dissociation in interstitial sites in the layers as a forerunner to the charge transfer from KC_8 to H and the structural transition.

On removal from the sample can under argon, the hydrogenated stage-1 sample was observed to have become a metallic blue colour reminiscent of KC_{24}.

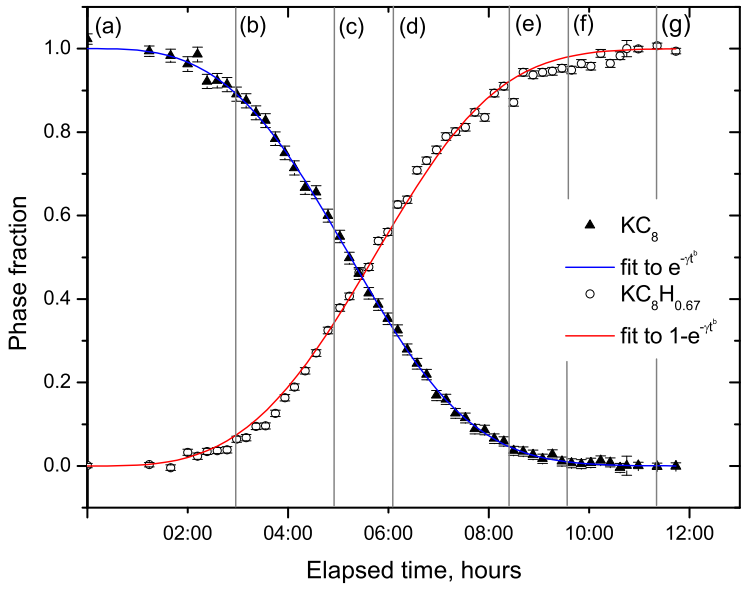

Figure 7.15: Phase proportions as a function of elapsed time in the transition from KC_8 to $KC_8H_{0.67}$. The letters refer to diffraction snapshots in Fig. 7.14. (a) lies at 00:00 hrs. Fits to the sigmoidal curves used the models labelled; their parameter values are discussed in the text.

Data were collected in all available detector banks; initial characterisation of the 90°-oriented sample was done utilising low-angle scattering to align the scattering vector, **Q**, as closely as possible to the preferred orientation axis. This enabled characterisation of the (00l) peaks as the transition occurred, the clearest signature of the completed transition being the disappearance of the KC_8 out of plane scattering in favour of that of $KC_8H_{0.67}$. Fig. 7.14 samples the diffraction data as a function of the elapsed time of the transition. The (004) and (008) peaks of KC_8 at 5.35 and 2.66 Å respectively reduce, diminishing rapidly after two hours as (00l) peaks of the hydrogen-saturated $KC_8H_{0.67}$ phase grow at 2.98 and 3.95 Å. The characterisation of these peaks depends on the stacking structure of the $KC_8H_{0.67}$ phase; for the simplest structure with 11.88 Å *c*-axis parameter, these are the (004) and (003) peaks respectively. The total transition time observed is considerably shorter than reported elsewhere [76] [112], which may be characteristic of the kinetic effect of the higher pressure of hydrogen. A transition time of 18 hours was reported in [66] for an exfoliated graphite sample similar to that used in the present case, however: the partially oriented nature of the crystallites in exfoliated graphite improves the sorption and transition kinetics.

Fig. 7.15 shows the phase fractions by integrated peak intensity of the two phases as a function of the elapsed time of the transition. It is not certain whether the rate-limiting factor on the transition is the absorption at the crystallite edges or diffusion of the hydrogen through the bulk material. From the relative rapidity of the transition in the exfoliated sample, either might be deduced, though an attempt to fit a function of the form

$$1 - \exp(-\frac{2}{3}\gamma t^{\frac{3}{2}}), \tag{7.1}$$

to the time-dependent growth of the hydrogenated phase, based on the diffu-

sion of hydrogen into the sample, was not successful: a fit of the form

$$1 - \exp(-\gamma t^b), \tag{7.2}$$

is shown in Fig. 7.15, where $\gamma = 86.25 \pm 7.72$ and b = 3.36±0.07. If compared to an Avrami model the time power, b, suggests the new phase nucleates in a manner between two and three-dimensional (3>b>4), characteristic perhaps of a planar solid such as KC_8, though as the process is not isothermal this cannot be confirmed with the present data.

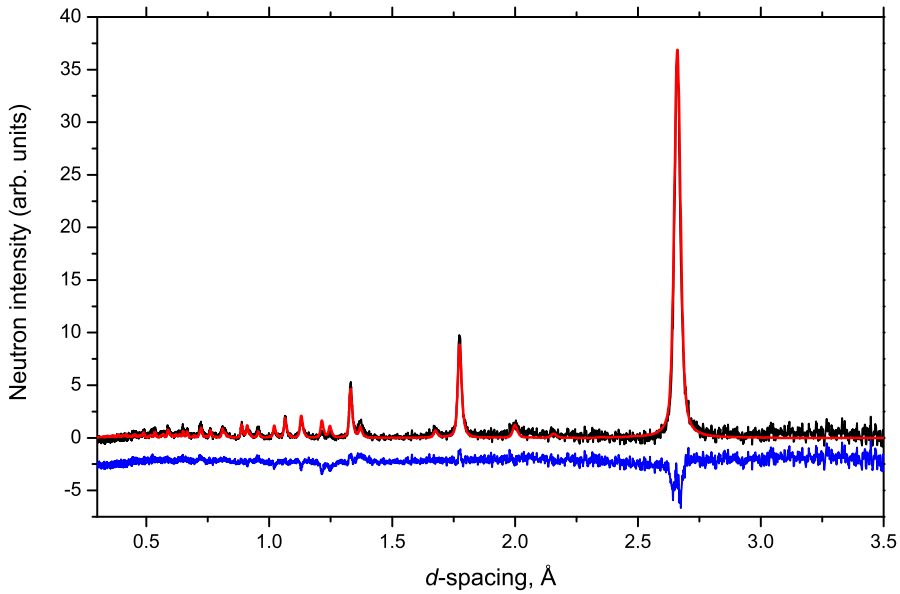

Figure 7.16: Diffraction pattern of KC_8 sample at 53 K showing principally out-of-plane structure. Black line = data, red line = GSAS fit to *Fdd2* structure, blue line = fit difference (offset for clarity).

Results of the fit for the initial KC_8 sample confirmed an *Fdd2* orthorhombic structure with lattice parameters $a = 4.97(\pm 0.01)$ Å, $b = 8.63$ Å, $c = 21.25$ Å. The fitted out-of-plane pattern is shown in Fig. 7.16. As in previous studies, the in-plane scattering, shown in Fig. 7.17 was harder to refine; in particular, certain peak intensities are fitted less successfully, such as the (404) reflection

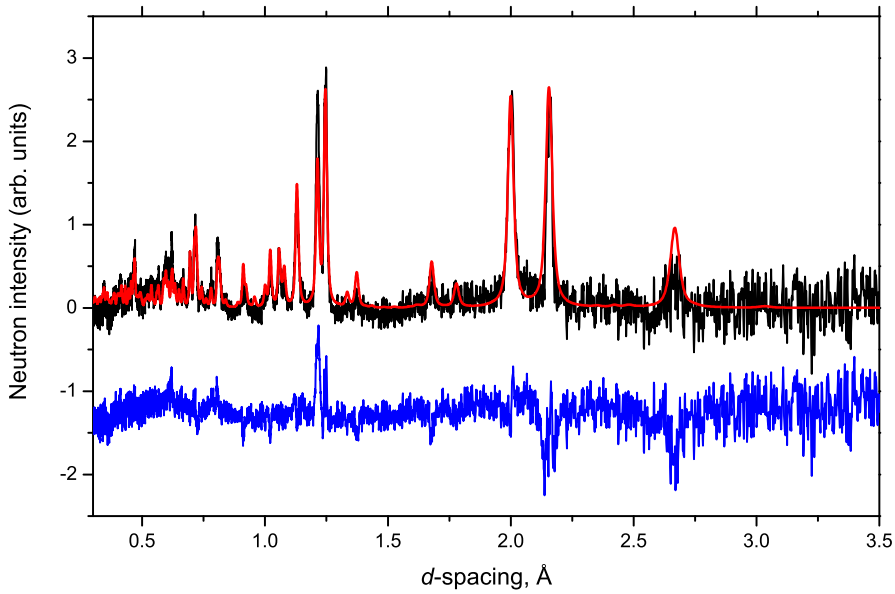

Figure 7.17: Diffraction pattern of KC_8 sample at 53 K showing principally in-plane structure. Black line = data, red line = GSAS fit to *Fdd2* structure, blue line = fit difference (offset for clarity).

at 1.21 Å and the (800) at 0.62 Å. The overall reduced-χ^2 for the fit was 1.419 for 10 variables.

Fitting the saturated $KC_8H_{0.67}$ sample proved more difficult due to the lack of a completely resolved in-plane structure. Proposed structures in the literature have assumed a single-layer graphite stacking, such that graphene sheets in adjoining layers can always be superposed in the *c*-direction. This is based on the graphite stacking in KC_8 which is characteristically AAA as the intercalated K ions lock the planes congruently. There is no such constraint on the empty galleries in $KC_8H_{0.67}$, however: by analogy with the second-stage compound KC_{24} or pristine graphite there could be graphite stacking AABBA or AABBCCA; the hydride intercalated layers lie between like planes with the C-K-H-K-C layer unit above translated by the length of a carbon-carbon bond over the empty gallery. Expanding the proposed structures to incorporate this possibility reduces their symmetry and hence increases the fitting calculations.

The three-layer structure of this material did not fit for this reason (Table 7.3).

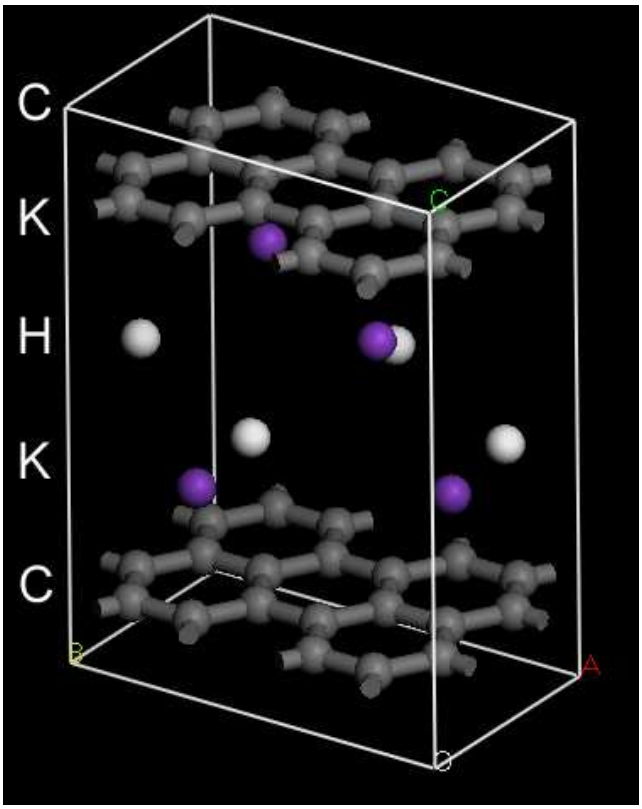

Figure 7.18: Single layer $(2\times2)R(0°)$ H_2 structure of $KC_8H_{0.5}$ with C-K-H-K-C filled gallery structure.

A single layer $KC_8H_{0.5}$ structure is shown in Fig. 7.18. This is the $(2 \times 2)R(0°)$ structure proposed by Miyajima *et al.* [76]. Two and three-layer structures were made by imposing graphite stacking AABBA and AABBCCA on this and the other potential structures. A single layer KC_8H_1 structure is seen in Fig. 7.19, and the three layer structure resulting from this in Fig. 7.20.

A list of the structures fitted appears in Table 7.3. together with the optimum fit χ^2 values found for each. The best-fitted structure of these is the tri-layer KC_8H_1, with space group *C1 2/m 1* and lattice parameters $a = 4.95$ Å, $b = 8.58$ Å, $c = 38.30$ Å, angles $\alpha = 90.0°$, $\beta = 105.1°$, $\gamma = 90.0°$. Fits of this structure to the c-axis and in-plane scattering are shown in Figs. 7.21

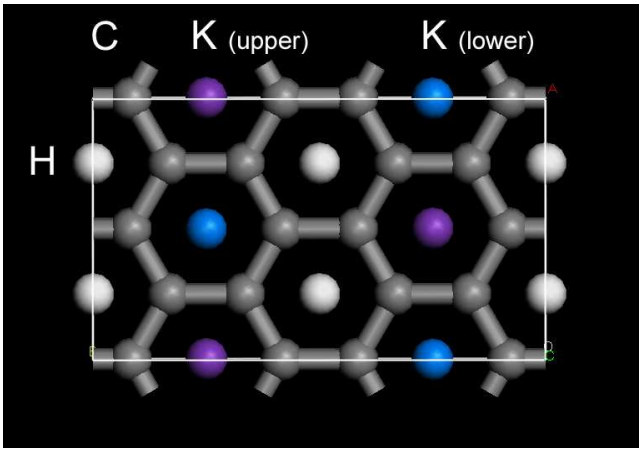

Figure 7.19: Single layer structure of KC_8H_1 with filled layer arrangement C-K-H-K-C as for Fig. 7.18. Upper layer K ions are purple and lower K ions are blue.

Table 7.3: Fitted structures to $KC_8H_{0.67}$ data, showing χ^2 values [113]

Structure	H superlattice	Stacking	Space group	χ^2
KC_8H_1 1 layer	$1 \times \sqrt{3}R(0°, 30°)$	AAA	*Cmma*	3.503
KC_8H_1 2 layer	$1 \times \sqrt{3}R(0°, 30°)$	AABBA	*Cmca*	2.375
KC_8H_1 3 layer	$1 \times \sqrt{3}R(0°, 30°)$	AABBCCA	*C1 2/m 1*	1.940
$KC_8H_{0.5}$ 1 layer	$2 \times \sqrt{3}R(0°, 30°)$	AAA	*Pccm*	9.096
$KC_8H_{0.5}$ 2 layer	$2 \times \sqrt{3}R(0°, 30°)$	AABBA	*Pcca*	6.198
$KC_8H_{0.5}$ 3 layer	$2 \times \sqrt{3}R(0°, 30°)$	AABBCCA	*P1 2/c 1*	—
$KC_8H_{0.5}$ 1 layer	$2 \times 2R(0°)$	AAA	*C222*	3.153
$KC_8H_{0.5}$ 2 layer	$2 \times 2R(0°)$	AABBA	*C2221*	2.763
$KC_8H_{0.5}$ 3 layer	$2 \times 2R(0°)$	AABBCCA	*C121*	2.061

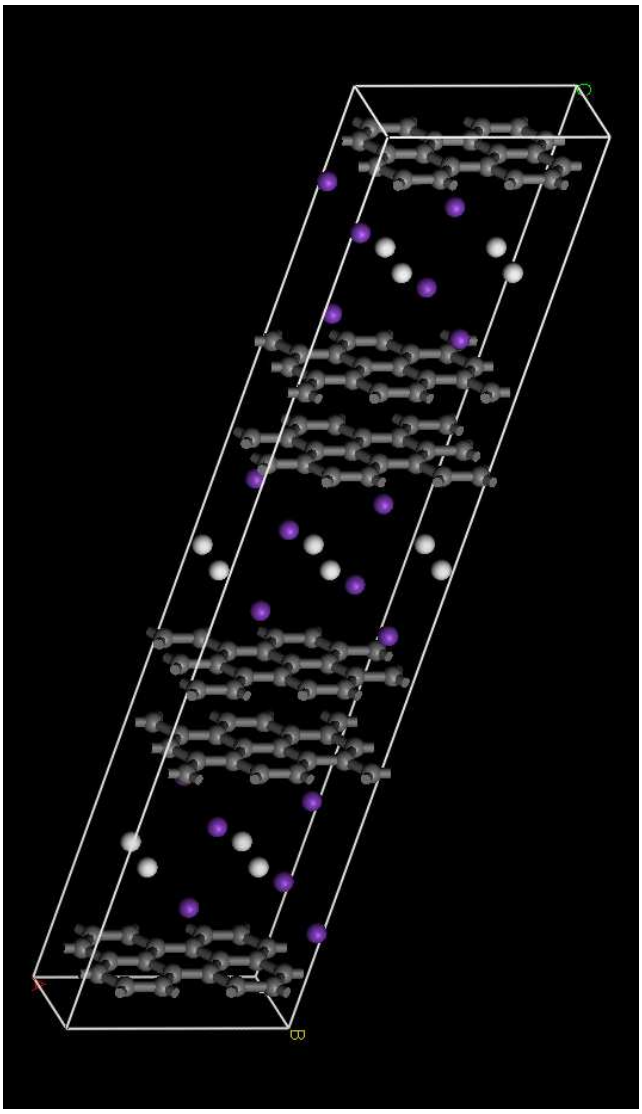

Figure 7.20: Triple layer *C1 2/m 1* structure of KC_8H_1.

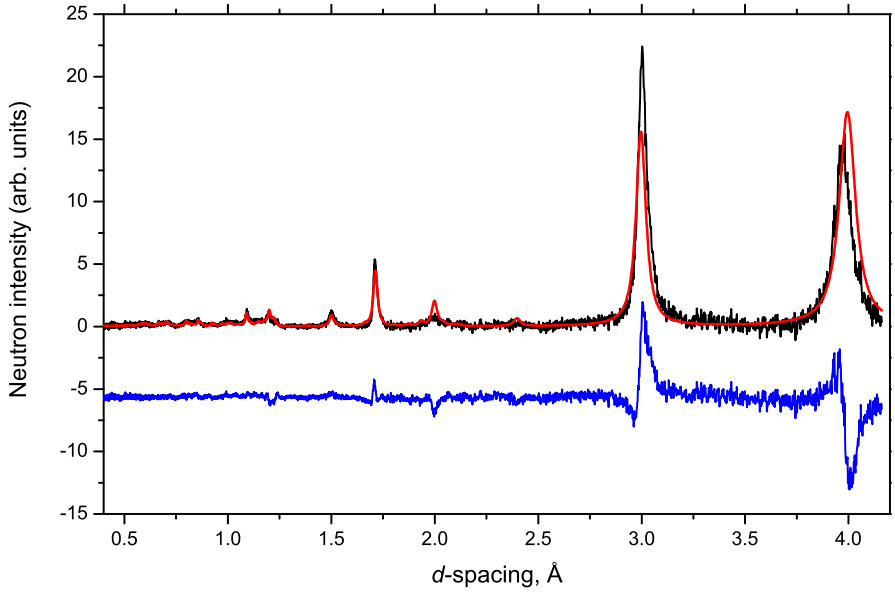

Figure 7.21: Diffraction pattern of $KC_8H_{0.67}$ sample at 317 K showing out-of-plane structure. Black line = data, red line = GSAS fit to 3-layer KC_8H_1 structure, blue line = fit difference (offset for clarity)

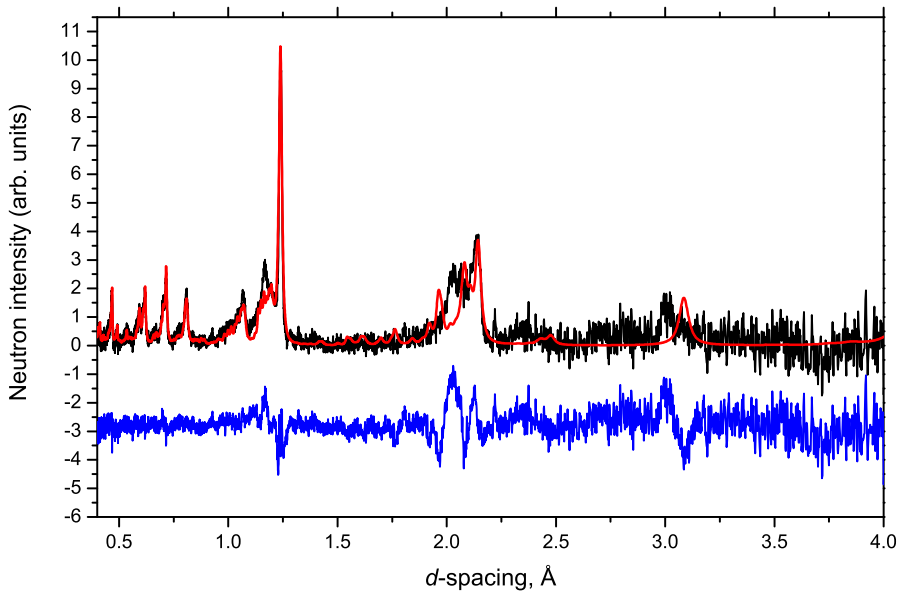

Figure 7.22: Diffraction pattern of $KC_8H_{0.67}$ sample at 317 K showing in-plane structure. Black line = data, red line = GSAS fit to 3-layer KC_8H_1 structure, blue line = fit difference (offset for clarity)

and 7.22. The fits are good at low *d*-spacing but have several deficiencies. The stoichiometry of KC_8H_1 is incorrect for the saturated sample but sample structures with 0.67 H/K were of too low symmetry to fit. Instead, attempts to fit the hydrogen occupation number for this structure were made but were inconclusive. The partial success of the fit qualitatively backs up the proposals for the in-plane K structure, which are unchanged across all models, but suggests more investigation and modelling could profitably be carried out to elucidate the in-plane hydrogen structure. This work has been published [113].

7.4 H_2 in CaC_6

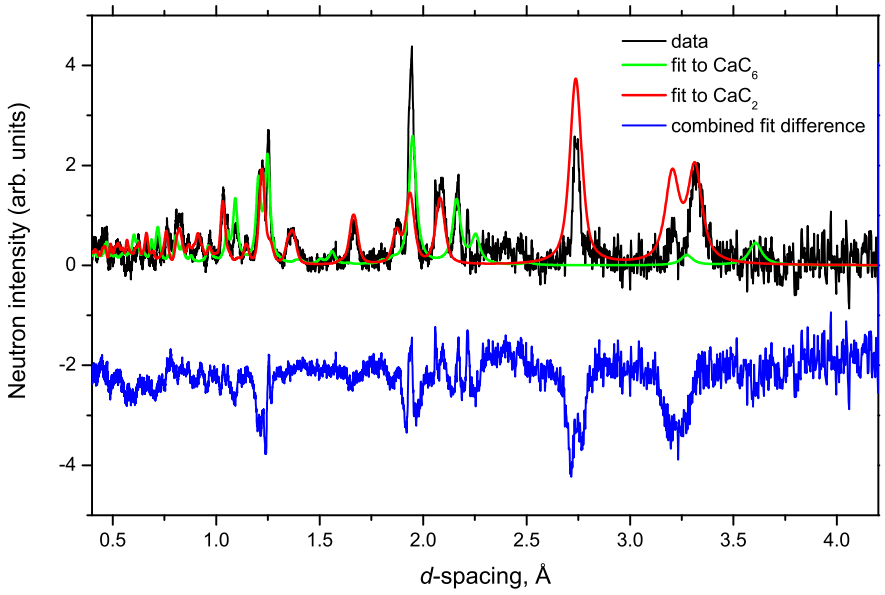

Figure 7.23: Diffraction pattern of CaC_6 sample at 50 K showing out-of-plane structure. Black line = data, red line = GSAS fit to CaC_6 structure, green line = GSAS fit to CaC_2 structure, blue line = combined fit difference (offset for clarity). These data had an 18-term Chebyschev fitted background removed.

The results from this experiment did not show any structural transitions associated with CaC_6 being exposed to H_2. It seemed clear that there was more

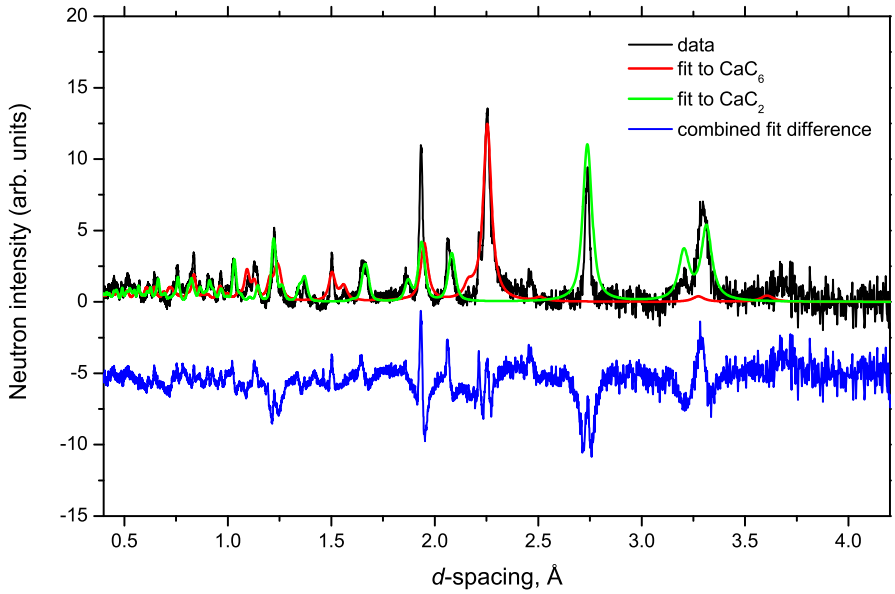

Figure 7.24: Diffraction pattern of KC_8 sample at 53 K showing in-plane structure. Black line = data, red line = GSAS fit to CaC_6 structure, green line = GSAS fit to CaC_2 structure, blue line = combined fit difference (offset for clarity). These data had a 16-term Chebyschev fitted background removed.

than one phase present in the sample as loaded; the impurity was suspected to be calcium carbide (CaC_2) as the sample was exposed to heat when melting it from the alloy. Although GSAS was not able to fit the peak shapes or intensities particularly well, it provided evidence for the presence of CaC_2 being quite substantive. Fig. 7.23 shows the out-of-plane scattering for CaC_6 at 50 K, taken in the right-hand 90° detector bank for a sample orientation of 45°. Fig. 7.24 shows the equivalent in-plane scattering in the left hand detector bank. It was not possible to run GSAS to determine the relative phase proportions because of hardware issues. The phases fitted are the CaC_6 $R\bar{3}m$ rhombohedral phase, with lattice parameters refined to $a = 4.29$ Å, $c = 13.52$ Å, and the $I4/mmm$ CaC_2 phase, with lattice parameters $a = 3.87$ Å and $c = 6.40$ Å. The CaC_6 unit cell is shown in Fig. 7.27.

Figs. 7.25 and 7.26 show the sample under hydrogen loading conditions at

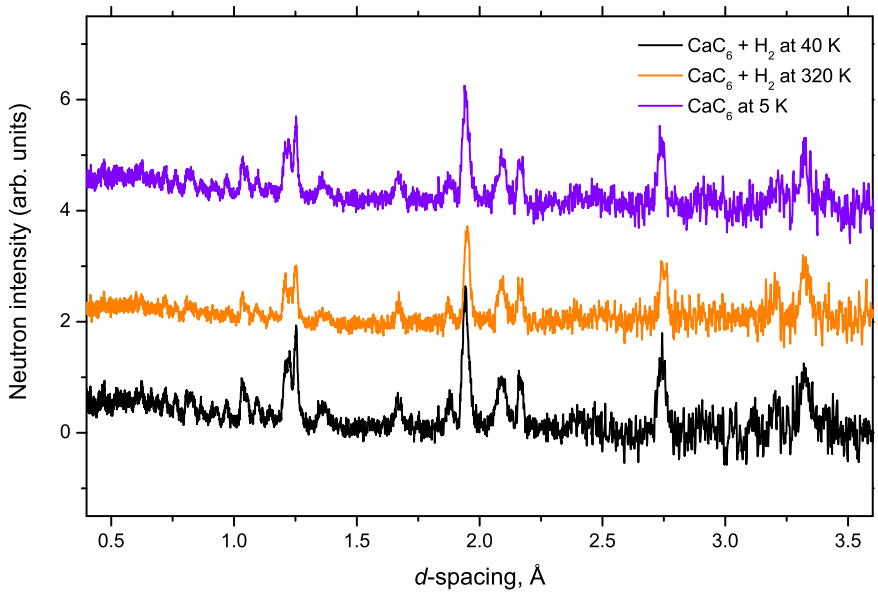

Figure 7.25: Diffraction patterns of CaC_6 sample showing out-of-plane structure. Black line = $CaC_6H_{0.37}$ at 40 K, orange line = CaC_6 under 1500 mbar hydrogen pressure at 320 K, purple line = CaC_6 with H_2 removed at 5 K (offset for clarity). These data had a normalised empty Ti-Zr can run subtracted.

40 K and 320 K after a gradual increase in temperature. They then show the sample after outgassing at 5 K. There is no evident structural change. A small increase in background is probably due to the hydrogen incoherent scattering. Small changes in (00l) peaks are probably attributable to thermal expansion. Measurements of the (006) CaC_6 peak at 2.25 Å under hydrogen imply that the *c*-lattice parameter expands from 13.51 Å at 40 K to 13.58 Å at 320 K. If any hydrogen is adsorbed into the sample, it does not appear to affect the interlayer spacing, which for the pure sample is found to be 4.507 Å, a little less than the literature value (see Table 3.2). There is the possibility that hydrogen is blocked from the interlayer spaces by a surface layer of metal or carbide; in this case, sample pre-treatment is critical to achieve a well-staged sample.

This experiment set a precedent for studying H_2 in Li alloy-produced bulk

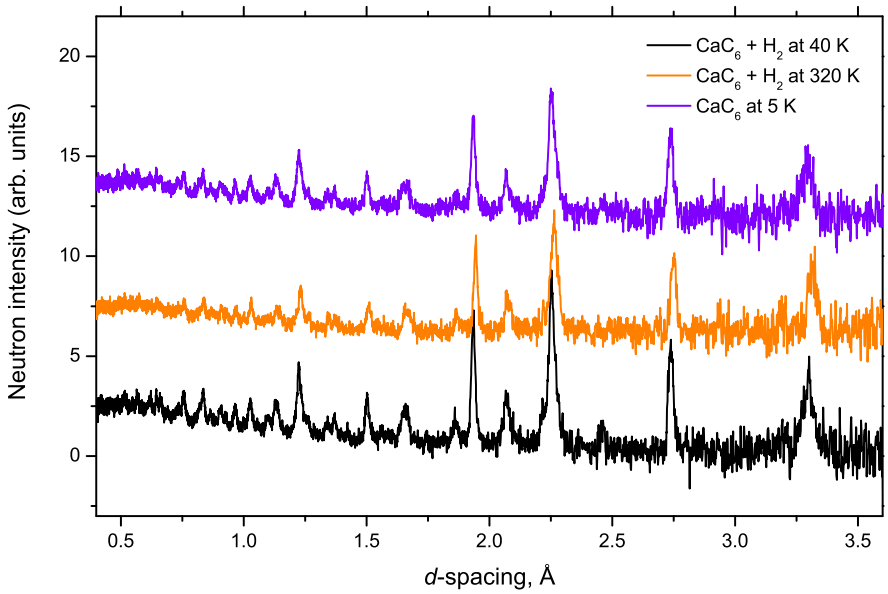

Figure 7.26: Diffraction patterns of CaC_6 sample showing in-plane structure. Black line = $CaC_6H_{0.37}$ at 40 K, orange line = CaC_6 under 1500 mbar hydrogen pressure at 320 K, purple line = CaC_6 with H_2 removed at 5 K (offset for clarity). These data had a normalised empty Ti-Zr can run subtracted

CaC_6. However, sample contamination took place with the formation of carbides. A further investigation is required, with a pure sample and with hydrogen loading up to at least 400 K to determine if any structural changes occur. As calcium forms an ionic hydride, a process akin to the KC_8 hydriding transition is suspected. Thermogravimetric data hinted at irreversible hydrogen uptake at 473 K (§ 6.8). For the pure CaC_6 material, there does not appear to be any physisorption, nor a structural change associated with the onset of superconductivity at 11 K. The construction of a thermogravimetric analyser able to fit into a neutron scattering instrument is a promising development, and should allow complete *in situ* measurement of uptake and structure. A further diffraction experiment on the ammoniated Ca-GIC structures under hydrogen using this equipment is envisaged.

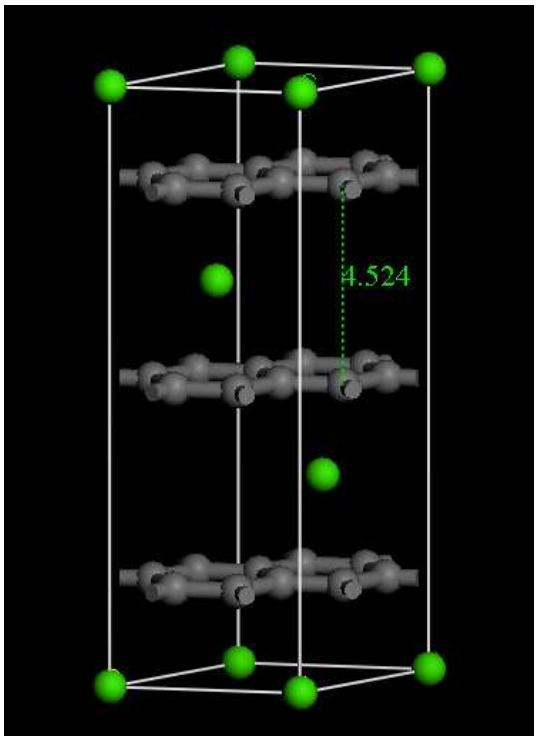

Figure 7.27: $R\bar{3}m$ unit cell of CaC_6 showing the interlayer spacing (in Å). The ions are located over benzene ring centres.

Chapter 8

Inelastic neutron scattering results

8.1 H_2 and ND_3 in KC_{24}

The dedicated diffraction measurements taken on IRIS for this experiment each consisted of 7 runs with different instrument settings which when combined gave a single diffraction pattern from 1 - 10 Å. Five of these were acquired during the experiment. They are shown in Fig. 8.1. Data from Lorentzian fits performed on the peaks are listed in Table 8.1.

The KC_{24} sample was shown to be of high purity, although a small proportion of KC_8 phase can be seen in the diffraction pattern. From analysis of the areas of the (002) peaks KC_8 is estimated to make up 2.6 % of the sample. *d*-spacings, which are the shortest repeat distance of the compound in the *c*-direction, found for the different compounds agree well with literature values. The lattice spacing for the stage-1 ammonia-saturated compound $KC_{24}(ND_3)_{4.3}$ is reported to be 6.65 Å [108], which compares well with 6.496

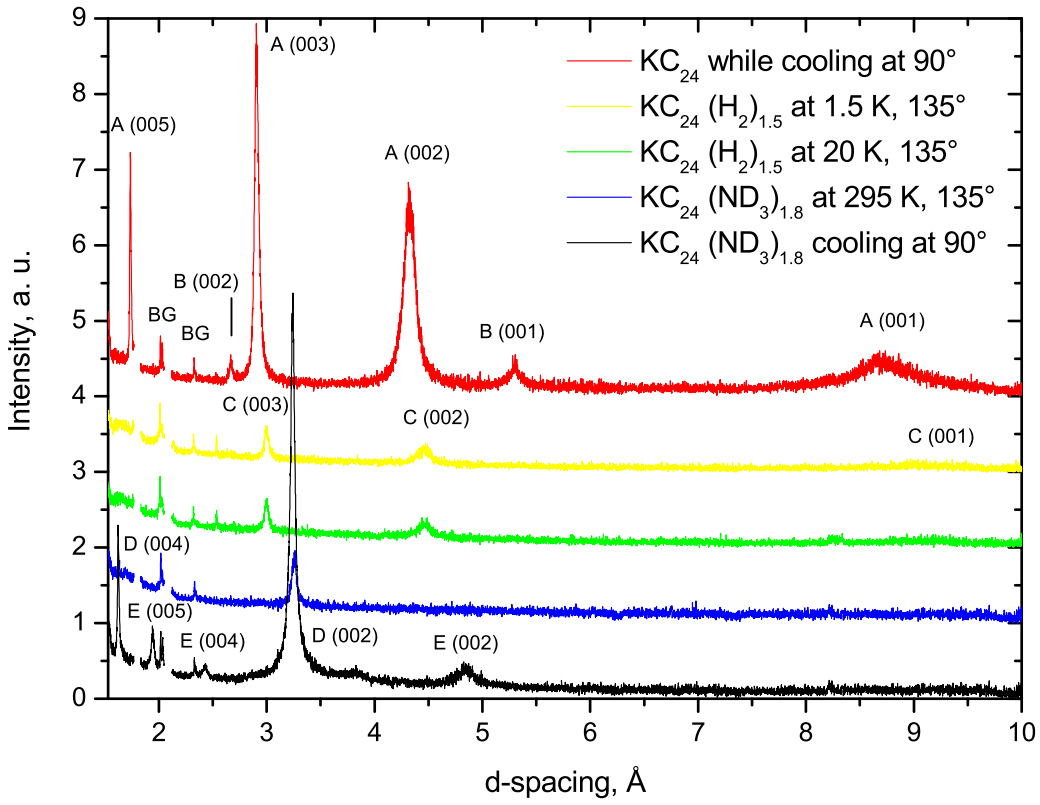

Figure 8.1: Diffraction data from IRIS experiment 20259, each combined from 7 runs. Two intense background peaks at 1.8 and 2.1 Å have been removed from all patterns. The peaks are labelled by phase and (hkl) values. Phases identified are: BG = background, A = KC_{24}, B = KC_8, C = KC_{24} saturated with H_2, D = $KC_{24}(ND_3)_{1.8}$, E = secondary phase of $KC_{24}(ND_3)_{1.8}$. The orientational angle of the sample in the beam (see Fig. 4.1) was 90° for the first and last patterns, and 135° for the others.

Table 8.1: Diffraction peak analysis from IRIS experiment 20259. Peak labels refer to Fig. 8.1.

Phase	Peak (hkl)	x-value Å	FWHM Å	Area arb. units	d-value Å
KC_{24}	A (001)	8.720±0.003	0.669	0.37±0.01	8.720±0.003
	A (002)	4.324±0.0003	0.124	0.483±0.003	8.648±0.0006
	A (003)	2.907±0.0001	0.044	0.314±0.002	8.722±0.0004
	A (005)	1.737±0.0001	0.013	0.060±0.002	8.684±0.0006
KC_8	B (001)	5.302±0.001	0.102	0.038±0.003	5.302±0.001
	B (002)	2.669±0.0007	0.033	0.013±0.001	5.337±0.002
$KC_{24}(H_2)_{1.5}$	C (001)	9.045±0.015	0.617	0.034±0.008	9.045±0.015
	C (002)	4.454±0.001	0.149	0.048±0.003	8.908± 0.002
	C (003)	2.998±0.0004	0.046	0.028±0.001	8.994±0.001
$KC_{24}(ND_3)_{1.8}$	D (002)	3.242±0.0001	0.0514	0.385±0.002	6.483±0.0002
	D (004)	1.624±0.0001	0.015	0.039±0.0009	6.496±0.0003
	E (002)	4.843±0.002	0.175	0.060±0.002	9.685±0.004
	E (004)	2.426±0.001	0.064	0.016±0.002	9.704±0.004
	E (005)	1.944±0.0003	0.029	0.023±0.001	9.720±0.001

Å for the residual compound (containing much less ammonia) here, itself only 0.5 % larger than the equivalent 6.46 Å spacing after ammonia removal in the Polaris experiment (§ 7.2). A small proportion of stage-2 K-ND_3-GIC is observed in the last pattern in Fig. 8.1 (black line); this is reported to have a *d*-value of 9.97 Å. This is composed of an ammoniated K-filled layer of depth 6.65 Å added to an empty graphite layer of ∼3.35 Å. The figures in Table 8.1 allow a plausible rationale for the derived *d* of 9.70±0.02 Å from the peaks assigned to this phase: it probably consists of the 6.49 Å stage-1 interlayer distance derived here in combination with an empty graphite layer of slightly reduced dimensions of ∼3.2 Å. Comparison of the areas of the (002) peaks of the two phases suggests that the sample at this point consists of 13.5 % stage-2 phase.

The diffraction patterns in Fig. 8.1 were taken at two different orientational angles. The intensity of the *c*-direction peaks was maximised for the first and last patterns shown, allowing a good structural characterisation, but this angle was not ideal for INS. INS measurements were taken at a 135° orientation; the strong Bragg scattering off the graphite planes was then directed away from the PG analysers where it would have created an unwanted background in the INS signal.

There was significant uncertainty on the dosing concentration due to the added volume of the gas rig pipework and capillary (estimated at 35 cm^{-3}), as well as the 5 % error on the buffer volume which exists, according to the manufacturer. The first dose of hydrogen was slightly over $x = 1$, and so the concentrations studied were $x = 1.08 \pm 0.09$ and, at saturation, $x = 1.55 \pm 0.13$. *In situ* diffraction measurements taken at 1.5 K while collecting inelastic measurements show the (003) peak evolving through the concentration sequence, which is shown in Fig. 8.2. It seems probable that, as for the Polaris measurements on this transition, the pure and H_2-expanded phases coexist and

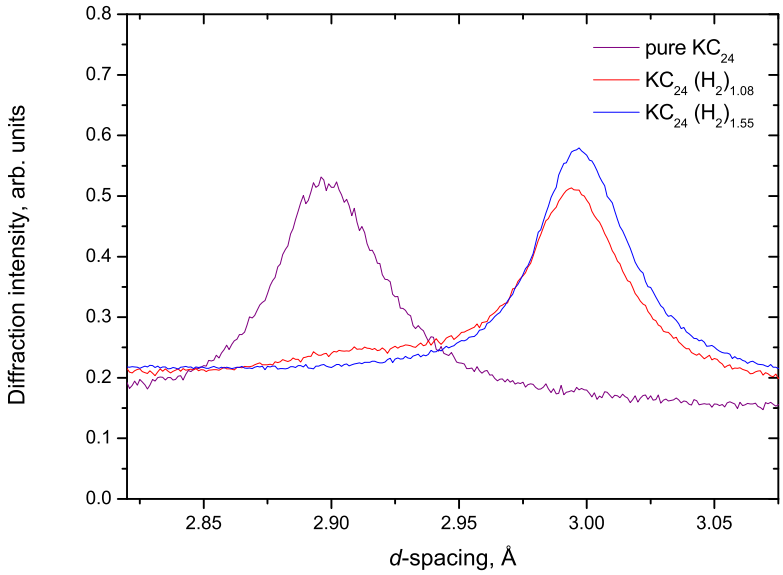

Figure 8.2: The evolution of the (003) diffraction peak of KC_{24} with increasing hydrogen concentration

are represented by the progressive extinction of the peak at 2.90 Å and the growth of the 2.99 Å peak. However, after the addition of the first amount of H_2, the original peak has almost disappeared. If the expansion of the lattice is a domain-registered process, then it is likely that insertion of hydrogen into empty sites expands the lattice about it, including other empty sites nearby which then show little extra expansion when they too are filled. In that case, half-filling the lattice with hydrogen might well lead to more than half of the domains expanding and leave relatively little of the original phase visible. However, adding almost 50 % more hydrogen until saturation only added 8.1 % to the intensity of the hydrogenated phase (003) peak. The background increases as a function of hydrogen content; between $x = 1.08$ and $x = 1.55$ it doubles.

By comparison with the later experiment (§ 8.2), where careful measurements determined the length of time for the ortho-H_2 to convert to para-H_2, it is clear that a lot of ortho-H_2 is present and contributes to a signal across the spectrum independent of energy. The sample had not been left for the required

$\sim$10 hours at the base temperature (1.5 K) for conversion to complete. The increase in 'background' in Fig. 8.2 can be seen in the peaks for both hydrogen concentrations, and some of the expected intensity of the unhydrogenated sample (003) peak is masked.

The INS data collected for the hydrogen excitations in the first part of this experiment were corrected for detector efficiencies and then the spectrum of pure KC_{24} was subtracted from each spectrum to leave only signal associated with the hydrogen dynamics. This also removed background features such as the fast neutron peak at 0.25 meV. The data collected in the -0.8 to 2.0 meV energy transfer window are shown in Fig. 8.3. There was no sign of a 14.7 meV H_2 roton peak when the window was extended to 20 meV for $x = 1.08$ concentration: although the flux was poor at that energy, the line should have been visible if present. This spectrum was not statistically good enough to present here.

The observed low-energy excitations in $KC_{24}(H_2)_x$ correspond qualitatively with those seen for hydrogen in CsC_{24} and RbC_{24} [77, 79]. At $x = 1.08$ and 1.5 K, the excitations seen are a well-resolved doublet at 0.56 ± 0.05 meV, and a set of excitations between 1.17 and 1.82 meV, consisting of broad peaks at 1.28 and 1.57 meV, the latter seemingly several modes combined, with a prominent shoulder in higher energy transfer. When hydrogen is added to $x = 1.55$, the doublet loses definition and a shoulder appears on the low-energy-transfer side, and a narrow peak appears at 0.29 meV. The second set of excitations moves lower in energy and the outermost peak appears to be a combination of at least three peaks, at 1.25, 1.45 and 1.56 meV. As the temperature is raised to 10 and 20 K, the peaks lose intensity and quasi-elastic scattering is seen to widen the elastic line, suggesting that rapid diffusive motions of H_2 are in train. However, the excitations do not vary in energy with temperature. Further, there was no **Q**-dependence of the elastic peak width, which could be an indication that

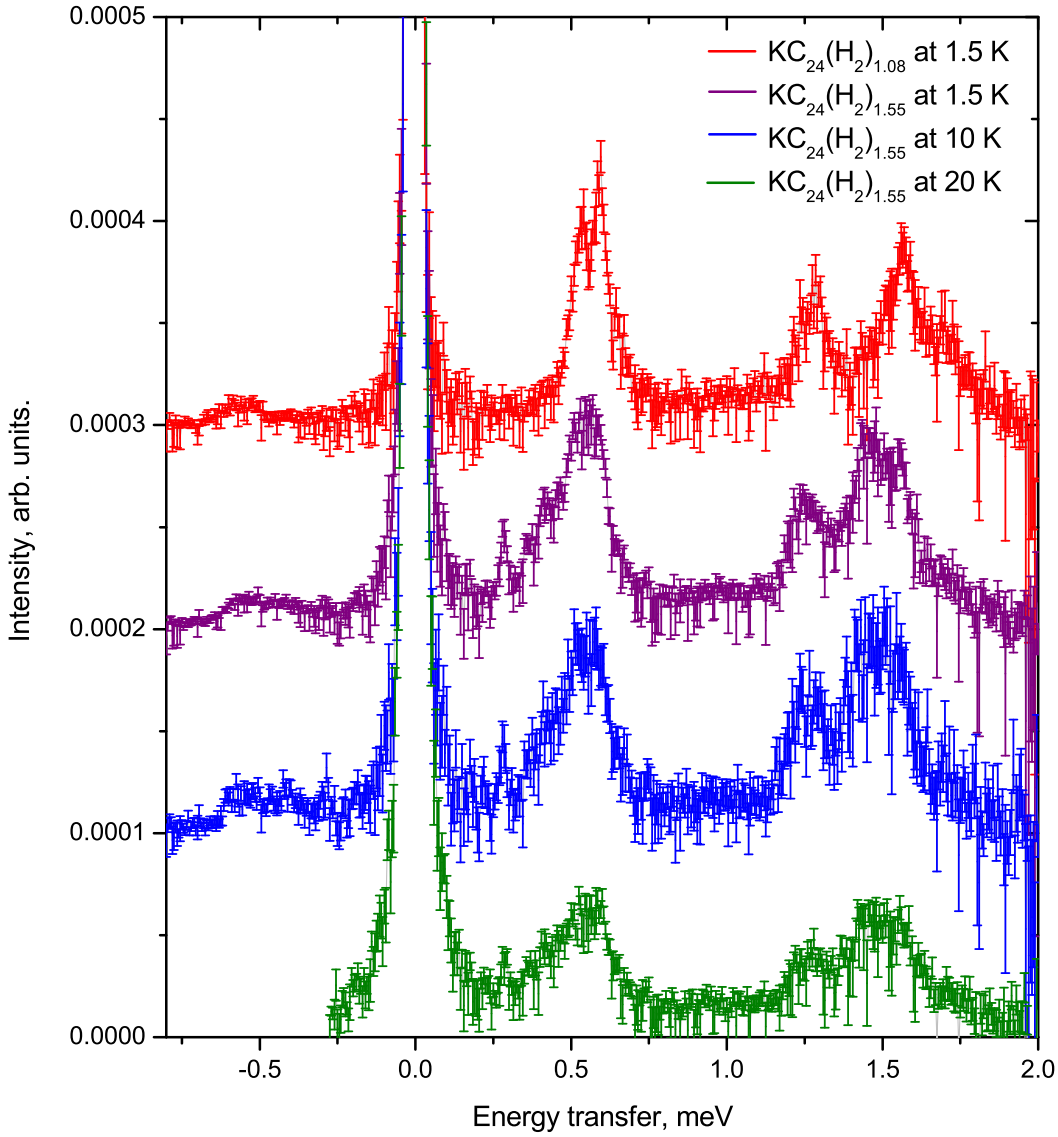

Figure 8.3: Spectra of KC_{24} $(H_2)_x$ for $x = 1.08$ at 1.5 K and $x = 1.55$ at 1.5, 10 and 20 K. A background taken of pure KC_{24} with identical sample geometry has been subtracted from each.

the 0.6 meV transition is indeed the lowest energy excitation in the system.

Unlike the Cs and Rb-GICs, there appears to be no preferential filling of one set of excitations over another at $x = 1.08$. This makes a heterogenous two-site model harder to justify, unless both sites fill at similar rates. As the hydrogen was easily detectable at the concentration $x = 1.08$ on IRIS, the possibility of exploring the low-coverage hydrogenated system for $x < 1$ was realised. This proposal led to the second IRIS experiment.

To describe the data it makes sense to invoke the Stead model and compare its predictions with the data. An exposition of this is given in § 3.3.3. The first $J = 1$ rotational level of the hydrogen molecule is perturbed under a cylindrically symmetric barrier potential $2V$. When $2V = 0$, one obtains the free rotor energy of 14.7 meV. Under the potential, this splits and the doubly-degenerate $M = \pm 1$ level rises in energy while the single $M = 0$ level lowers in energy. Under hydrogen loading of $x = 1.08$, low-energy tunnelling modes are apparent while the free rotor is not; this tends to fit the hypothesis. As it is not possible to see the higher energy librational modes on IRIS, this confirmation had to wait until the TOSCA experiment. It is possible to suggest that hydrogen enters two occupied sites which have different potentials and hence produce separate peaks in the low-energy spectrum. Although there are other possible assignments of the observed modes, in the RbC_{24} $(H_2)_{x<1.2}$ system it was possible to see one of the peaks develop before the other as the hydrogen concentration was increased [77]. For $x = 1.08$, peaks at 1.23 and 1.56 meV are characteristic of one site, whilst the split peak at 0.56 meV is assigned to the second site.

Both of the observed excitations also appear to be split, which could mean that they are in fact the $M = \pm 1$ level but with the degeneracy removed by the in-plane crystal field, but later analysis suggests the observed energy is too

low were this to be the case. It is much more likely that the splitting is due to hydrogen-hydrogen interactions, which is certainly possible given that the levels clearly change and broaden with increasing hydrogen concentration.

The low energy peaks grow with a time constant of $\sim$ 4 hours, which we assign to the ortho-para-H_2 transition, indicating that they are a indeed a transition between rotational and hence spin states and not due to lattice modes. It is also impossible for them to be due to a transition from the $J = 1$ $M = 0$ to $M = \pm 1$ states since these are forbidden by the selection rules of neutron interaction with the hydrogen $J = 1$ level [114] and in any case the population of the $J = 1$ level at 0.6 meV at 1.5 K would be vanishingly small. Heating the sample also broadens the peaks, but does not appear to produce any new excitations, which is expected if these excitations were due to two different sites broadened by hydrogen-hydrogen interactions. Thus far, the Stead model appears valid.

The hydrogen-doping post-ammoniation resulted in two -0.5 to 30 meV spectra, one of $KC_{24}(ND_3)_{1.8}(H_2)_{1.08}$ and one of $KC_{24}(ND_3)_{1.8}(H_2)_{4.2}$ (§ 5.4.2). The former was subtracted from the latter as no background was available. The resulting spectrum is shown in Fig. 8.4. Background peaks were largely removed by the subtraction, except for one between 2.6 and 3.1 meV which was omitted from the graph. This peak can be confidently assigned to an spurion of post-sample scattering on IRIS which scales with the amount of sample present and thus does not subtract completely with a background run. It can be seen that the low energy rotational peaks are no longer present. Instead, a broad split hydrogen free rotor 0.4$\pm$0.1 meV either side of 14.7 meV is coupled with a quasi-continuous hydrogen spectrum between 0 and 16 meV with a peak at 5.4 meV. This suggests a film of bulk liquid-like hydrogen exists in the sample, though without suggesting whether this is in macroscopic pore voids or within the GIC layers. The split hydrogen rotor is a consequence of a proportion of

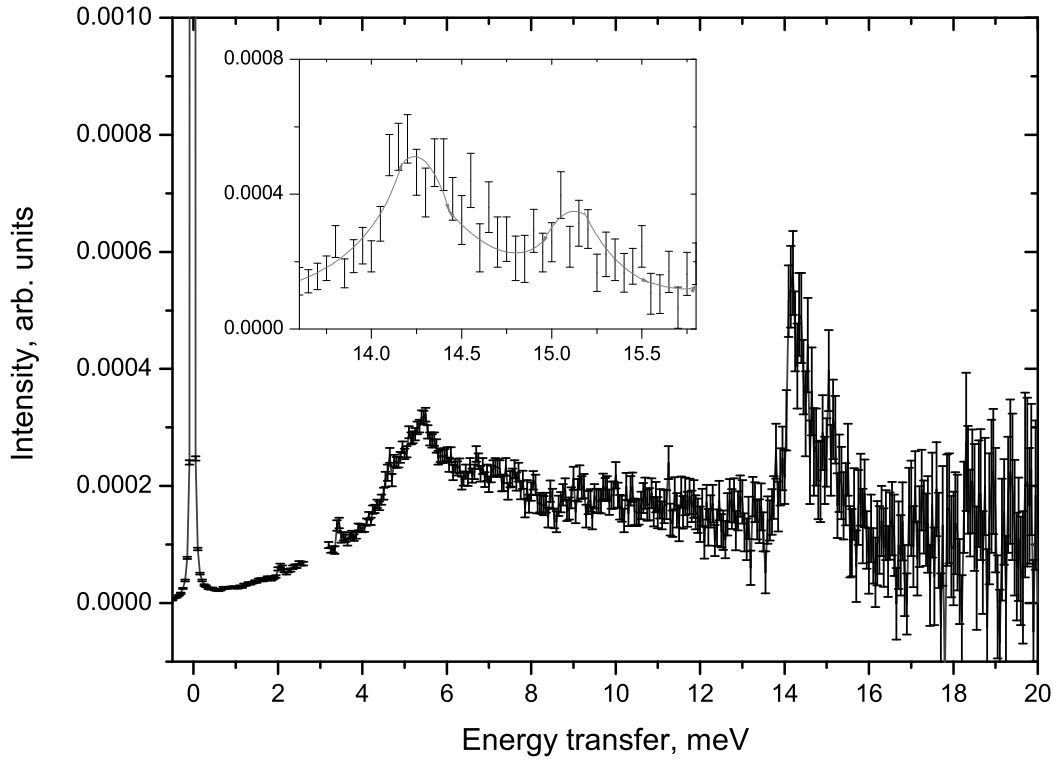

Figure 8.4: Spectrum of KC_{24} $(ND_3)_{1.8}$ with hydrogen at 1.5 K. A split hydrogen roton is visible at 14.7±0.4 meV with intensity ratio ∼2:1 (inset with line drawn as guide to eye). A quasi-continuous spectrum with a peak at 5.4 meV may be liquid-like hydrogen. One background peak at 2.9 meV resulting from post-sample scattering in the spectrometer has been omitted to improve clarity.

the hydrogen being slightly perturbed from the free rotor limit by a shallow cylindrically-symmetric potential. In this case, the splitting of the $J = 1$ level should result in the branches having an intensity ratio of 2:1, because the energy of splitting is proportional to $|M|$ under cylindrical symmetry, which is observed. Also expected is a ratio in energy offset of 1:2 from the lowered $M = \pm 1$ to the raised $M = 0$ bands, this latter not being obvious here but more so in a similar measurement in the second experiment on IRIS. This is explicable in terms of weakly bound H_2 either on graphite surfaces or inside the expanded GIC galleries. It is difficult to quantify how much of the hydrogen is adsorbed in this way. As little H_2 adsorption was seen except under pressure, by comparison with that in pure KC_{24}, one can conclude that the presence of residual ammonia in $KC_{24}(ND_3)_{1.8}(H_2)_x$ appears to hinder the uptake of hydrogen inside the graphite galleries despite a larger internal volume from *c*-axis expansion. It is probable that charge-shielding effects of the ammonia, as well as its excluded volume, greatly reduced adsorption of H_2 inside the GIC.

Data from this experiment were presented at the International Conference on Neutron Scattering in 2005 [115] but further attribution of the observed modes to a hydrogen site-specific model was difficult without additional studies. Because no clear preferential filling of the two sets of low energy excitations in $KC_{24}(H_2)_x$ for the two concentrations studied was observed, in contrast to literature studies of Cs- and RbC_{24} systems with H_2, it was important to collect data on lower hydrogen filling states. The energy windows available on IRIS did not extend far enough in energy transfer to observe the expected librational states at 39 and 51 meV. These states, if present, would provide good evidence for the tunnelling model as outlined above and in § 3.3.3. This was the motivation for the following experiments using identical H_2 dosing on IRIS (covering the energies -0.8 to 20 meV) and TOSCA (5 to 500 meV).

The presence of intensity on the anti-Stokes side of the elastic line (neutron energy gain) demonstrated that not all the hydrogen was in the ground state while scattering was taking place. This was evidence for the length of time in which the ortho-para conversion took to complete, even at temperatures below 50 K and incorporating the reported catalytic effect of the intercalate [61]. Time constraints for the experiment meant that a complete transition was not attainable. Accurate analysis of intensity of the various positive energy transfer modes required that all the hydrogen be in para-H_2 form, and this was planned for the follow-on experiments.

8.2 Low coverage modes of H_2 in KC_{24}

This IRIS experiment built on the experience gained from the previous one. To simplify the spectrum, it was important to let ortho-H_2 transform into para-H_2 before measuring the scattering. Ortho-H_2 in the sample added to the background intensity and elastic line and not to the para-hydrogen modes. This was effected by cooling the sample to the base temperature after each addition of hydrogen, and waiting, while observing the INS spectrum repeatedly. It was observed after experimentation that hydrogen in the intercalated sites would be catalysed more easily at low temperature; the process took $\sim$10 hours. A justification for this is given by the greater strength of electron-nuclear spin interactions for conversion than phonon interaction processes. As the sample is cooled, the hydrogen is able to approach the electron charge donated by the potassium to the graphite sheet and thus has a higher probability of entering the ground state. When there was little-to-no intensity in the modes on the energy gain side of the elastic line, and the incoherent energy-independent ortho-H_2 intensity was minimised, the transition was judged to be complete. The highest coverage of hydrogen was attained by condensing hydrogen that

had been at a pressure of 4630 mbar above the sample onto it by cooling. This was expected to form a liquid-like layer on the surface and in the large pores of the sample, because the physisorption sites would be saturated. The large extra mass and the lack of catalytic activity from the then fully-site-occupied intercalate meant that the ortho-para conversion rate was too slow to allow complete conversion. Thus the spectra of the highest coverage system had a large incoherent background resulting from ortho-H_2. This can be seen in Fig. 8.5.

The gas rig and capillary system were similar to the previous experiment; however, a 500 cm^3 rather than 300 cm^3 buffer was used to measure out the gas to be loaded. A 5.5 % error was associated with this value based on several factors, including the mole fraction of the total hydrogen in the sample can (neglecting the sample volume as negligible) rather than the buffer at equilibrium. This error was systematic and caused a slight under-dosing compared with the nominal concentration. Volumetric calculations on the rig were difficult because of the extra volumes of the capillary, centre stick tube and the internal tubing of the gas rig. In practice the error associated with the internal tubing, which effectively increased the buffer volume and hence the amount loaded by ~ 2 %, partly counteracts the systematic error above. The largest factor is a 5 % volume error on the buffer itself. The nominal saturated coverage is $x = 2$; an attempt to induce physisorption above that was not observed to succeed. To get the highest coverage, an overpressure of 4810 mbar of H_2 in the buffer, rig and capillary was placed on the sample at 55 K, which was cooled to 30±0.2 K (10 K above the boiling point of H_2). At this point, with an overpressure of 4630 mbar, the valve at the top of the cryostat centre stick was closed and the temperature lowered to 1.5 K. Thus, all the hydrogen remaining in the sample can and centre stick condensed into the sample can. This amount was calculated to be an extra coverage of $(H_2)_{4.13\pm0.15}$. It was

assumed that the hydrogen already on the sample did not desorb in significant quantity in the raising of the temperature to 55 K; this is not necessarily the case. This gave a nominal total coverage, however, of $KC_{24}(H_2)_6$, which was corroborated by comparison of the energy-independent incoherent intensity at this coverage with the same intensity from measurements taken shortly after dosing at the previous concentration (when a similar fraction of the hydrogen was in ortho-state) which also gave a ratio of 2:6.

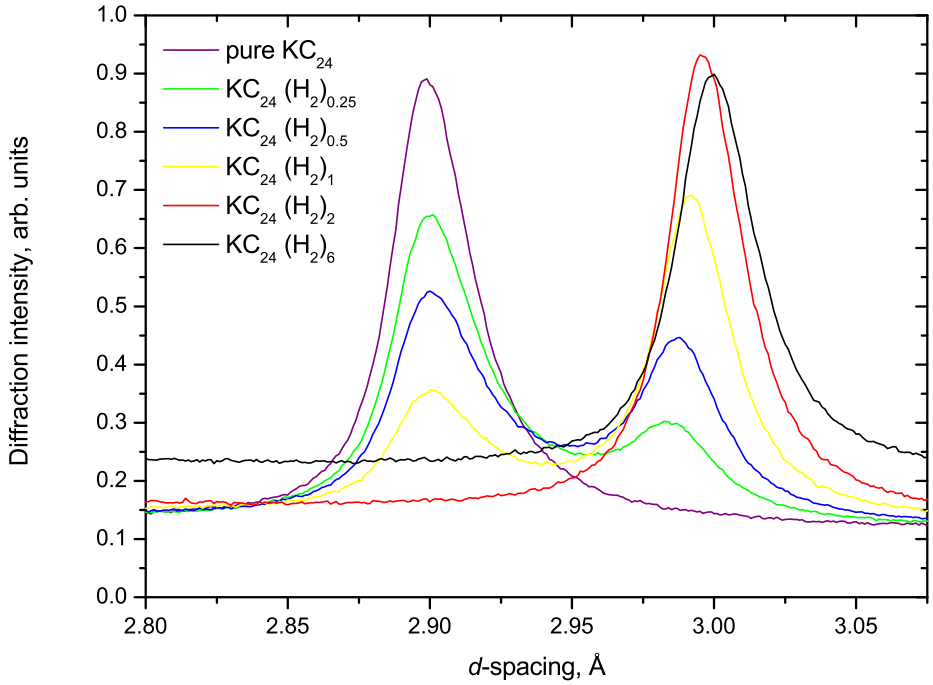

Figure 8.5: The evolution of the (003) diffraction peak of KC_{24} with increasing hydrogen concentration

Following this dosing there was evidence for the formation of bulk solid H_2 in the spectrum and so a small amount of H_2 was removed by annealing at 15 K. This seemed to remove any solid hydrogen; after cooling back to 1.5 K there was no evidence of it.

When the INS energy window was set to -0.8 to 2.0 meV, the diffraction detectors could observe the region of **Q** around the KC_{24} (003) peak, and

chart the phase transition to the hydrogenated sample from the reduction of this peak in favour of one representing the expanded graphite lattice with hydrogen. Quantitative analysis of this change was carried out. Fig. 8.5 shows the evolution of this peak through the increasing hydrogen concentrations. As the hydrogen content of the GIC increases, the intensity of the original peak diminishes and that of the hydrogenated peak increases. The peaks remain discrete, and coexist to suggest that domains of hydrogenated and pure KC_{24} are prevalent, with no other type of structure observable. The peak positions shift slightly with uptake. Only for $x = 6$ is there a significant incoherent signal across the spectrum, which implies that this was the only concentration with significant amounts of ortho-H_2 present, as predicted.

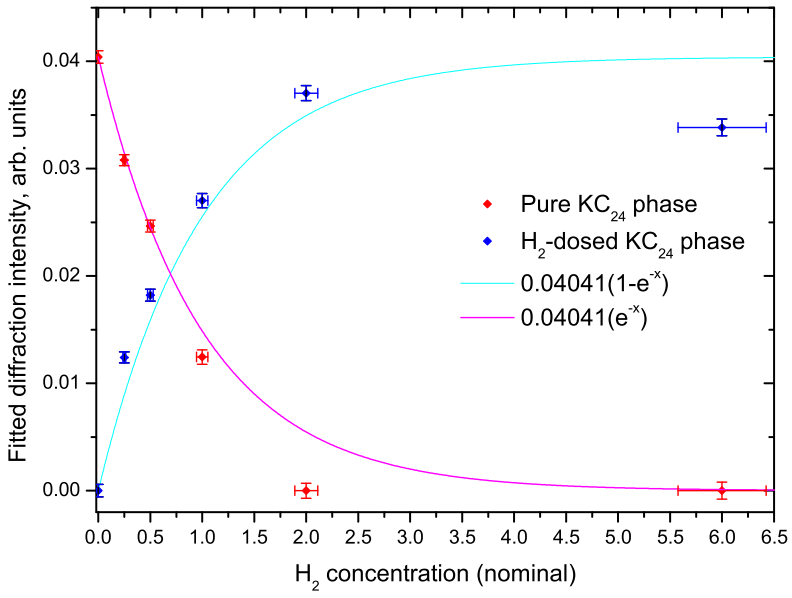

Figure 8.6: (003) peak area for the pure and hydrogenated phases of KC_{24} as a function of coverage

The peaks were fitted to a Lorentzian lineshape and area analysis performed. The fits are shown in Fig. 8.6 where they are compared with functions of the form

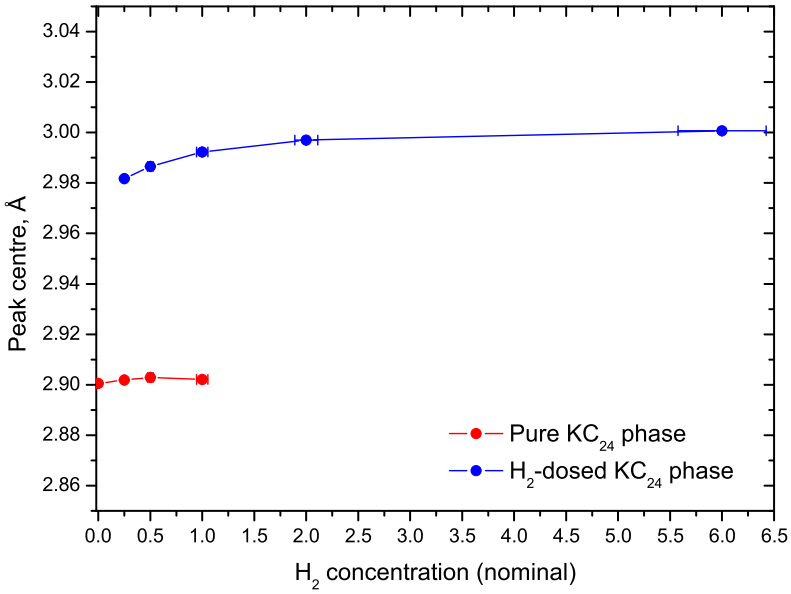

Figure 8.7: (003) peak position for the pure and hydrogenated phases of KC_{24} as a function of coverage

$$y_1 = A(1 - \exp(-x)) \tag{8.1}$$

and

$$y_2 = A\exp(-x), \tag{8.2}$$

where A is the area of the pure KC_{24} peak at $x = 0$, 0.04041. These functions describe the transition from the starting phase to a single hydrogenated phase, by describing the amount of adsorption of hydrogen in the material assuming the sorption probability is proportional to the number of unoccupied sites. This is further evidence for a single site model for the hydrogen in the intercalate. The point at $x = 6$ for the hydrogenated phase is significantly lower than that at $x = 2$, but with the additional ortho-H_2 present this is beyond the assumptions of the model. Fig. 8.7 shows how the fitted peak positions

change with concentration. The difference in *c*-lattice parameter between the single phase pure and hydrogenated KC_{24} is 3.3 %, explained by expansion of the galleries on hydrogen incursion. If the interlayer spacing of the empty galleries is presumed to be unchanged at 3.35 Å, the filled gallery increases in size from 5.35±0.01 to 5.64±0.01 Å.

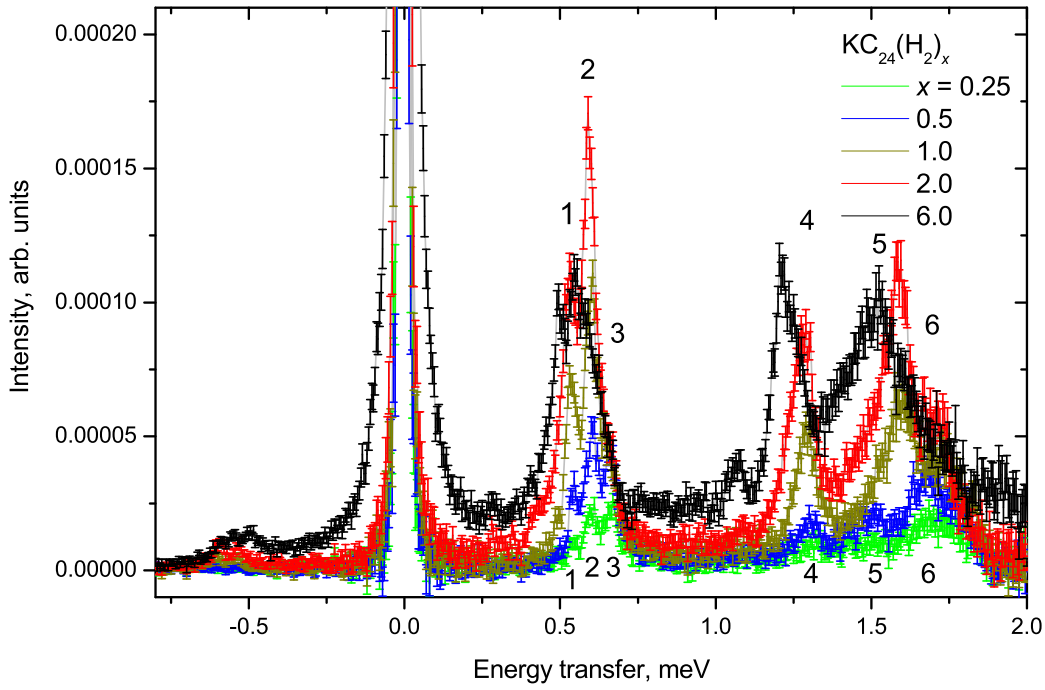

Figure 8.8: INS spectra of $KC_{24}(H_2)_x$ using 25 Hz energy window of IRIS. Two sets of peaks are seen, one around 0.6 meV and the other around 1.5 meV. The relationship between peaks and coverage is complex; however, six peaks are visible at all concentrations. These are numbered 1-6 and are analysed by peak fitting in the text.

Fig. 8.8 shows the spectra of the hydrogen excitations in KC_{24} in the -0.8 to 2.0 meV energy window. The spectrum of pure KC_{24} incorporating the instrument and sample can background and unwanted peaks from the fast neutron pulse has been subtracted from each data set. Visible in the black trace is the large incoherent contribution from unconverted ortho-H_2. Two sets of excitations are prominent; one centred around 0.6 meV, and one around 1.5

meV. These consist each of an apparent triplet system; they grow proportionally with coverage, supporting the single site model. The peak positions shift slightly towards lower energies with coverage until the over-saturation coverage is reached (black) whereupon they shift down more markedly. The higher intensity resulting from unconverted ortho-H_2 can be seen clearly in this pattern, as well as a broadening of the elastic line where the extra intensity is added. The elastic line for the highest coverage ($x = 6$) is 4.83 times the height of the next highest (red).

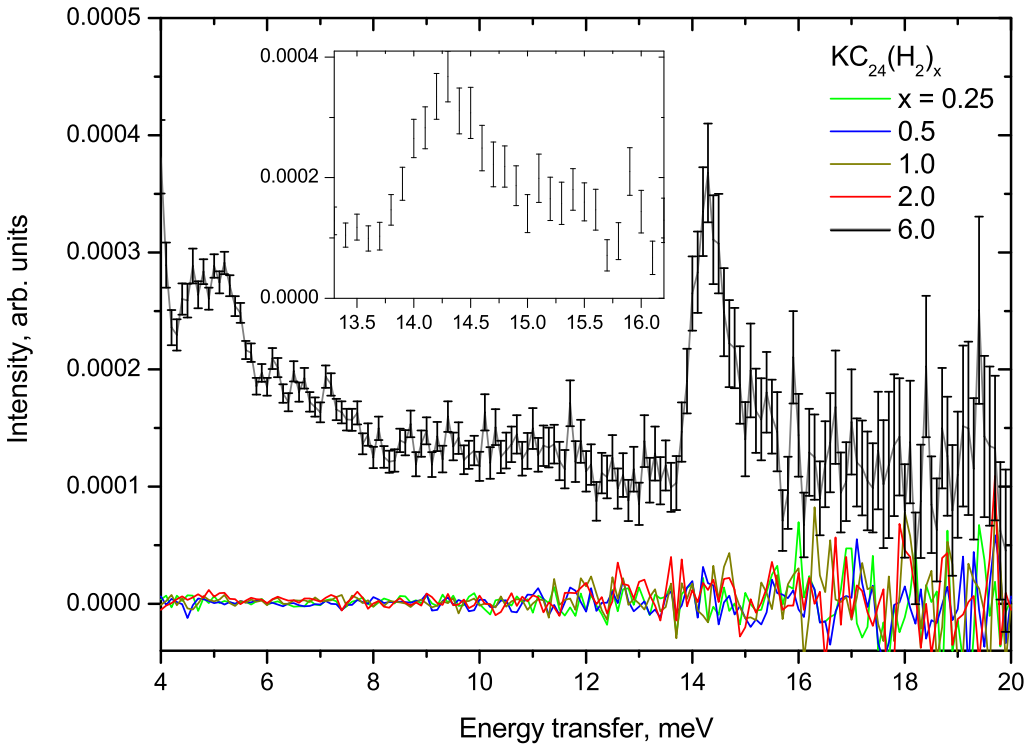

Figure 8.9: INS spectra of $KC_{24}(H_2)_x$ using 50 Hz energy window of IRIS. Error bars have been left off the spectra $0.25 < x < 2.0$ for clarity. The inset shows the split peak about 14.7 meV in detail.

For the lower-energy triplet, the right-hand peak stops growing after $x = 0.5$; the central and left-hand peaks continue to $x = 2$, but at $x = 6$ the central peak intensity is reduced and the peaks broaden and are less resolvable. Interactions of the hydrogen and GIC are likely to reduce the energy of the

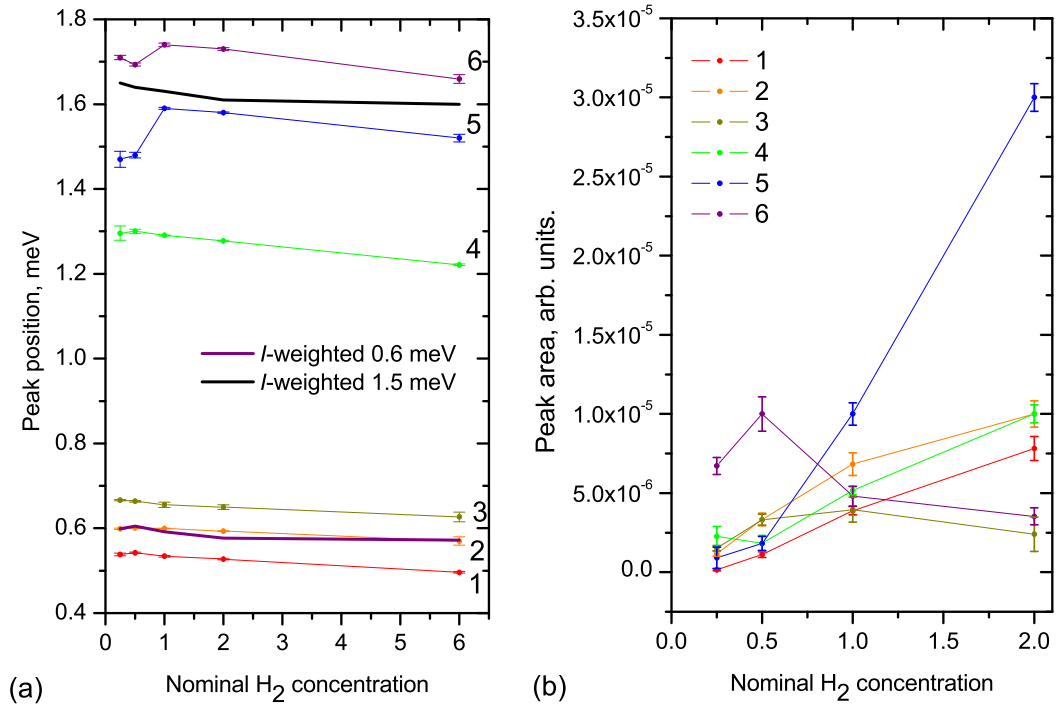

Figure 8.10: INS peak analysis from low-energy transfer spectra of $KC_{24}(H_2)_x$. Peak numbers as labelled in Fig. 8.8. The bold purple line is an intensity-weighted centre of the 0.6 meV multiplet from 0.33 to 0.85 meV and the bold black line an intensity-weighted centre of the 1.5 meV multiplet from 1.1 to 1.9 meV. (a) Peak positions as a function of x. (b) Area under peaks as a function of x.

Table 8.2: INS peak analysis from low-energy transfer spectra of $KC_{24}(H_2)_x$. Peaks as labelled in Fig. 8.8. Fitting was to Lorentzian peaks. Area fitting to $x = 6.0$ data unreliable because of peak overlap. Pos. = peak position

	Peak no.	1	2	3	4	5	6
x							
0.25	pos. (meV)	0.538	0.599	0.666	1.296	1.47	1.71
	area (arb. u.)	1.49×10^{-7}	1.16×10^{-6}	1.52×10^{-6}	2.25×10^{-6}	9.02×10^{-7}	6.72×10^{-6}
0.50	position	0.542	0.601	0.663	1.300	1.480	1.693
	area	1.12×10^{-6}	3.33×10^{-6}	3.32×10^{-6}	1.84×10^{-6}	1.81×10^{-6}	1×10^{-5}
1.0	position	0.534	0.599	0.655	1.291	1.59	1.74
	area	3.89×10^{-6}	6.83×10^{-6}	3.95×10^{-6}	5.16×10^{-6}	1×10^{-5}	4.8×10^{-6}
2.0	position	0.527	0.593	0.650	1.278	1.58	1.73
	area	7.82×10^{-6}	1×10^{-5}	2.4×10^{-6}	1×10^{-5}	3×10^{-5}	3.53×10^{-6}
6.0	position	0.496	0.57	0.627	1.221	1.52	1.660
	area	-	-	-	-	-	-

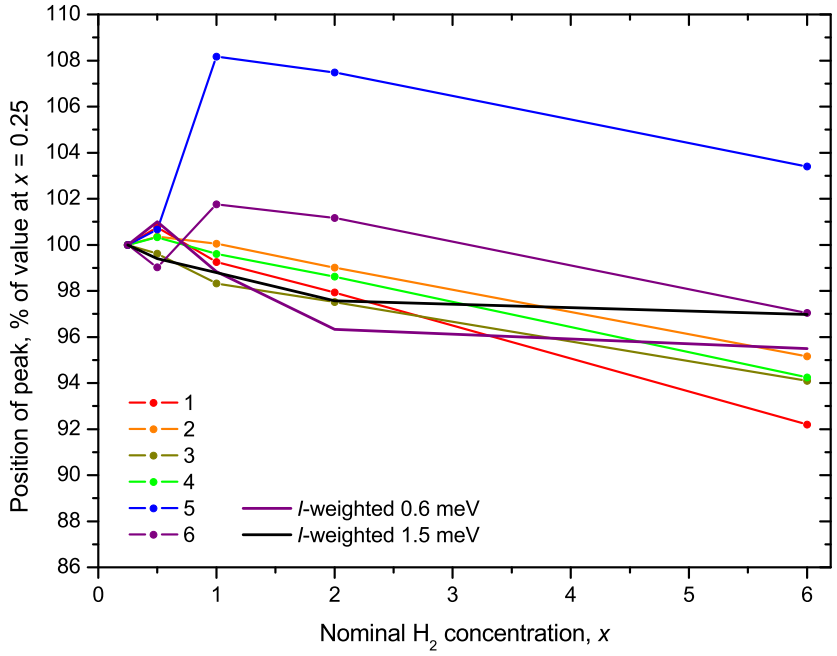

Figure 8.11: Renormalised INS peak analysis from $KC_{24}(H_2)_x$ showing peak positions as a percentage of their values at $x = 0.25$. Peak numbers as labelled in Fig. 8.8. The bold purple line is an intensity-weighted centre of the 0.6 multiplet from 0.33 to 0.85 meV and the bold black line an intensity-weighted sum of the 1.5 meV multiplet from 1.1 to 1.9 meV.

excitations as coverage increases; this seems to be observed (see Table 8.2 for a summary of the six peak positions and intensities). The peak positions and intensities from the table are shown in Fig. 8.10. All six peaks shift down in energy as a function of coverage, continuing proportionally for $2.0 < x < 6.0$ even though the GIC should be full and thus the site barriers at a maximum at $x = 2.0$. An intensity-weighted average of the scattering was taken for the 0.6 meV region between 0.33 and 0.85 meV, and another for the 1.5 meV region between 1.1 and 1.9 meV, which are also plotted in Fig. 8.10(a). They show that the centre of each transition does indeed not reduce as much for $2 < x < 6$, as would be expected if the sites with high potential barrier were filled. This is clearer when the positions are expressed as a percentage of the energy transfer at $x = 0.25$ in Fig. 8.11.

The peak intensities are harder to quantify due to overlap. For the higher energy triplet, the peaks are somewhat broader and the two higher energy peaks appear to coalesce as the concentration becomes higher than $x = 1$. The large increase in the area of peak 5 coupled with the peak position shift up in energy for 5 and 6 for $0.5 < x < 1.0$ suggest a more complex system here than can be fitted, with several unresolvable subpeaks. A new peak appears at 1.07 meV for $x > 1$ which is distinct from the ortho-H_2 background. The peak positions are renormalised to their values at $x = 0.25$ in Fig. 8.11. From this there does not seem to be any significant difference in peak energy shift between the 0.6 and 1.5 meV multiplets. As the energy splitting is greater for the 1.5 meV peaks they do not directly correspond to the 0.6 meV triplet.

Fig. 8.9 shows the excitations at identical coverages in the 4-20 meV range. The IRIS neutron flux decreases with energy transfer so that the statistical error is largest at 20 meV and to make the plot clearer the data was rebinned in 0.1 meV steps. It can still be seen that within the errors there is no intensity in this region for $0.25 < x < 2.0$. At the $x = 6$ concentration (black) considerable

intensity is observed; a quasi-continuous spectrum with a peak around 5 meV, and a possible split roton peak around 14.7 meV, as in the previous experiment when hydrogen was condensed onto the ammoniated sample (§ 8.1). The low neutron flux available at this energy on IRIS makes the precise delineation of the peaks difficult. The lower energy splitting, at 14.3±0.1 meV, has approximately double the intensity of the upper energy splitting at 15.4±0.1 meV, and is approximately half as far from the unperturbed 14.7 meV value, both characteristics predicted by the potential model. This can be quantified as a 2.5 meV barrier to free rotation. A likely explanation is that the para-H_2 fills the available tunnelling wells after conversion at $x = 2$, and the extra hydrogen delivered to the sample at $x = 6$, in the 3:1 ortho-para ratio, is filling extra interlayer space where a weak potential from the graphite sheets causes the weak splitting seen. Para-H_2 is a good probe of strongly-bound states in the intercalate; we see this especially as the quasi-continuous spectrum does not appear until a proportion of ortho-H_2 is in the sample. This is likely to be a combination of elastic scattering from ortho-H_2 and the para-ortho density of states.

8.3 High energy modes of H_2 in KC_{24}

The raw data from the TOSCA forward and backscattering detectors were focused separately. The 'background' spectrum of KC_{24} was subtracted from each hydrogenated data set. The forward scattering data are shown in Fig. 8.12 and the backscattering in Fig. 8.13. The data sets share principal features. A well-defined peak centred about 48 meV exists for all H_2 coverages. A smaller peak can be seen about 95 meV but the resolution limits the visible detail and it is arguable if any features higher in energy can be made out. In forward scattering there is the hint of a peak for the highest coverage just below 200

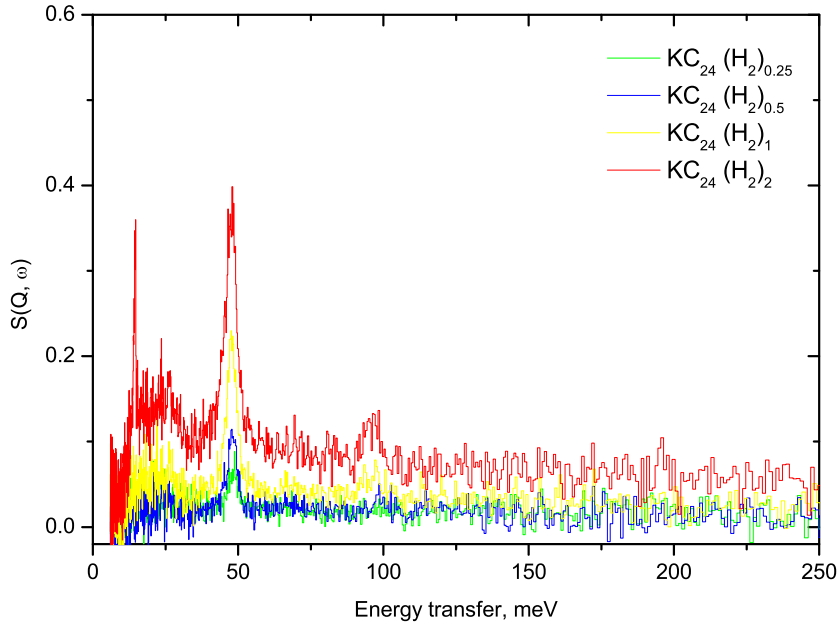

Figure 8.12: INS spectra of $KC_{24}(H_2)_x$ on TOSCA from forward scattering banks

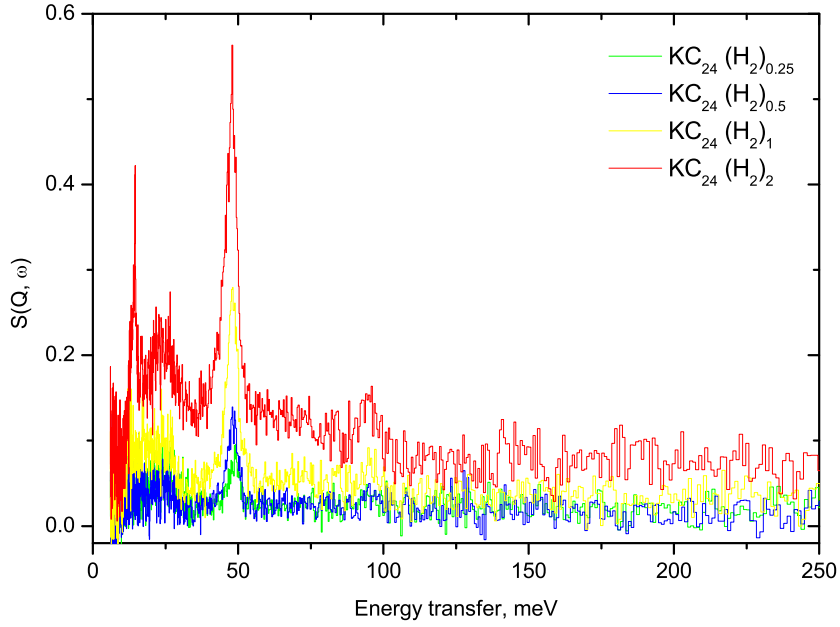

Figure 8.13: INS spectra of $KC_{24}(H_2)_x$ on TOSCA from backscattering banks

meV but it is very similar to the error amplitude. The intensity of both the features and the background increases with coverage, and for all coverages, a continuous spectrum with a peak at ∼25 meV can be seen in both scattering angles, pierced by a 14.7 meV rotor peak. The 14.7 meV rotor was not seen at the same nominal coverage on IRIS (compare with Fig. 8.9). This discrepancy may be a result of inaccuracies in the hydrogen dosing, or a sample orientational difference. The samples for the latter two experiments were from a single batch, making it improbable that there were large morphological differences. The systematic error on the concentration value for TOSCA was calculated to be +10.4 % from the extra volume of the pipework and sample can as measured during gas loading. This value, much larger than expected, would be increased by the low temperature of the gas in the sample chamber when loading at 50 K, by up to an extra 2.8 %. In this case the nominal loading values are somewhat inaccurate and would be better represented as $x = 0.28, 0.55, 1.11$, and 2.22. The appearance of the roton peak at "$x = 2$" is explicable because the real concentration is over-saturated and hydrogen unable to enter the sorption sites is engaging in nearly-free rotation somewhere in the sample. Unhappily, this makes the data more difficult to compare directly with the IRIS experiments. The integrated intensity under the peak at 48 meV for forward and backscattering is shown as a function of the refined concentration values in Fig. 8.14, with integrated intensities for the elastic line, 0.6 meV and 1.5 meV multiplet regions from the previous experiment, all normalised to the intensity at $x = 2$, as the coverage with the least uncertainty ($x = 2.22$ for the TOSCA data).

It can be seen that the intensities agree well for all the INS modes up to approximately $x = 1.5$. This is evidence that the different modes are products of a single process, the filling of the homogenous sites in the sample. The 48 meV peak intensity appears to grow linearly with coverage for both forward

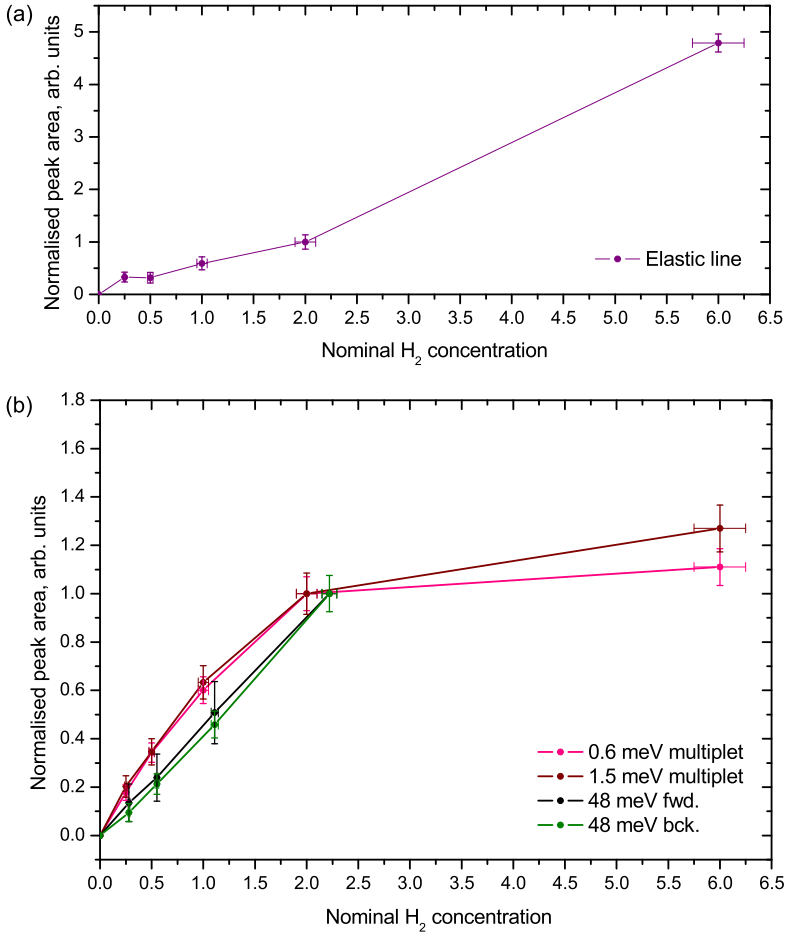

Figure 8.14: Integrated intensity of four spectral regions in KC_{24} $(H_2)_x$ as a function of coverage, normalised to $x = 2$ (2.22 for 48 meV plots): (a) the elastic line from -0.5 to 0.5 meV, (b) the 0.6 meV multiplet from 0.33 to 0.85 meV, the 1.5 meV multiplet from 1.1 to 1.9 meV, and the 48 meV excitations in forward and backscattering on TOSCA. The INS modes all grow in a like manner with time; the 0.6 meV and 1.5 meV multiplets do not fill linearly as far as $x = 6$ but saturate as expected if the sites fill. The elastic line does not grow significantly until after the sorption sites have been filled with para-H_2

and backscattering, but the errors are large as the scattered neutron flux is low. The intensity begins to saturate at $x = 2$ for the low-energy multiplets, and little intensity is added at $x = 6$; this is evidence to link the 0.6 and 1.5 meV modes. The elastic line grows slowly until $x = 2$ whereupon it gains almost an order of magnitude more intensity to $x = 6$. This is expected as the sites are full at $x = 2$ and the additional hydrogen has a large 3:1 ortho-para-H_2 proportion which adds to the elastic line as shown.

8.4 An improved model of H_2 sorption in KC_{24}

8.4.1 Reconciling the observed INS modes

It can be seen that the Stead model does not fully explain the data. Importantly, only one principal librational peak is seen, at 48 meV. (The TOSCA feature at ∼96 meV is most likely a multiple scattering event as it doubles the 48 meV energy and is far less intense than this fundamental; the same reasoning applies to the hint of a peak at 200 meV which quadruples the energy). This is evidence against there being two distinct sites in two potential wells: a distinct libration should be seen for each site if that were the case. This can be added to the observed proportional filling of all the low-energy modes simultaneously; neither is there evidence in the KC_{24} uptake isotherms to suggest two sites with separate sorption enthalpies. From this it is possible to conclude that only one site exists in KC_{24}, making it significantly different from Rb- and CsC_{24}. In this case, why are two separated sets of excitations visible at 0.6 and ∼1.5 meV? To explain this, Felix Fernandez-Alonso, instrument responsible for IRIS, has formulated a model following discussions with the author [116], which is henceforth explained.

Applying a $\cos^2\theta$ potential to the tunnelling transition at 0.6 meV results in an expected librational mode at 51.1 meV, which is close to the observed transition at 48 meV. The resolution of TOSCA is about 0.75 meV at 48 meV; the libron peak has a width of 4.96 ± 0.47 meV for coverage $x = 1$; the librational peak is therefore certain to be a composite of unresolvable combination excitations. The red-shift between the theoretical and experimental value of the transition energy was observed in similar circumstances in RbC_{24} by Smith *et al.* [81] as described in § 3.3.3; the first libron expected at 39 meV was seen experimentally at 32 meV. This may be interpreted in two ways: firstly, as renormalisation of the librational energies caused by a slight elongation of the H-H bond in the molecule. This value would be 3-4 %, which yields a reduced rotational constant of ∼6.9 meV. The offset seen by Smith represents about an 8-10 % elongation of the molecular axis if this picture holds, implying that some charge transfer is taking place between the H_2 and the graphite and that at least part of the H_2 site bonding is chemisorptive. The second possibility is that the well potential is not fully symmetric, in which case the H_2 in a site close to a K ion experiences a different component of the potential parallel and perpendicular to the K-H_2 direction. This was tested with modelling and is discussed below.

Table 8.3: Calculated librational energies (E_{lib} and resulting potentials (V_2) from the 0.6 meV triplet energies (E_{tunn}) in $KC_{24}(H_2)_x$ (all meV)

E_{tunn}	E_{lib}	V_2
0.54	52.3	140.5
0.60	51.1	136.0
0.67	49.8	131.0

It may be possible to attribute the 0.6 meV multiplet to H_2 in multiple sites with almost identical librational barriers. The potential model coupled to the

0.6 meV subpeaks was used to calculate expected libron energies and the well depth. The results are shown in Table 8.3. The potential differences are small compared with the well depth, and the first pure librational peaks expected are unlikely to be resolvable on TOSCA and may well be present in the broad peak at 48 meV, in combination with the translational modes. The librational splitting is approximately 50 μeV, the same as the width of the ground state splitting, which on TOSCA is resolution-limited at this energy: thus the main contribution to the width of this peak is the translational modes. The second set of features about 1.5 meV is then a combination of the tunnelling transition with H_2 centre-of-mass vibrations.

The pure vibrational transitions, which would be visible at 0.7 - 1.1 meV by this scheme, are apparently not present. Incoherent neutron scattering from H_2 tunnelling transitions causes a spin-flip, from para- to ortho-H_2. In the absence of this, such as in pure centre-of-mass motions, there is no observable intensity, as this would be weighted by the coherent cross-section of hydrogen which is $\sim$2 orders of magnitude weaker. One would however expect to see further vibrational modes higher in energy as noted for $RbC_{24}(H_2)_{1.0}$ by Smith *et al.* [81]. These are combinations of tunnelling and translational modes. There are no strong features that could be assigned to these modes in the TOSCA spectra. However, the 0° sample alignment in TOSCA caused the layer planes to be perpendicular to the incoming beam. If $\mathbf{u}$ represents an eigenvector of the mode, and $\mathbf{Q}$ is the momentum transfer vector, the scattering is $\mathbf{u}.\mathbf{Q}$ which for $\mathbf{u}\perp\mathbf{Q}$ is zero: as the H_2-K vibrations are parallel to the layers, these motions would not be detected. Looking at the spectra, it may be that the broad excitation centred on $\sim$25 meV is a manifestation of these modes, as it exists at all coverages. In this case it results from mosaic spread of the sample away from the $\mathbf{u}\perp\mathbf{Q}$ condition most probably.

8.4.2 A K^+-H_2 interaction model

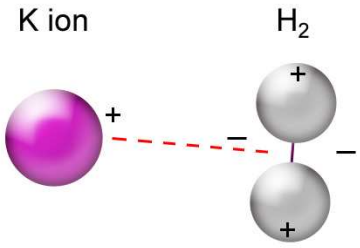

Figure 8.15: Proposed orientation of an adsorbed H_2 molecule with respect to a K ion in $KC_{24}(H_2)_x$

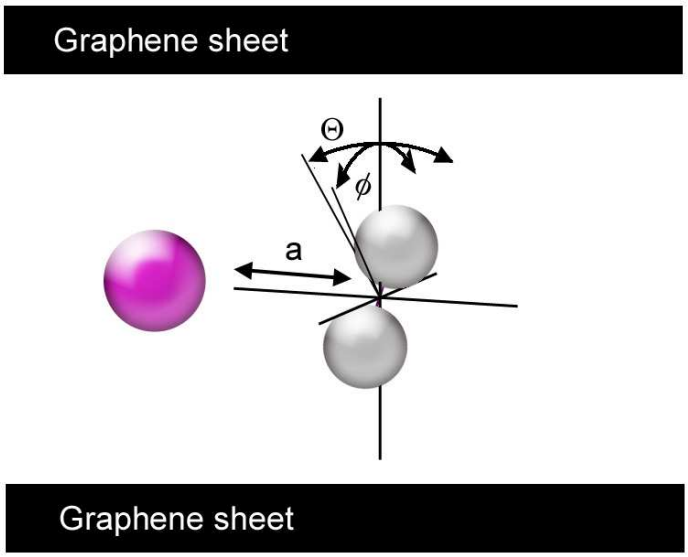

Figure 8.16: Oscillatory modes of an adsorbed H_2 molecule with respect to a K ion in $KC_{24}(H_2)_x$: (a) K-H_2 vibrations, (b) H_2 librations, (c) H_2 tunnelling rotations

The potential barrier V_2 for a tunnelling mode at 0.6 meV is calculated to be $18.5B$, where $B = 7.35$ meV as before; thus the potential well is 136±1 meV deep (§ 3.3.3). The potential well of a 1.2 meV excitation is calculated to be 110 meV deep; however, the more probable explanation for the 1.2-1.7 meV excitations is that they are a combination of the centre of mass motions and the low-energy tunnelling modes. To explore this it is necessary to adopt a

picture of the hydrogen interactions inside KC_{24}. From the fact that hydrogen is far more strongly bound than in undoped graphite, and that the saturation stoichiometry is linked to the density of metal ions, it is rational to conclude that the sorbed H_2 molecules are bound preferentially to the K ions. In that case, the molecule may orient itself with its axis parallel or perpendicular with the K-H_2 bond. If the K^+-H_2 complex is placed in the graphite gallery, as shown in Fig. 8.16, we can see it has several degrees of freedom: principally, H_2 centre-of-mass oscillations along the K-H_2 bonding distance, denoted a in the figure, can be combined with librations about the H_2 bond centre. These latter have two angular degrees of freedom, Θ, in the plane of the molecular bond and the K^+-H_2 distance, and ϕ, in the plane perpendicular to the K^+-H_2 distance. We can model the molecule as a quadrupole by examining the long range part of ion-molecule interactions, for which studies exist in the literature [117] [118], and then quantify it for for K^+-H_2. For a hydrogen molecule interacting with a point charge, the long-range potential is governed by two terms: an ion-quadrupole interaction, of the form

$$V_{quad}(R,\Theta) = (\frac{Q_{H_2}}{R^3})P_2(\cos\Theta) \tag{8.3}$$

where R is the ion-molecule distance, Q_{H_2} the quadrupole tensor, and an ion to induced dipole interaction, proportional to the polarisability of the H_2 and of the form

$$V_{dipole}(R,\Theta) = (\frac{1}{R^4})(\frac{\alpha}{2} + \frac{1}{3}(\alpha_{par} - \alpha_{per})P_2(\cos\Theta)) \tag{8.4}$$

where α is the polarisability average, α_{par} and α_{per} the components parallel and perpendicular to the H_2 axis. Values for these are taken from the literature [118]; they are expressed in atomic units as $Q_{H_2} = 0.460$, $\alpha = 5.179$,

$\alpha_{par} = 6.305$ and $\alpha_{per} = 4.578$. To calculate the orientational energies from the potential, a value for R of 2.92 Å is also taken from the literature [119]. As the value of R is reasonably large it can be seen that the ion-quadrupole interaction will dominate the ion-dipole interaction.

In this case, the most likely orientation is perpendicular (Fig. 8.15). In this scenario, the dominant interaction is where the positively-charged K ion is more strongly attracted to the inter-H bond where the electron density is high, and repels the H atoms equally strongly.

The resulting orientational potential for a free K^+-H_2 complex is ∼90 meV, which is 65% of the 136 meV value determined from INS. If this magnitude is correct, then the remainder of the real potential comes from H_2 interaction with the graphene sheets on either side. It can be deduced that there is likely to be a large Θ potential from electrostatic repulsion of the K ion, but there is no such hindrance in the ϕ direction and so, in this picture, nearly-free rotation in this plane should be possible. This would be modulated chiefly by the graphite-hydrogen interactions, which are not expected to be large, and which contribute equally to the potential in Θ. This is not seen in the spectra, because it would imply the lowest line in the librational spectrum would be $\sim B_{H_2}$, i.e. 7.35 meV.

The model arising from the observed INS spectral features is that of an orientational potential for molecular rotation of the form $V_\Theta \sin^2(\Theta)$, where V_Θ is the depth of the potential well. As the H_2 molecule is locked to a single axis in this picture, the ground and first excited states become degenerate as V_Θ goes to infinity. The experimental data is far closer to this limit than to free rotation; this is given credence by the band head at 0.6 meV. The additional fine structure in this para→ortho tunnelling transition cannot be librational in nature, as the upper and lower librational eigenstates are singly degenerate.

It and the split excitations at ∼1.5 meV must therefore be a consequence of the tunnelling and centre-of-mass translational modes. Pure translational bands do not involve the para-ortho transition and therefore scatter coherently rather than incoherently, and the H_2 coherent scattering strength is two orders of magnitude weaker.

8.5 *Ab initio* modelling of H_2 in KC_{14}

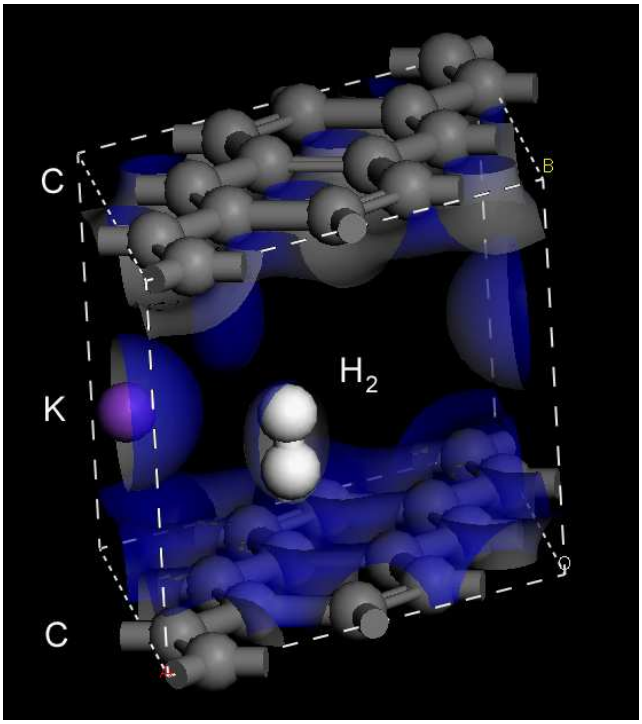

Figure 8.17: Position of H_2 molecule in CASTEP model of KC_{14} after relaxation, showing the minimum energy configuration of the molecular axis perpendicular to the layers and under a graphite ring centre [87].

As part of a wider collaboration arising from this investigation, first principles density functional theory (DFT) modelling using CASTEP [85] has been undertaken [87]. It promises to provide new insight into H_2 sorption in KC_{24}. The model structure is KC_{14}, a stage-1 version of KC_{28} with the same in-plane

K superlattice. It is presumed that there are no interactions between K ions in adjacent layers and that this approximates on a local scale to the stage-2 system. This is justifiable because DFT is not well able to calculate van der Waals-type forces; the interlayer spacing, set to the experimental pure KC_{24} value of 5.35 Å, is not allowed to relax. Initial results show that CASTEP is able to model the charge transfer from K ion to graphite layers, with most donated charge lying on the benzene rings above and below the metal. An H_2 molecule is placed in the layer and allowed to move to a minimum energy position; Fig. 8.17 shows the result. The H_2 takes up a position perpendicular to the layers and is sited under a benzene ring centre 2.89 Å from a K ion. This compares very well with the literature value of 2.92 Å [119] and the ion-quadrupole treatment of the K-H_2 interaction.

Following this, a series of calculations was performed assuming further H_2 molecules were able to sit under any of the five empty graphite rings surrounding an ion. As these are sited they come into contact with H_2 molecules around nearby ions. The minimum H_2-H_2 distance in found to be 2.98 Å in $KC_{14}(H_2)_2$ but 1.96 Å in $KC_{14}(H_2)_3$, leading to a repulsive energy cost in the latter, and providing evidence for why $x = 2$ appears to be the maximum uptake of H_2/K in these systems. As the distance between benzene ring centres in graphite is 2.48 Å, and this implies an H_2-H_2 repulsive energy of ∼61 meV, it does seem unlikely that H_2 density on graphite surfaces will be able to attain 1 molecule/ring, especially in the absence of charging.

The rotational model used has two independent rotational degrees of freedom, Θ and ϕ, defined as previously. When the molecule is assumed to be close to the K ion and treated classically, the ϕ-dependent potential V_ϕ is found by CASTEP to be 25.7 meV and the Θ-dependent potential V_Θ is found to be 126.3 meV: this latter is remarkably close to the potential inferred from the INS data, which is apparently symmetric at 136 meV for both ϕ and Θ di-

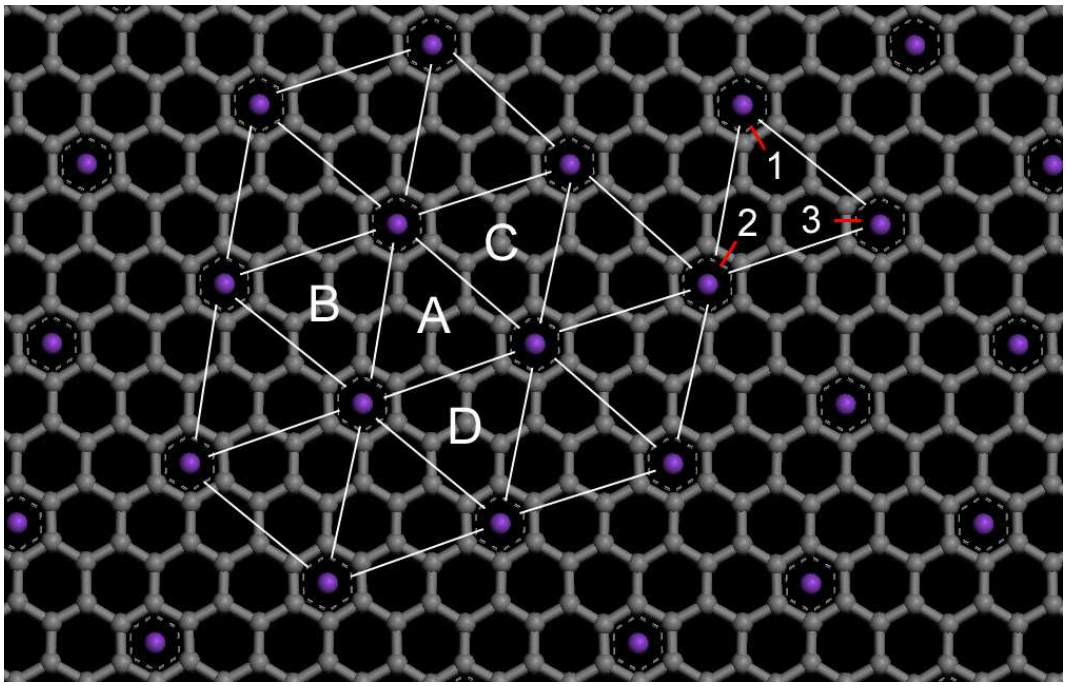

Figure 8.18: Possible sites for hydrogen molecules in KC_{28} lattice. Dividing the potassium network as shown (white lines) forms trigonal sites such as A-D and implies a saturated stoichiometry of $2H_2$ per K ion, as seen experimentally in KC_{24}. Site A has B, C, and D as nearest neighbour sites. Analysis of the K^+-H_2 potential and *ab initio* modelling suggests three local energy minima within each site, labelled 1, 2 and 3, with each relating to a different ion (red links show this) and in any one of which a hydrogen molecule can reside if the state is filled.

rections. The H-H bond distance varies by less than 10^{-2} Å, suggesting that the assignation of the librational red-shift 51 → 48 meV to bond elongation is erroneous. V_ϕ has no contribution from the ion-quadrupole interaction in this picture and is therefore assumed to represent graphite-hydrogen interactions: but this model fails to fit the experimental results, suggesting a different approach is needed for at least the ϕ-component modelling.

In a trigonal site such as those labelled A-D in Fig. 8.18, there are three potential positions for the hydrogen, under each of the three central graphite hexagons (labelled 1 to 3 in the figure). Each has a minimum energy configuration related to the nearest potassium ion of the three that define the site. The hydrogen is liable to jump between these three positions if the site is filled. The $V(\Theta, \phi)$ potential holds as long as the jump timescales are much longer than the librational period, as the H_2 molecule has time to achieve its minimum energy configuration relative to the nearest ion before the next jump. Θ and ϕ vary by 120° between each position as the ions are corners of an equilateral triangle.

A very different picture emerges if the hydrogen is delocalised, in the quantum mechanical sense, over the three sites. A seed idea for this was given by the Stead model, where the molecule was considered to reside at the centre of the trigonal site between three ions. CASTEP results show this to be unlikely as it would imply a site directly under a carbon atom. If the switching between sites occurs much faster than the librational period, the molecule will not reduce its orientational energy before relocating. Taking this to the limit of quantum delocalisation of the molecule between the three sites simultaneously, the potential experienced by the H_2 is an average of the potentials in all three sites, for an invariant molecular orientation. This is given by

$$\langle V(\Theta,\phi)\rangle = \frac{1}{N}\sum_{i=1,N} V(\Theta_i,\phi_i), \tag{8.5}$$

where i labels the sites 1 to N (1 to 3 in this case). This has been mathematically treated [87]. In the above equation, the co-ordinate frame is a sensible one for the K^+-H_2 complex in graphite. The z-axis is along the K-H_2 centre of mass axis, the x-axis is along the graphite c-axis, and thus the y-axis lies in the plane. To model the potential in three sites, these axes are redefined so that the z-axis points along the graphite c-axis. In the new frame, Θ will be invariant to rotation of the H_2 centre of mass as the three sites have a common z-axis and thus rotation will only involve ϕ. For a single site in this new frame, the potential resulting from a classical localised site model of the type outlined in the previous section, is found to be

$$V(\Theta_i,\phi_i) = V_\Theta\{1-(1-\frac{V_\phi}{V_\Theta})\sin^2\phi\}\sin^2\Theta, \tag{8.6}$$

which is a function of both angles as expected. When averaging over the three sites, the ϕ-dependence is removed as the ϕ components cancel around the triangle. The resulting potential is given by

$$\langle V(\Theta,\phi)\rangle = (\frac{V_\Theta+V_\phi}{2})\sin^2\Theta = \langle V\rangle\sin^2\Theta. \tag{8.7}$$

The potential is considerably simplified and only a function of Θ. To determine the delocalised potential, the Θ and ϕ components of the potential from DFT calculations were averaged. $\langle V\rangle^{INS}$ from experiment was 136 meV; the DFT calculation gives $V_\phi^{DFT} = 25.7$ meV and $V_\Theta^{DFT} = 126.3$ meV so $\langle V\rangle^{DFT} = 76.0$ meV. We interpret this discrepancy by assuming that DFT accounts successfully for the K-H_2 potential, as evidenced by the calculation

of the K-H_2 ion-quadrupole moment of 90 meV in the previous section, but underestimates the hydrogen-graphite interactions which compose a proportion of the experimental $\langle V \rangle^{INS}$. If the amount which the DFT fails to account for is labelled V_δ,

$$\langle V \rangle^{INS} = \frac{(V_\Theta^{DFT} + V_\delta) + (V_\phi^{DFT} + V_\delta)}{2}, \tag{8.8}$$

giving $V_\delta \approx 60$ meV. If the value $V_\phi^{DFT} = 25.7$ meV represents only the H_2-graphite potential captured by DFT, this suggests that the DFT is unable to model 70 % of the graphite-hydrogen interactions, an expected result as the method cannot reliably treat van der Waals interactions. As the graphite-H_2 potential, possessing 6-fold symmetry, is quasi-cylindrically symmetric, a similar amount contributes to $V_\Theta^{DFT} = 126.3$ meV as well and may be subtracted. The resulting K^+-H_2 component of the Θ potential is 100.6 meV, which is well-correlated with the 90 meV result from literature. The estimated H_2-graphite potential is ∼85 meV. As this is of the order of the K^+-H_2 interaction it seems quite large; however, the contribution from each graphene sheet is only 42.5 meV. If an interaction of this magnitude implies an electrostatic interaction of the H_2 with negative charge density on the graphene sheet (specifically the interlayer bands) then the result implies that a redistribution of donated electron density occurs away from the graphite rings above (below) the K ion, to the rings above (below) the H_2. This is something which CASTEP should be able to show and awaits further investigation.

If the 'hidden' graphite-H_2 potential V_δ of 60 meV is incorporated into the classical site model, the resulting potential well still does not match the experimental evidence, so it seems that the delocalisation model provides a better fit to experiment in this case too. Furthermore, the potential model can be fitted to the observed tunnelling and librational excitations to quantify

V_Θ and V_ϕ. The best fit is for $V_\Theta = 125$ meV and $V_\phi = 150$ meV which leads to predicted transitions at 0.590 and 48.2 meV. Thus an asymmetric well gives a likely explanation for the reduction in the first librational band from that expected for a cylindrically-symmetric one, without recourse to an H-H bond elongation picture. It is not certain without further modelling if this is a good picture for the RbC_{24} librational red-shift explored by Smith [81].

This theoretical approach, in conclusion, provides a novel interpretation of the hydrogen siting as a centre-of-mass delocalisation between three ring-centre positions in the original trigonal site. It negates the discrepancy in the classical K^+-H_2 site model because it explains why the molecule is not observed to rotate against a shallower potential in ϕ than Θ, and thus elegantly links the DFT results to the experimental values, providing quantitative predictions about the character and magnitude of the competing interactions in the system. DFT calculations are shown to successfully reproduce a classical K^+-H_2 complex although they are not able to handle interlayer potentials and by extension forces, underestimating these by a significant proportion. It is also necessary to adjust the interlayer spacing to the 5.65 Å layer spacing found when hydrogen is adsorbed. DFT is however likely to be of utility in the further investigation of this system, and the treatment so far outlined can be extended to hydrogen in Rb- and CsC_{24} systems and the original theoretical treatment by Stead *et al.*, and others. For those materials the in-plane structure has been more reliably determined; however, a good-sized question mark remains about the validity of the KC_{28}/KC_{14} structural model as a representation of the KC_{24}-stoichiometry sample and, in the Rb- and Cs-GICs, the identity of the second site observed from preferential filling in the INS data. The differences between the INS modes between KC_{24} and these stablemates may be explicable by the varying *c*-axis expansion under hydrogen loading: for RbC_{24} it is ∼2 % of the *c*-parameter and for CsC_{24}, zero [42]. This is possible because the effective

diameter of the Cs ion is greater than that of the H_2 molecule. The H_2-graphite potential would in this case be much smaller.

Isotopic substitution of D_2 and HD for H_2 in the K-GIC system should provide a useful test of the model as the molecular rotational constant varies with mass. It is also known that D_2 adsorption saturates more readily than H_2 [64], though the saturated concentration is the same. This implies a site preference for D_2 over H_2, and the model may be able to account for this.

This model does not explain the fine structure present in the tunnelling transition about 0.6 meV; it is difficult to draw rigorous conclusions about this from the data or the model as formulated. Below are outlined some possibilities:

One possibility is that the potential seen by a hydrogen molecule in a filled site, say at A in Fig. 8.18, depends on the number of occupied neighbouring sites in the KC_{28} structure by an as-yet-unspecified inter-site potential. One might expect four discrete energy splittings populating from highest energy to lower energies as coverage increases and the relative population changes in favour of sites with more neighbours, and hence deeper potentials. Comparison with the 0.6 meV structure in Fig. 8.8 shows a limited agreement with this prediction; however, there appear to be only three significant peaks present and the observed intensities with coverage do not follow the prediction.

An alternative interpretation is to assign the 0.6 meV peak splittings to varying homogenous sites in a number of co-existing hydrogenated phases, after Lindsell [78]. However, the splittings are close enough that the sites would be very similar, and they are well defined enough for $x < 2.0$ that a non-ordered incommensurate structure with a discrete site degeneracy of only three or four would have to be invoked. In debating this we are hamstrung by the difficulty of solving the in-plane structure; it is certain that further work in

this direction would be very useful, as our model is dependent on large parts of the sample taking on a KC_{28} distribution of metal ions. Several near-KC_{28} incommensurate structures may provide the splitting required, though the low symmetry of such structures makes DFT calculations and Rietveld refinement intensive. The delocalisation of hydrogen may help to explain the difficulty in obtaining an H_2/D_2 signature from the diffraction data; there is in effect no hydrogen lattice.

A greater likelihood in the light of the model is that the orientational barrier of the H_2 rotation caused by V_ϕ being greater than V_Θ causes an M-level splitting. This barrier has been fitted to $\sim$25 meV which could cause splitting of 50 μeV which is of the order of that seen for the 0.6 meV band. Investigating this as well as the higher-lying combination bands would require a detailed knowledge of the centre-of-mass potential energy surface of H_2 in the intercalate. This is a task beyond the remit of the present work, as it would require extensive electronic structure calculations.

Elucidation is sought as to whether any of these pictures can accurately determine not only the number of filled sites but also the site availability in the GIC using the INS data. Although the filling picture in Rb- and CsC_{24} is more complicated, a revisit of the earlier experiments using high-resolution INS, isotopic substitution and DFT may lead to a better understanding of the site symmetries in these systems as well.

Chapter 9

Conclusions and further work

9.1 Summary and discussion of achievements

The project aimed to explore hydrogen in graphite intercalates with the intention of understanding the physical behaviour of these materials and amassing evidence to outline a model for tuning their properties to make them more suitable for the storage of hydrogen. The key storage properties are set externally by bodies such as the US DoE and motor manufacturers and address the technological goals for a commercially viable storage medium. Thus the investigation was carried out with an eye to the end-use capabilities, although this did not prevent our investigation from following scientifically-relevant paths even where the technological potential was obviously limited. In this way, although the number of materials looked at was small, a comprehensive set of data was acquired to determine their properties and behaviour.

9.1.1 Sample synthesis

The early part of the project was concerned especially with equipment setup and sample synthesis, which were lengthy investigations in themselves. In the case of the potassium-GIC synthesis, an economic and successful synthesis route was achieved that enabled the production of large quantities of the two materials used. The Ca-Li alloy route for making CaC_6 is a newer development, though successful in the group. Equipment problems made the removal of the GIC from the alloy difficult, and consequently the sample was not pure when made for neutron diffraction, nor in all probability that measured by TGA. Therein lies a challenge which was not able to be overcome; gaining simultaneous thermogravimetry and structural analysis on a sample. The sample could be loaded into the TGA with minimal oxidation once the loading process had been adapted by the manufacturers (under at least the partial influence of our suggestions and feedback) but could not be removed unharmed for further study. Although samples used for diffraction were taken, where possible, from the same batch as those destined for the IGA, simultaneous measurement of uptake and structure would be a great improvement.

The first three ammoniated calcium-GIC samples were made for the project by a team which included the author, and the fourth by the author alone. Further improvements in this method are certainly possible, in particular the time for which the metal-ammonia is condensed on the graphite and the method of removing the ammonia and priming the sample by annealing and outgassing, which will be discussed quantitatively below. Structural characterisation is most likely critical for this process, to be able to repeat the remarkable uptake measurement found in the second sample studied by TGA.

9.1.2 Thermogravimetry

The thermogravimetric investigation was able to characterise the uptake in samples where literature values were available. Comparison with the literature was a useful tool to determine the reliability of the results, especially because there were a number of issues with the TGA equipment which had an adverse impact on the results. To get an idea of the scale of the systematic errors on the instrument, a null-absorbing steel sample was used. Once an altered loading procedure had been given to us, and the equipment adjusted by the manufacturers to allow this, the samples were loaded with far less oxidation and the data began to look correspondingly better. There was still a problem with drift of the zero weight of a sample, that could not always be attributed to irreversible uptake of hydrogen. Although the hydrogen was purified, there was the potential for some small impurity uptake in the sample; it was not possible to characterise the gas in the sample chamber. A mass spectrometer or similar instrument would be required for this. However, there was no suspiciously large irreversible uptake reminiscent of moisture impurities, and only minimal irreversible uptake in the 77 K isotherms irrespective of the sample.

The buoyancy corrections were a significant source of error on the data. After some inaccurate weight settings prevented the software from correcting for buoyancy automatically, the author was able to set up a spreadsheet to do this manually, cross-referencing with samples for which the automatic correction worked. These were in complete agreement where the input parameters were identical. In the event this was a very useful tool for understanding the impact of the buoyancy on the final mass uptake and all of the data presented in the thermogravimetry results were analysed by this method, with agreement with the automatic correction where relevant.

The most important source of TGA error was the sample density. Direct

measurement of this using the IGA appeared to over-estimate the value, perhaps because nitrogen was not completely inert to the sample. The nitrogen uptake measurements on Papyex showed a small but finite uptake (<0.1 % at room temperature) which may have affected the density determination. Direct measurement of the volume was not effective either, because of the large void space in Papyex samples. Thus, it wasn't until a volume/pressure method had been employed using He to determine the density with pycnometry, that realistic values of sample density were available, and when used for the buoyancy correction, they corrected the isotherms to appear monomolecular in character; following that, they could be fitted to a Langmuir model and thus compared to literature.

9.1.3 Neutron diffraction

This section of work acquired comprehensive data on the systems studied, including unprecedented time-resolution on the KC_8H_x and the $KC_{24}(D_2)_x$ and $KC_{24}(ND_3)_x$ phase transitions. The data were compared with structures from literature and fitted to novel multilayer structures using Rietveld refinement, with limited success. This was primarily due to the unsuitability of the GSAS program and the difficulty of fitting large candidate structures. The phase transitions were according to the literature. The in-plane potassium-hydrogen structure remains elusive; if, as we postulate, the hydrogen is delocalised in adsorption sites, it will be difficult to view in diffraction. A greater insight into the temperature and pressure regime for the KC_8H_x transition was achieved, though time did not permit an entirely isothermal investigation. More data are required to fully map the in-plane hydride structure of the saturated stage-1 intercalate. Although it should have been possible to use a KC_8H_1 structure in the fitting and arrive at a 2/3 H occupancy value to fit with the known

saturated uptake in this system, GSAS did not fit this to a physical number. A different or updated fitting method should be able to achieve this. Alternatively, a candidate $KC_8H_{0.67}$ structure could be modelled either manually or using a first-principles calculation such as DFT.

The structural data of CaC_6 showed that the alloy method had synthesised the correct structure without significant Li-containing crystalline impurities. The heterogenous phase which made a significant proportion of the sample was fitted to a CaC_2 structure, the presence of which was already suspected from the overheating of the sample upon melting the graphite from the alloy in the glovebox. Here, the issue was that hot-air guns do not run well under argon. Some improvements in the sample synthesis and purification may be required.

Unfortunately it was not possible to carry out a diffraction experiment on the ammoniated Ca-GIC, in the light of the high value for uptake found in one sample. This is planned for future work.

9.1.4 Inelastic neutron scattering

The high incoherent scattering of H_2 and the high energy resolution of the IRIS instrument in this work gave an unprecedented insight into the dynamics of the hydrogen sited in $KC_{24}(H_2)_x$. As these had not been studied in this system before, a comprehensive area of investigation has been added to the evidence canon of AM-GICs. Particularly important was the repeat experiment on IRIS and the higher energies using TOSCA where the ortho-para composition was carefully controlled and the hydrogen coverage increased harmonically. The data were of significantly better quality than previous experiments [59] [77] [79], because of improved flux and resolution compared with earlier neutron instruments, and because the literature investigations showed

no sign of appreciating the effect of requiring the H_2 to be in the para ground state, thus maximising the intensity of the tunnelling and librational lines. The comparative coverage between the second IRIS and the TOSCA experiments appeared to be inconsistent, with the 14.7 meV line indicating excess hydrogen appearing by $x = 2$ on TOSCA but not on IRIS. Careful analysis of the dosing method revealed that the hydrogen concentration for TOSCA was an underestimation and in fact the $x = 2$ concentration was $x = 2.22$, making this quite consistent with saturation and non-sorbed hydrogen contributions to the spectra.

The availability, subsequent adaptation and physical justification of a siting model for the hydrogen in Cs- and RbC_{24}, following an investigation using an *ab initio* method, enabled this part of the investigation to be analysed more comprehensively than the diffraction and has led to the novel insight that the hydrogen is likely to be delocalised among three positions in a filled site. This confirms and goes further than previous theoretical treatment of these systems and is consistent with the INS data and, with the exception of the *c*-axis graphite-H_2 potential, the DFT results. Further work may be able to fit the diffraction work to the model, although a consequence of delocalisation is that hydrogen in-plane structure will not be visible in diffraction. As the model being developed is now to a strong degree quantitatively consistent with the data, this aim of the project is a good way towards fulfilment. A consistent picture of H_2 dynamics in KC_{24} now exists, demonstrably different from that of the other second stage GICs, which require revisiting to provide the same high-resolution INS analysis and evolved theoretical treatment achieved in this project. In progression from this, we can formulate some important implications for hydrogen storage in charged graphitic structures.

9.1.5 Hydrogen in KC_{24}

The hydrogen sorption of KC_{24} is the largest weight uptake known in a binary donor GIC at ambient pressure. As the study of hydrogen dynamics in this system was novel, the TGA measurements were useful complementary data with previous studies for comparison. Although an H_2 concentration (x) of up to 2.1 per K ion was reported in the past [42] [45], TGA measurements for the project found x to be a maximum of 1.74, with saturated values as low as 1.52. This was also found for the first inelastic neutron scattering experiment, where the saturation coverage was calculated to be $x = 1.55 \pm 0.13$. This discrepancy may be the result of individual sample morphology differences. There is a possibility that sample uptake measurements in the past were over-estimated; some authorities [120] found the maximum uptake to be $\sim$1.9. It is at least likely that the H_2 saturation value would vary with the metal content of the GIC; this was not always fixed stochiometrically by early researchers [79]. Alternatively, a good rationale is provided by the Stead model [80]; if, on cooling KC_{24} through the phase transition temperature T_{cl} (§ 3.3.1), KC_{28} domains are not seeded correctly or are pinned at domain edges, which may be c-axis Daumas-Hérold stacking domains (§ 3.1.2), then the domains may not be able to grow on hydrogen loading to provide two sorption sites per K ion. Without more comprehensive structural analysis of the domains, it is not possible to make this model definitive. In the case of the KC_{24} samples made during the current work, later samples were annealed at a slightly higher temperature than those used for the first INS experiment where this low saturation was recorded. The second INS experiment, for example, appeared to achieve saturation at $x = 2$. The evidence for this was that there was no 14.7 meV roton for this coverage, as would appear if some of the loaded H_2 was not physisorbed and instead took on liquid or solid form on the GIC outer surfaces. We have shown that high-resolution INS measurements reveal an apparently complex

variety of H_2 site barriers, have determined that a one-site model with fine structure best fits the observations, and have formulated an improved model of the siting that successfully reconciles a physical model and the experimental evidence, in which the hydrogen dynamics are explained by delocalisation of the molecule. It is clear that these data may be more informative about the in-plane structure of the hydrogenated GIC than diffraction measurements, although limited to short-range interactions. Further investigation of the ammoniated $KC_{24}(NH_3)_{1.8}$ system as a tuned hydrogen storage medium is required, although the uptake appears more promising in the divalent-metal-ammonia GIC with calcium.

9.1.6 Ammoniated Ca-GICs

The second ammoniated Ca-GIC sample placed in the IGA showed the remarkable uptake of 3.25±0.05 wt.% at 15 bar and 77 K, after a preliminary run showed 0.25 wt.%. Although certain measurements on the IGA were of questionable reliability (and were left from the results), this uptake measurement is reliable, firstly because it was repeated in another run after complete desorption, and secondly because it can be compared to the first in the sequence which was run shortly before and shows a far less noteworthy uptake. It seems as if some combination of the secondary annealing at 130°C and the presence of hydrogen from the first sorption improved the uptake capabilities by some 13 times! Later, taking the sample to room temperature was seen to destroy this capability. It is unfortunate that no structural data are known for this sample. In character, and depending on how quickly the ammonia was removed during the synthesis, the graphite is likely to be partially exfoliated, expanded considerably by remaining ammonia, and may be to a good degree amorphous. This would hint at a good volumetric potential for hydrogen stor-

age, though in comparison with the ammoniated K-GIC which did not seem to take up hydrogen (§ 8.1), the major difference is the size and charge of the Ca ion compared with the K. Further investigation of these expanded intercalate frameworks is essential as they appear to have potential for storage in excess of binary compounds.

9.2 The outlook for hydrogen storage

9.2.1 Project findings

To achieve the highest storage in a solid-state material such as an intercalate, it is important that all the host materials are lightweight. Even a material like K (atomic weight 39.1) is probably too far down the periodic table to be able to achieve more uptake than the 1.2 % in $KC_{24}(H_2)_2$ at 77 K. Graphite is lightweight and readily available; if doping or pillaring is able to optimise H_2 sorption, it must be done with species such as ammonia (molecular weight 17.03), lithium (atomic weight 6.9), or magnesium (atomic weight 24.3). Such considerations already underpin research into storage hydrides. In respect of intercalates, these materials are a challenge to use, either because they do not intercalate well, or do not readily dissolve in liquid ammonia.

The work on KC_{24} implies that pure binary GICs may only achieve monomolecular coverage, and in the case of monovalent-metal GICs, a maximum uptake of 2 H_2 molecules per metal ion is rationalised by modelling the binding energies of hydrogen in the layers and the H_2-H_2 repulsion. This suggests a surface density of 1 H_2 per graphite hexagon is very unlikely in GICs and nigh-on impossible in undoped graphites.

Fundamental implications for the understanding of hydrogen adsorption in

doped graphites and perhaps other materials follow from the delocalisation model for H_2 in KC_{24} we have formulated. The effect of delocalisation is with little doubt liable to increase the H_2-H_2 repulsion in the saturated material, decreasing the possible surface density in KC_{24} and similar compounds. The unexpectedly important contribution to the adsorption model from the quantum mechanics of H_2 suggests that successful models to explain adsorption will have to incorporate this if they are to reproduce experimental findings.

How the adsorption changes when the doping ion is divalent, and whether more charge can be transferred to the lattice by intercalating trivalent species, is a priority for future research. In this case, DFT calculations may provide a more ready route to test the hypotheses. Remembering that KC_{24} has empty graphite layers from which, conceivably, hydrogen is barred, one can see a potential improvement by manufacturing a stage-1 dilute KC_{12-14} material, with attendant uptake of 1.9-2.2 wt.%. This might be achieved using a route similar to Akuzawa *et al.* [65] or by using ammonia, in which case residual NH_3 would impose a weight penalty on the system; however, opening up the layers should provide much more volume for H_2. There is the hint [115] that the presence of ammonia impedes the uptake of hydrogen, either by excluding internal volume or by charge-shielding the ions so no deep tunnelling site exists. In this case, removing as much ammonia as possible without the structure collapsing is the target, and increasing the charge transfer by using divalent intercalants.

Looking at hydride-style storage in graphite is not likely to be a productive path to follow, because the same energetic and kinetic issues associated with 'bare' hydride research attend, with a weight penalty from the graphite. The potential up-side of this, however, is that the sorption kinetics might be improved by the high surface area represented by the graphite. The project has attained useful insights into this process and an ongoing attempt should

be made to model the transition in KC_8H_x.

The advantage physisorptive storage routes have over chemisorption is relative ease of sorption and good reversibility. It is necessary to improve their storage density and bring their temperature of operation up from cryogenic regions if they are to be successful storage media. Improving the enthalpy of adsorption by increasing it from the AM-GIC $\sim$12 kJ mol^{-1} to perhaps 20-25 kJ mol^{-1} should lead to a better sorptive ability at room temperature without requiring too much effort to desorb. In this there is a role for moderate pressurisation, perhaps up to 20 bar, if this is required to attain maximum weight uptake at 300 K. Further studies of nanostructured carbons are required, but without additional doping in the manner of intercalates there is little chance of the requisite storage capabilities in these alone.

In the near term, it seems likely that a nano-engineered metal-hydride will become the first successful solid-state hydrogen storage material. However, there is still potential for large-scale hydrogen storage in expanded intercalates and this is an area in which research will continue to be rewarding. We shall now consider the possibilities...

9.2.2 New pillared GICs

The intercalation of fullerenes into graphite would create a GIC with interlayer spacing of 12.530 Å [47]. This is an exotic example of how expanded intercalates can be constructed to increase internal volume. It has been noted in the discussions following the current investigation that the charge-doping of the graphite appears to be equally vital to increase the potential of hydrogen sites. The work done on doping with ammonia and potassium shows that expanded pillared GICs are not difficult to construct. A suitable hydrogen

storage material requires multilayer hydrogen coverage within layers. For a monovalent-metal binary GIC such as KC_{24}, we assume the 5.35 Å interlayer spacing is the minimum which H_2 may enter. On entering, the lattice expands locally to 5.64-5.67 Å (§ 8.2). To achieve double layer coverage, a conservative estimate of the layer spacing is this value added to the long-axis dimension of H_2, 2.4 Å [42]; that is, 8.04-8.07 Å (Of course, it is unlikely that both H_2 molecules will orient exactly perpendicular to the graphite planes, but this estimate has not added an H_2-H_2 buffer zone either). No donor GIC with this spacing looks likely to provide this sort of uptake (the $Mg(NH_3)_{2-3}C_{32}$ GIC in Table 3.2, interlayer spacing 15.95 Å, is stage-4), so new pillaring mechanisms are required. Intercalation of divalent or even trivalent metals by alloy or liquid ammonia routes may well allow an expanded GIC with strong graphite charging; this is likely to be conducive to a higher density of binding sites and will enable multilayer sorption of hydrogen. The five lightest metals are Li, Be, Na, Mg and Al and it is these, singly or in combination, which would ideally be used, although there seems to be good potential in Ca-GICs; this will become apparent with further research. As more is learned about the physisorption process and H_2 siting in GICs, an optimised route can be followed to tune them for hydrogen storage.

Bibliography

[1] R. C. Duncan and W. Youngquist. *Natural Resources Research* **8**, 219-232 (1999).

[2] R. W. Bentley. *Energy Policy* **30**, 189-205 (2002).

[3] "Contribution of working group I to the Fourth Assessment Report of the Intergovernmental Panel on Climate Change: Summary for policy-makers", tech. rep., IPCC, 2007.

[4] N. Oreskes. *Science* **306**, 1686 (2004).

[5] IPCC. "Fourth Assessment Report", available at http://www.ipcc.ch/, 2007.

[6] C. D. Keeling and T. P. Whorf. "Atmospheric CO_2 records from sites in the SIO air sampling network", http://cdiac.ornl.gov/trends/CO2/graphics/mlo145e_thrudc04.pdf, 2005.

[7] D. M. Etheridge, L. P. Steele, R. L. Langenfelds, and R. J. Francey. *J. Geophys. Res.* **101**, D24115 (1996).

[8] J. R. Petit, J. Jouzel, D. Raynard, N. I. Barkov, and J.-M. B. et al. *Nature* **399**, 429-436 (1999).

[9] P. Brohan, J. J. Kennedy, I. Harris, S. F. B. Tett, and P. D. Jones. *J. Geophys. Res.* **111**, D12106 (2006).

[10] P. D. Jones and M. E. Mann. *Rev. Geophys.* **42**, RG2002 (2004).

[11] N. Stern, *Stern Review on the Economics of Climate Change*. Cambridge University Press, 2006.

[12] U. N. F. C. on Climate Change. "Kyoto protocol", available at http://unfccc.int/kyoto_protocol/items/2830.php, 1998.

[13] M. Schuckert, "CUTE: a detailed summary of achievements", tech. rep., EvoBus GmBH, 2006.

[14] M. Wharmby. "The London Bus page", http://www.londonbuspage.com/040119.htm, 2004.

[15] "History of fuel cells", http://www.fuelcelltoday.com/FuelCellToday/EducationCentre/EducationCentreExternal/EduCentreDisplay/0,1741,History,00.html

[16] S. Tanisho and Y. Ishiwata. *Hydrogen Energy* **19**, 807-812 (1994).

[17] G. A. Deluga, J. R. Salge, L. D. Schmidt, and X. E. Verykios. *Science* **303**, 993 (2004).

[18] N. Jacobsen, B. Tegner, E. Schroeder, P. Hyldgaard, and B. I. Lundqvist. *Comp. Mat. Sci.* **24**, 273-277 (2002).

[19] "www1.eere.energy.gov/hydrogenandfuelcells/pdfs/freedomcar_targets_explanations.pdf" US Department of Energy.

[20] A. Züttel. *Naturwissenschaften* **91**, 157-172 (2004).

[21] A. Weisberg, "Hydrogen, fuel cells and infrastructure technologies", US Department of Energy, FY2003 progress report, 2003.

[22] J. Wozniak, "Development of a compressed hydrogen gas integrated storage system (CH2-ISS) for fuel cell vehicles", US Department of Energy, FY2003 progress report, 2003.

[23] N. Sirosh, "Hydrogen composite tank project", US Department of Energy, FY2003 progress report, 2003.

[24] W. Dubno, "Low cost, high efficiency, high pressure hydrogen storage", US Department of Energy, FY2006 progress report, 2006.

[25] L. Zhou. *Renew. and Sust. Energy Rev.* **9**, 395-408 (2005).

[26] L. Schlapbach and A. Züttel. *Nature* **414**, 353-358 (2001).

[27] A. M. Seayad and D. M. Antonelli. *Adv. Mat.* **16**, 765-777 (2004).

[28] G. Sandrock. *J. All. Comp.* **293-295**, 877-888 (1999).

[29] A. Zaluska, L. Zaluski, and J. O. Ström-Olsen. *J. All. Comp.* **298**, 125-134 (2000).

[30] K. J. Gross, G. J. Thomas, and C. M. Jensen. *J. All. Comp.* **330-332**, 683-690 (2002).

[31] I. P. Silvera. *Rev. Mod. Phys.* **52**, 393 (1980).

[32] S. Patchkovskii, J. S. Tse, S. N. Yurchenko, L. Zhechkov, T. Heine, and G. Seifert. *Proc. Nat. Acad. Sci.* **102**, 10439-10444 (2005).

[33] S. L. James. *Chem. Soc. Rev.* **32**, 276-288 (2003).

[34] R. B. Weisman. *Nature Mat.* **2**, 569 (2003).

[35] A. Chambers, C. Park, R. T. K. Baker, and N. M. Rodriguez. *J. Phys. Chem. B* **102**, 4253 (1998).

[36] Y. Ye, C. C. Ahn, C. Witham, B. Fultz, J. Liu, A. G. Rinzler, D. Colbert, K. A. Smith, and R. E. Smalley. *Appl. Phys. Lett.* **74**, 2307 (1999).

[37] P. Chen, X. Wu, J. Lin, and K. L. Tan. *Science* **285**, 91 (1999).

[38] E. Poirier, R. Chanine, and T. K. Bose. *Int. J. Hydrogen Energy* **26**, 831-835 (2001).

[39] F. E. Pinkerton, B. G. Wicke, C. H. Olk, G. G. Tibbetts, G. P. Meisner, M. S. Meyer, and J. F. Herbst. *J. Phys. Chem. B* **104**, 9460-9467 (2000).

[40] P. Bénard and R. Chahine. *Scripta Materialia* **56**, 803-808 (2007).

[41] M. S. Dresselhaus and G. Dresselhaus. *Adv. Phys.* **51**, 1-186 (2002).

[42] T. Enoki, S. Suzuki, and M. Endo, *Graphite Intercalation Compounds and Applications*. Oxford University Press, 2003.

[43] G. J. Martin, *Computational and Experimental Studies of Ternary Intercalation Compounds of Graphite*. PhD thesis, UCL, 2002.

[44] N. Daumas and A. Hérold. *C. r. hebd. Séanc. Acad. Sci. Paris C* **268**, 373 (1969).

[45] S. A. Solin and H. Zabel. *Adv. Phys.* **37**, 87-254 (1988).

[46] T. E. Weller, M. Ellerby, S. S. Saxena, R. Smith, and N. Skipper. *Nature Phys.* **1** (2005).

[47] S. Saito and A. Oshiyama. *Phys. Rev. B* **49**, 17413-17419 (1994).

[48] A. C. Dillon, K. M. Jones, T. A. Bekkedahl, C. H. Kiang, D. S. Bethune, and M. J. Heben. *Nature* **386**, 377-379 (1997).

[49] W. Deng, X. Xu, and W. A. Goddard. *Phys. Rev. Lett.* **92**, 166103 (2004).

[50] N. Emery, C. Hérold, and P. Lagrange. *J. Solid State Chem.* **178**, 2947-2952 (2005).

[51] Z. Kurban and F. Norris, "An Investigation into the Synthesis of CaC_6 and its Superconducting Properties", final year project rep., UCL, 2006.

[52] C. Howard and M. Ellerby, "Investigations into GICs". Ongoing investigation, 2007.

[53] W. Rüdorff and R. Zeller. *Z. Anorg. allg. Chem.* **279**, 182 (1955).

[54] W. Rüdorff. *Chimia* **19**, 489 (1965).

[55] S. A. Solin. *J. de Physique IV* **1**, C5-311 (1991).

[56] B. R. York and S. A. Solin. *Phys. Rev. B* **31**, 8206-8220 (1985).

[57] A. Lovell, "The Search for Exotic Superconductivity in Yb-intercalated MoS_2", final year project rep., UCL, 2003.

[58] S. Leake, "Search for Superconductivity and Hydrogen Uptake in Calcium-intercalated Graphite Powder", final year project rep., UCL, 2006.

[59] C. J. Carlile, G. J. Kearley, G. Lindsell, and J. W. White. *Physica B* **241-243**, 491-494 (1998).

[60] E. P. Gilbert, P. A. Reynolds, and J. W. White. *J. Chem. Soc.; Farad. Trans.* **94**, 1861-1868 (1998).

[61] T. Enoki, S. Miyajima, M. Sano, and H. Inokuchi. *J. Mater. Res.* **5**, 435-466 (1990).

[62] P. Lagrange, D. Guerard, and A. Hérold. *Ann. Chim. E* **3**, 143 (1978).

[63] K. Watanabe, M. Soma, T. Onishi, and K. Tamaru. *Nature, Phys. Sci.* **233**, 160 (1971).

[64] K. Watanabe, T. Kondow, M. Soma, T. Onishi, and K. Tamaru. *Proc. R. Sci. Lond. A* **333**, 51-67 (1973).

[65] N. Akuzawa, T. Sakamoto, H. Fujimoto, T. Kasuu, and Y. Takahashi. *Synth. Met.* **73**, 41-44 (1995).

[66] T. Trewern, R. K. Thomas, G. Naylor, and J. W. White. *J. Chem. Soc., Faraday Trans. I* **78**, 2369-2385 (1982).

[67] W. Rüdorff and E. Schultze. *Z. Anorg. Chem.* **277**, 156-71 (1954).

[68] D. E. Nixon and G. S. Parry. *Brit. J. Appl. Phys.* **1**, 291 (1968).

[69] H. Zabel, A. Magerl, A. J. Dianoux, and J. J. Rush. *Phys. Rev. Lett.* **50**, 2094 (1983).

[70] J. B. Hastings and W. D. Ellenson. *Phys. Rev. Let.* **42**, 1552-1556 (1979).

[71] M. J. Winokur and R. Clarke. *Phys. Rev. Let.* **54**, 811-814 (1985).

[72] M. J. Winokur and R. Clarke. *Phys. Rev. B* **34**, 4948-4951 (1986).

[73] D. Saehr. *Bull. Soc. chim. Fr.,* , 1287 (1964).

[74] A. Hérold and P. Lagrange. *Mat. Sci. Eng.* **31**, 33-37 (1977).

[75] M. Colin and A. Hérold. *Bull. Soc. Chim. Fr.* **6**, 1982 (1971).

[76] S. Miyajima, T. Chiba, T. Enoki, H. Inokuchi, and M. Sano. *Phys. Rev. B* **37**, 3246 (1988).

[77] J. P. Beaufils, T. Crowley, T. Rayment, R. K. Thomas, and J. W. White. *Mol. Phys.* **44**, 1257-1269 (1981).

[78] G. Lindsell, *Structure and Dynamics of Graphite Intercalation Compounds*. PhD thesis, Australian National University, 1998.

[79] W. J. Stead, P. Meehan, and J. W. White. *J. Chem. Soc., Faraday Trans. 2* **84**, 1655-1668 (1988).

[80] W. J. Stead, I. P. Jackson, J. McCaffrey, and J. W. White. *J. Chem. Soc., Faraday Trans. 2* **84**, 1669-1682 (1988).

[81] A. P. Smith, R. Benedek, F. R. Trouw, M. Minkoff, and L. H. Yang. *Phys. Rev. B* **53**, 10187-10199 (1996).

[82] N. T. Skipper. "Electronic solutions and GIC hydrogen storage", presentation, 2007.

[83] E. Stumpp, H. Alheid, M. Schwarz, J. Janssen, and W. Müller-Warmuth. *J. Phys. Chem. Solids* **57**, 925-930 (1996).

[84] P. R. Hirst, J. W. White, Z. A. Bowden, L. M. Needham, and A. D. Taylor. *Chem. Phys. Let.* **147**, 228-230 (1988).

[85] S. J. Clark, M. D. Segall, C. J. Pickard, P. J. Hasnip, M. J. Probert, K. Refson, and M. C. Payne. *Zeitschrift für Kristallographie* **220**, 567-570 (2005).

[86] H. Cheng, G. Pez, G. Kern, G. Kresse, and J. Hafner. *J. Phys. Chem. B* **105**, 736-742 (2001).

[87] F. Fernandez-Alonso and K. Refson, "CASTEP modelling of H_2 in GICs", unpublished work, 2007.

[88] G. L. Squires, *Introduction to the Theory of Thermal Neutron Scattering*. Dover Publications, 1996.

[89] H. Thompson, *The Structure and Dynamics of Alkali-metal Amine Solutions*. PhD thesis, UCL, 2004.

[90] C. A. Howard, *Metal-ammonia-fulleride Solutions*. PhD thesis, UCL, 2005.

[91] A.-J. Dianoux and G. Lander, eds., *Neutron data booklet*. Institute Laue-Langevin, 2002.

[92] CCLRC, "ISIS facility annual report 2005", Rutherford Appleton Laboratory, RAL-TR-2005-050, 2005.

[93] R. Eccleston, "ISIS facility annual report 1997", Rutherford Appleton Laboratory, http://www.isis.rl.ac.uk/ISIS97/, 1997.

[94] A. Larson and R. V. Dreele, "General Structure Analysis System (GSAS)", Report LAUR 86-748, Los Alamos Nat. Lab., 2004.

[95] B. H. Toby. *J. Appl. Cryst.* **34**, 210-21 (2001).

[96] H. M. Rietveld. *J. Appl. Cryst.* **2**, 65-71 (1969).

[97] W. A. Dollase. *J. Appl. Cryst.* **19**, 267-272 (1986).

[98] "IGA systems user manual", Hiden Isochema Ltd., 2002.

[99] K. S. W. Sing. *Pure & Appl. Chem.* **54**, 2201-2218 (1982).

[100] I. Langmuir. *J. Am. Chem. Soc.* **38**, 2221 (1916).

[101] S. Brunauer, P. H. Emmett, and E. Teller. *J. Am. Chem. Soc.* **60**, 309 (1938).

[102] S. Brunauer, L. Deming, W. E. Deming, and E. Teller. *J. Am. Chem. Soc.* **62**, 1723 (1940).

[103] M. Avrami. *J. Chem. Phys.* **7**, 1103 (1939).

[104] M. Avrami. *J. Chem. Phys.* **8**, 212 (1940).

[105] G. W. C. Kaye and T. H. Laby, *Tables of Physical and Chemical Constants (15th. ed.)*. Longman, 1986.

[106] R. I. Smith and S. Hull, *User guide for the Polaris powder diffractometer at ISIS*. Rutherford Appleton Laboratory, RAL-TR-97-038, 1997.

[107] M. A. Adams, W. S. Howells, and M. T. F. Telling, *The IRIS user guide: 2nd edition*. Rutherford Appleton Laboratory, RAL-TR-2001-002, 2001.

[108] J. K. Walters, N. T. Skipper, and A. K. Soper. *Chem. Phys. Lett.* **300**, 444-450 (1999).

[109] S. F. Parker, J. Tomkinson, A. J. Ramirez-Cuesta, and D. Colognesi, *The TOSCA user guide*. Rutherford Appleton Laboratory, RAL-TR-2003-015, 2003.

[110] "Papyex factsheet", Le Carbone (UK)

[111] T. Enoki, M. Sano, and H. Inokuchi. *J. Chem. Phys.* **78**, 2017 (1983).

[112] T. Enoki, M. Sano, and H. Inokuchi. *Phys. Rev. B* **32**, 2497 (1985).

[113] A. Lovell, N. T. Skipper, S. M. Bennington, and R. I. Smith. *J. All. Comp.* **446-447**, 397-401 (2007).

[114] J. A. Young and J. U. Koppel. *Phys. Rev.* **135**, A603-A611 (1964).

[115] A. Lovell, S. M. Bennington, N. T. Skipper, C. Gejke, H. Thompson, and M. A. Adams. *Physica B* **385-386**, 163-165 (2006).

[116] F. Fernandez-Alonso, private communication, 2007.

[117] A. D. McLean and M. Yoshmin. *J. Chem. Phys.* **45**, 3676 (1966).

[118] W. Kolos and L. Wolniewicz. *J. Chem. Phys.* **46**, 1426 (1967).

[119] J. G. Vitillo, A. Damin, A. Zecchina, and G. Ricchiardi. *J. Chem. Phys.* **122**, 114311 (2005).

[120] P. Lagrange, A. Metrot, and A. Hérold. *C. r. hebd. Scéanc. Acad. Sci., Paris C* **275**, 765 (1972).